DO DO DO DO
DO DO DO DO
DO DO
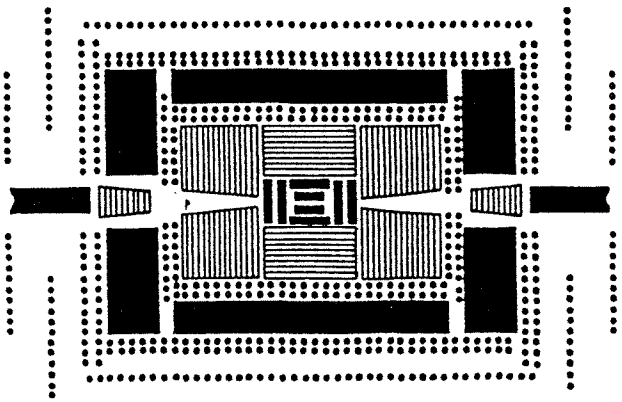
DO DO
DO DO
DO DO
DO DO
DO DO DO DO
DO DO DO DO

DESIGN REPORT

THE DO EXPERIMENT
AT THE FERMILAB ANTIPROTON-PROTON COLLIDER

OCTOBER 1984

THE DØ COLLABORATION

S. Aronson, B. Gibbard, H. Gordon, W. Guryn, S. Kahn, M. Month, M. Murtagh,
S. Prototopescu, I. Stumer, and P. Yamin
Brookhaven National Laboratory

D. Cutts, J. Hoftun, R. Lanou, and R. Zeller
Brown University

P. Franzini, D. Son, P. M. Tuts, and S. Youssef
Columbia University

C. Brown, B. Cox, R. Dixon, G. Dugan, D. Eartly, H. Fenker,
D. Finley, D. Green, H. Haggerty, S. Hansen, A. Ito,
H. Jostlein, E. Malamud, P. Martin, P. Mazur, J. McCarthy,
R. Raja, R. Smith, M. Takasaki and R. Yamada
Fermi National Accelerator Laboratory

H. Goldman
Florida State University

A. Clark, L. Kerth, S. Loken, M. Strovink, and W. Wenzel
Lawrence Berkeley Laboratory

S. Kunori and P. Rapp
University of Maryland

M. Abolins, R. Brock, D. Edmunds, J. Linnemann, D. Owen,
B. Pope, S. Stampke, M. Tartaglia, and H. Weerts
Michigan State University

D. Buchholz and B. Gobbi
Northwestern University

E. Gardella, W. Kononenko, W. Selove, G. Theodosiou, and R. Van Berg
University of Pennsylvania

T. Ferbel, F. Lobkowicz, and P. Slattery
University of Rochester

Y. Ducros, R. Hubbard, P. Mangeot, B. Mansoulié, J. Teiger,
H. Zaccone, and A. Zylberstejn
CEN Saclay

M. Adams, R. Engelmann, G. Finocchiaro, P. Grannis, D. Hedin,
J. Kirz, J. Lee-Franzini, S. Linn, D. Lloyd-Owen, M. Marx,
R. McCarthy, L. Romero, and R. D. Schamberger,
State University of New York at Stony Brook

and

J. Ficenec
Virginia Polytechnic Institute

1. INTRODUCTION

The experiment described here for the D0 intersection of the Fermilab Collider has come into being over the course of the past fifteen months. The impetus was a decision by the Fermilab Program Advisory Committee to call for a new general purpose detector whose focus (electron and muon identification, excellent calorimetric energy and spatial resolution) would complement the CDF detector at B0. The basic design goals and intended implementation were described in a Design Report (December 1983). This report served as a guide for various reviews by external committees and internal panels; it also gave the focus for continuation of design effort, cost analyses, time sequencing, and a program of research and development projects undertaken within the collaboration.

At the present time, the design of the detector has matured to the point where its details are much better understood. Constraints upon the detector have been explored, both with respect to internal conflicts for available space in the collision hall and also with respect to cost optimization. Considerable research has been conducted upon detector components, techniques for fabrication, and data collection. In addition, new physics results have been presented which have refined our aims and priorities. For all of these reasons, it is appropriate to give a new statement of the goals and design of the D0 detector. This is found in the succeeding chapters of this Design Report.

The justification for building a major second detector at the Collider is several-fold. The most general is that new results and discoveries must be subjected to confirmation in more than one independent experiment. Since the energy regime available at TeV I is attainable in no other machine, a second general experiment is called for. A second general justification comes from

the need to exploit the TeV I facility as fully as possible, given its large capital expense. This is underscored by the current plans to proceed with the SSC and the need to explore alternate detector strategies for that collider. The vitality of the U.S. High Energy Physics program in the 1990's is dependent upon a vigorous effort at the existing machines and by the influx of the best new talent available. The third major justification stems from the anticipated physics discoveries at the Collider. All signs point to an extremely rich harvest of new results; maximum exploitation of this potential requires a set of detectors with complementary strengths.

In examining the physics menu (Chapter 2) we should keep in mind two classes of phenomena that the DØ experiment will be called upon to study. The first is the examination of known phenomena with predictable improvements in precision. These programmatic issues are described in sections 2.1 and 2.2 and include a large variety of specific questions, e.g., the Z and W widths and masses, measurements of direct photons, studies of QCD processes, etc. All of these questions bear upon our knowledge of the currently existing models of particle structure and dynamics; the experimental goal in this area is to refine the parameters of these models and even to show the way toward extensions of them by revealing quantitative discrepancies among the parameters. These topics form the knowable backbone of the DØ program (and also the programs of the Z° factory e^+e^- experiments now planned). Because these questions are known and are being addressed in a variety of other experiments, it is natural to expect some evolution in our understanding in these areas.

The second class of phenomena which the DØ experiment will address are more difficult to itemize and describe--but because of the unique opportunity afforded by the TeV I collider, the most important to consider carefully.

This class is the range of new and unexplored physics which is opened up by the combination of energy and luminosity increase over the CERN Collider. Here it should be borne in mind that hadron collisions have historically been enormously fruitful in uncovering major new discoveries, owing to the large event rates and the relatively broad-band searches that are enabled. In addition to these well-known advantages for hadron colliders, there is now emerging a gratifying simplicity to hadronic events; the number of truly fundamental measurable states is small (jets and leptons) and their multiplicity in very high energy collisions is also small. The searches for new phenomena are themselves partly guided by tentative models for major new theoretical frameworks and each such model predicts certain types of new states or behavior. The experiment should measure up to this list very well, since we believe that these models are at least representative of the kinds of new physics which will emergy in the energy domain uniquely explored at TeV I. A representative sample of these new particle searches is described in section 2.3.

An even more crucial benchmark for the DO experiment can be found in the collection of peculiar indications from UA1 and UA2 known as the "Zoo events." These events, though not yet substantiated as evidence for new physics, do strongly reinforce our belief that the mass scale from 100 to 500 GeV/c^2 should yield some striking new phenomenology. They have the arresting property that, if correct, they do not fit easily into any of the existing frameworks. We have therefore the prospect that experimental observations in the TeV I range will lead to the theoretical understanding of particle physics by suggesting frameworks which are not yet formulated. It is very instructive to examine the general properties of the Zoo events, since they provide an apt guide to the desired properties of a newly designed experiment like DO. These

This class is the range of new and unexplored physics which is opened up by the combination of energy and luminosity increase over the CERN Collider. Here it should be borne in mind that hadron collisions have historically been enormously fruitful in uncovering major new discoveries, owing to the large event rates and the relatively broad-band searches that are enabled. In addition to these well-known advantages for hadron colliders, there is now emerging a gratifying simplicity to hadronic events; the number of truly fundamental measurable states is small (jets and leptons) and their multiplicity in very high energy collisions is also small. The searches for new phenomena are themselves partly guided by tentative models for major new theoretical frameworks and each such model predicts certain types of new states or behavior. The experiment should measure up to this list very well, since we believe that these models are at least representative of the kinds of new physics which will emergy in the energy domain uniquely explored at TeV I. A representative sample of these new particle searches is described in section 2.3.

An even more crucial benchmark for the DO experiment can be found in the collection of peculiar indications from UA1 and UA2 known as the "Zoo events." These events, though not yet substantiated as evidence for new physics, do strongly reinforce our belief that the mass scale from 100 to 500 GeV/c^2 should yield some striking new phenomenology. They have the arresting property that, if correct, they do not fit easily into any of the existing frameworks. We have therefore the prospect that experimental observations in the TeV I range will lead to the theoretical understanding of particle physics by suggesting frameworks which are not yet formulated. It is very instructive to examine the general properties of the Zoo events, since they provide an apt guide to the desired properties of a newly designed experiment like DO. These

events are described in more detail in section 2.3.7. They can be characterized collectively as rare configurations of three elements--jets, leptons, and missing p_T--in such combinations as to be unlikely from known phenomena. The indications include peculiar di-jets, single jets plus missing p_T, correlations of jets, leptons, and missing p_T, and multilepton signals. The DØ detector described in this report has been optimized to measure the three main ingredients of the Zoo events as fully and accurately as possible. With its stress on measurement of jets, both electrons and muons, and on missing p_T, the DØ Detector is truly the first of the second-generation large hadron collider experiments.

The detector itself is described in Chapters 4 through 8. Its design has been guided by the desire for maximum simplicity and homogeneity. There are just three major detector systems in the detector, each of which subtends the maximum possible solid angle. Although the coverage is broken into central, forward, and backward angular regions, the detector systems in these regions are as nearly similar as can be made. The detector is made as compact as possible in order to keep its cost down; this has been achieved by avoiding a central magnetic field and by using uranium as the absorber material for the calorimetry. Use of the minimum number of types of detectors has been stressed also in order to keep development and fabrication times as short as possible. The goal is to bring the DØ detector into operation as rapidly as possible so as to obtain the greatest possible utilization of the Fermilab Collider.

The detector described in this report is, in most general properties, similar to that presented in the December 1983 Design Report. The efforts of collaboration since that time have resulted in a number of detailed changes, improvements or specifications. The present detector design has removed the

ambiguities or conflicts present in the earlier report and represents a coherent and complete picture of the experimental apparatus. We imagine however that some further detailed evolution will occur. In many areas, we are pursuing and evaluating options which will improve the performance or reduce the overall cost. This activity will continue for the next year or so in the form of research and development programs, beam tests of prototypes, continuation of mechanical design studies, and bench tests of models of mechanical, electronic, or data acquisition systems.

2. PHYSICS AT DØ

The range of physics which can be addressed at Tev I is enormous and has been discussed at length in many reviews,[1] proposals[2]--and recently in terms of results from the CERN $Sp\bar{p}S$ Collider experiments. In this chapter, we give a selection of experimental questions which have focused our thinking about an experiment at DØ, with particular emphasis on those which we feel can benefit from the strengths built into the DØ design. In presenting this list, we should bear in mind the likely modifications of CERN $Sp\bar{p}S$ experiments prior to our turn-on as well as the strong points of the CDF design for BØ.

The success of UA1 and UA2 in isolating the intermediate vector bosons is well known. The utility of good lepton identification and energy measurement, together with a hadron calorimeter capable of resolving jets and inferring the presence of missing transverse energy has been amply demonstrated. The CERN program will continue over the next few years and upgrades of the two major detectors are likely. Making the assumption[3] that the mean luminosity of $Sp\bar{p}S$ will be 5×10^{29} $cm^{-2}sec^{-1}$ over the next three years and that the experimental live time will be 1.6×10^{7} sec, leads to the expectation of about 200 $Z^0 \rightarrow e^+e^-$ events and 2000 $W^{\pm} \rightarrow e^{\pm}\nu$ events. Plans to raise the energy to 630 GeV are being made which should increase the cross sections by about 30%. With event samples of this order it is clear that many of the main features of W and Z should be well established. In particular, we may expect that the W mass will be measured to within about 0.3 GeV and the Z-W mass difference to within 0.8 GeV. The V,A structure of the charged current should be clearly manifest in the W-decay asymmetry. Jet physics should be well studied out to p_T = 200 GeV/c, yielding cross sections, angular distributions, fragmentation functions, and multijet to two-jet ratios. We may expect that the evidence relating to the top quark existence, seen through $W \rightarrow t\bar{b}$ decay, will be

solidified. The various hints of new effects in the mass region above the W and Z will also be solidified.

In the face of these expected results from CERN, it is useful to reexamine the program of physics that can be anticipated at Tev I. The general situation is that the standard model has been enormously successful thus far. However, much of the theoretical literature of the past several years has focused on the necessity of augmenting the standard model in some way. Although the popular notions on how to complete the picture may be wrong, it is useful to note that almost all such models postulate observable new phenomena emerging in the mass region $100 \leq m \leq 500$ GeV/c^2--or in deviations from orthodoxy in W and Z parameters at the level of radiative corrections. It is also true that the CERN experiments themselves see weak evidence for new phenomena in this mass range. If correct, some of these effects may not fit easily into the usual extensions to the standard model. Thus the role of experiments at Tev I will be, in our view, to search for evidence of new ingredients and to solidify and clarify the existing anomalies. The combination of good luminosity and high energy should combine to give marked improvement in our ability to find such new phenomena. The fact that the mass scale accessible will be well into the region where new states are predicted to exist should make Tev I a premier search machine.

In the discussion of specific topics below, we shall assume a standard run to be four months of running with 50% efficiency, at $\mathcal{L} = 10^{30}$ cm^{-2}sec^{-1} ($\int \mathcal{L} dt = 5\times10^{36}$ cm^{-2} = 5 pb^{-1}). Given the cross section in Fig. 2.1,[4] one expects about 1500 $Z^0 \to e^+e^-$ (and as many $Z^0 \to \mu^+\mu^-$), depending on the scaling violations assumed, and about 15,000 $W^\pm \to e^\pm\nu$ (and also $W^\pm \to \mu^\pm\nu$). Thus even for standard studies of the W and Z, the improvement in statistical error could be nearly a factor of three, compared with the integrated running of the CERN collider up to 1988.

2.1. PRECISION TESTS IN THE INTERMEDIATE BOSON SECTOR

2.1.1 Z and W Mass Measurements

A measurement of particular interest, accessible only in hadron machines until LEP II, is the mass ratio of W and Z. The measured masses, m_W and m_Z can be used to determine

$$\sin\theta_W = \frac{38.5\ \text{GeV}}{m_W},$$

and

$$\rho = \frac{m_W^2}{m_Z^2 \cos^2\theta_W}.$$

The mass of the Z^0 can be best measured via the decay $Z \to e^+e^-$. Simulations indicate an error δm_Z of less than 50 MeV from statistical sources alone. However m_W cannot be measured directly by this method so the precision in m_Z is less useful. An interesting method which can be employed for both m_W and m_Z has been suggested[5]; it employs the distribution in the transverse mass constructed from the p_T for an observed lepton and an inferred neutrino,

$$m_T^2 = 2E_T^{\ell} E_T^{\nu} (1 - \cos\theta_{\ell\nu}),$$

where E_T^{ℓ} is the transverse energy of e or μ, E_T^{ν} is the missing transverse energy in the event (after ignoring the second charged lepton in the case of the $Z^0 \to \ell^+\ell^-$), and $\theta_{\ell\nu}$ is the angle in the transverse plane between the two. Figure 2.2 shows the expected m_T distribution for the W under two extreme assumptions on the p_T for the W. The Jacobian peak near $m_T = m_W$ is quite pronounced and is largely insensitive to the p_T of the W.[6] The dominant effects in smearing this peak are the physical width of the boson and the resolution in missing E_T. A study[6] of this method, using missing E_T resolutions appropriate to UA1 ($\delta E_T = 0.6\sqrt{\Sigma E_T}$) indicates mass errors δm_W = 80 MeV

and δm_Z = 250 MeV, for decays involving electrons. The corresponding muon decays would yield errors about twice as large if muon momenta were measured to within 20%. (The missing E_T resolution is dominated in a hermetic detector like UAl by hadron energy resolution; improvement in that resolution is expected to yield proportional gains in missing E_T resolution.)

Given these mass measurements of the W, the value of $\sin^2\theta_w$ can be determined with statistical precision of ±0.0005, so systematic effects must obviously be considered. Theoretical uncertainties in the radiative correction (itself about 6% of m_W) will also be present. The major systematic error here is in the energy scale for electrons. In principle, this can be calibrated through the Z^0 mass measurement and comparison with the e^+e^- determination of m_Z. This should give control of systematic errors on m_W to within 0.5% and thus an error on $\sin^2\theta_w$ of about 0.0025. Such a measurement would be most useful, both in comparing against theoretical values from Grand Unified Theories and with low energy measurements from neutrino scattering.

The measurement of the ρ parameter is a direct look at possible new ingredients in the standard model.[7] For the standard model without modification, ρ = 1. New states (heavy quarks, Higgs, Technicolor bosons, etc.) modify the value of ρ if present. Measurement of m_W and m_Z by the same method in the same experiment should give a nearly systematic free measurement of ρ to a precision of about 0.005. This, for example, would translate into an upper bound on the t-quark mass of about 130 GeV[8] if only Standard Model ingredients were present.

2.1.2 Z and W Width Measurements

Measurement of Γ_Z has been identified as being of particular interest due to its sensitivity to extra generations of light neutrino pairs. Cosmological

constraints[9] suggest an upper bound on light neutrino generations of 3 or 4. The direct experimental current limit on N_ν is about 44 (at 95% confidence level), based on an upper limit to the Z^0 width.[10] With high statistics and good electromagnetic energy resolution, considerable improvement can be made. Figure 2.3 shows the e^+e^- invariant mass distribution for $Z \rightarrow e^+e^-$, assuming Γ_Z = 3 GeV and two different electron energy resolutions.

A study of the precision in measuring Γ_z has been undertaken. This study used an ensemble of Monte Carlo experiments measuring $Z \rightarrow e^+e^-$ with variable energy resolutions and event sample sizes. The error on Γ_Z was found to be well fitted by

$$\delta\Gamma_Z = \left(\frac{2}{N}\right)^{1/2} \sqrt{\Gamma^2_Z + (2.35\sigma_m)^2} \ ,$$

where N = number of events and σ_m = mass resolution. Figure 2.4 shows $\delta\Gamma_Z$ versus N for different mass resolutions and indicates that with the good energy resolution of this proposal a sample of 1500 events should yield an error of 130 MeV/c^2.

The expected contribution to Γ_Z from each additional neutrino pair is 181 MeV/c^2. Theoretical uncertainties exist, both in the size of radiative corrections (these are estimated to be small) and due to lack of knowledge of the t-quark mass. The latter uncertainty is small if the t-quark is found or is heavier than 40 GeV/c^2.

An interesting measurement, accessible only in hadron colliders at present, is a direct comparison of Γ_W and Γ_Z. The method is again the study of the m_T distribution described in 2.1.1. Figure 2.5 shows the calculated[6] m_T distribution for three different values of Γ_W. The measurement of the m_T distribution places a particular premium on missing E_T resolution. A study[6]

of the errors on Γ_W using conservative assumptions on the missing E_T resolution gives $\delta\Gamma_W$ = 200 MeV. Taken in conjunction with the measurement of Γ_Z, we estimate an error on (Γ_W/Γ_Z) of 8%. Measurement of both widths offers the interesting possibility of testing for the effect of QCD radiative corrections. The W has no decays into a new lepton pair generation if the charged lepton is heavier than the W. Its sensitivity to the t-quark mass is less than for the Z width. Measurement of Γ_W to within 200 MeV may well help limit the range of accessible values for m_t since the expected contribution to Γ_W from each (low mass) quark pair is 800 MeV.

2.1.3 Search for Narrow States

Recently there have been indications of an unexpectedly large branching ratio for $Z^0 \to e^+e^-\gamma$ (and one event of $Z^0 \to \mu^+\mu^-\gamma$) from UA1 and UA2.[11] The data themselves are insufficient to draw conclusions, but calculations of the probability for radiative effects are too small by nearly two orders of magnitude to explain these events. The interesting possibility exists that there is a decay mode $Z \to X\gamma$; $X \to \ell^+\ell^-$. With the good EM energy resolution of the DO detector, the invariant mass resolution for two or three particle combinations will be better than for UA1, UA2, or the CDF detector. If such a signal does indeed exist, it will be most interesting to search for the companion decay, $W \to e\nu\gamma$; again, good EM energy resolution will be at a premium.

A useful supplement to these searches will be examination of the muonic analogs. Here the DO detector has the interesting possibility of triggering on muons over the full solid angle. Should these radiative decays exist, comparison of electron and muon rates is essential to disentangle the physical mechanism.

An additional requirement for these searches is the ability to distinguish γ from π^0. The observed events have quite energetic γ candidates (tens of GeV). At these energies, unambiguous identification of γ versus π^0 is virtually impossible by looking for separated γ showers. The DO detector, with its fine-grained longitudinal segmentation, does offer a good statistical measure for distinguishing 1, 2, or multigamma showers.

Searches for new quarkonium states ($t\bar{t}$) are also aided by the very good mass resolution of the DO detector. Our estimates give sensitivity to a potential ($t\bar{t}$) state up to masses of 55 GeV/c^2 (thirty events over a small background). In this calculation we have used the ansatz of Gaisser scaling[12] and scaling functions determined from ISR data.[13,14]

2.1.4 Decay Asymmetry in $W^{\pm}$ Production and Decay

It is well understood[15] that the combined asymmetry of production of W^+ and W^- (the W^- tends to follow the incident $\bar{p}$) and V-A asymmetry in decay (charged leptons are anticorrelated with the W momentum) yields a sizable asymmetry in ℓ^+/ℓ^- production from W decay. This asymmetry, expressed in terms of the decay angle, θ^*, of ℓ^- from W^- in the W rest frame measured with respect to the proton beam direction, is expected to be $(1 + \cos\theta^*)^2$. The UA1 experiment reports[16] good agreement with this finding and gives $\langle\cos\theta^*\rangle = 0.4 \pm 0.1$. Given our sample of $W^{\pm} \rightarrow \mu^{\pm}\nu$ with sign-selected muons, we can expect an error on $\langle\cos\theta^*\rangle$ of less than 1%.

The potentiality that heavy W's or Z's exist reinforces the desire to measure the decay muon asymmetry over the full solid angle. Such heavy bosons could have a range of possible decay couplings, resulting in arbitrary asymmetries. This possibility suggests that the experiment retain good muon sign

determination out to the maximum p_T values where cross sections allow heavy W', Z' production to be seen [i.e., for $p_T(\mu) \lesssim 150$ GeV/c].

Clearly the premium on detector capability here is upon good muon identification at large p_T. Decay backgrounds from π and K decay can be expected to be small ($h/\mu < 10^{-3}$ for $p_T > 30$ GeV/c). The dominant background will likely be hadron punchthrough; this component will be minimized using a relatively thick muon filter. In the case of $W \to \mu\nu$, the muon is expected to be relatively isolated and balanced in the transverse plane by missing p_T. Studies[17] have shown that a rejection factor of about 100:1 can be achieved from these two criteria; these studies use the topological properties of background jet events embodied in the ISAJET Monte Carlo program.[18]

2.1.5 Search for the Gauge Boson Coupling

Measurement of associated production of gauge bosons would be extremely interesting, as it would reveal the character of the boson self couplings. These trilinear couplings are exactly specified in the standard model.[19] The largest of these reactions is expected to be $\bar{p}p \to W^{\pm}\gamma X$ for which the cross section is calculated[19] to be about 350 pb^{-1} (for the sum of both charges). The distribution of the angle θ_γ of the γ with respect to the $\bar{p}$ in the center-of-mass has a very pronounced dip at $\cos\theta_\gamma = -0.33$ in the standard model. Both cross-section magnitude and angular distribution are affected if the standard model constraints are removed. Figure 2.6 shows the effect of altering the effective coupling on the angular distributions.

The detection of associated $W^{\pm}\gamma$ production is most straightforward if one demands the decay $W \to \ell\nu$ (ℓ = e or μ). The photon must be required to carry some minimum transverse momentum. Assuming $p_T(\gamma) > 10$ GeV/c, and standard W branching ratios yields[20] a reduction in observable signal of approximately

0.017 if one uses both e and μ. The resulting sample of $W^{\pm}(\ell\nu) + \gamma$ events in our luminosity interval is then about 20.

This small signal exists in a background from $W^{\pm}$ + jet events which is estimated[20] to be about 200 times larger. This background can be considerably reduced, first by requiring the γ candidate to be relatively isolated from other particles and secondly by applying cuts which reject 2γ showers relative to single γ.

Clearly, the size of the event sample is too small to measure detailed properties of the angular distribution. However, the cross sections computed in the standard model depend upon a particular cancellation of diagrams involving quark exchange and the gauge coupling. Removal of these constraints would result in a larger cross section. While a small deviation in the cross section would be hard to measure, a large deviation would signal a significant violation of the standard model. Other potential searches exist which may prove of interest. The production of $Z^0\gamma$, expected to be unobservably small in the standard model, could be enhanced if the Z^0 were composite.

2.1.6 W, Z Production

The detailed measurement of W and Z production cross sections yield interesting results. The standard picture of the boson production involves a nearly identical process as for Drell-Yan production of lepton pairs. For Tev I, the scaling variable $\sqrt{\tau} = m/\sqrt{s} \simeq 0.045$, smaller than can be reliably probed at lower energies. It is precisely this region where the QCD non-scaling corrections are expected to enhance the cross section.

The x-dependence of W and Z production reveal the parton x-distribution in the same way as in Drell-Yan production. Comparison of W and Z distributions offer the possibility to probe differences in the structure functions for u, d and sea quarks.

The p_T distribution of produced bosons is interesting for a study of radiative processes in QCD. Early results from UA1[16] indicate the existence of $W^{\pm}$ + jet production in agreement with the idea that high p_T W's are made by initial state gluon radiation. We may expect that about 30 such W + jet and 6 Z^0 + jet events will exist in our standard sample for $p_T(\text{jet}) > 100$ GeV. The rate of such processes, as a function of $p_T(\text{jet})$ should allow extraction of useful information on $\alpha_s(Q^2)$.

2.1.7 Quark Decays of W and Z

The decays of W and Z into quark pairs are well understood within the standard model (subject to a knowledge of the t-quark mass). Decays of W and Z into a pair of quark jets is in principle observable, if the QCD jet production backgrounds can be controlled. This study places a large premium upon good hadron energy measurement in order to reduce the error on jet invariant mass. Good segmentation of calorimetry is also desired.

Flavor tagging of jets can be accomplished in some circumstances. Quark semileptonic decays yield observable electrons and muons whose components of momentum parallel and perpendicular to the jet axis differ for different quark flavors. Ability to use these signatures demand good lepton identification in the presence of the remaining hadronic debris in the semileptonic decays. An explicit Monte Carlo study of $W^+ \to t\bar{b}$ is shown in Figs. 2.7 and 2.8. Although the QCD backgrounds exceed the signal by a factor of about 100, simple topological cuts can be found which reduce them below the signal, leaving useful numbers of signal events (150 events for $m_t = 60$ GeV).

2.2 HIGH p_T STUDIES OF QCD

2.2.1 Jet Production

The emergence of small angle clustering of energetic particles in UA2[21] and UA1[22] have dramatically confirmed the prediction of parton jets in hadron collisions. Many properties of these jets of $p_T \leq 200$ GeV/c have been studied including multiplicity distributions, energy flow, transverse momenta within the jets, angular distributions, and cross sections. The presence of three jet events has been established to be in rough agreement with QCD predictions. Hadronization distributions have been studied for a mixture of quark and gluon jets.

At TeV I, again assuming a run of 5 pb^{-1} and the expected QCD jet cross section,[23] we may expect to have jets up to 500 GeV/c. Extension of the measured properties to this smaller distance scale is of great interest in itself. Measurement of the ratio of three or more jets to two jets at very large p_T will enable measurement of the strong coupling constant at much larger q^2 than available elsewhere. Measurement of the p_T dependence of the jet cross section is an interesting place to look for effects of quark compositeness. A recent calculation[24] suggests that compositeness that enters with a mass scale parameter of $\Lambda \sim 2$ TeV ($\sim 10^{-17}$ cm) can be sensed through a (non-scaling) deviation from lower p_T jet cross-section behavior. The major detector requirements for these jet studies are good hadronic energy resolution and good segmentation.

2.2.2 QED/QCD Ratio Tests

The ratio of single γ to single gluon production is sensitive to the ratio of coupling constants, α / α_s. At the CERN ISR and Fermilab, useful measurements of the γ/π^0 ratio have confirmed QCD expectations. These are

roughly that the γ/π^0 ratio increases like $x_T = 2p_T/\sqrt{s}$, so one may expect $\gamma/\pi^0 = 0.05$ at $p_T = 50$ GeV/c. An explicit calculation[25] is shown in Fig. 2.9 which indicates appreciable rates of single γ out to $p_T = 50$ GeV/c. The related measurements of the ratios (jet + γ)/(2 jets) or (2 jets + γ)/(3 jets) contain even more direct information on the α_s/α_{EM} ratio. Finally, it has been calculated[26] that a measurement of 2γ production at large invariant mass can give complementary information to the Drell-Yan dilepton production, with perhaps less background.

The measurement of single photons (as opposed to π^0, η, or ω) is a delicate experimental problem. Our studies have shown that in an electromagnetic calorimeter with fine longitudinal segmentation, it is possible to measure γ/π^0 to within a few percent in the presence of multigamma backgrounds, based upon the distribution of the depth of first conversion. Additional discrimination has been shown[27] to be given from detailed multilayer shower deposition correlations.

2.3 SEARCHES BEYOND THE STANDARD MODEL

The potential of Tev I, with high energy and good luminosity, is likely to be most fully realized in searching for new particles or phenomena at very high masses. Many such particle spectroscopies have been suggested and explored in the theoretical literature.[28] With luck, we may find that Nature is even more inventive. In any case, the known set of hypothetical objects possess interesting properties that can be used for a search with the detector proposed here.

2.3.1 Heavy Vector Bosons

A search for additional Z or W bosons can be performed in a similar manner to those that have led to discovery of the standard ones. The possibility that more bosons exist has been incorporated into several grand unification schemes. If one assumes the cross section scales in the usual manner,[20] one finds that the sensitivity for Z' should extend to m ≃ 230 GeV and to m ≃ 150 GeV for W'. For such searches, we may expect the background sources will be rather small and the main requirement of the experiment will be identification of electrons and muons over the largest possible solid angle. Measurement of the charge sign would be desirable for examination of asymmetries. The transverse momentum spectra of the decay leptons would be expected to peak at roughly m/2, setting the scale for the momentum resolution desired--namely good charge determination to at least 100 GeV/c.

2.3.2 Heavy Leptons

In the absence of any understanding of the number of fermion generations that may exist, it is natural to search for new leptons of mass larger than the current limits.[29] For new charged leptons, $L^{\pm}$ of the standard type (e, μ, τ...), the experimental signatures are well understood. Production of $L^{\pm}$ via the Drell Yan mechanism can occur, but at a rate that precludes detection for masses allowed by the current limits from e^+e^- machines. A more useful means of making $L^{\pm}$ lies in decays such as $W^{\pm} \rightarrow L^{\pm}\nu_L$ or $Z^0 \rightarrow L^+L^-$, providing the L masses are kinematically accessible. In such a case, the number of $L^{\pm}$

produced is comparable to the number of electrons or muons from W and Z decay, inhibited only by a phase space factor.

The decays of $L^{\pm}$ are expected to proceed in the well understood manner[28]

$$B(L^{\pm} \to \ell^{\pm} \nu_{\ell} \nu_{L}) = 1/9 \text{ for } \ell = e, \mu, \text{ or } \tau$$

$$B(L^{\pm} \to \nu_{L} + \text{hadrons}) = 2/3,$$

providing that $m(\nu_L) < m(L^{\pm})$ and $m(L^{\pm}) < m_t$. The ingredients of a search then involve a combination of good lepton identification (e and μ), good missing p_T resolution (due to the presence of several neutrinos in the decays), and good hadron jet identification (for tagging the more prevalent hadronic decay modes of $L^{\pm}$). The decay asymmetry for the decay $W \to L\nu_L$ with $L \to \mu\nu_L\nu_\mu$ may also be a useful indicator of the presence of a heavy lepton for $m_L \leq 60$ GeV/c^2.[30]

The number of events of various types to be expected are summarized in Table 2.1. Typically the missing energy carried off by neutrinos in these events will be large, and the ratio of observable electron or muon energy to missing energy small, thus enabling some useful cuts to be made.

There also exists a possibility that heavy neutral leptons, L^0, may exist.[28] Such states may have appreciable two-body decay modes such as $L^0 \to \mu^{\pm}\pi^{\mp}$. With good lepton energy measurement and good hadron calorimetry, these two-body signatures, well isolated from jet-like activity, should be quite distinctive. Using the standard model estimate for the $Z^0 \to L^0\bar{L}^0$ branching ratio of 6% we expect of order 6000 L^0 and $\bar{L}^0$ produced. Taking the branching ratio of $L^0 \to \ell^{\pm}\pi^{\mp}$ of 3% (in analogy with $\tau^{\pm} \to \nu_{\tau}\pi^{\pm}$, with a mixing angle factor included) we then expect 360 cases of $L^0 \to \ell^{\pm}\pi^{\mp}$ with ℓ either electron or muon. The particularly interesting case $L^0 \to e^-\pi^+$ or $\to \mu^-\pi^+$, $\bar{L}^0 \to e^+\pi^-$ or $\mu^+\pi^-$ would yield 10 events.

In the case of composite models, the possibility of excited leptons exists. Decays such as $e' \to e\gamma$ or $e' \to ee^+e^-$ would then occur and give useful signatures for detection. Good energy resolution and the ability to detect photons are of prime importance here.

2.3.3 Supersymmetry

In supersymmetry models,[30] all fermions acquire boson partners of identical quantum numbers, except for spin (and vice versa for the known bosons). These supersymmetric partners generally possess a common property that is conserved, implying that the lightest of them are absolutely stable (and very weakly interacting). The rational for supersymmetry is that it can be naturally incorporated into grand unified theories giving an explanation for the disparity between observed particle masses and the unification mass, and that such theories are relatively free from divergence difficulties. These powerful theoretical motivations are only slightly tarnished by the complete lack of any experimental sighting of a supersymmetric particle.

The phenomenological aspects of supersymmetry are confused by the large amount of flexibility in the mass scales and ordering of particles in that scale. However it is clear that if the ideas are correct, the counterparts of the gluon (gluino) and quarks (squarks) will be copiously produced in energetic hadronic collisions. Detection of such particles is limited only by the availability of sufficient energy to exceed the appropriate mass thresholds, and by the somewhat indirect means for identification of their decay products.

One of the most favorable cases for search is the reaction $\bar{p}p \to \tilde{g}\tilde{g}x$ ($\tilde{g}$ is gluino). This process has been studied in some detail[31] for a range of $\tilde{g}$ masses. Supersymmetry allows the cross sections to be calculated using standard QCD. The $\tilde{g}$ decays into $q\bar{q}\tilde{\gamma}$ ($\tilde{\gamma}$ is photino). The Monte Carlo study

used detector parameters similar to that we propose. The essential features are good missing p_T resolution for sensitivity to the non-interacting $\tilde{\gamma}$ and good lepton identification. The latter feature is important for tagging the main source of background from heavy quark semileptonic decay in which neutrinos give the missing p_T and in which leptons are always present. Figure 2.10 shows the signal and background events as a function of the maximum "jet" p_T after application of cuts on p_T imbalance and lack of energetic leptons. A signal persists from $\tilde{g}$ production for $m_{\tilde{g}} \lesssim 100$ GeV/c^2.

Other detection strategies exist which utilize the four jet plus missing energy topology of the gluino pairs production. Since each quark jet in $\tilde{g} \to q\bar{q}\tilde{\gamma}$ carries on average one third of the gluino rest energy, it is imperative here to have a detector with good hadronic energy resolution and good segmentation.

Finally, it is possible[32] that the C noninvariant gluino decay $\tilde{g} \to g\tilde{\gamma}$ occurs with appreciable branching ratio. Such a decay mode is experimentally simpler to isolate (two energetic jets plus large missing p_T). Again, the requirement on the detector is for superior hadron calorimetry.

2.3.4 Heavy Quarks

Another result of our uncertainty on the number of fermion generations (c.f. sections 2.1.2 and 2.3.2) is that we may expect to find additional quark species beyond the presently expected u, d, s, c, b, t. Assuming that the new flavor pair has a combined mass above the W mass, it is impossible to produce them via $W \to Q_u\bar{Q}_d$. However, for $M_Q > M_W$, the dominant decay mode is $Q \to Wq$, where q is the next lighter quark. The final state for $p\bar{p} \to Q\bar{Q}$ production would then be $W^+W^-q\bar{q}$. The cross section[23] is such that a pair of 120 GeV/c^2 heavy quarks would yield 100 such events (in 5 pb^{-1}). Non-leptonic detection

would require identification of W's through di-jet invariant masses in a six jet final state. This rather fanciful scenario would clearly push the hadron calorimetry to its limit! However if one W decays leptonically, the signature would be quite striking; finding it would require good detection of jets, leptons and missing p_T.

2.3.5 Technicolor

The technicolor models[33] were invented to give the Higgs bosons a firm position in gauge theories; this is accomplished with of a large number of new exotic objects. The properties of two of these appear to warrant a useful search in a 5 pb^{-1} run at Tev I. The first is the technicolor octet state, η_T, for which the mass estimate of 200-250 GeV/c^2 is fairly firm. Its decay is expected to be a pair of top quarks. Estimated production rates are large (of order 1000 events). A crude calculation[34] showed that with a high resolution vertex chamber (σ = 20 μ), the η_T signal would survive above background with roughly 10% efficiency.

The second potentially observable technicolor states are the leptoquarks whose mass is estimated at 150 GeV/c^2. The decays would be a lepton and a quark jet. Pair production of leptoquarks should yield about 30 events in 5 pb^{-1} with rather distinctive final states (two isolated leptons and two heavy quark jets). It may even be possible to study lepto quark decays into t + τ, since the energetic τ yields its neutrinos along the lepton axis. Using the τ mass constraint one can infer their magnitude.

2.3.6 Quark-Gluon Plasma

Much theoretical work has been directed recently at the possible formation of new states of matter in very high-energy collisions. One such possible state is a quark-gluon plasma, which is expected to be formed at sufficiently high-energy density. Among the suggested signals for such a state of matter is an increase in the photon/hadron ratio at low-p_T values, resulting from the fact that photons can escape from the interior of a hot region of high-energy density more easily than hadrons can. It appears unlikely that exact predictions can be made as to whether such a plasma could be formed at the TeV I collider, or what the temperature would be if such a plasma were formed. However, if sufficiently accurate measurements can be made of the photon spectrum down to momenta as low as possible, one can investigate, purely experimentally, whether this spectrum changes with $\sqrt{s}$, or with general characteristics of the events such as multiplicity. Note that it is not necessary to develop thermal equilibrium, in such a plasma, in order to have a detectable effect. Nor is it necessary to form or observe a phase transition. The experimental sensitivity for observing an effect depends on how well one can detect low-energy photons in an interesting energy range, and on how well one can measure the energy spectrum of such photons in events covering a large range of multiplicities.

Although it is not necessary to observe a phase transition in order to have an interesting signal, the theoretical estimate of the temperature at which such a transition might occur is pertinent in estimating what photon energies are of particular interest. The transition temperature is estimated to be of order 100-200 MeV.[35] The requirement on the detector then is that it be capable of identifying and measuring the energy of photons down to 100 MeV, even in events of abnormally high multiplicity.

2.3.7 Recent Anomolies from the CERN Collider

There are several indications from the UA1 and UA2 experiments, based on 130 nb^{-1} runs, of major surprises at large masses. While we cannot at this time take any of these as established, we can use these hints as illustrative of the new physics to be explored using the DO detector, and ask whether DO is well matched to the problem.

The anamolous signatures include (i) a large p_T jet unbalanced by observable transverse energy[36], (ii) large p_T photon(s) unbalanced by observable energy,[36] (iii) observation of apparent $Z^0 \to \ell^+\ell^-\gamma$ events above the radiative decay predictions,[11] (iv) large p_T W candidates with balancing jet activity,[37] (v) small bumps in the dijet mass spectrum above the W and Z masses,[38] and (vi) evidence for anomalous multimuon production, including like sign dimuons.[39] The common elements in these most interesting possibilities are these: jet measurement and identification are crucial; electron, photon, and muon identification and energy resolution are essential--finding them close to other particles is strongly rewarded; and recognition of missing p_T in an event is of enormous utility. The ability to isolate events in the various new categories (and in such cases as the search for the t quark in $W \to t\bar{b}$) is directly related to the experimental properties of energy resolution, lepton identification and p_T resolution. It is precisely these features which the DO detector has striven to optimize.

2.3.8 Unexpected Objects

When searching in a new energy regime, it is important that we retain a sensitivity to phenomena which have not been foreseen by theory. Although it is rare that something completely unexpected turns up, such occurrences are

often harbingers of a major change or advance in our understanding. Historical examples include the discovery of the τ, J/ψ, CP violation and the Υ.

In this sector one cannot test the performance of a detector against expected yields or signatures. Instead, we can only point to the general capabilities of the proposed experiment which may enable some interesting searches. Since the new phase space uncovered at Tev I is the very small distance scale ($\gtrsim 10^{-17}$ cm), we feel that emphasis upon good energy measurement and particle identification at the very largest transverse momenta are the key ingredients for a search for new physics. Our detector is designed to identify all five of the observable particles at the largest accessible p_T : electrons, muons, neutrinos, jets, and photons. Its solid angle coverage is virtually complete. Owing to its emphasis on calorimetry, fractional energy resolutions will improve as energy increases. The detector is sufficiently simple and homogeneous that sensing the presence of new phenomena should be made more straightforward.

REFERENCES CHAPTER 2

1. See the many discussions in Proceedings of the 1982 DPF Summer Study on Elementary Particle Physics and Future Facilities, ed. R. Donaldson, R. Gustafson, and F. Paige; hereafter referred to as Snowmass 1982.

2. Design Report for the Fermilab Collider Detector Facility (CDF), August 1981. See also Fermilab proposals P714, P724, P726, and P728.

3. UA1 Upgrade Proposal, CERN-SPSC/83-48 August 1983.

4. F. Paige, BNL-27066.

5. W. L. van Neerven, J. A. M. Vermaseren, and K. J. F. Gaemers, NIKHEF-H/82-20a; V. Barger, A. D. Martin, and R. J. N. Phillips, DPT/83/2.

6. J. Smith, W. L. van Neerven, and J. A. M. Vermaseren, ITP-SB-83-11.

7. W. J. Marciano and Z. Parsa, Snowmass 1982, p. 155.

8. M. Veltmann, Nucl. Phys. **B123**, 89 (1977); M. Chanowitz, M. Furman, and I. Hinchliffe, Phys. Lett. **78B**, 285 (1978).

9. V. Shvartsman JETP Letters **9**, 184 (1969); G. Steigman, D. Schramm, and J. Gunn, Phys. Lett. **68B**, 202 (1977).

10. M. Banner, Xlth International Conference on Neutrino Physics, Dortmand (June 1984).

11. G. Arnison et al., Phys. Lett. **126B**, 398 (1983).
P. Bagnaia et al., Phys. Lett. **129B**, 130 (1983).

12. T. Gaisser, F. Halzen, and E. A. Paschos, Phys. Rev. **D15**, 2572 (1977).

13. D. Antreasyan et al., Phys. Rev. Lett. **47**, 121 (1981).

14. C. Kourkemelis et al., Phys. Lett. **91B**, 481 (1980).

15. C. Quigg, Rev. Mod. Phys. **49**, 297 (1977).

16. G. Arnison et al., Phys. Lett. **129B**, 273 (1983).

17. Fermilab Proposal P728.

18. F. Paige and S. D. Protopopescu, BNL 29777 1981.

19. R. W. Brown, D. Sahdev, and K. O. Mikaelian, Phys. Rev. **D20**, 1164 (1979).

20. G. Bunce et al., Snowmass 1982, p. 489.

21. P. Bagnaia et al., CERN-EP/83-94 and CERN-EP/83-135.

22. G. Arnison et al., CERN-EP/83-118 and CERN-EP/83-119.

23. F. Paige, Snowmass 1982, p. 484.

24. E. Eichten, K. Lane, and M. Peskin, Phys. Rev. Lett. **50**, 811 (1983).

25. I. Hinchliffe and R. Kelly, LBL-12274.

26. F. Paige and I. Stumer, Proceedings of the 1981 Summer Workshop (ISABELLE), p. 479.

27. R. L. Engelmann et al., Nucl. Instrum. and Methods **216**, 45 (1983).

28. G. Kane and M. Perl, Snowmass 1982, p. 18.

29. S. Yamada, Proceedings of the 1983 International Symposium on Lepton Photon Interactions at High Energies, Cornell University, August 1983.

30. D. Cline and C. Rubbia, CERN-EP/83-61.

31. S. Aronson et al., Snowmass 1982, p. 505; L. Littenberg, BNL preprint and private communication.

32. G. Kane and H. Haber, UM-TH 83-18.

33. E. Farhi and L. Susskind, Phys. Rept. **74C**, 277 (1981).

34. C. Baltay and H. Gordon, Snowmass 1982, p. 500.

35. M. Jacob and J. Tran Thanh Van, Phys. Rept. **88C**, 321 (1982).

36. G. Arnison et al., Phys. Lett. **139B**, 115 (1984).

37. P. Bagnaia et al., Phys. Lett. **139B**, 105 (1984).

38. J. R. Hansen, Proceedings of the Bern Workshop on $\bar{p}p$ Collisions (March 1984).

39. C. Rubbia, Proceedings of the Bern Workshop on $\bar{p}p$ Collisions (March 1984).

TABLE 2.1

Decay Chain	B. R.	Events	Signature
$W \to L\nu_L$	1/12		mean $p_T(\ell) \sim 10$ GeV
$L \to \ell\nu_L\nu_\ell$	1/9	1650	large missing p_T;
(ℓ = e or μ)			no hadron jets
$Z \to L^+L^-$	1/30	75	two moderate p_T leptons;
$L^+ \to \ell^{+-}\nu_L\nu_\ell$	1/9	(sum of e and μ)	large acoplanarity and
$L^- \to \ell^-\nu_L\bar{\nu}_\ell$	1/9		missing energy
(ℓ = e or μ)			
$Z \to L^+L^-$	1/30	220	moderate p_T lepton,
$L^+ \to \ell^{+-}\nu_L\nu_\ell$	1/9	(sum of e and μ)	acoplanar with single
$L^- \to \nu_L$+hadrons	2/3		hadron jet. Large
			missing energy.

FIGURE CAPTIONS - CHAPTER 2

2.1 Cross sections from Ref. 4 for $W^{\pm}$ and Z^0 versus energy.

2.2 Distribution of events with transverse mass, m_T, for $W \to e\nu$, from Ref. 6. The solid line assumes $p_T^W = 0$; The dashed line is for $p_T^W = 50$ GeV/c.

2.3 Mass distribution for e^+e^- from Z^0, with no resolution smearing and two cases of finite resolution.

2.4 Error on Z^0 width versus number of events using the mass resolution of this proposal.

2.5 Distribution of events with transverse mass for $W \to e\nu$ with Γ_W = 1 GeV (dashed), 2.5 GeV (solid), and 5 GeV (dot-dashed).

2.6 Distribution of events with $\cos\theta$, where θ is the angle of the γ with respect to the $\bar{p}$ direction in $pp \to W^{\pm}\gamma x$. The parameter K is related to the gauge coupling and has value 1 in the Standard Model.

2.7 (a) Distribution of events versus E_T for the electron in $t \to be\nu$; Δ:m_t = 30 GeV, •:m_t = 60 GeV. The points (x) are backgrounds from QCD jets.

(b) Transverse mass, m_T, distributions for $t \to be\nu$ and QCD jet backgrounds.

Detector resolutions have been folded in and a cut E_T (electron) > 5 GeV imposed.

2.8 Distribution of events for $t \to be\nu$ and background (shaded bands) after cuts on an isolated electron, E_T (electron) > 10 GeV, and E_T (missing) > 10 GeV.

2.9 Cross section for single π^0 and γ production versus p_T from Ref. 25.

2.10 Gluino cross section for various gluino masses. The backgrounds shown after missing p_T cuts, with and without lepton veto cuts.

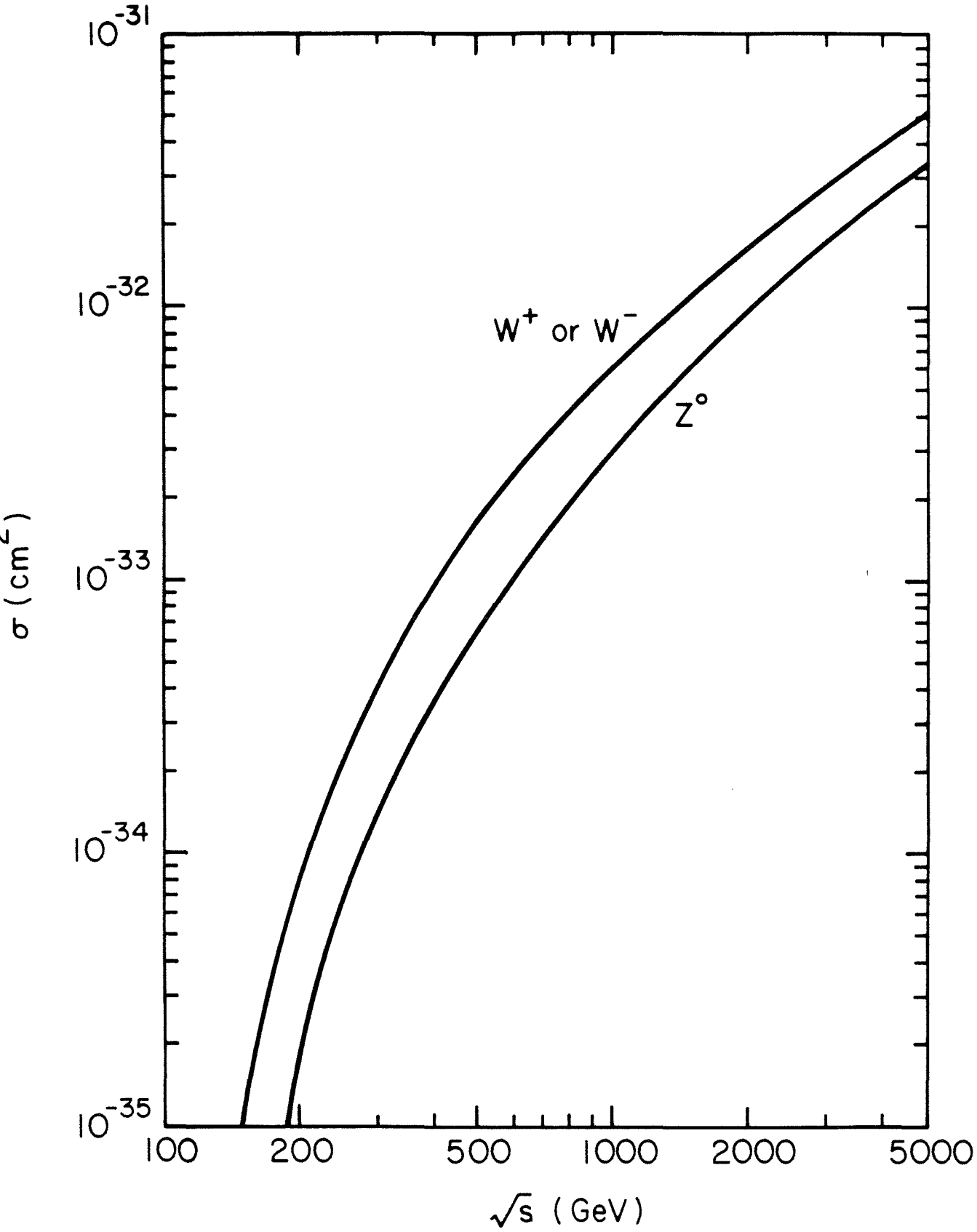
10^{-31}
10^{-32}
10^{-33}
10^{-34}
10^{-35}
σ (cm^2)
W^+ or W^-
Z°
100
200
500
1000
2000
5000
$\sqrt{s}$ (GeV)

Fig. 2.1

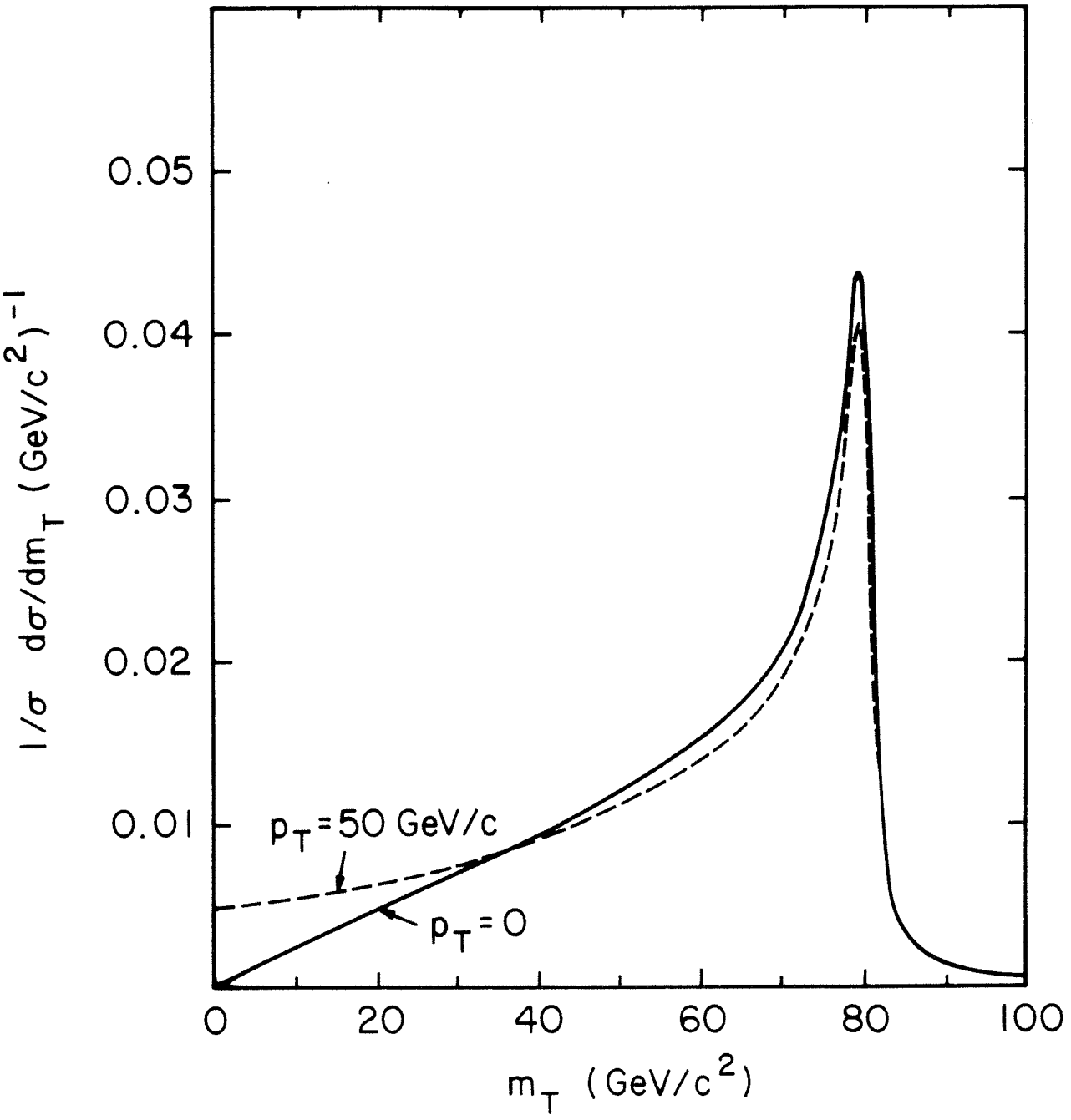
0.05
0.04
0.03
0.02
0.01
$1/\sigma \; d\sigma/dm_T \; (GeV/c^2)^{-1}$
$p_T = 50$ GeV/c
$p_T = 0$
0
20
40
60
80
100
m_T (GeV/c^2)

Fig. 2.2

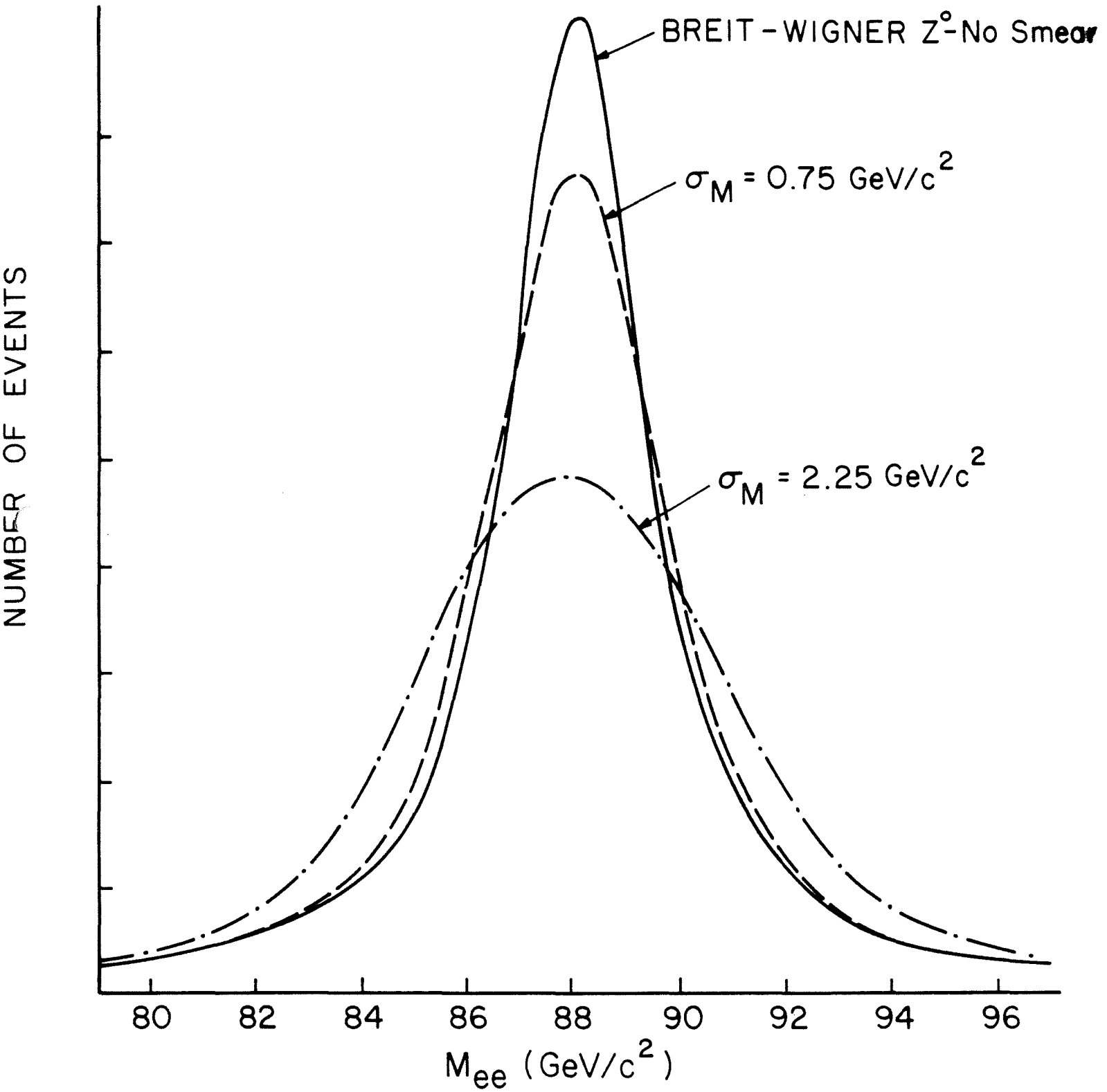
BREIT-WIGNER Z°-No Smear
σ_M = 0.75 GeV/c^2
σ_M = 2.25 GeV/c^2
NUMBER OF EVENTS
80
82
84
86
88
90
92
94
96
M_{ee} (GeV/c^2)

Fig. 2.3

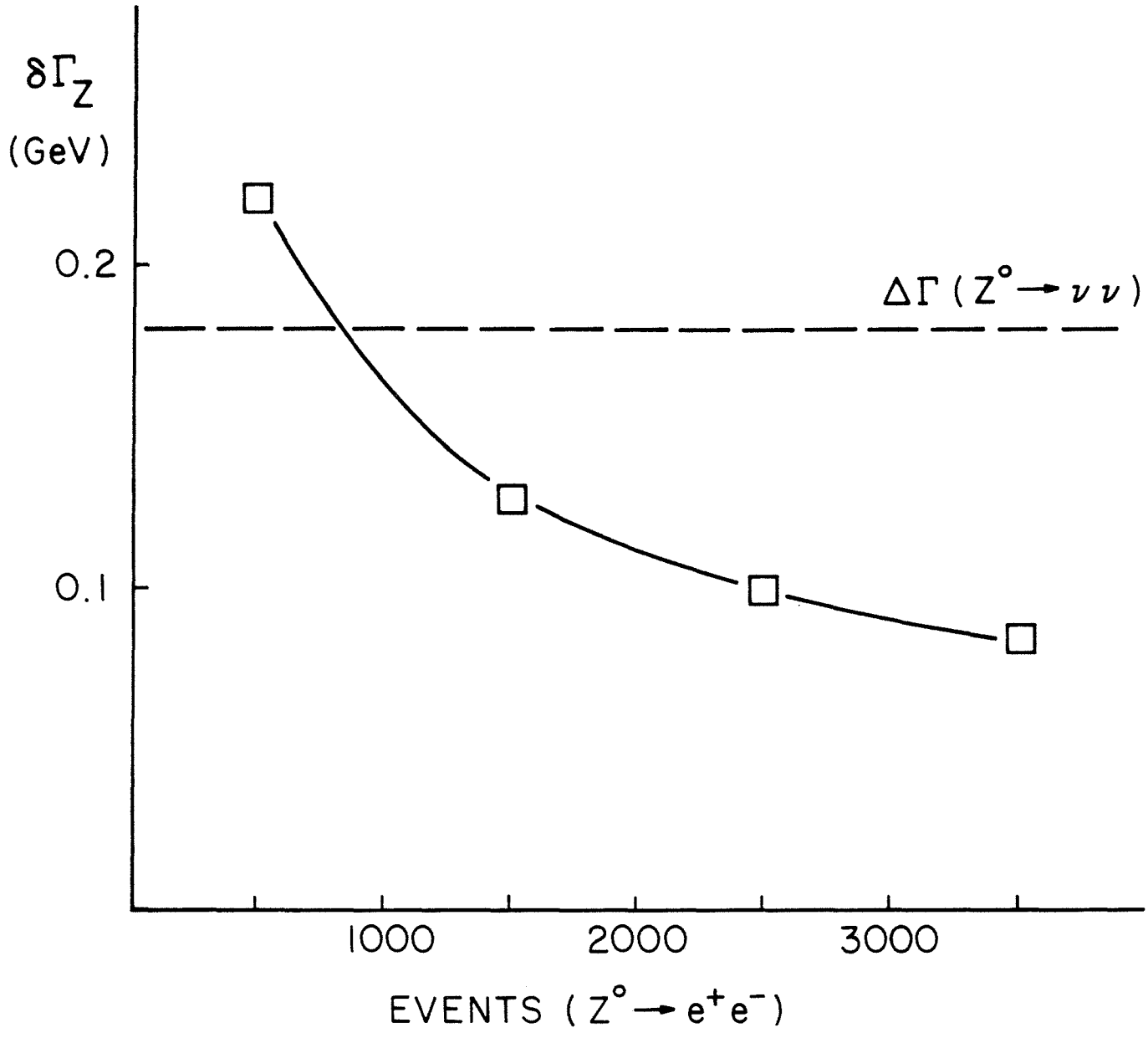

Fig. 2.4

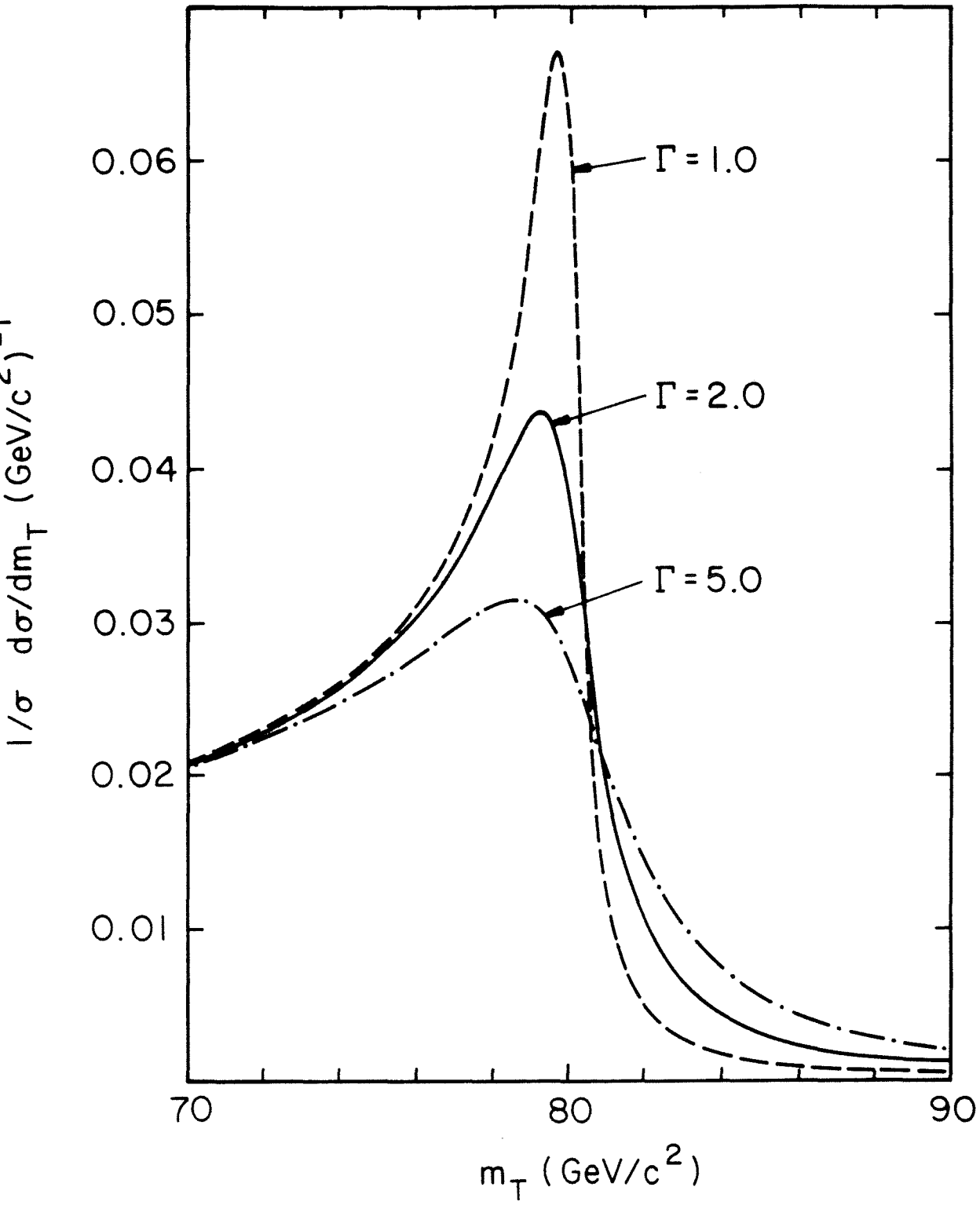
0.06
0.05
0.04
0.03
0.02
0.01
Γ = 1.0
Γ = 2.0
Γ = 5.0
1/σ dσ/dm_T (GeV/c²)⁻¹
70
80
90
m_T (GeV/c²)

Fig. 2.5

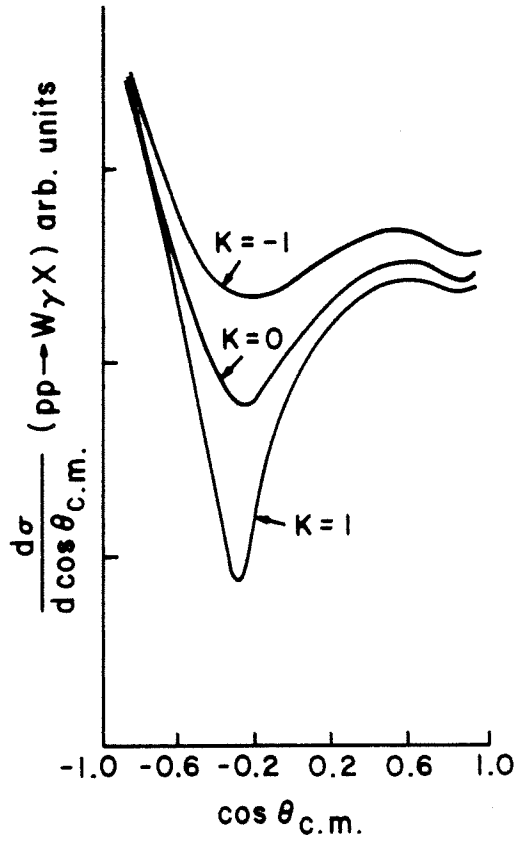
$\frac{d\sigma}{d\cos\theta_{c.m.}}$ (pp→WγX) arb. units
K=-1
K=0
K=1
-1.0
-0.6
-0.2
0.2
0.6
1.0
cos $\theta_{c.m.}$

Fig. 2.6

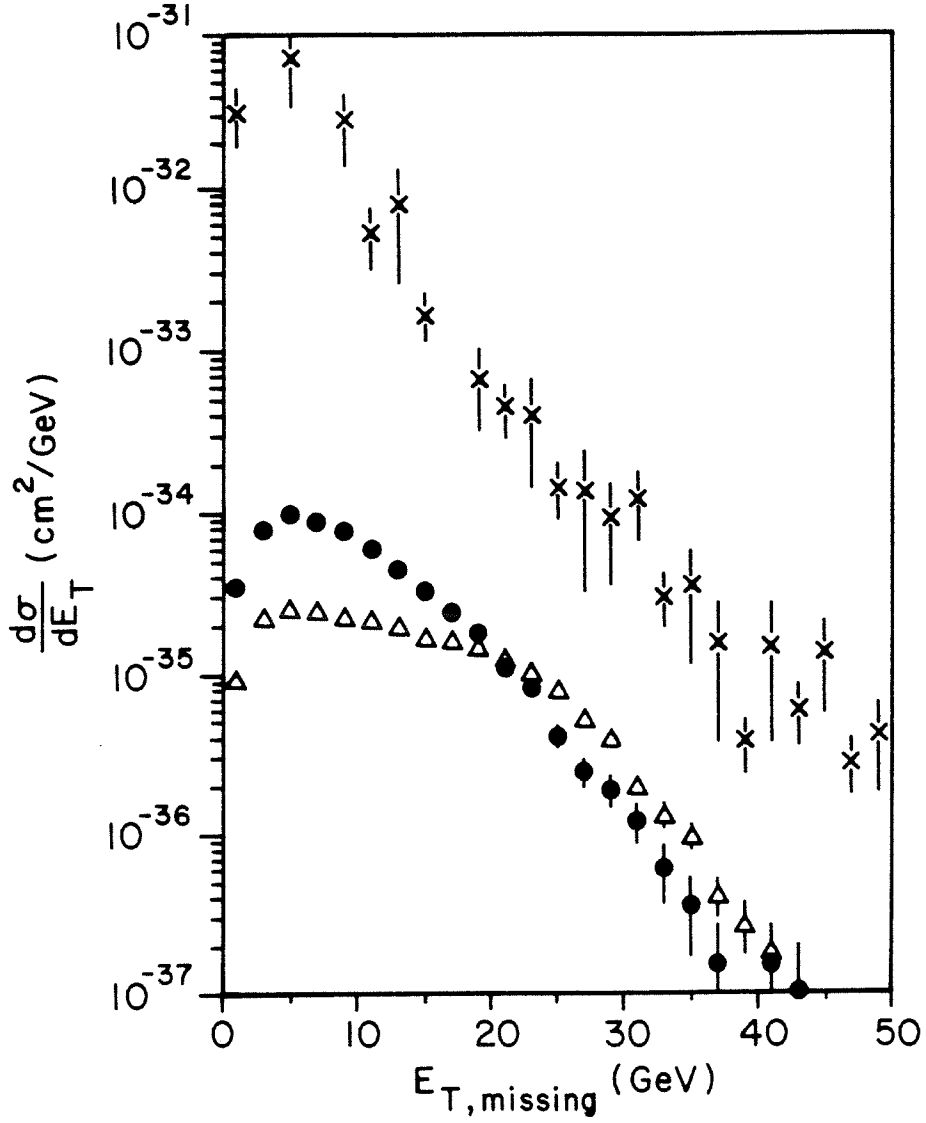
10^{-31}
10^{-32}
10^{-33}
10^{-34}
10^{-35}
10^{-36}
10^{-37}
$\frac{d\sigma}{dE_T}$ (cm^2/GeV)
0
10
20
30
40
50
$E_{T,missing}$ (GeV)

Fig. 2.7a

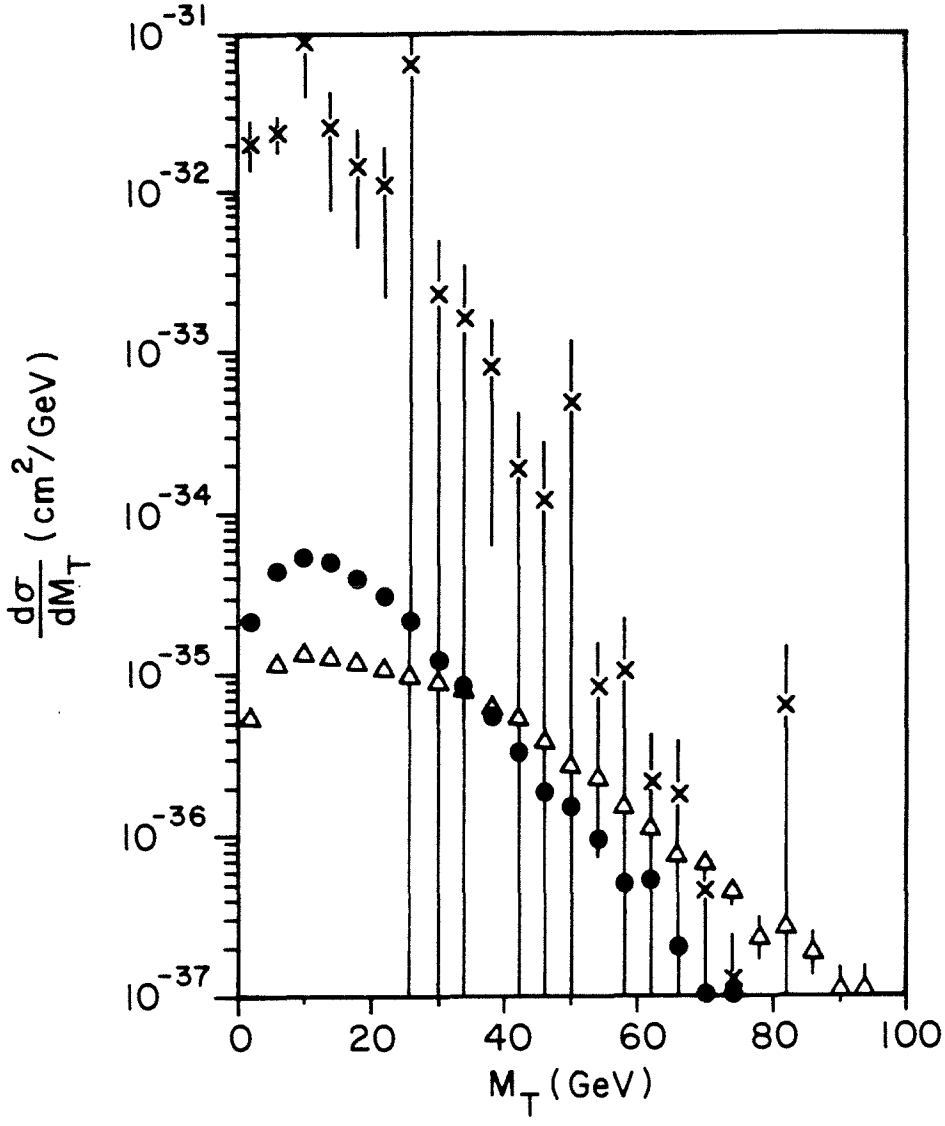
10^{-31}
10^{-32}
10^{-33}
10^{-34}
10^{-35}
10^{-36}
10^{-37}
$\frac{d\sigma}{dM_T}$ (cm^2/GeV)
0
20
40
60
80
100
M_T (GeV)

Fig. 2.7b

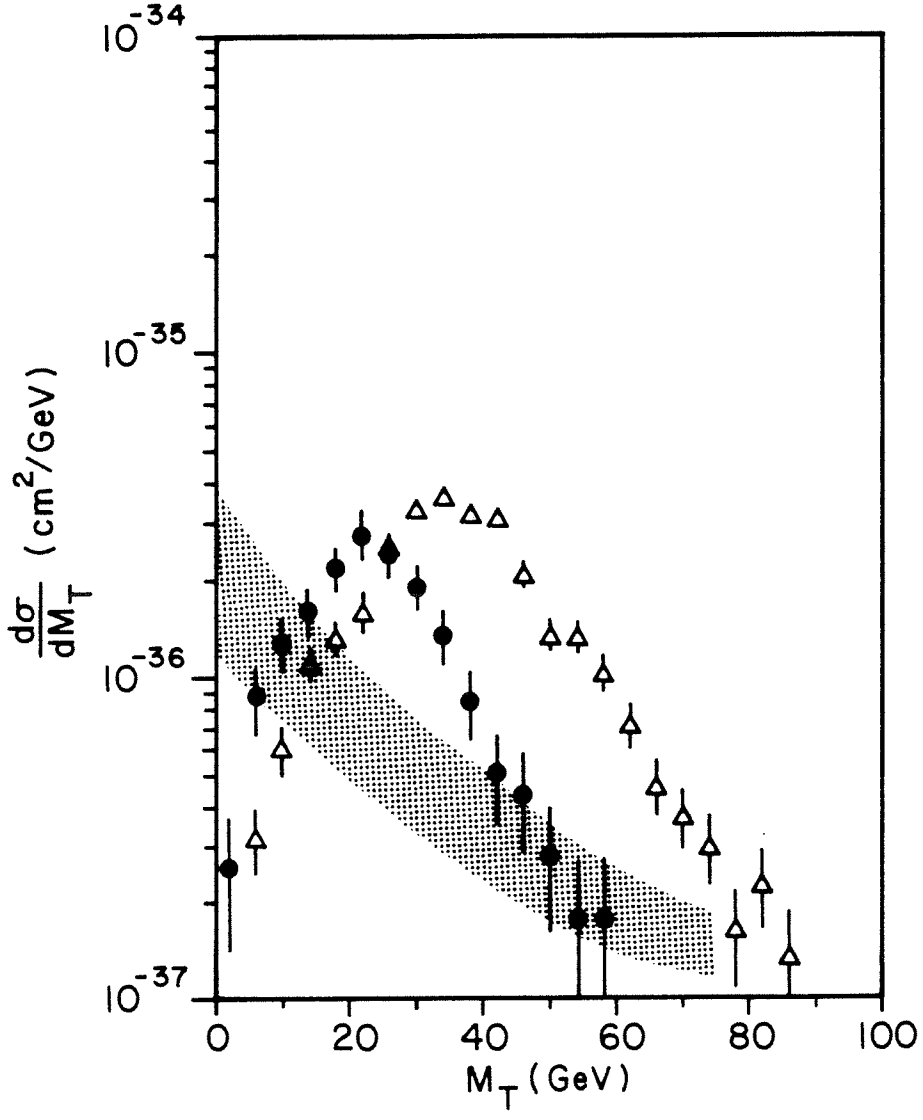
10^{-34}
10^{-35}
10^{-36}
10^{-37}
$\frac{d\sigma}{dM_T}$ (cm^2/GeV)
0
20
40
60
80
100
M_T (GeV)

Fig. 2.8

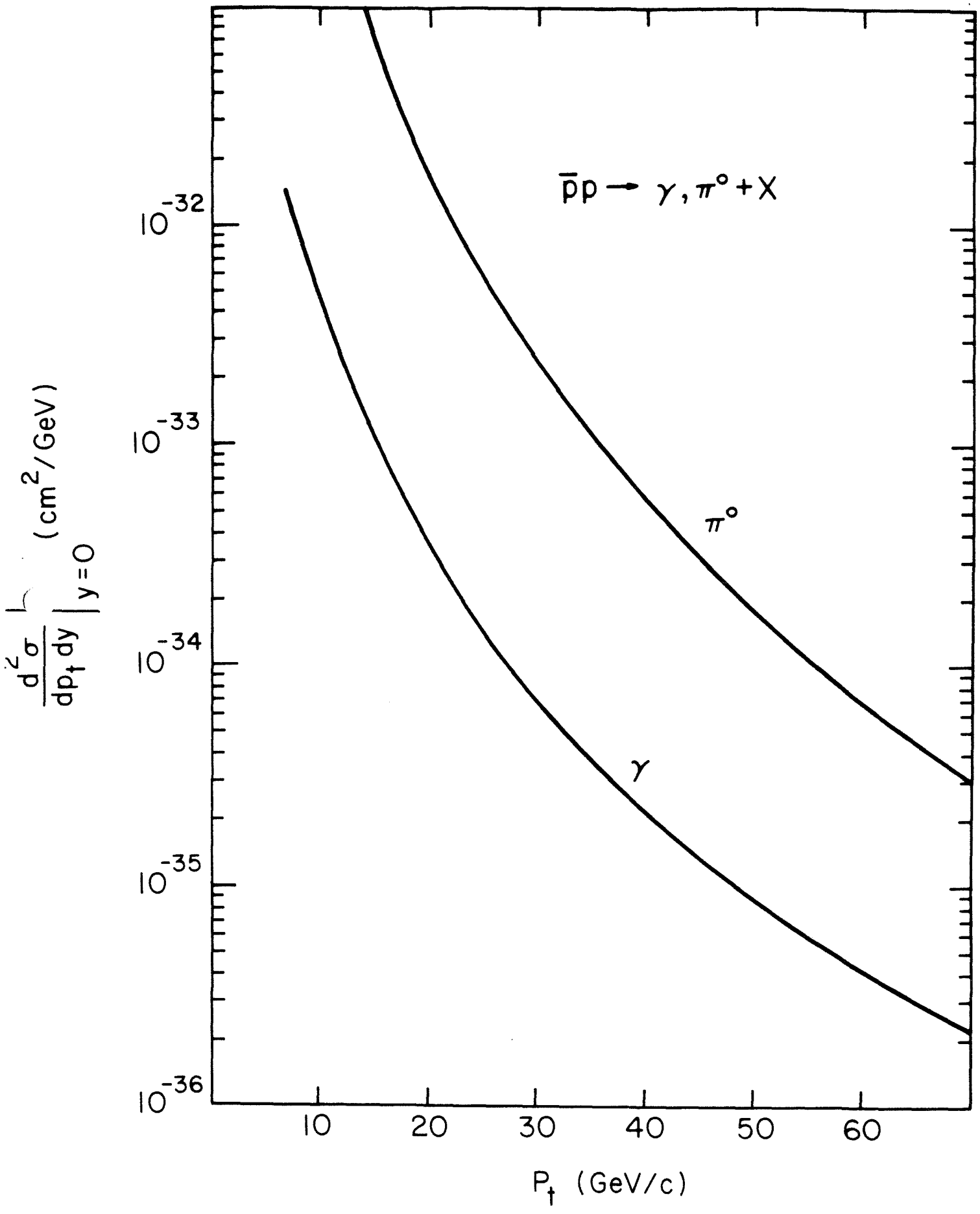
$\bar{p}p \rightarrow \gamma, \pi^0 + X$
π^0
γ
10^{-32}
10^{-33}
10^{-34}
10^{-35}
10^{-36}
10
20
30
40
50
60
P_t (GeV/c)
$\frac{d^2\sigma}{dp_t dy}\Big|_{y=0}$ (cm^2/GeV)

Fig. 2.9

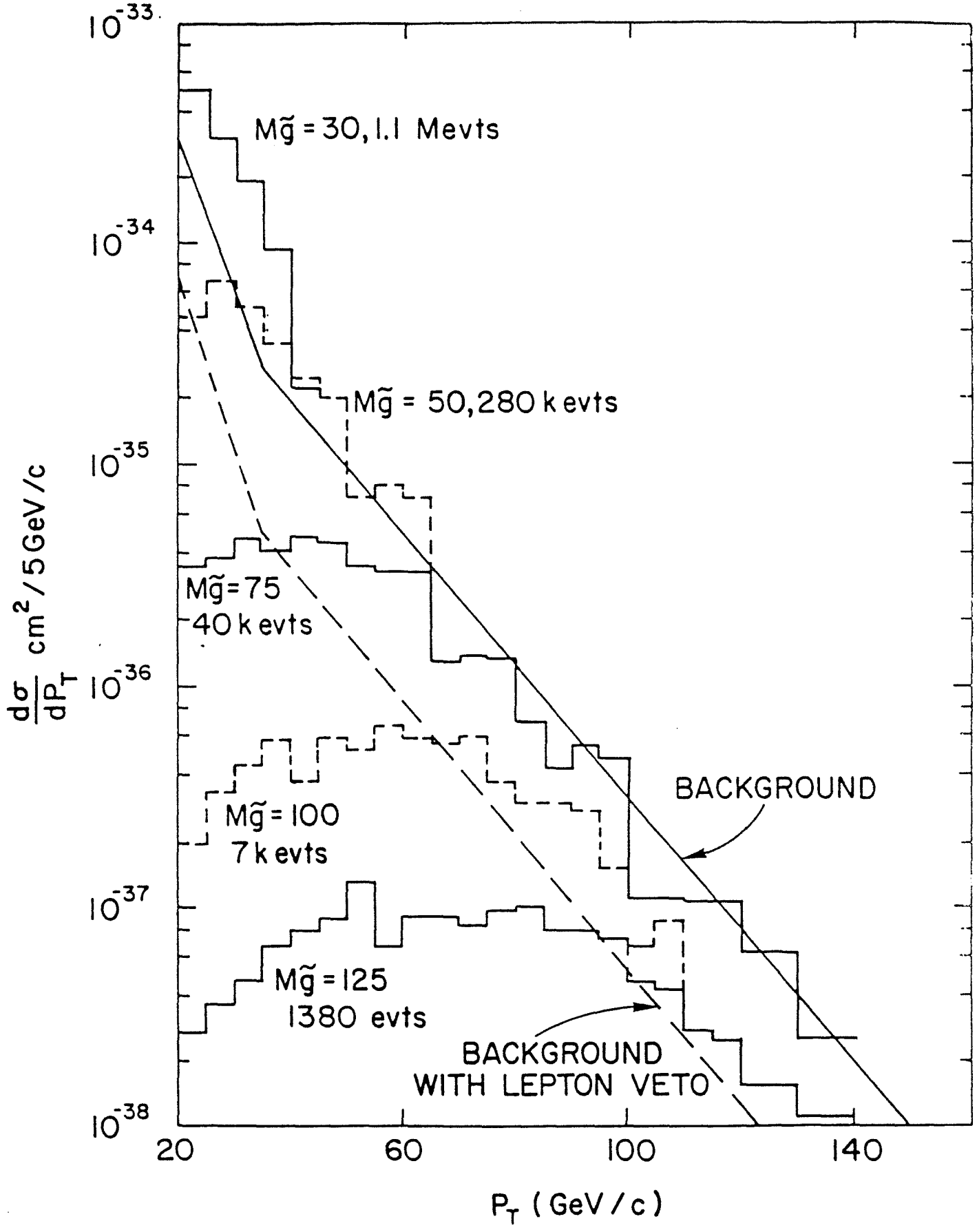
10^{-33}
10^{-34}
10^{-35}
10^{-36}
10^{-37}
10^{-38}
$\frac{d\sigma}{dP_T}$ cm^2/5GeV/c
$M\tilde{g}$ = 30, 1.1 Mevts
$M\tilde{g}$ = 50, 280 k evts
$M\tilde{g}$ = 75
40 k evts
$M\tilde{g}$ = 100
7 k evts
$M\tilde{g}$ = 125
1380 evts
BACKGROUND
BACKGROUND
WITH LEPTON VETO
20
60
100
140
P_T (GeV/c)

Fig. 2.10

3. MAIN FEATURES OF THE DETECTOR

3.1 DESIGN CONSIDERATIONS

The list of physics questions discussed in Chapter 2 has strongly influenced our design of the DO experiment, as filtered through our collective taste and prejudice. We have also kept in mind the emerging experience with the CERN $Sp\bar{p}S$ detectors and their strengths, weaknesses, and potential upgrades. The CDF detector at BO has been designed with specific characteristics aimed at a rather broad range of physics topics; inevitably that detector has stressed certain features at the expense of others. To some extent, the DO detector has been designed to give complementary focus upon the same collection of general questions.

3.1.1 Central Magnetic Field

From the beginning, the DO group has believed that there should be no magnetic field in the central region. This is in part motivated by our physics judgement that the relevant "particles" to be detected are jets, leptons, and missing p_T and that for each of these calorimetry is the paramount tool. Measurement of these "particle" energies or directions is not aided by having a central field. The central role of the calorimetry is stressed by making this choice, since it allows the coverage of the maximum solid angle unobstructed by supports, magnet coils, etc. Since tracking in a non-magnetic detector is simpler, this choice allows compression of the central drift chamber and brings the calorimeter volume (and cost) down. We feel that the traditional uses of magnetic analysis for all charged tracks in a 4π collider detector are vitiated in the Tev I environment. At the large energies of particles encountered in this experiment, calorimetric energy resolution will

exceed magnetic resolution. Also, to the extent that jets represent the quanta of real interest, one needs a detector which treats all fragmentation products (photons, charged and neutral hadrons) of the jet on equal footing.

3.1.2 Lepton Identification

We have stressed the ability to identify and measure leptons well; both electrons and muons are important in meeting the physics objectives outlined in Chapter 2. For electrons, excellent energy resolution is desired, primarily to permit the accurate study of narrow massive states, as discussed in Section 2.1. Very good energy resolution for electrons is readily obtained. We would also like to be able to identify electrons well enough to be able to distinguish them in the vicinity of hadron tracks, or of jets. Searches now underway at CERN for t-quark signatures are in part limited by the possibility of misidentifying a jet as an electron.[1] We expect to have unusually good electron identification; the quite fine segmentation of the calorimetry should give an e/jet discrimination, by itself, comparable to that achieved at CERN--about 1 in 5000. In addition, the use of Transition Radiation Detectors (TRD), in the central detector region, should give another factor of about 50, as well as extend identification closer to the core of jets.

The muons on the other hand are less well energy analyzed (but are sign selected); they can however be identified even when emitted at the core of a high p_T hadron jet due to the containment of hadronic showers. The ability to study muons even inside jets is important for heavy flavor studies, heavy lepton searches, and technicolor searches. It is a capability which is missing, or rather severely restricted, in other collider experiments. Having good identification for both leptons is important in supersymmetry searches,

where it is the lack of leptons in the event that can be used to suppress backgrounds.

3.1.3 Missing Transverse Energy

Good missing transverse energy resolution is the key to inferring the existence of neutrinos in an event. Its utility in the discovery of the W and in top quark searches has been amply demonstrated. Many of the searches for new phenomena described in Section 2.3 require such a capability. The detector we propose should be superior in its ability to sense missing E_T. Missing E_T resolution depends heavily upon good hadron energy resolution; use of uranium-liquid argon calorimetry is thus the optimum choice. The effect of cracks in coverage, both at small angle beam-exit holes and in large angle calorimetry is to worsen the missing E_T resolution; attention must be paid in design to minimizing these holes and cracks. Figure 3.1 shows the effects of finite energy and angle resolution, and beam hole size in detector coverage upon the missing p_T distributions. Given the energy resolution characteristics of uranium calorimetry and no contributions from cracks or dead zones, we see that coverage down to about 1° with respect to the beams is required for a good match.

The effect of introducing dead zones of coverage due to supports, cable pathways, and services is to worsen the missing transverse energy resolution, due to fluctuations in the shower energy deposited in these zones. Very careful attention must be given to locating and minimizing these zones, if this effect is not to dominate all others in determining missing E_T resolution. They are particularly damaging in that they can contribute non-Gaussian tails,

and thus rather substantially enlarge the E_T value where the instrumental resolution curve falls below the physical contribution from neutrino production.

3.1.4 Calorimetry Segmentation

The desire for good segmentation of calorimetry is dictated by much of the physics program in Chapter 2. Figure 3.2 shows the spatial distribution of energy distribution for two events from UA2.[3,4] In Fig. 3.2a, the two jets of approximately 100 GeV/c each are clearly visible, but any detail within a jet is unresolved. In Fig. 3.2b, the $Z^0 \rightarrow e^+e^-\gamma$ event is displayed showing a small angle separation between one electron and the photon. Clearly $e-\gamma$ separation could not be much smaller and still be detectable, although study of these events versus opening angle would be highly useful for elucidation of the mechanism. Study of multijet production is also clearly dependent upon a fine-grained subdivision of the calorimetry, subject only to the constraint imposed by the transverse shower sizes themselves.

The control of backgrounds to electron and muon identification also requires relatively fine segmentation. The relevant background for electrons consists of near spatial overlaps of charged hadrons and photons; small cell sizes will help, both by better measurement of shower centroid and better matching between shower and cell dimensions. Additional information from fine longitudinal segmentation and positive electron identification in the TRD external to the calorimetry also help. Similarly, muon identification will be aided if a muon candidate can be seen to be minimum ionizing in a series of calorimeter cells of the smallest possible size.

3.1.5 Hadron Energy Resolution

Hadron energy resolution plays an important role in many parts of our physics menu. Measurement of jet energies and masses are critically dependent upon it, as is the missing E_T resolution. Hadron calorimetry based upon sampling in iron plates (with appropriate fine early sampling for electromagnetic energy) can probably achieve a resolution of $\sigma/E = 0.7/\sqrt{E}$. This technique for energy measurement is ultimately limited by fluctuations in the energy associated with nuclear breakup and low-energy fragments[4] and also the difference in response to the fluctuating fraction of electromagnetic and hadronic components of the shower. We have felt that obtaining the best available energy resolution, namely that obtained using uranium sampling throughout the calorimetry, will have many extremely important advantages. Chief among these are an improved ability to isolate two jet decays of W and hence better ability to identify jet flavors. The improvement on missing p_T resolution leads to more accurate measurement of m_W/m_Z and better searches for new phenomena.

The use of uranium as an absorber in calorimeters has been discussed intensively in recent months. The original measurements[5] showed excellent energy resolution for hadrons and electrons with nearly equal response for these two. The interpretation of these results was that the energy lost in hadron cascades due to nuclear breakup was nearly compensated by neutrons and γ-rays resulting from neutron induced fission of uranium. Recent calculations[6] suggest that other mechanisms may be at work and that energy resolution may be less good. However, the electromagnetic and hadron response equality is not called into question. Several discrepancies remain between measurement and calculation[7]; several alternate solutions for absorber medium (W, Pb, etc.) suggested by the Monte Carlo results[6] have in fact been tried and found

to give poor results.[7] For the calorimetry in DO, we propose the use of uranium for several reasons: it clearly gives improved energy resolution over other choices; it allows equal EM and hadronic response which is of particular importance in measuring jet energies; it is extremely dense, allowing maximal detector compactness.

3.1.6 Photon Detection

Several of the physics issues at TeV I depend upon the ability to recognize high p_T single photons. The requirements placed upon the detector by this goal are quite severe. For example, at p_T = 30 GeV/c, the minimum separation distance for the two photons from a $\theta = 90°$ π° is 0.65 cm at 70 cm. Since this is less than the shower size, it is not possible to distinguish π° from single γ solely on this basis.

A way of distinguishing single photons from overlapping multiple photons from π°, η, or ω uses the depth of first conversion. This distribution has been used in a crude way to isolate single γ's at the ISR[8] with only two depth segments. Figure 3.3 shows the distribution of first conversion for single and multigamma showers. Studies have shown [9] that the fraction of single gammas can be found in a sample of 1, 2, 3, and 6 γ events with a precision of a few percent, for a sample of 10,000 events. Given the importance of sensing single photons, our aim is to use as many means as possible (good lateral and longitudinal sampling) to signal their presence.

3.2 SUMMARY OF THE DETECTOR

The detector design which has emerged based upon the physics issues and criteria discussed above is summarized in this section. There are three major components to the detector: the central detector system which measures tracks and gives electron identification; the calorimeters, composed of five separate uranium-liquid argon (ULA) detectors spanning most of the solid angle; and large solid angle muon identification and momentum measuring system. These components are supported on a single rolling platform table which transports the experiment to and from the collision hall. Most of the front-end electronics is mounted directly on the detector elements or in the table. Considerable use is made of signal multiplexing near the detector so that the cable volume and number of digitizing circuits outside the radiation enclosure are minimized. There is one additional system of scintillators near the beam lines, used for luminosity monitoring and fast vertex coordinate location.

The plan and elevation views of the detector are shown in Figs. 3.4 and 3.5. A cutaway isometric drawing of the detector is shown in Fig. 3.6.

3.2.1 Central Detectors

The central detector system consists of three separate devices with coverage split between the central region ($45° \leq \theta \leq 135^0$) and forward and backward regions. As seen going outward from the intersection region, the system consists of an inner tracking and vertex detector, a transition radiation detector (TRD), and the outer drift tracking chamber. The layout of the central detectors is shown in Fig. 3.7.

The inner tracking chamber in the barrel region serves a dual purpose. It establishes the existence of charged tracks incident upon the TRD so as to distinguish true electron candidates from background due to photon conversions

in the transition radiator itself. It also measures tracks with sufficient precision that decay vertices of long-lived particles, well separated from the colliding beams themselves, can be measured. This latter role is of particular use in tagging charm or bottom quark decays. The radial extent of this chamber is from just outside the beam pipe ($r \simeq 3$ cm) to the inner radius of the TRD ($r = 10$ cm).

The barrel region TRD extends from $r = 10$ to $r = 40$ cm and serves to identify electrons through the X-ray emission due to the discontinuity in dielectric constants at a series of thin lithium foils. Two separate sections of Li foils create the transition radiation, each followed by an X-ray detector. Each radiator section consists of 640 foils of 30 μm thickness, separated by 150 μm. The X-ray detector is separated from the stack of foils by a thin window and consists of a xenon-filled proportional wire chamber, with wires running parallel to the beams. The chamber has an inner conversion region of depth 1 cm in which most of the X-rays convert via the photo-effect and yield localizated ionization clusters. The clusters of electrons drift toward the multiplication region at the back of the gap and create avalanches on anode wires, separated by $r\Delta\phi = 8$ mm. Due to the localized character of transition radiation energy deposits in the gas, compared with the more continuous deposition from traversing ionizing particles, it is advantageous to count clusters of collected energy over some minimum threshold (3 keV). This method of tagging electrons has been shown to be superior to integration of the total deposited energy.[10] Realistic estimates of the rejection power against hadrons give a factor of at least 50 for our geometry.

The outer drift chamber is primarily responsible for measuring the charged particle tracks in an event. The large-angle barrel drift chamber measures tracks in the polar angle region $90° \pm 45°$ within the radial interval

$40 \leq r \leq 70$ cm. The chamber contains four supercells of six sense wires each for a total of 24 sense wire measurements per track. It is constructed from 32 azimuthal sectors of $\Delta\phi = 11.25°$ each; alternate radial supercells are rotated by a half cell (5.625°) in order to minimize left-right ambiguities and to aid in resolving two nearby tracks. In addition to the six sense wires, there are two delay lines at the inner and outer radii of each supercell, oriented parallel to the wires. Measurement of the arrival time at both ends of the delay line allow the measurement of the longitudinal coordinate of a track to within ±5 mm and give a true set of space-point determinations of track coordinates. The accuracy of measurement in the azimuthal coordinate is expected to be 200 μm; waveform digitization of the anode wire signals will allow two track separations of 5 mm. Two closely separated tracks will be better resolved due to the azimuthal offset of alternate supercells. Measurement of specific ionization on the 24 sense wires is also accomplished using the waveform digitizations; in this way, rejection of overlapped e^+e^- pairs from photon conversions relative to single $e^\pm$ can be made at the level of a few percent. This capability is necessary, and sufficient, to reduce the background to the electron signal from photon conversion sources to the level from hadron misidentification set by the TRD and the calorimetry.

The devices in the forward and backward regions follow the same pattern as those in the large angle barrel region. The chief distinction is that the chamber set nearest the interaction region is so far away that useful decay vertex information cannot be obtained. Accordingly, the drift chambers before and after the forward/backward TRD's are nearly identical and share the track direction and ionization measuring role.

The inner and outer drift chambers in the forward/backward regions each consist of two supercells of seven sense wires each. The two supercells are

oriented orthogonally in the two transverse directions. Ambiguity resolution is achieved within each supercell by introducing a small wire offset in the drift direction for alternate sense wires. Space-point location of tracks is again achieved in each supercell through the introduction of two delay lines per supercell orientated parallel to the sense wires. Resolutions and two-track separations are expected to be similar to those for the outer barrel drift chamber. Wave form digitization of signal pulses is incorporated to improve double track resolution and to provide ionization information suitable for e^+e^- pair suppression.

The TRD system in the forward/backward arms is similar to that in the barrel region. Two Li foil stacks produce the transition radiation X-ray photons; Xe filled proportional wire chambers record the ionization clusters from these photons and give rejection of hadrons.

3.2.2 Calorimetry

Based on the arguments summarized in Sections 3.1.4 and 3.1.5, we have made the uniform choice for calorimetry in which liquid argon is the sampling medium and a mixture of uranium and copper are the absorbing media. The driving factors for this choice are the proven ability of liquid argon calorimeter to function reliably and stably, the high density afforded by the combination of uranium and thin argon gaps, the radiation hardness, and the superior performance in terms of energy resolution and equalization of hadronic and electromagnetic response. The admixture of copper and uranium is motivated by the need for cost reduction; studies[11] have shown that Cu/U mixtures up to 40%/60% by weight have only minimal effect on energy resolution. The liquid argon technique lends itself naturally to readout segmentation in small towers in $\Delta\eta$ and $\Delta\phi$, as well as segmentation along the shower

axis. The relative ease of calibration of the liquid argon system pays large dividends for the high-energy particle measurements which are central to our physics program. Finally, the choice of liquid argon over potential room temperature liquid candidates[7] was made because of the superior signal sizes collected in argon, the difficulty in purifying the known room-temperature liquids, and because of the inflammability of these substances.

There are five separate uranium/copper liquid argon (ULA) calorimeters which span the polar angle region symmetrically about $\theta = 90°$. These are shown in Figs. 3.4 and 3.5. The central calorimeter (CC) spans the polar angle range $45^0 \leq \theta \leq 135^0$. Two end-cap calorimeters (EC) cover the ranges $5° \leq \theta \leq 45°$ and $135° \leq \theta \leq 175^0$. Two smaller plug calorimeters (PC) complete the coverage down to about 1° with respect to either $\bar{p}$ or p beams.

The central calorimeter is a polygonal approximation to a cylinder, concentric with the beam axes. Its active region extends from $75 \leq r \leq 222$ cm and for 226 cm along the beam direction. Individual modules of uranium/argon/copper/readout board stacks occupy the full length of the active volume and 1/32 of the azimuth. There are three radial layers of such modules; successive modules are rotated by half of the azimuthal width so as to avoid presenting continuous cracks to particles emerging from the intersection region. All modules reside within a common liquid argon cryostat so that interval cracks are minimal. The CC has a large proportion of uranium due to the spatial constraints upon its inner and outer radii.

The calorimeter is divided into three separate sampling structures along the radial direction. The first is a 20-radiation length (1 absorption length) section for electromagnetic shower detection in which the uranium plates are 2 mm thick. The second section is the main hadronic shower detection in which the uranium plate thicknesses are 5 mm, for a total depth

of about 4 absorption lengths. The final section is intended to sample the end of the hadronic shower development (the leakage section) and is about 1.8 absorption length of thick copper plates.

Each gap contains readout boards for collection of the ionization from the adjacent argon gaps. The segmentation of these boards is achieved using copper-clad G10 boards with the copper surfaces etched or scribed into the desired pad structure. Each azimuthal wedge module of the calorimeter ($\Delta\phi$ = 11.25°) contains two of these pads in the ϕ direction for a segmentation of $\Delta\phi \simeq 0.1$. The dimension of the pad along the beam is chosen to give a rapidity coverage of $\Delta\eta \simeq 0.1$, with the boundaries of the pads aligned to give approximate projective geometry towers as seen by the center of the interaction region. These readout segments are internally ganged together to give eight separate longitudinal samples of shower energy: the electromagnetic section is subdivided into 2, 2, 6, and 10 radiation length compartments; the hadronic section is subdivided into three compartments and the leakage section is a separate compartment. The first hadronic section is relatively thin (0.7 absorption lengths) to serve as an EM leakage section.

The third compartment of the electromagnetic section, which occurs at the peak of the EM shower development, is subdivided more finely in the transverse dimensions. Each standard tower area, $\Delta\eta\times\Delta\phi = 0.1\times0.1$, is divided into four in this particular compartment. This fine segmentation is necessary to measure the shower centroid locations accurately. Such measurement is necessary for comparing shower coordinates with incident track coordinates in order to discriminate against near overlaps of charged hadrons and photons masquerading as electrons.

The two end-cap calorimeters are cylindrical stacks of vertical plates, centered on the two beam lines. The active volumes begin at z = 153 cm and

end at 340 cm; they extend from an inner conical surface at $\theta = 5°$ out to a radius of 270 cm. The individual absorber plates are wedge-shape sections, joined together to make 16-fold polygonal approximations to circles. Rotation of these polygons by $\Delta\phi = 2\pi/32$ at successive depths assures there are no continuous cracks into which particles can penetrate. Each EC is housed in a common liquid volume cryostat.

The gap and plate structures in EC are quite similar to those in CC. The first 20 radiation lengths are composed of 2-mm thick alternating U and Cu plates with four separate longitudinal compartments for signal readout. The next 5.5 absorption lengths use 5-mm thick alternating U and Cu plates and are subdivided into three hadronic shower readout sections. The last 1.5 absorption lengths are made solely from Cu plates and comprise the hadronic shower leakage section. The overall depth of the EC calorimeters is 9 absorption lengths.

The signal readouts in the EC are subdivided in the transverse plane into constant $\Delta\phi$ and $\Delta\eta$ intervals of 0.1×0.1 units. The readout boards are made from scribed copper-clad G-10 sheets, with the electrical signals brought to the edge of each $\Delta\phi = 2\pi/16$ sector for longitudinal ganging. The third EM compartment has its $\Delta\phi\times\Delta\eta = 0.1\times0.1$ segment subdivided into four separate signal pads in order to get fine spatial resolution on shower locations.

The two PC calorimeters are located just upstream of the low-beta quadrupoles, with active regions between $Z = 500$ cm and $Z = 650$ cm and $r \leq 65$ cm. The inner radius of the plate array is at $r = 9$ cm, corresponding to a minimum angle of coverage of $\theta = 1^0$. The total depth of these calorimeters is 9 absorption lengths. The spatial constraints on the PC are quite severe, so that maximizing the density of these devices is essential. Accordingly, the

PC are built using all uranium absorber plates whose thickness is 6 mm throughout the full depth.

The segmentation for the PC is $\Delta\phi \times \Delta\eta = 0.15 \times 0.1$ at the outer radii, increasing to 0.3×0.3 at the inner radii due to the constraint that readout pad size should not be smaller than 2×2 cm^2 (the EM shower transverse size). The PC's are subdivided into six longitudional compartments for readout purposes.

The front-end electronics for the liquid argon calorimetry consists of the following elements: a low-noise charge-sensitive preamplifier for each channel; base-line subtractors which sample signal levels before and after beam crossings and yield a dc voltage proportional to the accummulated channel charge; and multiplexers which sequence these voltages for presentation to the digitizing electronics. All of these circuits will be housed on the detector. The preamps must be as close as possible to the outer surface of the calorimeter cryostats for noise limitation. The base-line subtractor cards will be housed within the rolling table which supports and moves the detector. The multiplexing level prior to transport of the signals through the radiation enclosure to the electronics house is chosen to be 16-fold. This choice of dc voltage multiplexing allows substantial reduction of cable volume and cost, with negligible signal degradation. Further multiplexing of signals will occur before digitization in the electronics house. The total channel count for the calorimeter electronics is about 42,000.

3.2.3 Muon System

The measurement of muons in DØ consists of identification by penetration of muons through a large absorber medium, and determination of the momentum through deflection in magnetized iron toroids. The coverage of muons extends

down to $\theta = 11°$ with respect to either beam. Three magnetized iron toroids outside the calorimeters provide the bending strength of about $\Delta P_T = 600$ MeV/c.

The three toroids are shown in Figs. 3.4 and 3.5. The central toroid (CF) is a square cross-section shell whose axis is aligned with the beam direction and is 850 cm long and about 100 cm thick. Coil packages excite a mean magnetic field in this toroid of about 2T, whose direction is approximately azimuthal. CF is physically constructed in three pieces. The bottom section is a long fixed bar centered under the beams which also serves as the support members for the CC and EC calorimeters. The two remaining C-shaped sections can be split and removed transversely to allow access to the central detectors and calorimeters.

The two end toroids (EF) are square cross-section iron slabs whose outer dimensions are 820 cm. The inner surfaces of EF are square holes of width 240 cm; the plug calorimeters (PC) rest on the inner surface of these holes. The iron is excited magnetically by a set of toroidal coils yielding a field of 2T at the inner radius, decreasing to about 1.6T at the outer radius. The EF toroids must be penetrated by a hole (about 15 cm diameter) for passage of the displaced main ring beam pipe; exclusion of field from this region must be accomplished by magnetic shield inserts. The EF must be capable of movement along the beam axis, away from the intersection region, in order to create access space for servicing the internal detectors.

The total amount of material traversed by muons is sufficiently large that the probability for hadronic showers to yield particles leaking out of the system is very small. At 90°, the calorimetry presents a total of 6.9 absorption lengths(λ_0); at perpendicular incidence, the iron toroids give a total thickness of 6.4 λ_0 for a total of 13.3 λ_0. At the minimum angle of

11°, the calorimeter thickness is 8.9 λ_0. the iron is 9.1 λ_0 for a total of 18 λ_0.

The muon trajectories are measured with planes of proportional drift tubes (PDT) situated in the space between calorimeters and iron and in the space outside the iron toroids. The PDT elements are extruded Al tubes 10 cm×2.5 cm of lengths up to 600 cm. Field shaping electrodes are included to give good space-time uniformity over the full cell. In each tube, the wire direction is aligned approximately parallel to the magnetic field direction so as to give good bend-plane coordinate resolution through the drift-time measurement. The orthogonal transverse coordinate is measured in each tube via charge measurements on two vernier cathode strips located above and below the wire. One vernier strip is etched into a repetive saw-tooth pattern of wavelength about 10 cm. Measurement of the induced charge ratio for upper and lower elements of the sawtooth yield the coordinate alone the wire to a precision of about 1 mm, modulo the uncertainty on which the section of the sawtooth was struck. This uncertainty is removed by the second vernier strip which is a single sawtooth over the full PDT length. Charge ratios on this strip give a position accuracy of ±5 cm--sufficient to determine which of the smaller wavelength sections was struck.

The PDT's are arranged so as to measure a line segment over 30 cm. in the space between the calorimeters and the iron and to measure a line segment over a longer lever arm in the space outside the iron (120 cm in the central region and 320 cm in the end regions). The PDT's inside the iron consist of four planes of tubes, with wires offset by one half cell to remove left-right ambiguities in the drift time measurement. The PDT's outside typically have three planes just after the iron and three planes after the free space. Again, adjacent planes are offset by one half drift cell. The total count of PDT's

is about 12,700. Each tube readout requires measurement of one time and four charge measurements.

Measurement of muon momenta are limited by multiple Coulomb scattering in the calorimeters and iron up to some maximum momentum set by the measurement accruacy of the PDT's. This multiple Coulomb scattering limit is about $\Delta p_T/p_T$ = 20% (depending on whether or not the muon track inside the iron is available). The p_T value at which measurement errors begin to dominate the uncertainty in bend angle depends upon both polar and azimuthal angles, as well as the intrinsic position resolution in the bend plane coordinate. Typically, for coordinate errors of 0.5 mm, resolution effects overtake multiple scattering at p_T = 200 GeV/c.

The front-end electronics for the PDT's will be located near one end of each of the planes; all signals from each plane are taken from that end. The charge signals are integrated and placed on sample and hold circiuts in the form of d.c. voltage levels. The time signals are shaped, discriminated and the time is converted to a voltage level. Both charge and time d.c. level information are then multiplexed and sent on signal cables through the radiation shield to the electronics house. Due to the low level of occupancy in the muon chambers, the multiplexing level can be quite deep: 32 fold for the time information and 64 fold for the charge information, thereby reducing the total signal cable load leaving the detector.

3.2.4 Trigger and Data Acquisition

The trigger for the experiment proceeds in three successive levels, each providing further reduction in the rate of events to be examined. At the design luminosity, the interaction rate is expected to be approximately 10^5 Hz. This rate is selected by the level 0 trigger consisting of

coincidence of the beam-crossing timing signal and coincidence of the luminosity monitor counters. The first stage of reduction is achieved by the level 1 trigger system during the 3.5 μsec before the next beam crossing can occur; thus no dead time is incurred in this level. The goal of the level 1 triggering is a reduction in rate of events to a few hundred per second. The final selection of events in the level 2 system is achieved in a parallel microprocessor system in which each event is analyzed more fully and subjected to more complex requirements than in the level 1 trigger. The resulting successful events are passed to the host computer for data logging, monitoring, and on-line physics summaries.

The level 1 trigger consists of two basic components: the calorimeter trigger and the muon trigger. The calorimeter trigger is based upon fast sums of signals taken from the preamplifiers. There are 1600 electromagnetic trigger towers summed over the full EM depth within $\Delta\phi\times\Delta\eta \simeq 0.2 \simeq 0.2$. Similarly, 400 hadronic section trigger towers are summed within $\Delta\phi\times\Delta\eta \simeq 0.4\times0.4$. These signals are then combined to form levels corresponding to total transverse energy (EM and hadronic), the missing transverse momentum, as well as searching for clusters of EM or hadronic energy above a preset threshold which signal jet activity.

The muon trigger is based upon latches set from the PDT wire discriminators which record the presence of a muon candidate track within a half cell outside the toroids. Two-dimensional matrix logic then selects patterns of hits which correspond to muon transverse momenta above 5 GeV/c. This cut reduces the trigger rate to below 1 Hz, including the contribution from π and K decays.

The results of the level 1 calorimeter trigger and muon trigger (number of clusters, number of muon candidates, missing p_T, total E_T, etc.) are then

presented to an AND/OR network in which up to 32 combinations of requirements on multiplicity or thresholds can be selected under computer control. Indication of an acceptable trigger results in initiation of the digitization sequence. The digitized information from all systems, together with digitized values of the quantities used in the level 1 trigger decision, are passed on the the level 2 system.

The level 2 trigger consists of about 50 parallel microprocessors, each equipped with a set of dual port memories which collect digitized information from a set of eight parallel 32 bit wide data cables. Each cluster of dual port memories serves a dedicated processor which, based upon the data block transmitted from the level 1 trigger information, refines the various energy, cluster, and track variables. The microprocessor (targeted to be a MicroVAX with approximately 1 VAX 11/780 equivalent CPU power). Then analyzes the event, searching for valid correlations involving electron and muon candidates, missing p_T and total E_T, and jet-like clusters. The average time available to analyze and reject unwanted triggers is about 100 msec, in order to reduce the final event rate passed along for data logging to 1 Hz.

3.2.5 System Parameters

The performance specifications of the DO detector summarized above and discussed in the succeeding chapters are collected in Table 3.1. The main detector parameters are shown in Table 3.2.

REFERENCES CHAPTER 3

1. C. Rubbia, Proceedings of the Dortmund Conference on Neutrino Physics, June 1984. P. Darriulat, private communication.

2. P. Bagnaia et al., CERN preprint CERN-EP/83-94.

3. P. Bagnaia et al., CERN preprint CERN-EP/83-112.

4. W. J. Willis and V. Radeka, Nucl. Instrum. Methods **120**, 221 (1974); J. H. Cobb et al. Nucl. Instrum. and Methods **158**, 93 (1979).

5. C. Fabjan et al., Nucl. Instrum. and Methods **141**, 61 (1977).

6. J. Brau and T. Gabriel, private communication and SLD note.

7. H. A. Gordon and P. D. Grannis, Calorimetry at the SSC, Proceedings of the 1984 Workshop on SSC (Snowmass).

8. A. L. S. Angelis et al., Phys. Lett. **94B**, 106 (1980).

9. Fermilab proposal P714, addenda 6, 12, and 29.

10. A. Bungerer et al., Electron Identification Beyond 1 GeV by Means of Transition Radiation, Siegen Univ. Preprint (1983); C. Fabjan et al., CERN-EP/83-45.

11. O. Botner et al., IEEE Transactions on Nucl. Science, **NS-28**, No. 1.

TABLE 3.1 Performance Specifications

Drift Chamber	
Spatial resolution in $r\Delta\phi$	200 μm
Spatial resolution in z	5 mm
Two track resolution	5 mm in $r\Delta\phi$ 5 cm in Δz
2 overlapped track rejection by dE/dx	50:1
Transition Radiation Detection	
e/π discrimination	50:1
Calorimetry	
Energy resolution - electromagnetic	$12\%/\sqrt{E}$(GeV)
- hadronic	$40\%/\sqrt{E}$(GeV)
Segmentation - transverse	$0.1(\Delta\phi)\times 0.1(\Delta\eta)$
- longitudinal	4 in EM 4 in hadronic
Position resolution - EM showers	8 mm/$\sqrt{E}$(GeV)
Muon System	
Momentum resolution in multiple scattering limit	20%
Transverse momentum for sign determination at 3σ	300 GeV/c
Solid Angle Coverage	
Drift chamber system	$\|\eta\| < 3.5$
Transition radiation	$\|\eta\| < 3.1$
Calorimetry	$\|\eta\| < 4.7$
Muon detection	$\|\eta\| < 2.34$ ($\Delta\Omega$ = 98%)

TABLE 3.2 Detector Parameters

Vertex Detector	$3 \leq r < 10$ cm $\|z\| < 40$ cm
Transition Radiation Detectors	
Central	$10 \leq r \leq 40$ cm $\|z\| < 70$ cm
End	$92 \leq \|z\| \leq 122$ cm $r < 65$ cm
Number of Channels	1080
Drift Chamber	
Central	$40 \leq r \leq 70$ cm $\|z\| \leq 74$ cm
Number of sense wires	768
Number of delay lines	256
End	$80 \leq \|z\| \leq 137$ cm $r < 65$ cm
Number of sense wires	784
Number of delay lines	224
Calorimeters	
Central	$75 \leq r \leq 222$ cm $\|z\| \leq 113$
Gross Weight	280 t
Number of towers	1536
Number of channels	13952
Liquid volume	4300 gal
End cap (each)	$142 \leq \|z\| \leq 340$ cm $r \leq 207$ cm
Weight	216 t
Number of towers	1536
Number of channels	12192
Liquid volume	5000 gal
Plug (each)	$500 \leq \|z\| \leq 650$ cm $r < 65$ cm
Weight	25 t
Number of towers	352
Number of channels	2112
Liquid volume	400 gal
(Total number of channels)	42560
Muon System	
Central Toroid	$\|z\| < 425$ cm
perpendicular inner distance	$r = 308$ cm
perpendicular outer distance	$r = 410$ cm
weight	2070 t
End Toroid (each)	$447 \leq \|z\| \leq 599$ cm
perpendicular inner distance	$r = 86$ cm
perpendicular outer distance	$r = 410$ cm
weight	875 t
Proportional Drift Tubes - number	12720
Total weight including platform	4700 t

FIGURE CAPTIONS - CHAPTER 3

3.1 Cross section vs. missing p_T for various contributions. The solid line is for losses in a 1° beam hole only; -o- is for 1° beam hole and energy resolution in calorimetry. The dashed line includes the effect of beam hole, energy resolution, and angular smearing effects (all hadron impact points are smeared with σ_x, σ_y = 2 cm). The effect of 8 azimuthal cracks of width 2.5 cm over the central calorimeter (not shown) is to broaden the missing p_T-distribution for $p_T^M > 10$ GeV/c without appreciable effect below 10 GeV/c. The contributions from signals due to ν (heavy quark) production and 100 GeV gluinos are also shown.

3.2 (a)Energy deposition pattern for a two-jet event from UA2 (Ref. 2). (b)Energy deposition pattern for a candidate $Z \to e^+e^-\gamma$ event from UA2 (Ref. 3).

3.3 Distribution of first conversion point for single photons and multiphoton events from π^0, η, and ω.

3.4 Elevation section of the detector through beam line.

3.5 End view of the detector at z = 0.

3.6 Isometric view of the detector.

3.7 Plan view of the central detectors (scale in cm).

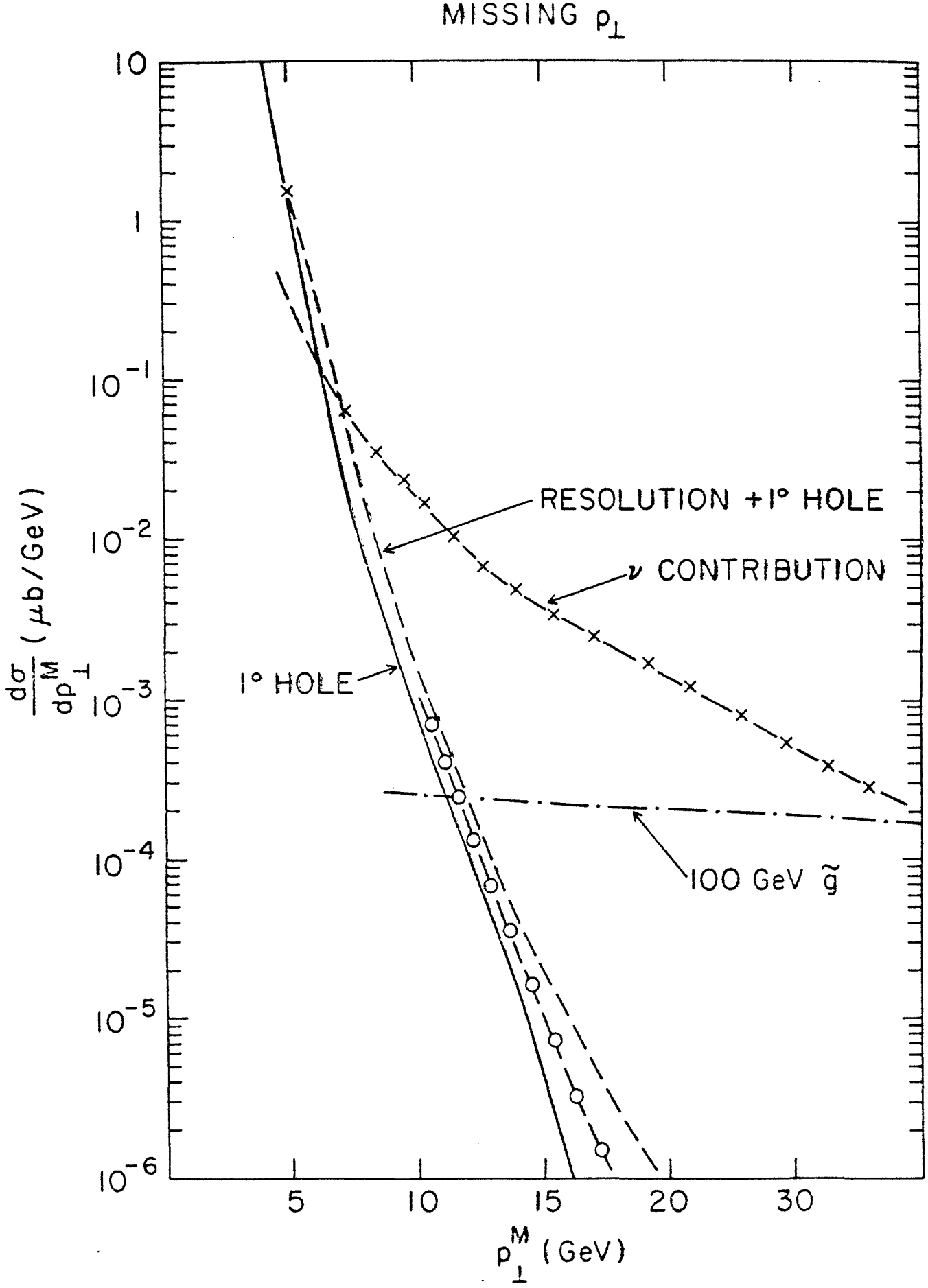
MISSING $p_\perp$
$\frac{d\sigma}{dp_\perp^M}$ (μb/GeV)
$p_\perp^M$ (GeV)
RESOLUTION +1° HOLE
ν CONTRIBUTION
1° HOLE
100 GeV $\tilde{g}$
10
1
10^{-1}
10^{-2}
10^{-3}
10^{-4}
10^{-5}
10^{-6}
5
10
15
20
30

Fig. 3.1

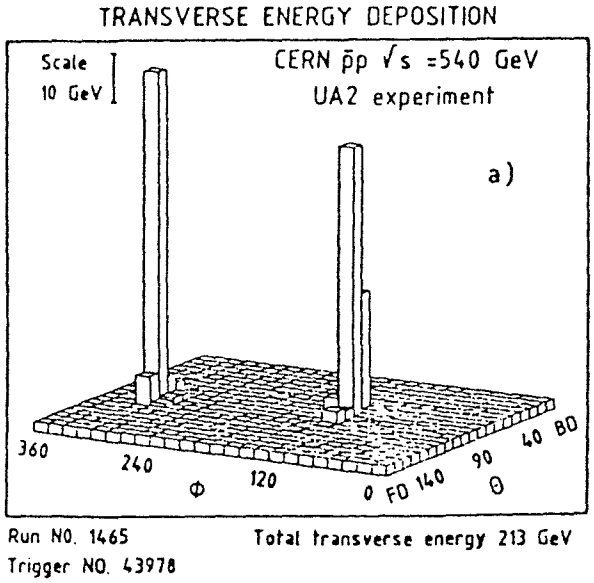
TRANSVERSE ENERGY DEPOSITION
Scale
10 GeV
CERN p̄p √s =540 GeV
UA2 experiment
a)
360
240
Φ
120
0
FD
140
90
Θ
40
BD
Run NO. 1465
Trigger NO. 43978
Total transverse energy 213 GeV

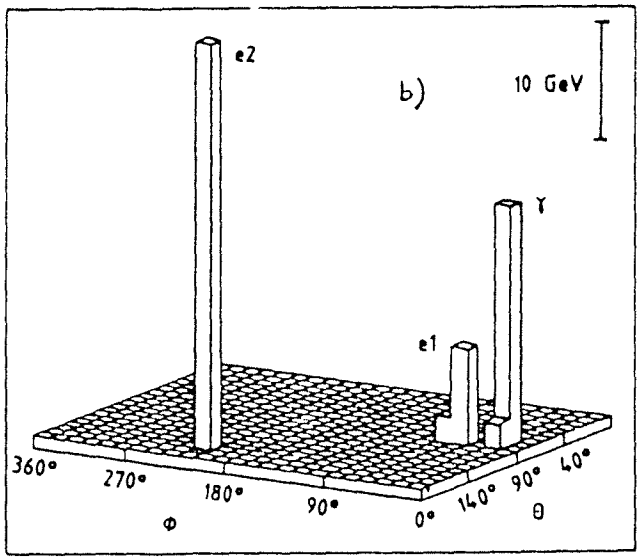
e2
b)
10 GeV
γ
e1
360°
270°
180°
90°
Φ
0°
140°
90°
40°
Θ

Fig. 3.2

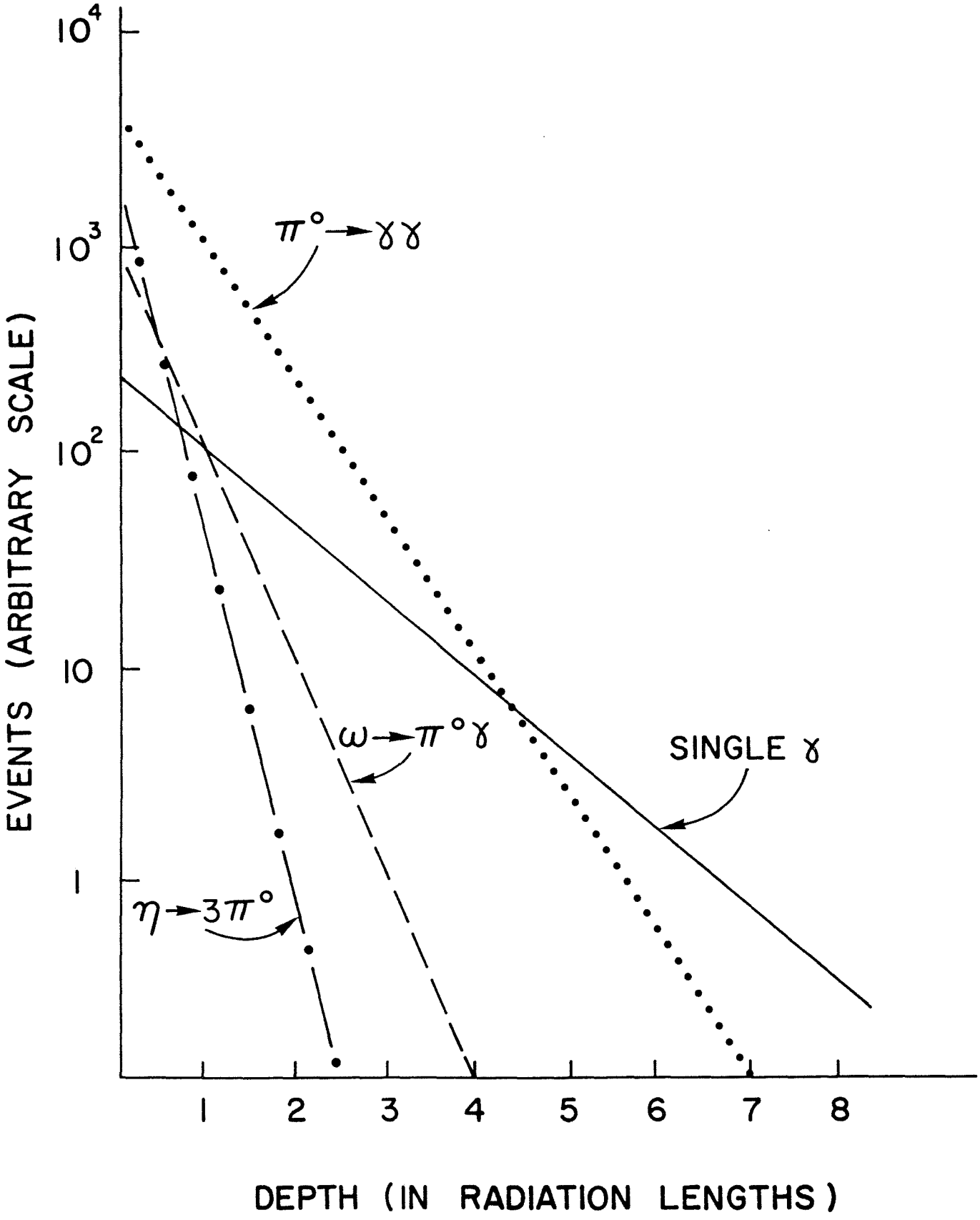
EVENTS (ARBITRARY SCALE)
10^4
10^3
10^2
10
1
$\pi^\circ \rightarrow \gamma\gamma$
$\omega \rightarrow \pi^\circ\gamma$
$\eta \rightarrow 3\pi^\circ$
SINGLE γ
1
2
3
4
5
6
7
8
DEPTH (IN RADIATION LENGTHS)

Fig. 3.3

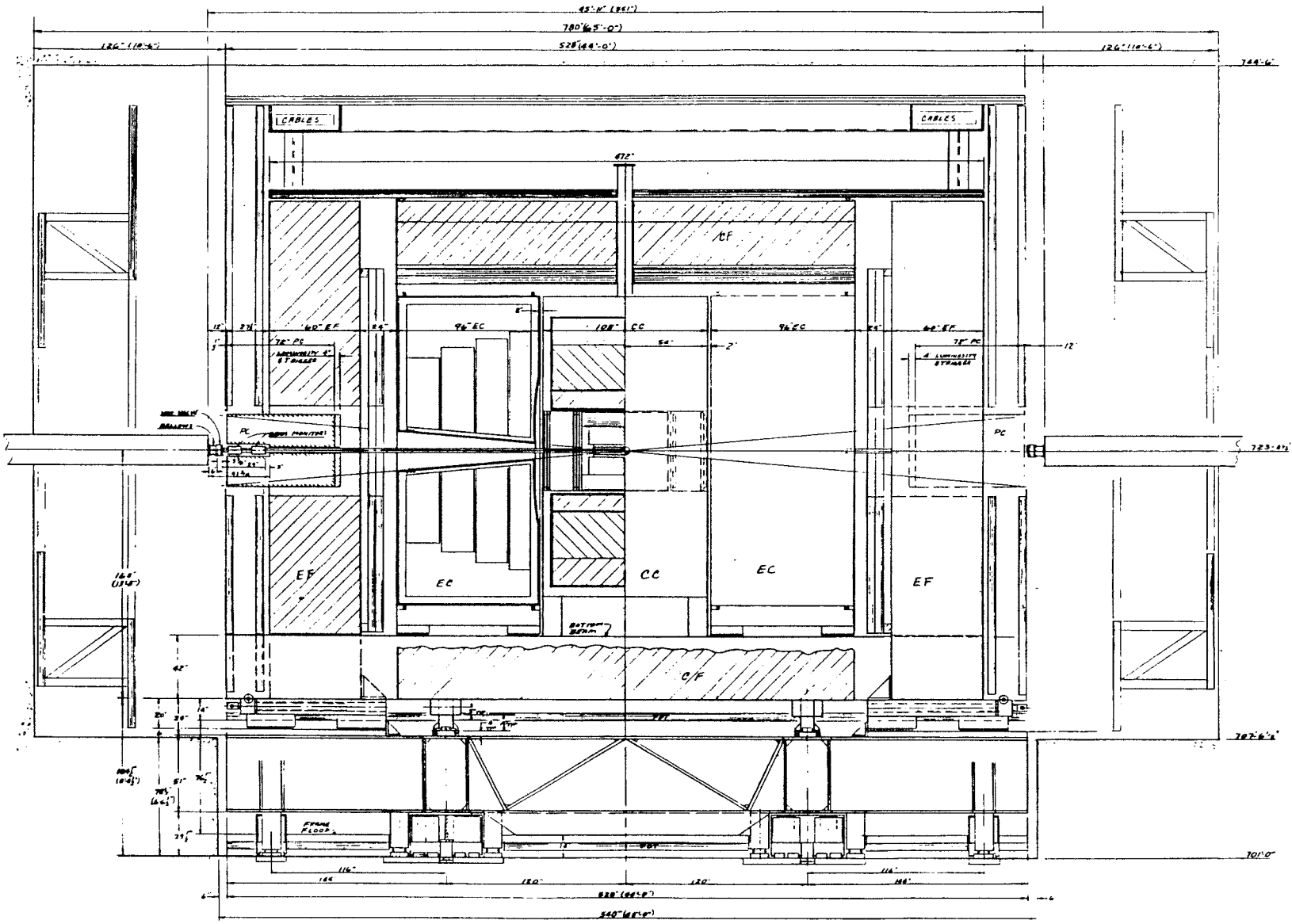

PARTS LIST

FERMI NATIONAL ACCELERATOR LABORATORY
UNITED STATES DEPARTMENT OF ENERGY

D-Ø DETECTOR
ELEVATION IN COLLISION HALL

9220.740-ME 201746

SHEET #1 of 3

Fig. 3.4

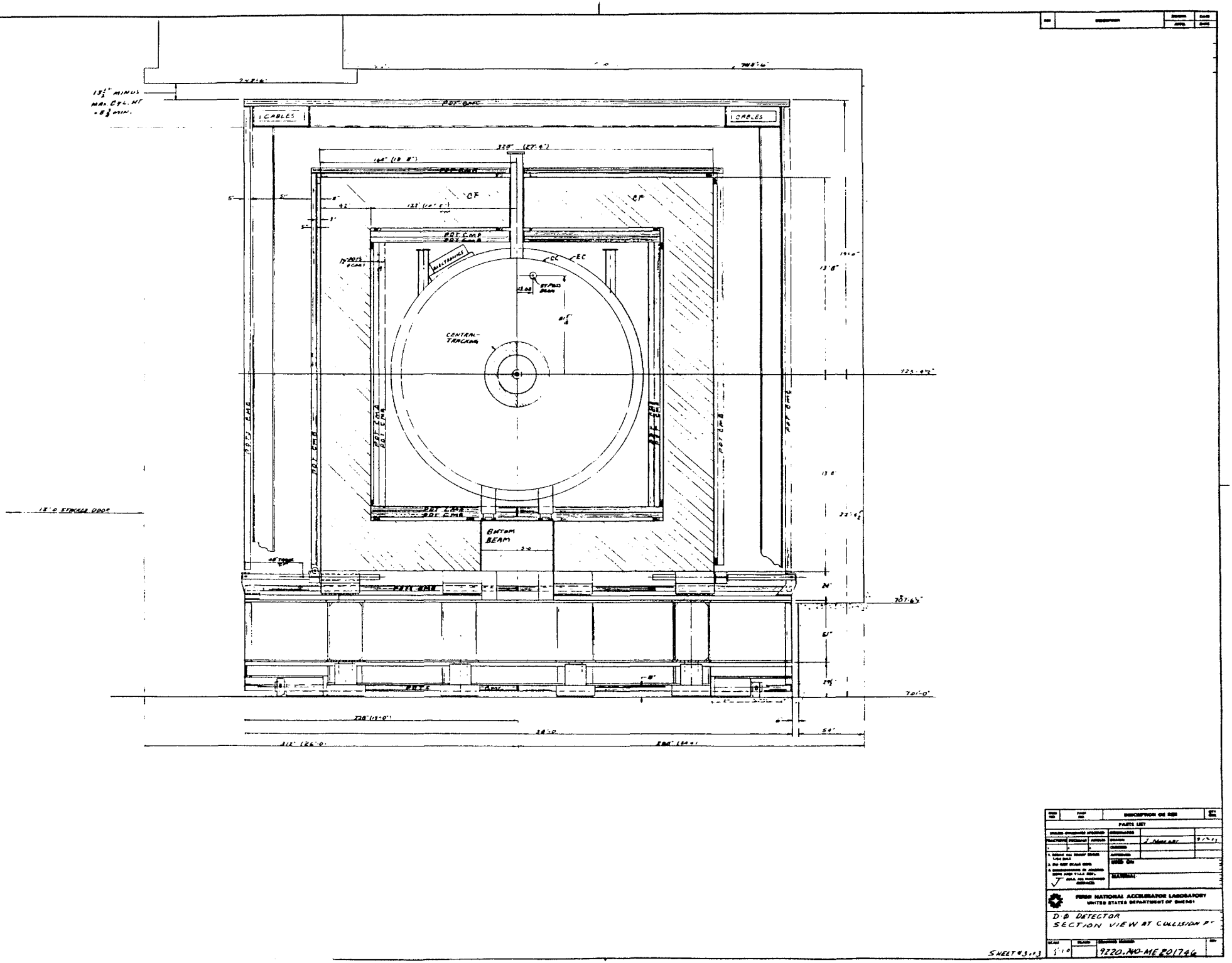
CABLES
CABLES
CF
CF
CC
EC
CENTRAL TRACKING
Bottom BEAM
13'-0 STRAIGHT DOOR
725'-4½"
701'-0"

Fig. 3.5

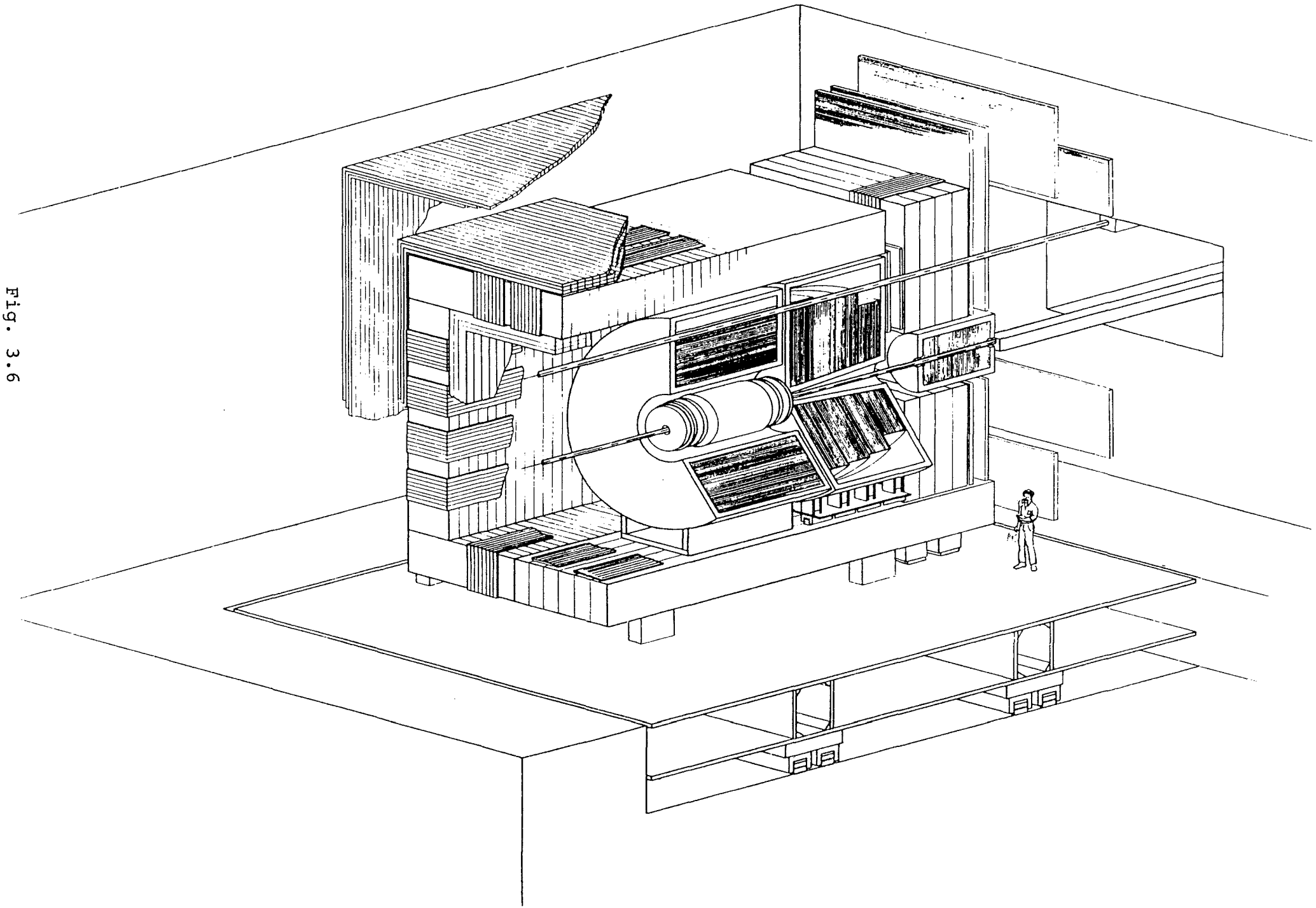

Fig. 3.6

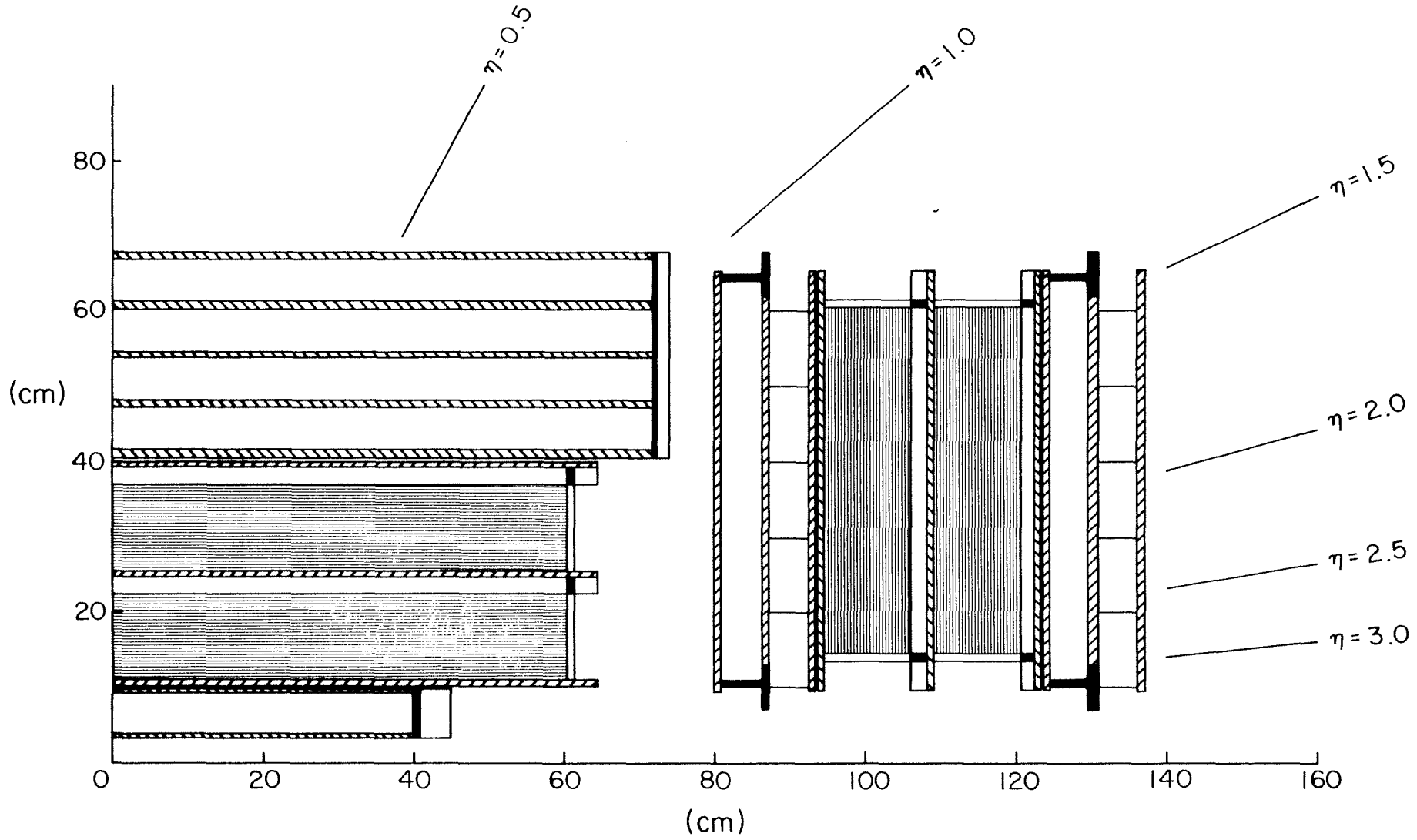
η=0.5
η=1.0
η=1.5
η=2.0
η=2.5
η=3.0
80
60
40
20
(cm)
0
20
40
60
80
100
120
140
160
(cm)

Fig. 3.7

4. CENTRAL DETECTORS

The central detector systems consist of the inner vertex detector, transition radiation detectors (TRD's) in both central and forward-backward regions, and drift chambers in both central and forward-backward regions (Fig. 4.1). These detectors provide the particle tracking information, electron identification, and photon conversion rejection.

4.1 VERTEX DETECTOR

The vertex detector occupies the space between the beam pipe and the central TRD. This chamber has not been subjected to detailed design. Its functional requirements are presented here; evaluation of the desired parameters and a specific design choice is underway.

The vertex chamber is essential for rejecting photons which convert before the transition radiation detector. In addition, it will be used to detect secondary vertices as a means of identifying heavy quarks and leptons.

To provide good photon rejection, the chamber must have high efficiency for charged particle tracks over a large solid angle. To minimize conversions within the chamber, the design must minimize the amount of structural material, especially with high Z. The choice of detector length will be a compromise between large solid angle for acceptance and a large minimum angle to reduce pile-up.

The resolution and the segmentation required of the detector are being investigated using the ISAJET Monte Carlo. In particular, the question of longitudinal coordinate determination and resolution must be answered early in this study. To achieve a very high track-pair resolution, the chamber must have fine effective segmentation. This may be achieved by spatial segmentation or by time sampling. Coverage at small angles may be reduced to minimize multitrack pile-up.

In addition to the physics issues that affect the design, a number of construction, assembly, and maintenance issues must be resolved. It will be necessary to sustain wire loading and maintain positional tolerance while minimizing the amount of material in the chamber. Some electronics must be placed close to the chamber in a high-radiation environment. The chamber should be integrated with the beam pipe but must be accessible for repair.

4.2 CENTRAL DRIFT CHAMBERS

The tasks to be performed by the central drift chambers are to obtain the trajectories of charged particles produced in the central region ($|\eta| < 1$); to complement the central TRD in its role of electron tagging, and thus to identify photon-induced EM showers in the calorimeter; and to identify overlapping e^+e^- pairs from photon conversions or Dalitz decay in the material in front of the calorimeter. The chamber has, therefore, been designed to optimize multiple-track efficiency and specific ionization measurements.

The chamber is not required to measure momenta, and the absence of a magnetic field leads to certain simplifications that impinge on the design: tracks are straight; low-momentum tracks do not produce large numbers of space points in spiraling; drifting electrons are not subject to a Lorentz $\vec{E} \times \vec{B}$ effect; and track curvature measurements are not the aim of the design, so the need for very high position resolution is relaxed. These advantages are balanced by the disadvantage that overlapping tracks of different momenta remain overlapping.

The major constraint on the design of the chamber is the limited space available between the central TRD and the central calorimeter. An additional consideration is its transparency to electromagnetic particles.

The design chosen to satisfy these demands embodies the following principal features: a cylindrical geometry; large drift cells; the use of delay lines to measure the second coordinate; drift-cell staggering; and multiple-hit digitization of analog and time information on all channels.

4.2.1 Mechanical Design

The chamber is shown schematically in Figs. 4.1 and 4.2. It is a roughly

cylindrical shell centered on the nominal crossing point with inner and outer radii of 40.5 and 68.0 cm and a length of 148.0 cm. Wires run parallel to the beam line and the drift field is approximately circumferential.

The chamber is radially segmented into four superlayers separated by light laminated walls which provide structural integrity and support the delay lines and some of the field-shaping electrodes. Each superlayer is azimuthally segmented into 32 supercells which are separated by thin foils supporting additional field-shaping electrodes.

Each supercell is an independent drift volume equipped with six sense wires located in the median plane (ϕ = constant) of the supercell (Fig. 4.2 inset) The sense wires are spaced radially apart in 8 mm steps, and are separated by potential wires, to reduce the cross-talk between adjacent sense wires and to focus the drift field onto the sense wires. Delay lines mounted on supercell walls are associated with the two sense wires nearest the inner and outer walls. The drift field is produced and shaped by the conductive strips on the inner surfaces of the supercell walls and the foils isolating supercells. Wall surfaces are coated with high-resistivity paint to avoid the accumulation of static charges and to improve the uniformity of the drift field close to the field-shaping strips. The field so produced is a uniform field normal to the plane containing the sense wires. The drift field and consequently the drift velocity are the same in all supercells.

The maximum drift distance in the chamber is 6.5 cm. Since the shortest interval between beam crossings ultimately may be 3.5 μs, it is feasible to use a drift gas which is slower than conventional mixtures in order to enhance multiple-track efficiency by spreading multiple avalanches on the sense wires apart in time.

In a chamber with relatively large drift cells, the use of delay lines is a more natural means of obtaining the second coordinate than charge division, stereo geometry, or cathode-pad readout. The position resolution of delay lines is better than that of charge division; delay lines lead to a more compact detector than does stereo geometry; the channel count and the cost is less for delay lines than for cathode pads; and--most importantly--delay lines offer good multiple-hit efficiency at low cost. In the case of cell occupancy by a pair of tracks close in azimuth but separated longitudinally, for example, the pulses observed at one end of the delay line can be unambiguously correlated with those at the other end through the requirement that the sum of transmission times along the line correspond to its length.

The azimuthal segmentation in adjacent superlayers is staggered by half the azimuthal width of a cell, an arrangement that serves the following purposes: (1) the right/left ambiguity within supercells is resolved; (2) two-track separation is enhanced--of two azimuthally close tracks, one is detected in the two supercells of one orientation while the second is detected in the other two; and (3) a continuous drift-velocity calibration is possible--the sum of drift times for any given track in the two sets of supercells corresponds to a fixed azimuthal angle.

The chamber samples the drift coordinate and the specific ionization of a charged particle at 24 locations along its trajectory, and samples the delay-line coordinate at 8 locations. The 768 sense wires are read out at one end only; the 256 delay lines are read out at both ends. Readout consists of time digitization of the leading and trailing edges of all pulses above threshold, coupled with 50-MHz sampling and digitization of pulse heights. This form of readout is capable of identifying partially overlapping pulses.

4.2.2 Construction

The basic constructional unit is the wedge shown in Fig. 4.3. Thirty-two identical such wedges constitute the chamber as a whole.

The walls are laminates of Rohacell-30 polymethacrylamide foam, milled to the required shape, and foils of kapton bearing the copper-conductive elements necessary for field-shaping. Wall segments, with the delay lines glued in place, are attached to G10 end frames, and the intercell foils with their field-shaping strips are soldered into position. At this stage, a wedge is a self-supporting unit. The G10 end frames support wire feedthroughs in which the sense and potential wires are precisely located and crimped.

The final stage of the assembly is to locate the wedges into a "drum," which consists of two thin cylindrical aluminum cylinders at the inner and outer radii with spoked end plates which accurately position the wedges.

4.2.3 Drift-Chamber Performance

An exploratory test of a prototype central-drift-chamber cell has been made in a BNL test beam. The test has given us an indication of the performance to be expected of the full chamber.

Our requirements in terms of spatial resolution for a single sampling of a track are not very stringent: we found $\sigma_{r\phi}$ = 200 to 300 μm for the drift coordinate and σ_z < 5 mm for the delay coordinate. In the test, the delay lines used were, in fact, shorter than in the final design (86 cm instead of 150 cm), but the quoted resolution has been routinely obtained with 150-cm lines.[1] In addition, the delay lines in the final design will benefit from electronically cooled terminations[2] to enhance their performance (see section 4.5), and by the measurement of pulse amplitudes which allows offline correction of discriminator slewing.

The resolution in the vertex coordinate is determined by the delay line resolution. For a single track, our geometry gives σ_z(vertex) $\approx 3\ \sigma_z < 1.5$ cm. By reconstructing the vertex with many tracks and then refitting tracks with this extra constraint, an ultimate resolution σ_z (vertex) $\approx$ 2 mm will be attained.

The separation of two azimuthally close tracks is performed in staggered drift cells of different orientations, as noted above. The distance at which such pairs can be resolved is thus of the order of the resolution in the drift coordinate. The minimum double-track separation on a single sense wire is $\approx$ 4 mm.

Specific ionization measurement is needed to identify fully overlapping tracks. The test showed that the best estimator of specific ionization is the median of individual samples along the track(s), which, for minimum-ionizing particles, rejects at least 95% of overlapping tracks, while maintaining 95% efficiency for single tracks. This capability is important in discriminating single high-p_T electrons from e^+e^- pairs whether from Dalitz decay or from photon conversions.

4.3 FORWARD-BACKWARD DRIFT CHAMBERS

The forward and backward drift chambers are symmetrically located with respect to the center of the interaction region, covering the approximate angular regions $3.5° \leq \theta \leq 40°$ with respect to each beam (Fig. 4.1). The tasks to be performed are the same as in the case of the central drift chamber (section 4.2) with the additional requirement that the chambers project charged tracks into the forward and backward TRD's. Because of the latter requirement, the forward-backward drift chambers are split into similar sections before and after the TRD. Again, there is a premium on multiple-track efficiency and specific ionization measurement in these chambers.

4.3.1 Mechanical Design

The design of the endcap drift chambers retains two of the main features of the central chamber: the "pictorial geometry" and the use of delay lines to measure the coordinate along the sense wire. The drift gas and the readout electronics are also identical. However, the chambers are necessarily of different construction; Fig. 4.4 shows an exploded view of the chamber construction at one side of the interaction region. Each arm contains four superlayers; two before the TRD and two after. Alternate superlayers are rotated with respect to each other by 90°.

Each superlayer is a plane of drift cells with an approximately circular outline. Figure 4.5 is an artist's view of the drift cell, and Fig. 4.6 shows the cell structure and the relevant dimensions. The cells have a height of 5.5 cm, a drift region of 5.0 cm, and their lengths vary between 60 and 160 cm. Seven sense wires run along the median plane of the cell. The two sides of the cell parallel to the sense wires are enclosed by aluminized mylar

foils. Two holes in each foil allow the chamber gas to flow from one cell to its neighbors. Copper strip electrodes are etched on the kapton walls of the cells to shape the drift field. These walls also support the delay lines which are used to determine the positions of the tracks along the sense wires. Guard wires near the sense wires contribute to field-shaping in the vicinity of the sense wires. The two ends of the drift cell (perpendicular to the sense wires) are made of G10, and have holes for alignment pins to position the cell with respect to the rigid frame discussed below. Wires are crimped to feedthroughs mounted on a flange which is, in turn, mounted on the G10 end plate. The alignment of the feedthrough plate with the G10 is done with nylon pins. Sense wires are 30 μm stainless steel under tensions of 50 g; guard wires are 175 μm copper/beryllium under 400 g tension.

Of the seven sense wires in a cell, four are displaced by 300 μm on one side of the center and three are displaced the same distance on the other side. This is done to resolve left-right ambiguity locally. Each wire measures, in a constant z plane, the distance of the track orthogonal to the sense wire. This measurement is obtained from the drift time. Delay lines measure the distance of the track along the sense wire, and have the ability to resolve ambiguities when two or more tracks cross the same cell at the same distance from the sense wire.

Our goals regarding the spatial resolutions are the following: $\sigma \leq 200$ μm for the drift coordinate; $\sigma \leq 5$ mm for the coordinate determined by the delay line, and a double track resolution of 2 cm. All these values are quite conservative. Multiple track separation is dependent on the gas used, as discussed in section 4.2.1.

4.3.2 Construction

Figures 4.7 and 4.8 indicate how we envision the assembly of the drift chambers. An aluminum jig plate of circular shape is cut to leave open the sensitive area common to both planes of drift cells. Alignment holes for positioning the G10 endplates of each drift cell are drilled in this plate with a precise milling machine. The aperture in the plate is filled with honeycomb and the plate is sandwiched between two foils of aluminum, to which kapton films with the field-shaping electrodes have been glued. An aperture for the beam pipe is then opened, and the drift cell units (the G10 endplates with the aluminized mylar sides) are glued on top of the kapton layer. Precision in positioning these cells is ensured by alignment pins. The plates with the wire feedthroughs are then mounted on the G10 plates.

Wires are hand strung in drift cell units with one side open. The proper tension is applied to each wire, one end of the wire is crimped to the feedthrough, and the other end is attached to a spring. After all the wires have been strung, the cover plate is positioned on the open face and glued. The top plate consists of a sandwich of honeycombs with an aluminum foil on each side. The side of the aluminum foil facing the drift cells has kapton films bearing field-shaping strips. All cells are then prestressed except one. The correct tension is applied to the wires of this cell, and the sprung end of the wires are crimped to their feedthroughs. The prestressing on another cell is released and its wires are connected, and so on.

4.4 TRANSITION RADIATION DETECTORS

Transition radiation detectors (TRD's) are installed in the central and endcap regions of the inner detector (Fig. 4.1) to provide e-π discrimination over as much of the solid angle as possible. The aim has been a hadron-rejection factor of 50 while maintaining over 90% efficiency for electrons with energies above 2 GeV. The major constraint in attaining this goal is the space limitation set by the compactness of the uranium calorimeters.

4.4.1 Mechanical Design

A number of alternative designs have been studied by realistically simulating their performance. The simulation was based on detailed models of the transition radiation process,[3] of ionization loss,[4] and of event topologies at $\sqrt{s}$ = 2 TeV,[5] and has resulted in the design outlined below.

The number of detectable photons (X-rays with energies of about 5 to 10 keV) emitted at a dielectric interface due to the transition effect is small (typically ~0.01), and a large number of interfaces are thus required for an effective detector. The emitted X-ray intensity increases with the atomic number of the optically dense component of the radiator as $Z^{1/2}$. The X-ray absorption coefficient, on the other hand, also increases with Z, but as Z^5. A radiator best satisfies the contradictory requirements of high-density for yield and low-density for transparency, therefore, by having low Z, and we have chosen lithium foils (Z = 3) as the radiator.[6]

A lower limit is set on the useful thickness of the foils by the formation-zone effect.[3] (This can be understood as a minimum distance in which the electromagnetic field of the charged particle can reach a stable configuration after crossing the interface.) By adjusting the spacing of the foils relative to their thickness, a coherent superposition of the radiation fields from

individual interfaces can be obtained.[7] We have found an optimal stack which has foil thicknesses of 30 μm and an inter-foil spacing of 150 μm.

Since the radiator and the X-ray detector compete for a fixed amount of space, one wants to minimize the number of stacks. Due to reabsorption of the X-rays, however, increasing the depth of a stack indefinitely leads to diminishing returns in terms of total X-ray yield. The best solution in our case (a 30-cm depth for both the central and endcap TRD's) turns out to be two radiator stacks, each followed by its own X-ray detector.

The detector must be sufficiently opaque to X-rays to detect them with reasonable efficiency, but it should be relatively transparent to charged particles, so that it can discriminate between the two sources of energy deposition. A high-Z gas is indicated and the obvious candidate is xenon (Z = 54).

The mean free path of a 10 keV photon is roughly 1 cm in xenon at normal pressure, and, when absorbed, the photon deposits its energy in a localized cluster since the range of a 10 keV photoelectron is ≈ 100 μm in xenon. Minimum ionizing particles, on the other hand, are characterized by a most probable energy deposition of about 3.5 keV/cm with the usual large fluctuations. It has been shown[8] that the different features of track ionization and photo-ionization could be exploited to register transition radiation photons more efficiently than in the conventional method of integrating the ionization from both sources. The method simply consists in the counting of ionization clusters that exceed a relatively high preset threshold. The only background to this method is the registration of occasional keV δ-rays, but their numbers are small: in xenon the number with energies above 3 keV is ≈ 0.1 cm^{-1}. A second advantage of cluster counting is that the distribution of the number

of clusters is Poisson and thus better behaved than the distribution of deposited energy with its long Landau tail.

The type of chamber that is used to detect the X-rays is a two-step, longitudinal drift chamber (Fig. 4.9). The first section is the absorption/drift zone, which is 1-cm deep and in which the electrons drift in the direction of the incident particles. The second section, separated from the first by a grid of potential wires (2 mm spacing), is the amplification zone, which has the structure of a standard type of drift chamber. The wire spacing is 8 mm with the sense wires strung parallel to the beam. The drift gas is a xenon/methane (70/30) mixture, and the drift field is adjusted to obtain the best time resolution for cluster counting.

The central TRD has inner and outer radii of 10 and 40 cm and extends ±60 cm along the beam line with respect to the crossing point as shown in Fig. 4.1. Each of the two stacks consists of 640 lithium foils in a sealed container filled with helium. The window between the stack and the chamber has to be transparent to X-rays but extremely non-porous to protect the very hygroscopic lithium: it is a sandwich of 3 mm polyethylene foam, 50 μm mylar or kapton foils, and a 2 μm aluminum foil.

The first chamber (r = 24.0 cm) has 180 sense wires ($\Delta\phi = 2°$), and the second chamber (r = 38.6 cm) has 300 sense wires ($\Delta\phi = 1.2°$). The sense wire preamplifiers (fast, low-noise current amplifiers) are mounted on the end faces of the detector, and the amplified signals are brought out on twisted pairs to shaping amplifiers located in the collision hall. The shaping amplifiers output is adapted to FADC digitization. For ease of installation the central TRD is made of two parts with a resulting dead space corresponding to $\Delta\phi = 12°$. The design of these detectors is shown in Fig. 4.10.

The endcap TRD is roughly circular in shape with a radius of 60 cm, and occupies the region of z between the endcap drift chambers ($93 \leq z \leq 123$ cm). A 12×12 cm^2 square hole accommodates the beam pipe to pass through. The sense wires in the two chambers are horizontal and have the same spacing as in the central TRD, giving 150 channels per plane. The design of the end cap TRD is shown in Fig. 4.11.

The thickness of both central and endcap modules corresponds to 3.3% X_0 or 4.4% λ_0 for normally incident particles.

4.4.2 Performance of the TRD

The expected performance of the transition radiation detector has been computed in a Monte Carlo simulation, assuming foil spacing, foil thickness, and chamber construction as described above. Transition radiation and ionization information has been included using published data.[3,4] Clusters of ionization were counted if they deposited more than 3 keV of energy in the chamber. Figure 4.12 shows the rejection against pions versus the efficiency of detecting 2.5 GeV electrons (γ = 5000). For an ideal detector, the pion rejection is about 400:1 with 95% electron efficiency. The effects of doubling the number of ionization clusters due to pions and of removing one of the two chambers are also shown. Figure 4.13 shows the effect on the pion rejection of increasing the total TRD depth. The angular dependence of the number of ionization clusters and of transition radiation clusters is shown in Fig. 4.14; the overall dependence of pion rejection on angle of incidence is shown in Fig. 4.15. Figure 4.16 shows that the location of the first of the two chambers within the allowed radial space ($10 \leq r \leq 40$ cm) is not critical.

The ideal performance of the TRD is seen from these calculations to be a pion rejection factor of about 400:1. Effects which will reduce this factor in practice ideal include: (a) loss of ionization from the early part of the conversion gap; (b) losses in radiated photons due to irregularities in the foil spacing; and (c) particle overlap on a single wire. Tests of detectors in pion and electron beams[9] show some effects of types (a) and (b), and lead us to expect that the operational pion rejection will be about 100:1.

The effect of overlapping hits depends upon the event type under consideration. We have measured the probability that a second particle enter the same drift cell as an electron using ISAJET generated events of the types $W \to e\nu$, $W \to t\bar{b}(t \to e\nu b)$, and $W \to t\bar{b}(\bar{b} \to \bar{c}e\nu)$. The overlap probabilities in the central (end) TRD's for these samples are 4% (2%), 9% (6%), and 18% (11%) respectively. In the case of such an overlap, the ability to reject pions is reduced by about a factor three from the non-overlap case. Thus, even in the case of semileptonic decays of b-quarks from W's, the mean degradation of rejection factors due to overlap is only about 25%.

4.5 ELECTRONICS FOR THE CENTRAL DETECTORS

The tracking chambers and the TRD's produce similar signals and have sufficiently similar signal-processing requirements that it is possible--and, therefore, desirable--to unify much of the electronics for the 3600 channels of TRD and tracking chamber readout (see Table 4.1).

The overall scheme calls for preamplifiers mounted on the detectors as close as possible to wire terminations. Preamplified signals are carried to shaping amplifiers located inside the detector platform within a cable path of 10 m from the preamps. Digitization is performed in the counting room.

Our main requirements of the preamplifiers and shaping amplifiers are: low noise; rise time < 8 nsec; low power dissipation; and small physical size. The preamplifier best adapted to processing fast signals from wire chambers is a fast current amplifier with a common-base configuration.[10] The basic circuit of such an amplifier is shown in Fig. 4.17. The pulse arriving at the shaping amplifier has a long exponential shape, which would produce undesireable pile-up. The shaping amplifier is designed to convert the input to a semi-Gaussian output and maximize the signal/noise ratio. The circuit is shown in Fig. 4.18. Gain adjustment is foreseen in the first stage, which is followed by a pole-zero circuit designed to cancel the exponential tail of the preamplifier output. A second pole-zero circuit cancels the tail generated by the twisted pair. The circuit also incorporates an active low-pass Butterworth filter. The output is Gaussian with rise/fall time (10% to 90%) $\approx$ 10 ns.

The preamplifier circuits (and possibly the shaping amplifier circuits) are hybridized for high-packing density in the restricted space inside the calorimeter.

The tracking chambers combine dE/dx measurement with second-coordinate readout via delay lines, and the combination implies delay line pulses of small amplitude. In order to improve the position resolution in the delay line coordinate with the chambers operating in the proportional mode, we plan to reduce noise by using preamplifiers which provide an active impedance termination of the delay line instead of a passive one.[2]

The digitization scheme currently foreseen for the central detectors is a combination of the 1860-Series Image Chamber Analyzers (ICA's) and the 1870-Series TDC's produced by LeCroy Research Systems.[11]

The ICA's are pipeline ADC's based on 50 MHz analog-shift registers (CCD's). They offer a dynamic range of 10 bits with 8 effective bit accuracy. Models will be available with sampling rates of up to 100 MHz.

The TDC's are again pipeline, and are based on 250 MHz digital shift registers. Both the leading and the trailing edges of input pulses are recorded.

The way in which use will be made of these devices is different for the TRD's and the tracking chambers. In the case of the TRD's, timing information is less important, and so TRD pulses will be digitized by 100 MHz ICA's only. The tracking-chamber pulses will have separate time and amplitude digitization, using a 500 MHz TDC and a 50 MHz ICA on each channel.

Both the ICA's and TDC's are FASTBUS modules containing 48 and 96 channels per module respectively. The 100 MHz ICA may be packaged with 24 channels per module. The high density of data produced by the ICA's and TDC's means that some form of data compaction must occur before event filtering and recording take place. One such system proposed by LeCroy[11] is illustrated in Fig.4.19.

4.6 SAFETY CONSIDERATIONS

The central detector system occupies a volume of 3.98 m^3, and 73% of this space is filled by gas used in the detectors as listed in Table 4.2. All these detectors are operated at normal pressure and temperature. None of the gases used is toxic. Only a small fraction of the gas that we envision using is flammable and could be ignited when mixed with air, as could happen in the case of a leak. To prevent this possibility, gas supplies and gas lines will be installed according to the FNAL safety regulations. Possible leaks will be monitored with mass flow comparison in supply and return lines. Dry nitrogen gas will constantly replace the volume of gas surrounding the CDS. This replaced air will be sampled by a gas detector to monitor possible leaks. In such an eventuality, alarms will be triggered, gas supplies shut down and high voltages on the CDS switched off automatically.

In the unlikely event of a major cryogenic spill, some gas lines may become clogged and gases may freeze in the detectors. Particular care will have to be used in the warm-up phase, to prevent the mixture of high concentrations of flammable gas with air.

REFERENCES CHAPTER 4

1. L. Camilleri et al., Nucl. Instrum. and Methods **156**, 275 (1978); and P. T. Cox, private communication.

2. V. Radeka, IEEE Trans. Nucl. Sci. **NS-21**, 51 (1974).

3. X. Artru, G. B. Yodh, and G. Mennessier, Phys. Rev. **D12**, 1289 (1975).

4. V. C. Ermilova, L. P. Kotenko, and G. I. Merzon, Nucl. Instrum. Methods **145**, 555 (1977).

5. F. E. Paige and S. D. Protopopescu, BNL Internal Report No. 29777.

6. J. Fischer et al., Phys. Lett. **49B**, 393 (1974); and Nucl. Instrum. Methods **127**, 525 (1975).

7. C. W. Fabjan and W. Struczinski, Phys. Lett. **57B**, 483 (1975).

8. T. Ludlam et al., Nucl. Instrum. Methods **180**, 413 (1981); and C. W. Fabjan et al., CERN preprint CERN-EP/83-45 (1983).

9. DO Internal Notes 119 and 120 (June 1984).

10. A. Hrisoho and K. Truong, Orsay preprint LAL-RT/79-4 (October 1984).

11. LeCroy Research Systems Application Note, September 1984.

TABLE 4.1 Summary of Channel Counts

	# Units	# Depth Layers/ Unit	# Cells/ Depth Layer	Active Elements/ Cell	Channels/ Active Element	Element Type	Channel Counts
Central T.R.D.	1	1	180	1	1	Inner sense wire	180
	1	1	300	1	1	Outer sense wire	+300 480
Endcap T.R.D.	2	2	150	1	1	sense wire	600
T.R.D							1080
Central D.C.	1	4	32	6	1	sense wire	768
	1	4	32	2	2	delay line	512
Endcap D.C.	2	4	14	7	1	sense wire	784
	2	4	14	2	2	delay line	448
D.C.						sense wire	1552
						delay line	960
Grand Total							3592 channels

TABLE 4.2 Composition of Gases in Detector Components

Component	Gas Volume (liters)	Gas	Flammability in Air % Gas in Air Mixture
Vertex Drift Chambers	30		
TDR	86	Xenon/Methane 70/30	Methane 14%
Central	320	Helium	
Drift Chamber Central	1300	Argon/Methane 90/10	Methane 14%
Drift Chambers Sides	800	Argon Methane 90/10	Methane 14%
TRD	78	Xenon/Methane 70/30	Methane 14%
Sides	294	Helium	

FIGURE CAPTIONS - CHAPTER 4

4.1 A cross-section through the central detectors in one quadrant of the rz-plane. The large-angle region contains the vertex detector, two transition radiation stacks, and the central drift chamber; the small-angle region contains two transition radiation stacks sandwiched between the two modules of the forward-backward drift chamber. The scale is in cm.

4.2 A cross-section through the large-angle central detectors in one quadrant of the $r\phi$-plane, showing the segmentation of the central drift chamber. The inset shows the wire arrangement within supercells (x - sense wire, • - potential wires, o - delay lines). The broken lines delimit a constructional unit. The scale is in cm.

4.3 The basic constructional unit of the central drift chamber. The sense wires and delay lines of one supercell are shown.

4.4 An exploded view of the forward-backward drift chamber on one side of the crossing point showing the arrangement of supercells.

4.5 A schematic view of a forward-backward chamber supercell indicating its construction.

4.6 A cross-section through a forward-backward chamber supercell showing the wire arrangement.

4.7 A view of the front face of a forward-backward chamber module. Cut-aways indicate the laminar construction of the structural plates.

4.8 A cross-section through one module of the forward-backward chambers indicating its construction.

4.9 A cross-section through the two-step xenon drift chamber used for transition X-ray detection.

4.10 Design of the central transition radiation detector foil boxes and chambers.

4.11 Design of the end transition radiation detector foil boxes and chamber.

4.12 Pion rejection factor vs. electron efficiency for $\gamma = 5000$. The points ● refer to the standard conditions; ■ show the situation when the ionization deposition is doubled; and ▲ show the effect of removing the signals from one chamber.

4.13 Pion rejection factor versus TRD depth.

4.14 Number of produced X-rays from transition radiation (●); number of detected X-rays (▰); and five times the number of detected ionization clusters from delta rays (◢) versus angle of incidence.

4.15 Pion rejection versus angle of incidence, for 97% electron efficiency.

4.16 Pion rejection vs. location of the first X-ray detecting drift chamber.

4.17 Schematic of the preamplifier for the drift chambers and TRD's.

4.18 Schematic of the shaping amplifier for the drift chambers and the TRD's.

4.19 Schematic of the digitization scheme foreseen for the drift chambers.

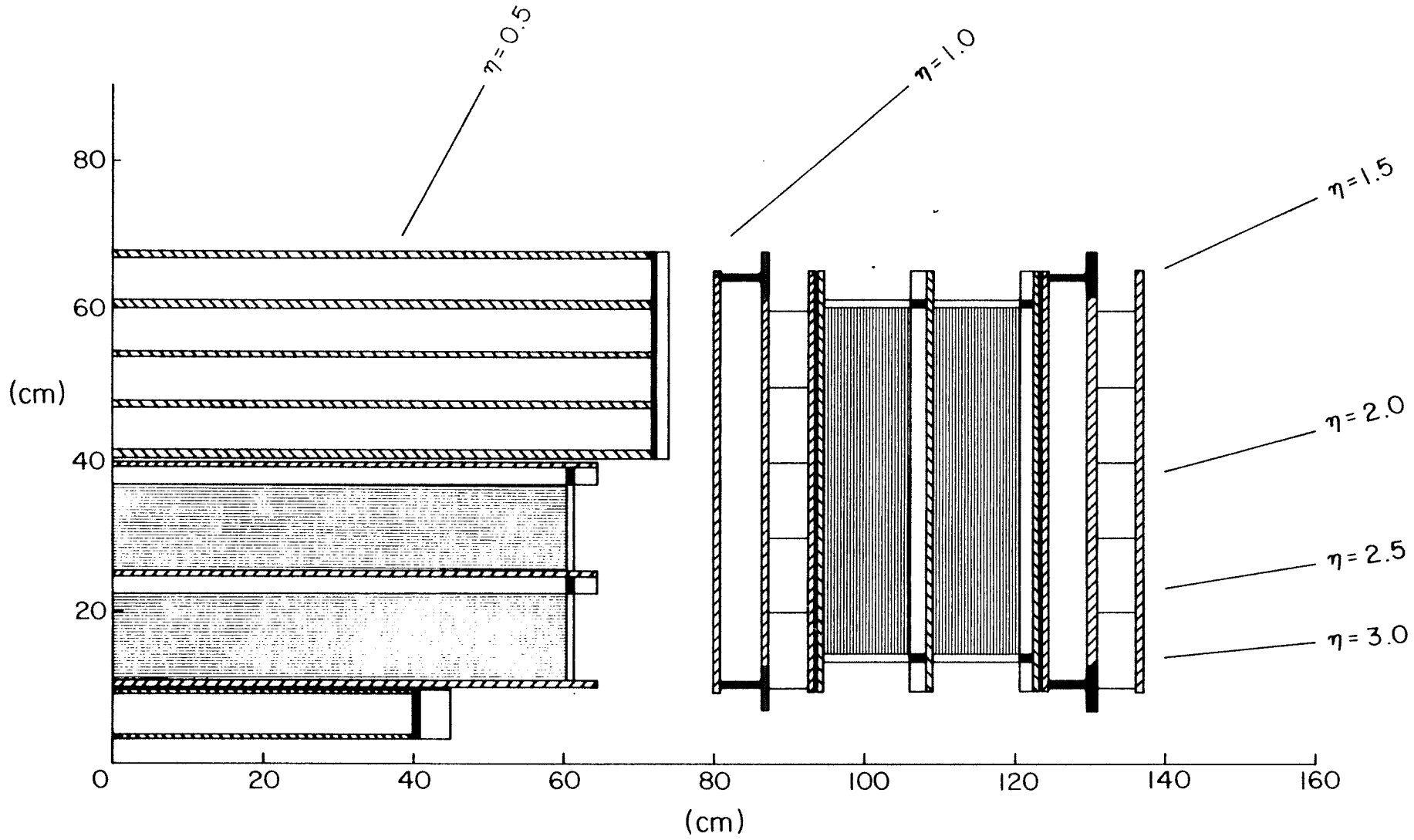
η=0.5
η=1.0
η=1.5
η=2.0
η=2.5
η=3.0
80
60
40
20
(cm)
0
20
40
60
80
100
120
140
160
(cm)

Fig. 4.1

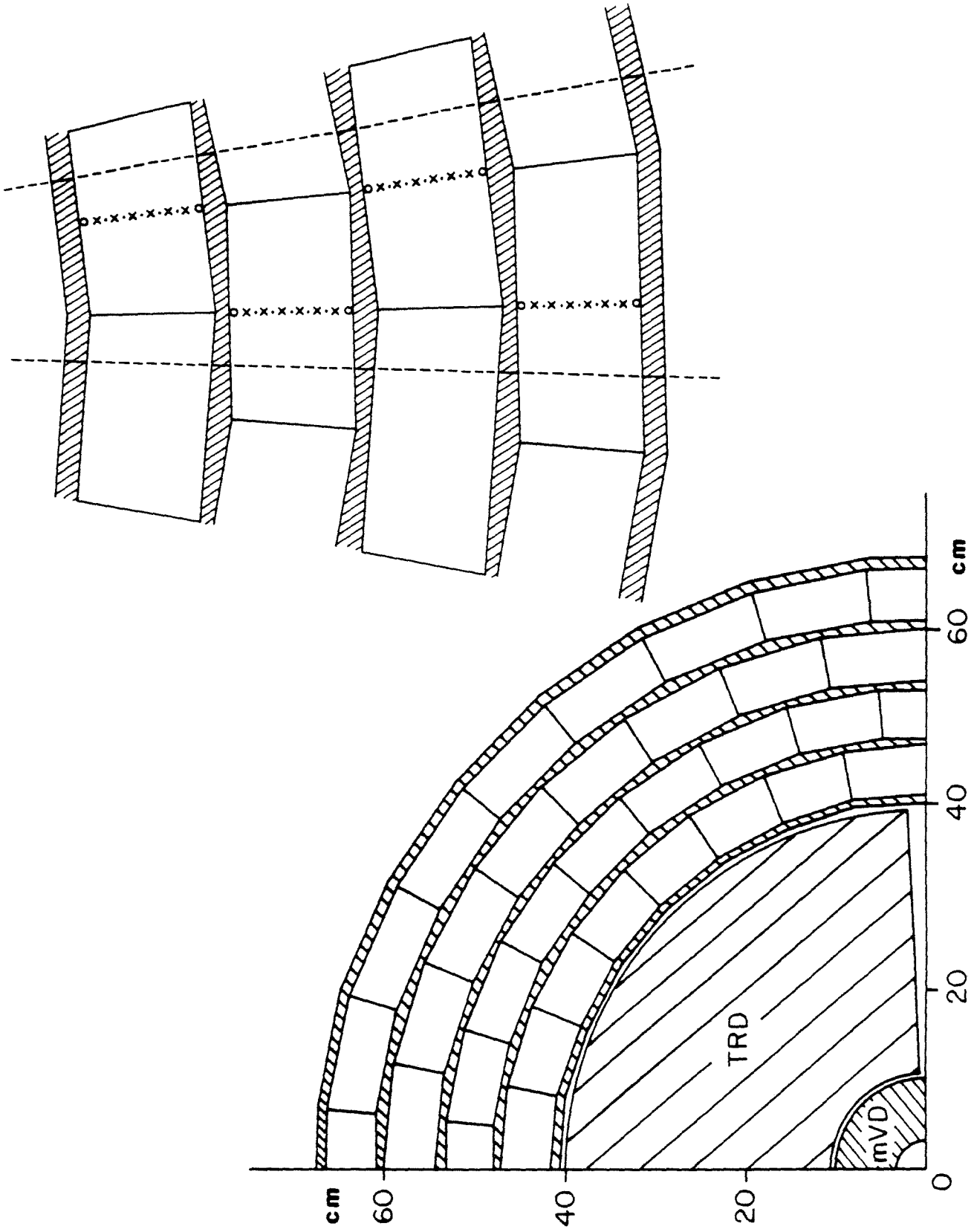

Fig. 4.2

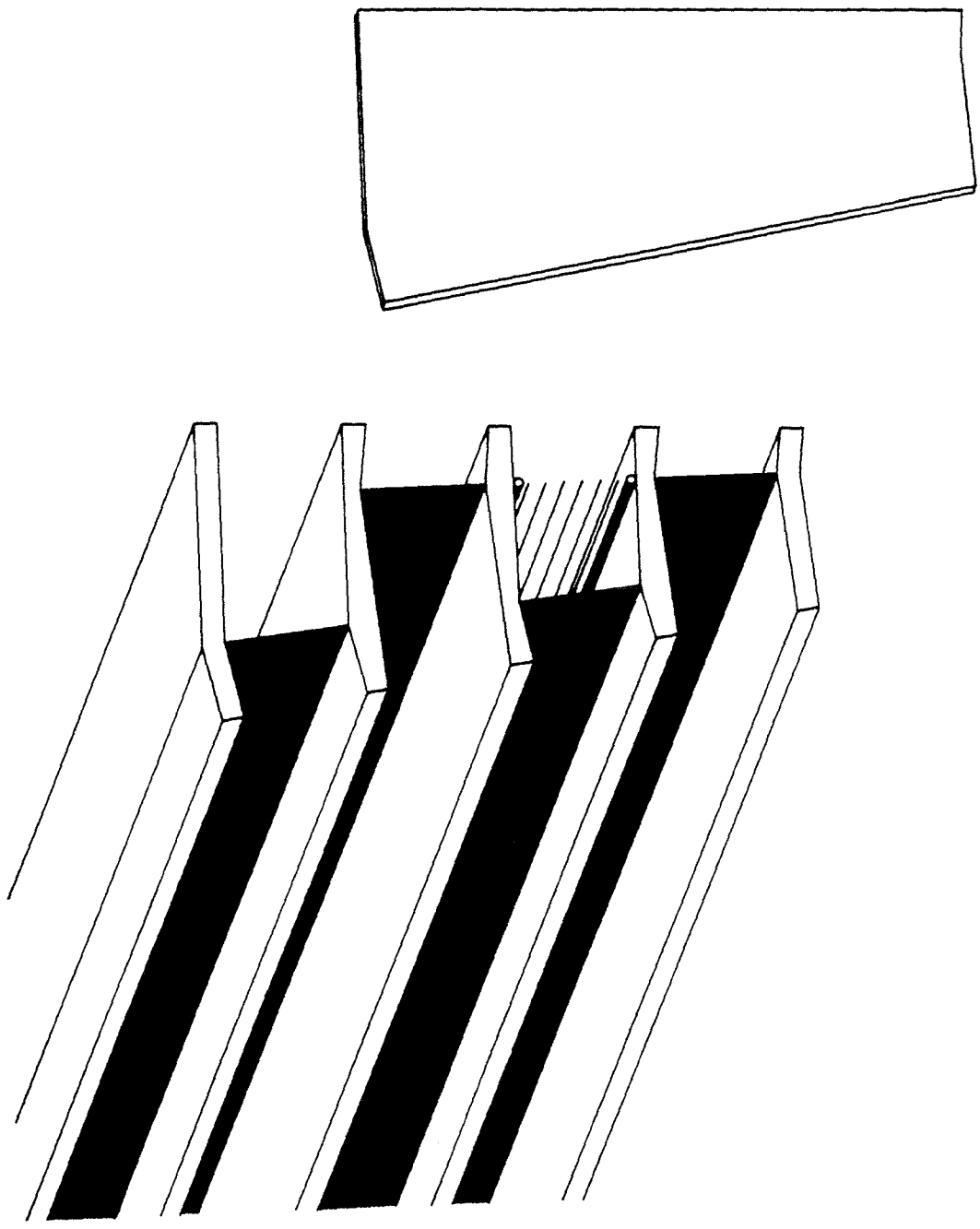

Fig. 4.3

DØ Endcap Drift Chambers

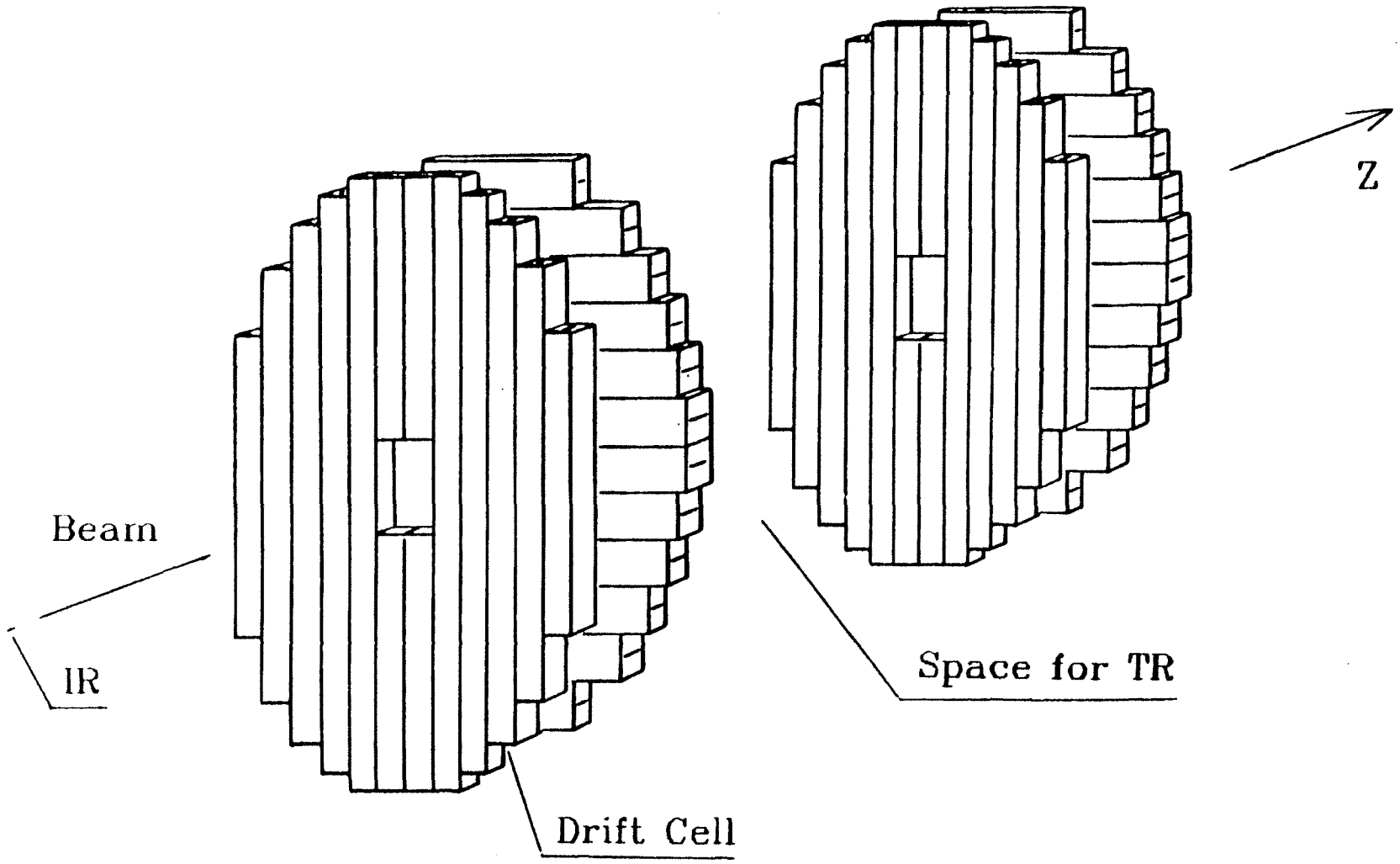

Fig. 4.4

DRIFT CELL

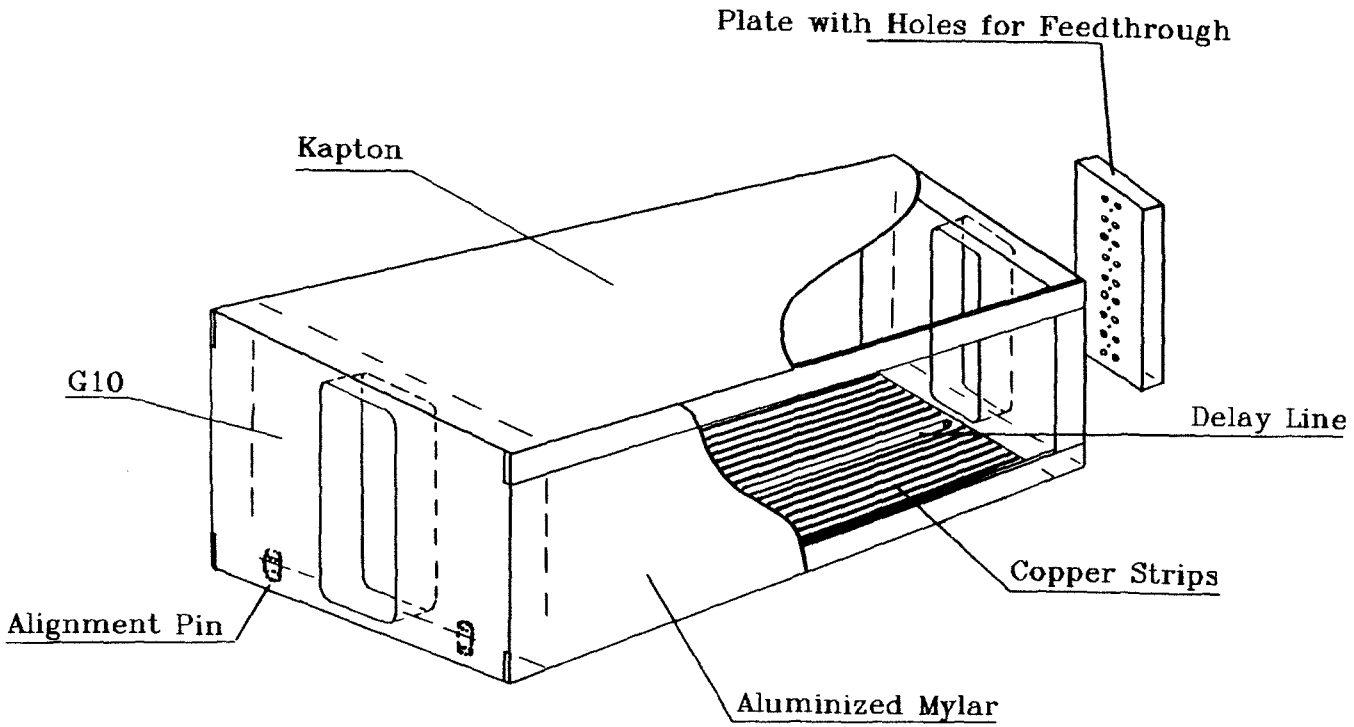
Plate with Holes for Feedthrough
Kapton
G10
Delay Line
Copper Strips
Alignment Pin
Aluminized Mylar

DRIFT CELL

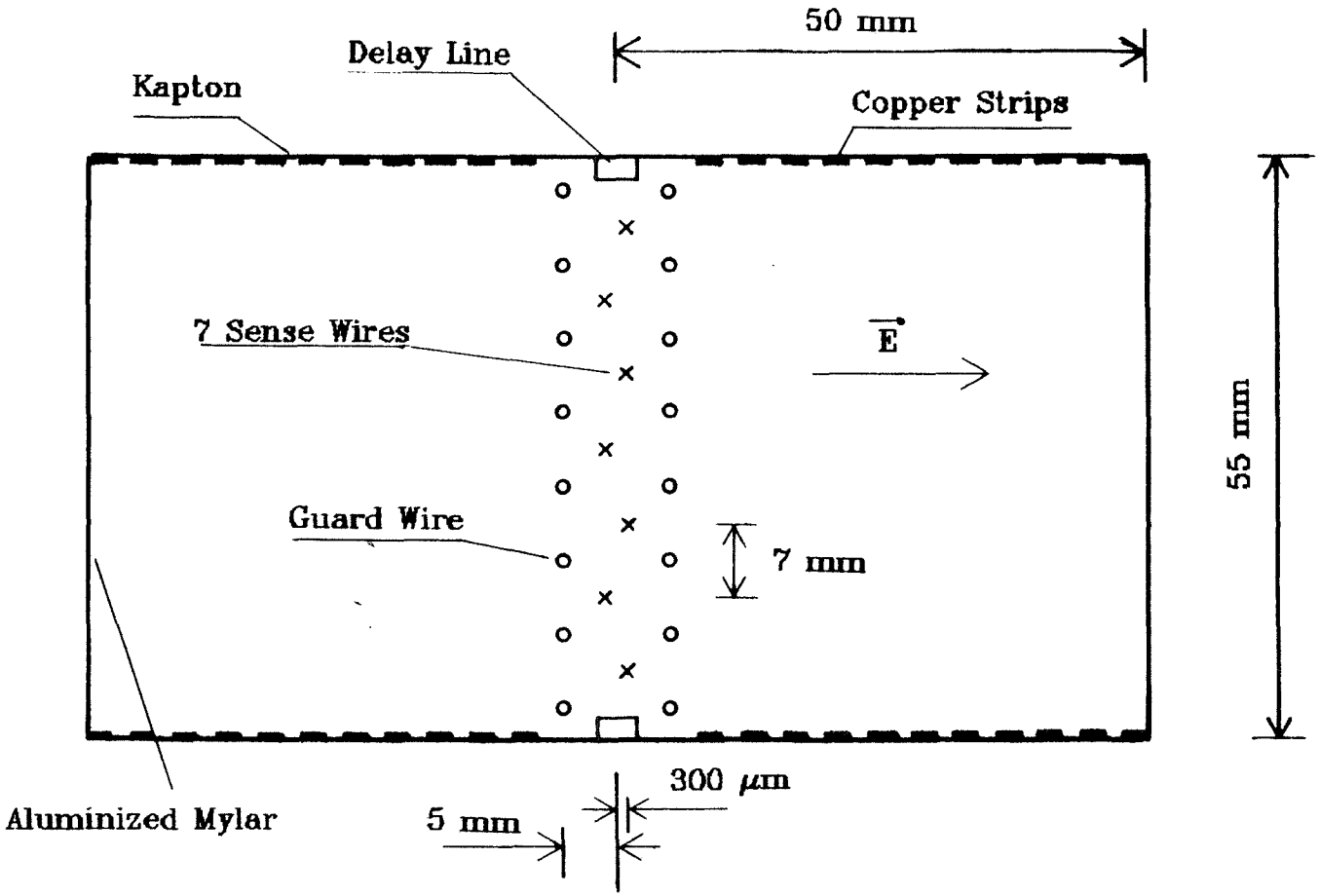
50 mm
Delay Line
Kapton
Copper Strips
7 Sense Wires
E
Guard Wire
7 mm
55 mm
Aluminized Mylar
5 mm
300 μm

Assembly of Endcap Driftchambers

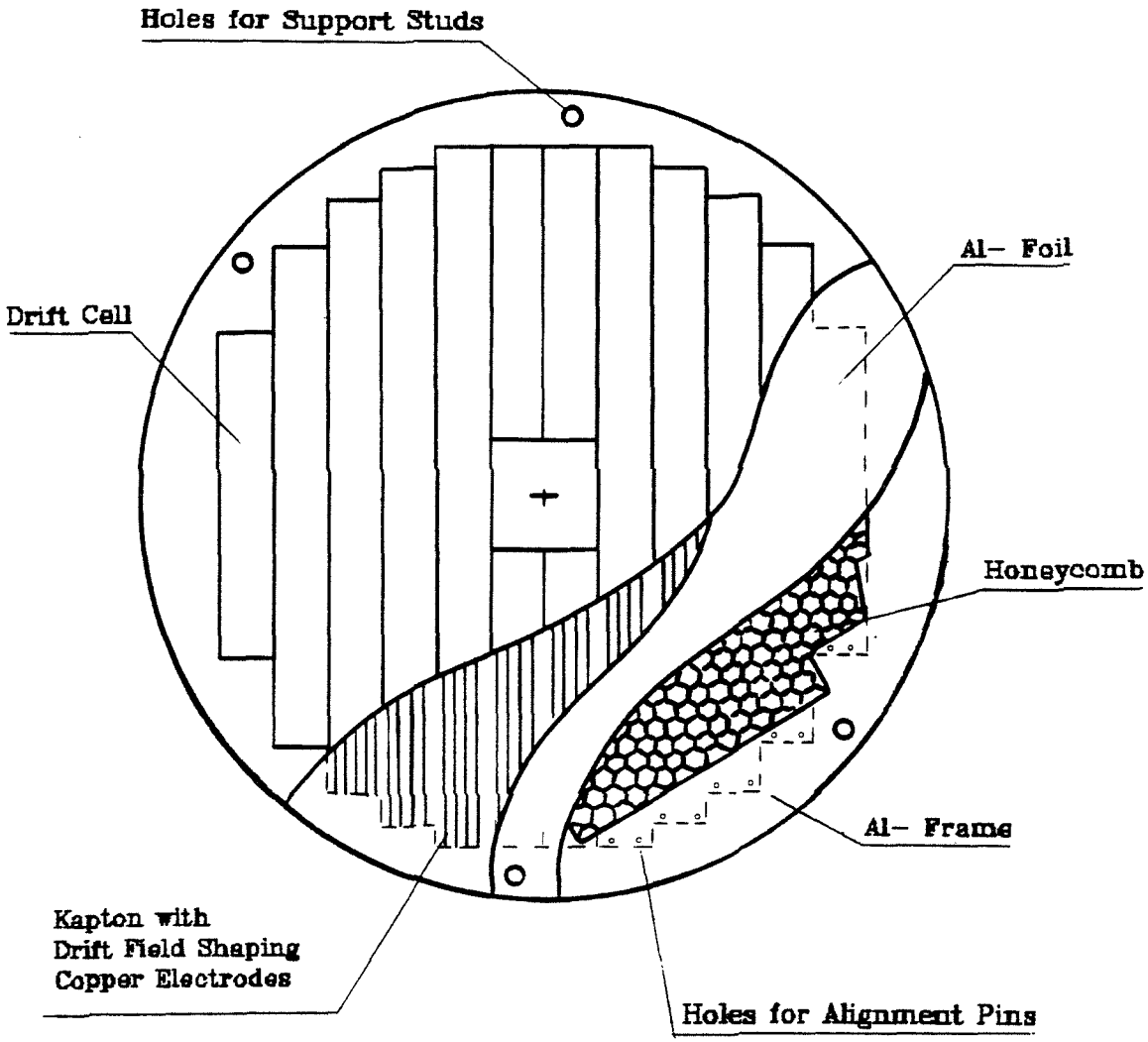

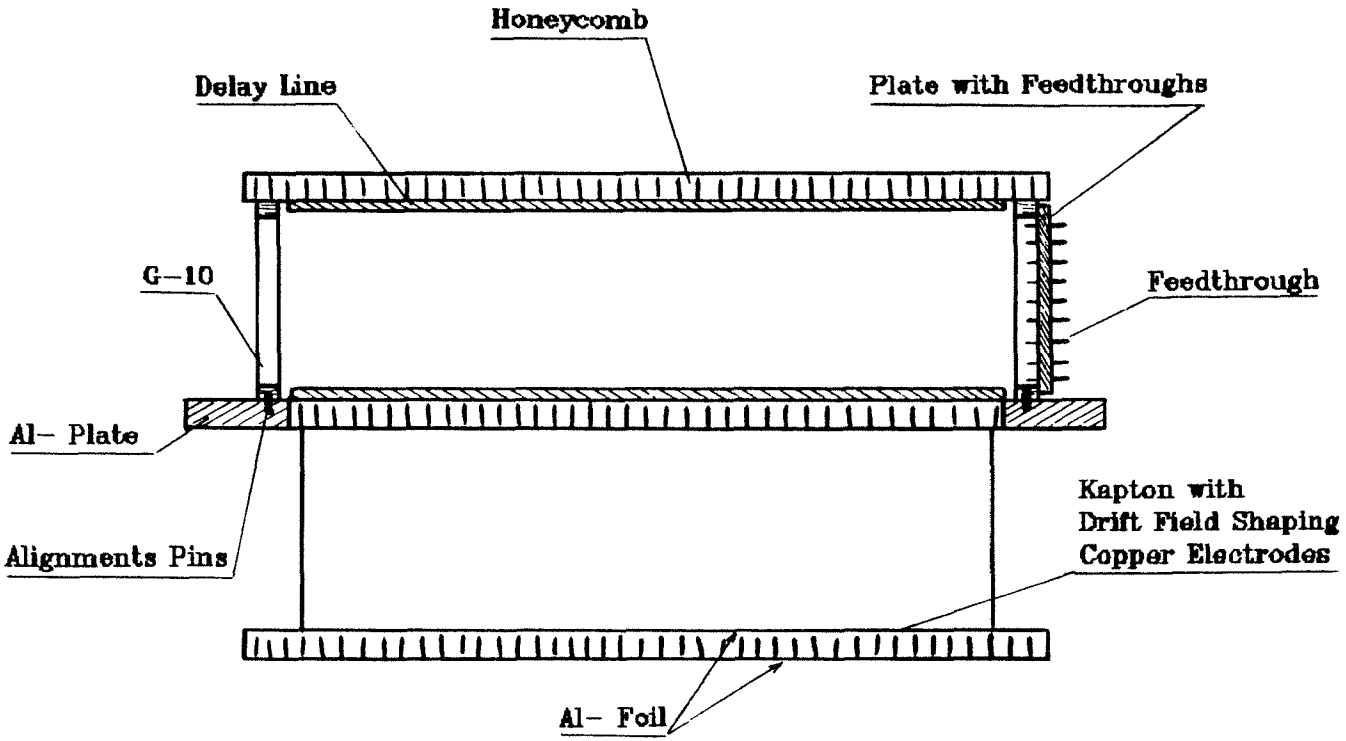

Drawing not to Scale

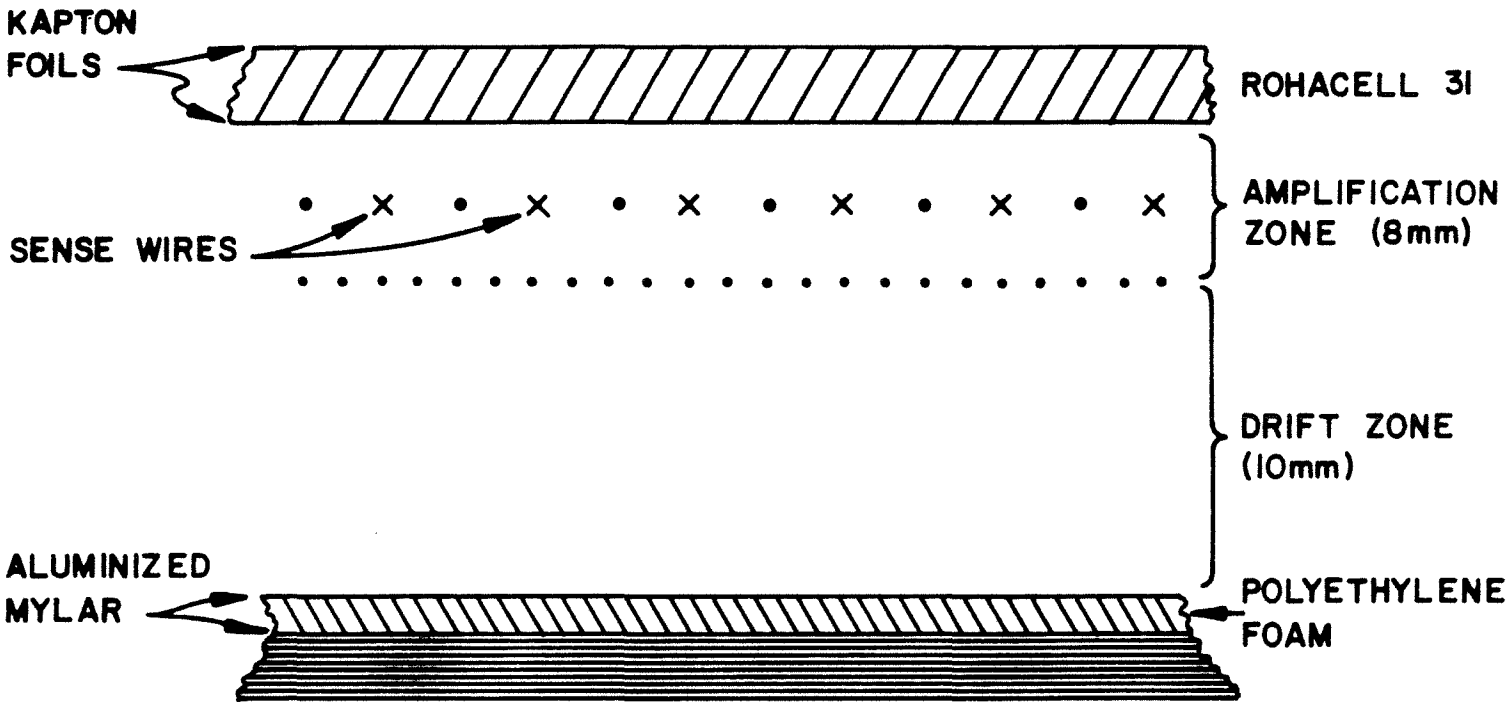
KAPTON
FOILS
ROHACELL 31
AMPLIFICATION
ZONE (8mm)
SENSE WIRES
DRIFT ZONE
(10mm)
ALUMINIZED
MYLAR
POLYETHYLENE
FOAM

Fig. 4.9

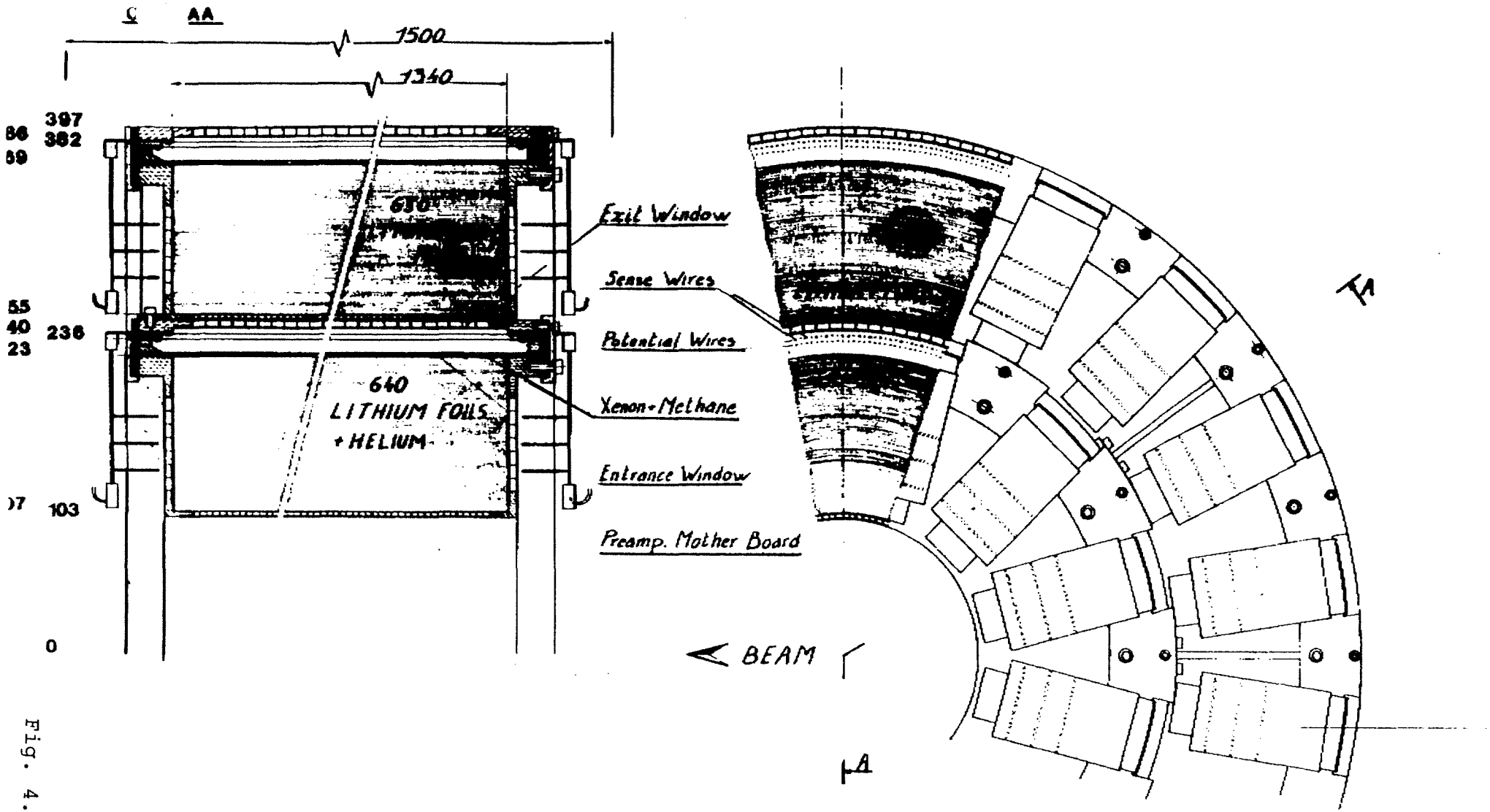

Fig. 4.10

D
Detecteur a Radiation de Transition Cylindrique Monobloc
STIPE

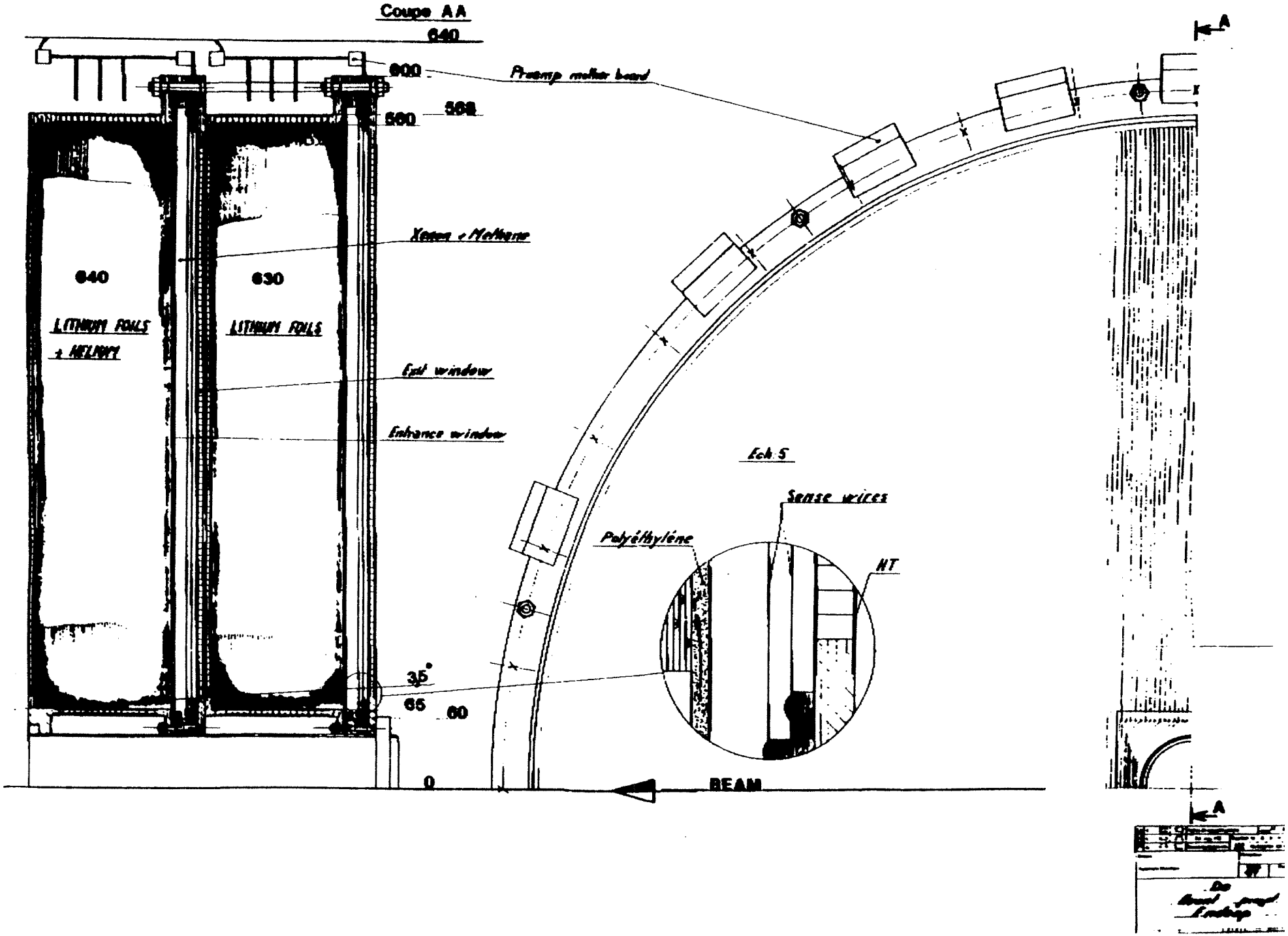
Coupe A A
640
900
500
508
Preamp motherboard
Xenon + Methane
640
630
LITHIUM FOILS
+ MELINVY
LITHIUM FOILS
Exit window
Entrance window
Ech 5
Sense wires
Polyéthylène
MT
35°
65
60
0
BEAM
A
A

Fig. 4.11

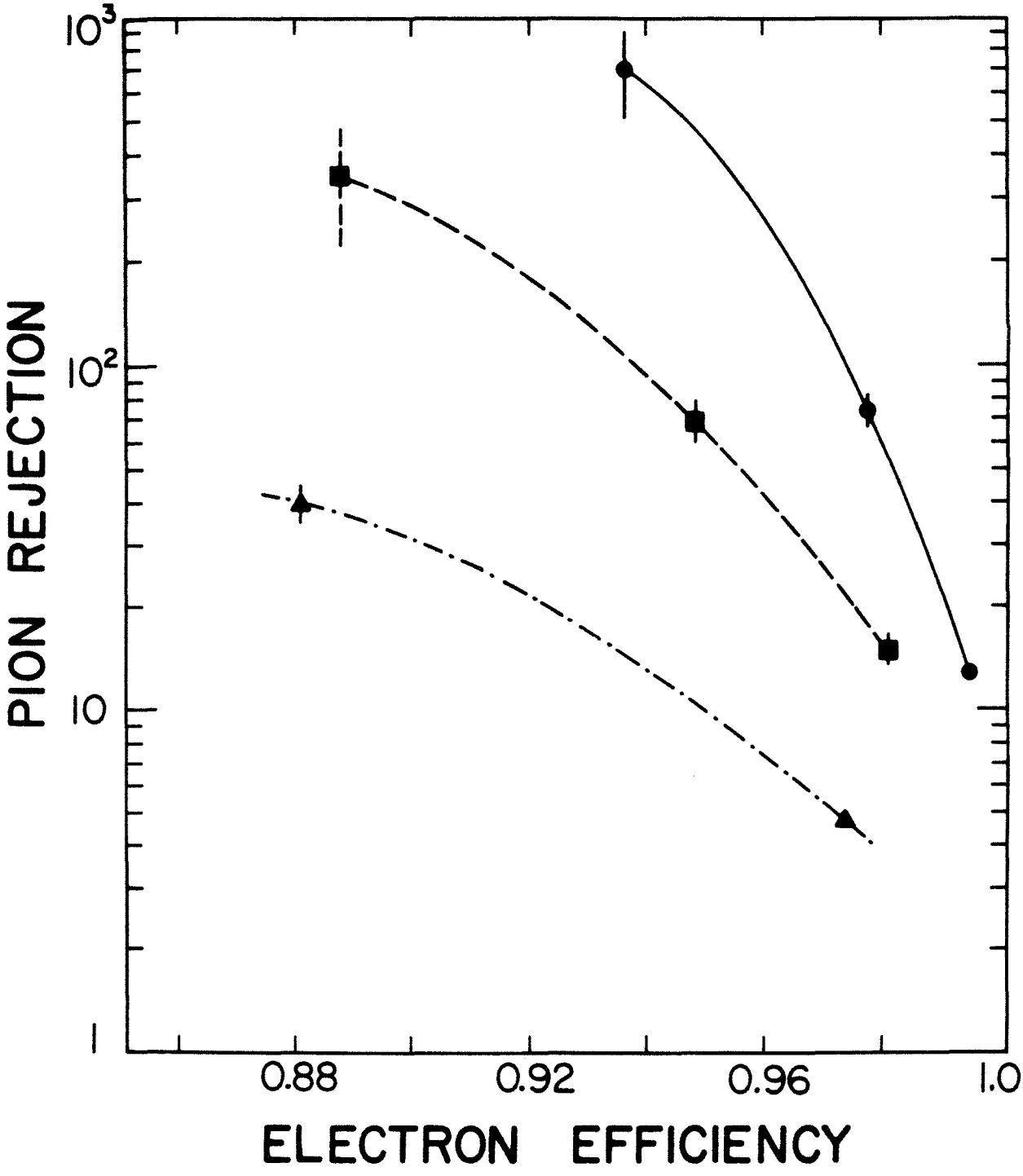
PION REJECTION
10^3
10^2
10
1
0.88
0.92
0.96
1.0
ELECTRON EFFICIENCY

Fig. 4.12

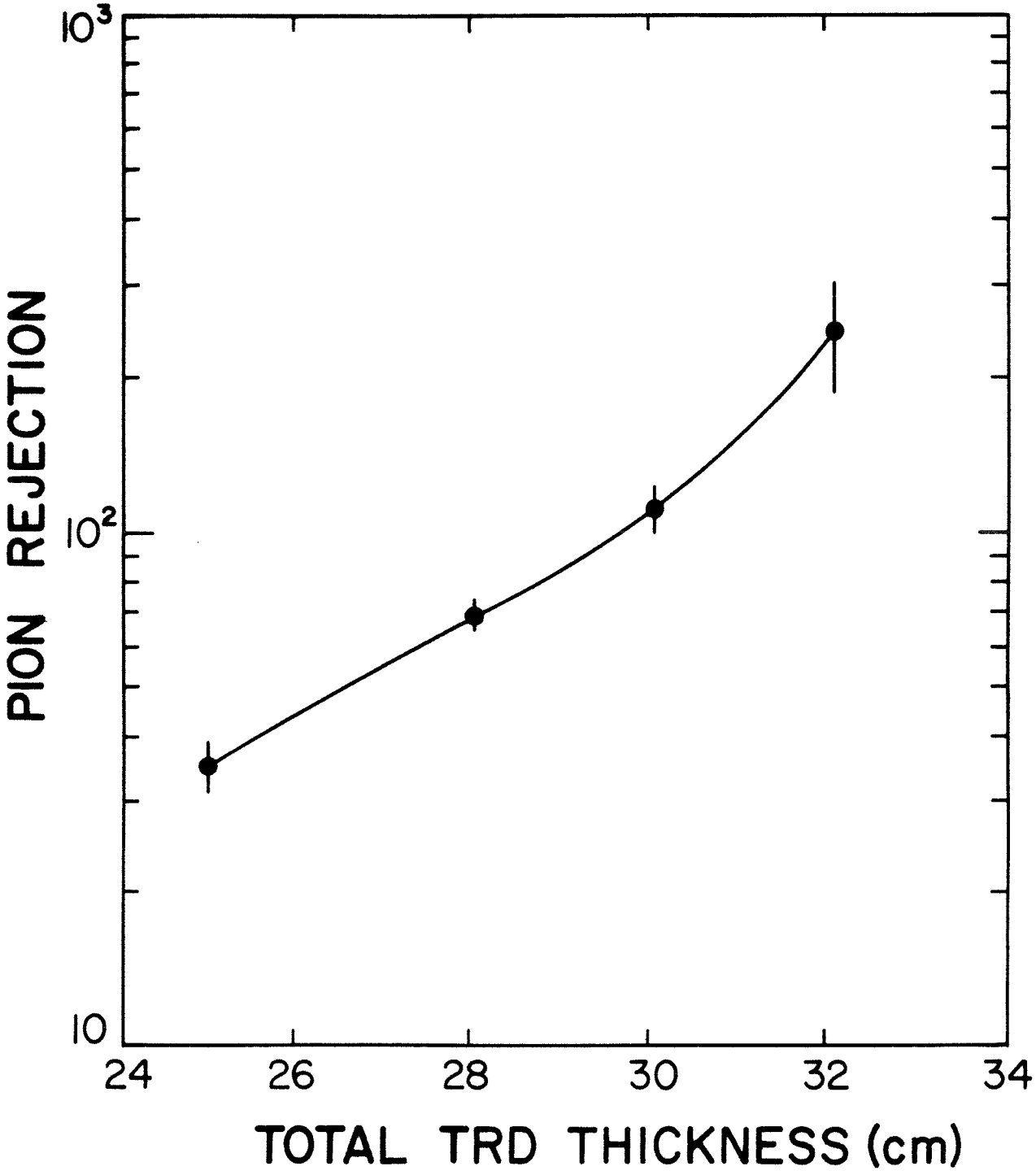
PION REJECTION
10^3
10^2
10
24
26
28
30
32
34
TOTAL TRD THICKNESS (cm)

Fig. 4.13

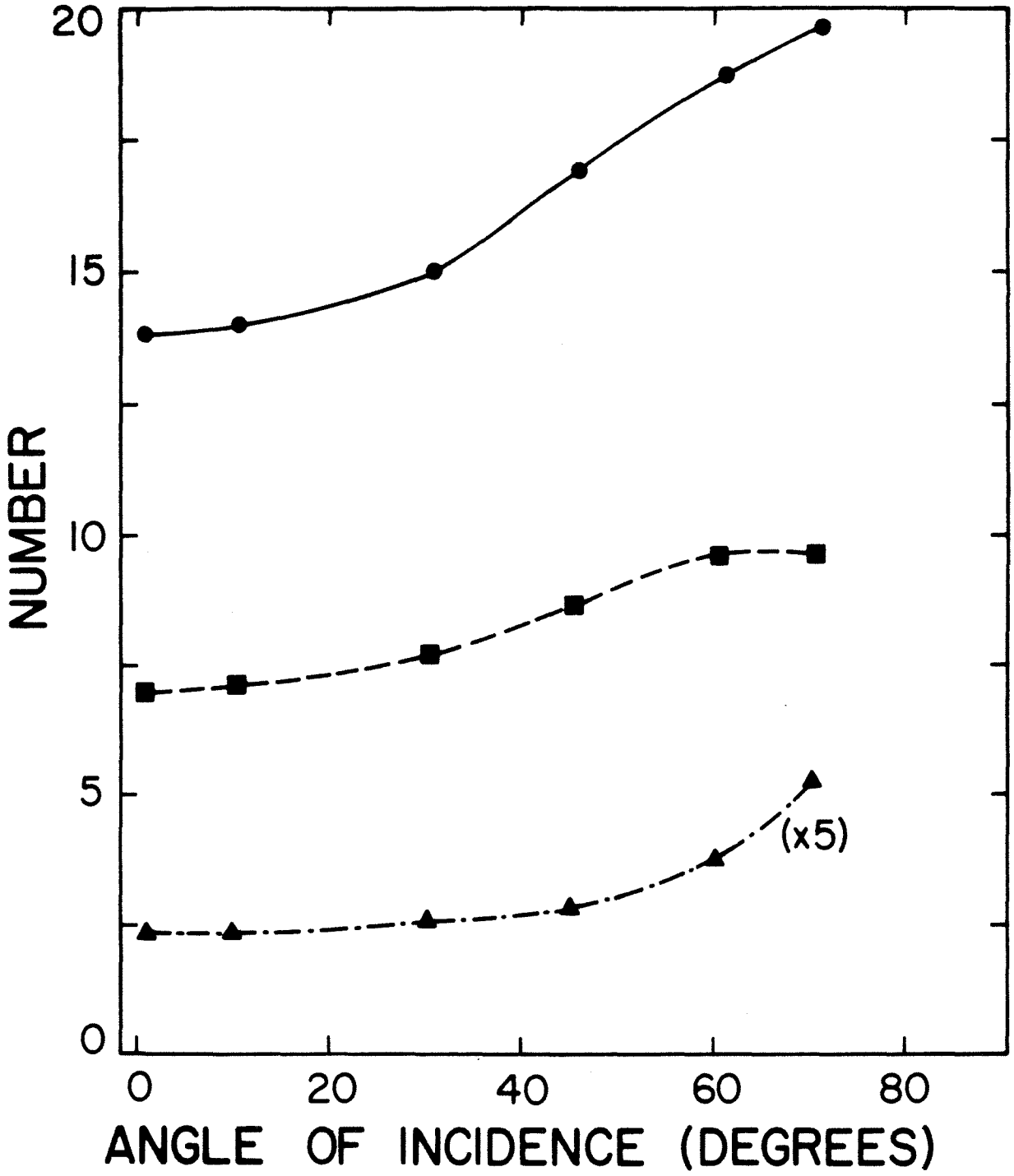

Fig. 4.14

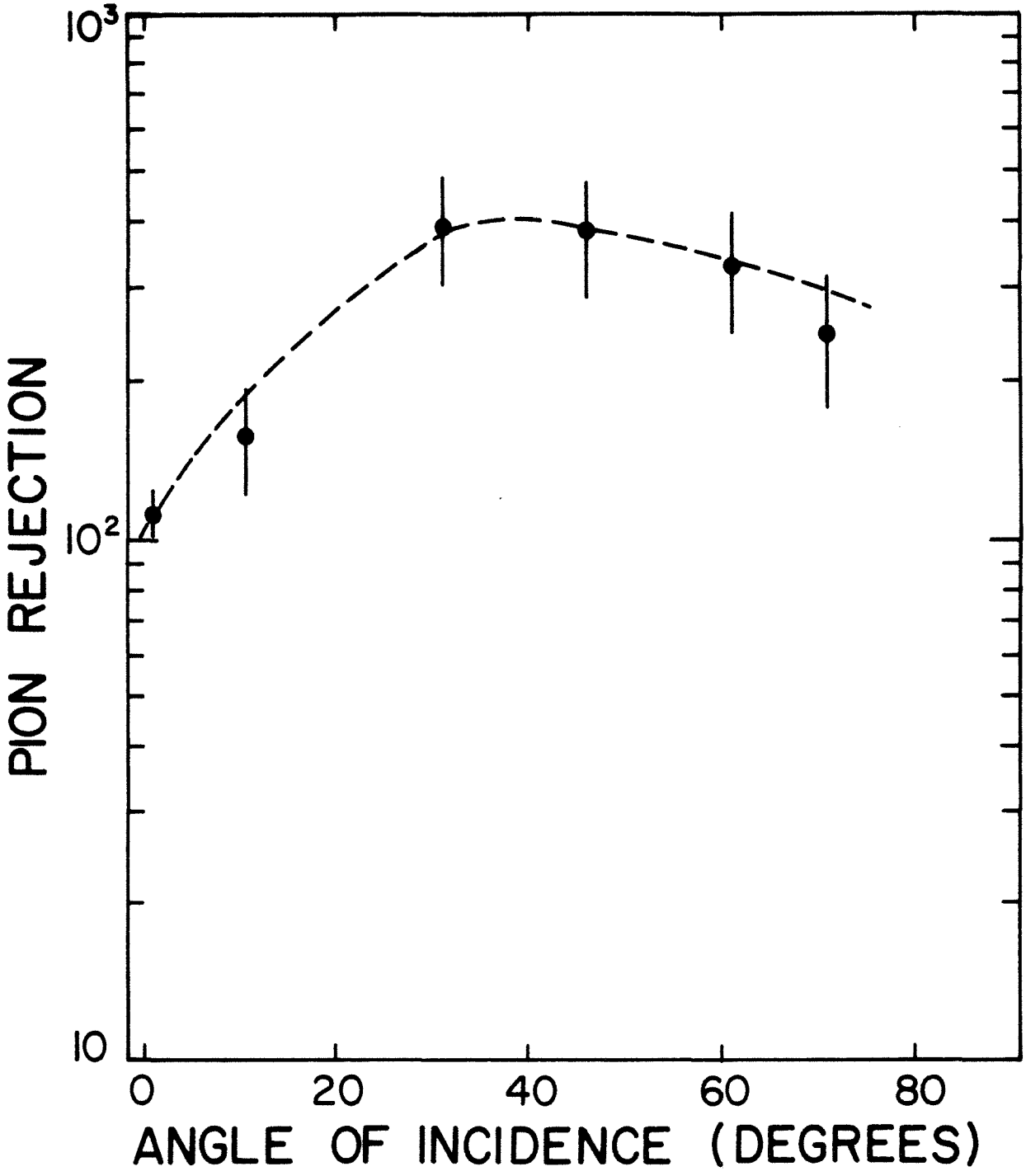
10^3
10^2
10
PION REJECTION
0
20
40
60
80
ANGLE OF INCIDENCE (DEGREES)

Fig. 4.15

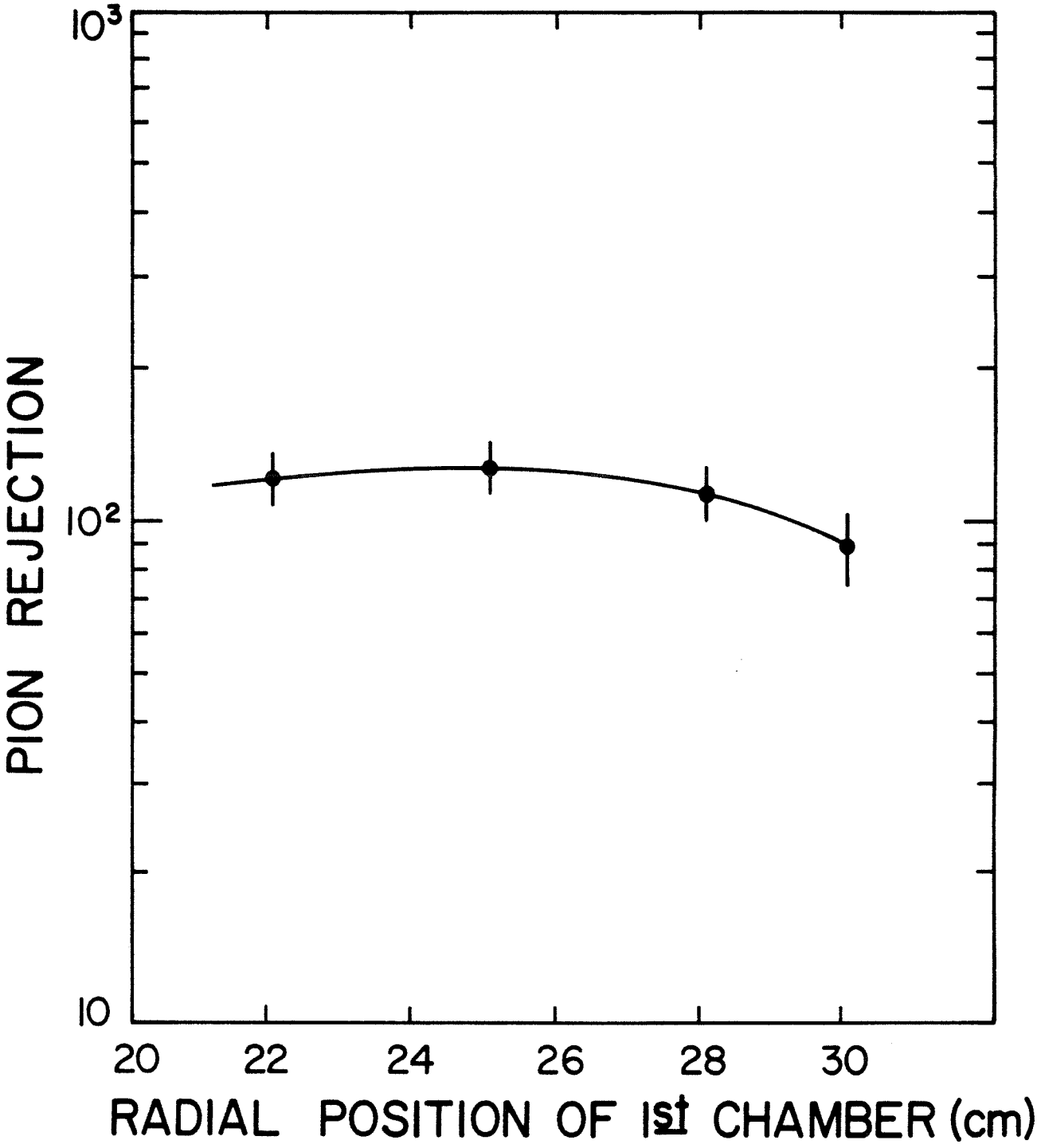
PION REJECTION
10³
10²
10
20
22
24
26
28
30
RADIAL POSITION OF 1st CHAMBER (cm)

Fig. 4.16

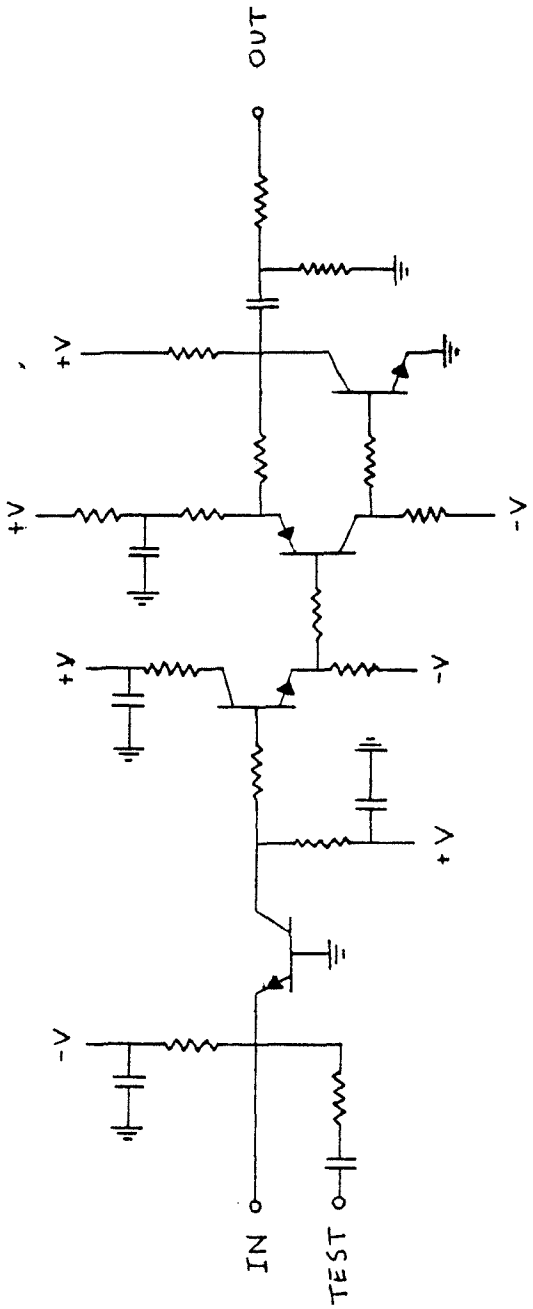

Fig. 4.17

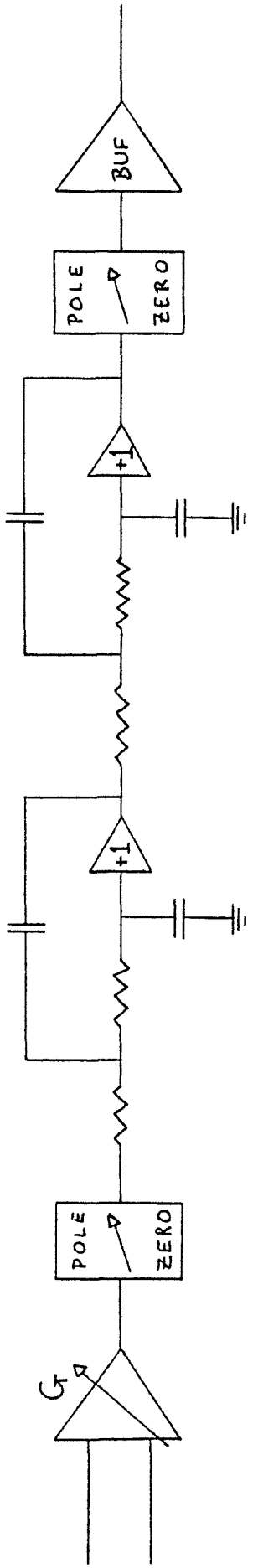

Fig. 4.18

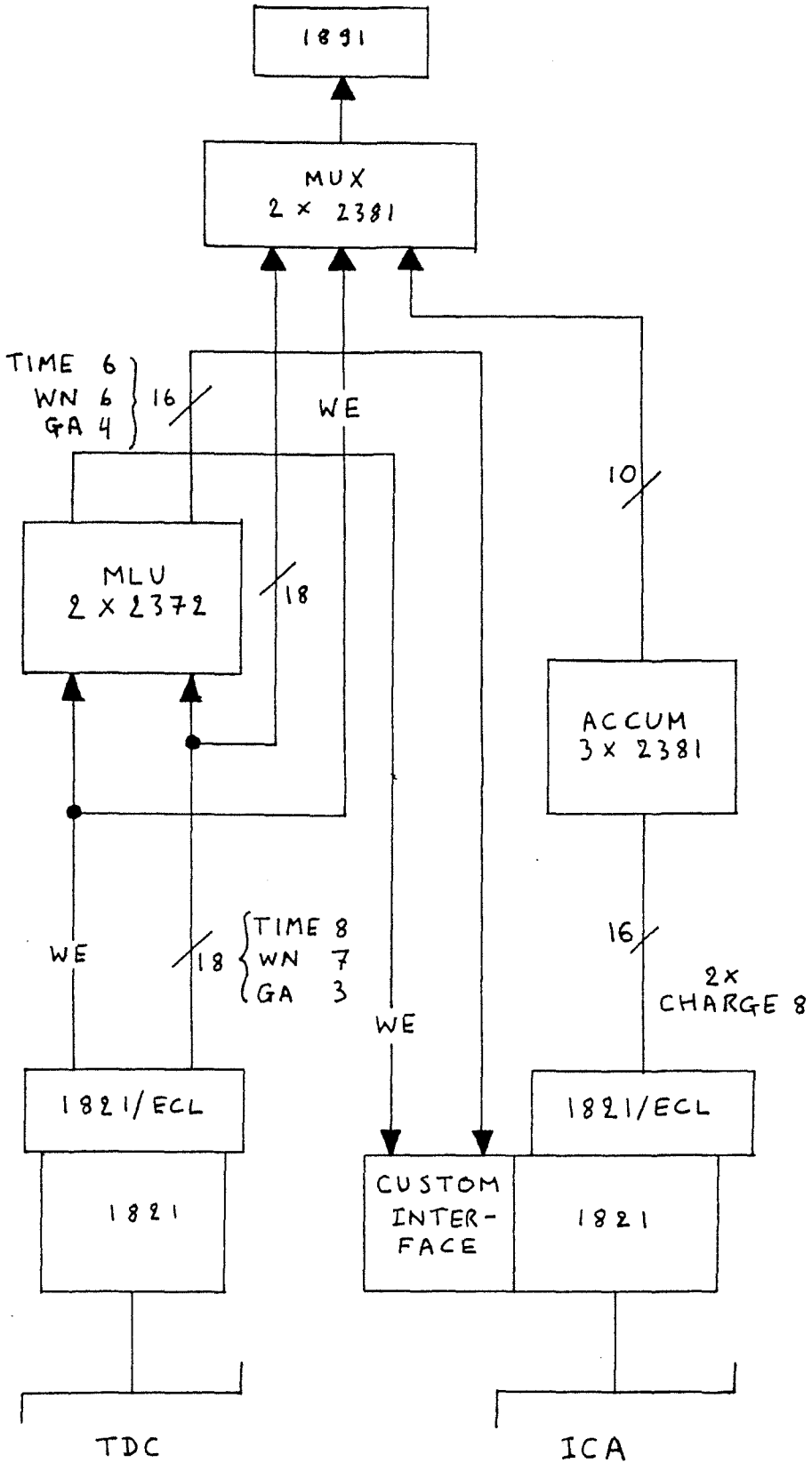
1891
MUX
2 x 2381
TIME 6
WN 6
GA 4
16
WE
10
MLU
2 X 2372
18
ACCUM
3 x 2381
WE
18
TIME 8
WN 7
GA 3
16
2x
CHARGE 8
WE
1821/ECL
1821/ECL
1821
CUSTOM
INTER-
FACE
1821
TDC
ICA

Fig. 4.19

5. CALORIMETRY

The calorimetry plays several crucial roles in the DØ detector, as discussed in section 3.1. These include good energy resolution, good segmentation to allow accurate jet determinations and aid electron identification, and hermetic coverage to enable the best possible missing p_T resolution. Liquid argon calorimetry with uranium (and copper) absorber has been chosen to give maximum density, ease of calibration, straight-forward projective tower segmentation, and excellent energy resolution. The equalization of electromagnetic and hadronic response is especially important in measuring high energy multiparticle jets. Figure 5.1 shows the comparison of a uranium calorimeter with the more conventional iron calorimeter in controlling missing p_T resolution. In the important region of missing p_T from 10 to 30 GeV/c, there is about a factor of ten potential gain in background suppression using uranium. The high density of uranium is also vital to the design in allowing the overall dimensions of the detector to be kept as small as possible.

The calorimeters described in this chapter have been designed to avoid projective internal cracks in the coverage. The questions of holes or thin spots in the coverage due to mechanical supports and the loss of coverage around the beam pipes has been given careful attention. These effects have been studied using detailed hadron and electromagnetic shower Monte Carlo calculations; the mechanical supports, cryostats and access corridors described reflect these calculations. Figure 5.2 shows a calculation of the effect of two such effects upon the rms witdth σ for the missing p_T distribution (relative to the width σ_0 with no holes). The detector modeled is indicated in Fig. 5.2; the dotted region represents the combined cryostat wall thicknesses of the central (CC) calorimeter and the endcap (EC) calorimeter.

Each quarter of this region was taken to be dead (uninstrumented) material in turn; the effect of each is indicated, at the appropriate rapidity, as a bar on the graph in Fig. 5.2. We see that the outer three quarters of cryostat wall have a small effect on missing p_T, whereas the inner quarter gives a severe deterioration. We have incorporated this into the design of EC and CC walls. The effect of the beam hole is also shown as the dotted line in Fig. 5.2, where the deterioration in missing p_T is seen to become severe for $\eta(\text{hole}) \lesssim 4.0$ ($\theta\text{min} = 2°$). We have accordingly given calorimeter coverage down to $\theta = 1°$ in order to reach full efficiency for detection at $\theta = 2°$.

In pursuing the design of the separate calorimeters, we have attempted to find common solutions to the problems of readout planes, feedthroughs, high voltage distribution, plate support, cryostat, and liquid delivery systems. The three types of calorimeters incorporated in our design do impose different constraints in space and in mechanical support arrangements. We have therefore made adjustments in each case to satisfy these constraints without sacrificing the general uniformity.

The electronics for the calorimetry discussed in this chapter is based upon our experience with a test uranium liquid argon calorimeter incorporating over 600 channels of signal readout. The detailed choices of sampling fraction, shaping times, cell capacitances, etc. have been guided by this experience and the optimization of signal to noise ratios calculated from considerations of electronic noise and uranium radioactivity induced background. We expect in all cases, individual channel signal-to-noise ratios exceeding 5:1 for single muon tracks.

The cryogenic systems described in this chapter are based upon careful examination of the requirements for stable operation, the constraints imposed by the need for access to the detector systems, and by the overall

requirements to build a system which will ensure the safety of operating personnel.

5.1 Central Calorimeter

The function of the central calorimeter (CC) is to provide full azimuth coverage for electromagnetic energy ($\geq$ 20 radiation lengths in the range $35° \leq \theta \leq 145°$) and hadronic energy ($>$ 7 absorption lengths in the range $60° \leq \theta \leq 120°$). The CC, shown in Fig. 5.3, is cylindrical in shape and is composed of 96 wedge-shaped modules, arranged in three layers so that no cracks extend through the entire array at any angle. Figure 5.4 shows the end view of a typical module and gives radial dimensions and thicknesses of the module elements. The modules are full-length so that there are also no cracks through the array at any longitudinal (z) position along the beam between the ±44-in. end points of the CC.

In sections 5.1.1 and 5.1.2 we present details of the cell structure and of the readout segmentation. In 5.1.3 we discuss the design of the individual modules and the construction techniques to be employed. Signal considerations are also discussed. In 5.1.4 the design of the CC cryostat is presented, together with a plan for assembly of the CC array in the cryostat. Cryogenic properties and operating conditions of the CC system are found in 5.1.5.

5.1.1 Cell Structure; Longitudinal Segmentation

The detail in Fig. 5.4 shows a typical sampling cell in the calorimeter. Dense absorber plates alternate with readout boards throughout the array; the material used for the absorber plates and the dimensions of the plates and boards depend on the radial depth in the array.

The CC is formed from three concentric cylindrical layers of 32 azimuthal wedge modules each. The innermost layer (EM) has the finest sampling; all absorber plates are depleted uranium (see the tables in Fig. 5.4 for more details). The second layer (Fine Hadronic) also has uranium absorber plates but coarser sampling. The outer layer (Coarse Hadronic, or Leakage) has the coarsest sampling and copper absorber. The three layers are discussed in more detail below.

i) EM layer. This layer contains approximately 21 radiation lengths (X_0) of material in 32 cells. The uranium plates are 0.079 in. thick; the argon gaps are 0.063 in. yielding a sampling fraction of 12.7%. The readout in this and in the other two layers is accomplished as follows. The readout boards each consist of a double-sided copper-clad G10 sheet etched or routed into an array of rectangular readout pads as shown in Fig. 5.5. Each side is covered with an insulating mylar film, and each film is in turn coated with a resistive layer[1] to which the high voltage is applied. The thickness of the readout boards is 1/16 in. The absorber plates and readout pads are at d.c. ground; thus the readout pads are capacitively coupled to the adjacent argon gaps, and the charge drifting in these gaps induces signals on the pads. This method of building capacitive coupling into the cell structure eliminates discrete blocking capacitors in the calorimeter.

The EM layer is read out in four separate sub-layers of 2.0, 2.0, 5.9, and 11.1 X_0. This fine longitudinal segmentation in the early part of the array contributes to the excellent π/e discrimation of the calorimeter.

Simulations of the cell structure detailed here lead to an expected electromagnetic energy resolution of

$$\sigma_{EM}/E \simeq 12\%/\sqrt{E}$$

with a small ($\lesssim$ 1%) additional systematic term.

ii) Fine Hadronic Layer. The EM layer contains 0.82 nuclear absorption lengths (λ_0). The Hadronic layer is comprised of 80 cells totaling 4.32 λ_0. The cells all contain 0.197-in. uranium plates and 0.063-in. argon gaps (5.9% sampling fraction). For readout it is subdivided in depth into three sub-layers of 0.81, 1.89, and 1.62 λ_0.

iii) Coarse Hadronic or Leakage Layer. This is actually a fourth hadronic sub-layer. It is in a physically separate module and has substantially coarser sampling. The absorber plates are copper (0.500 in.), as compensation is not expected to be important in the determination of the last few percent of shower energy. The argon gaps are 0.063 in., giving a 3.8% sampling fraction. The 20 cells correspond to 1.79 λ_0, giving a total CC depth of 6.93 λ_0.

Based on the experience of R807[2] and on tests[3] of uranium liquid argon calorimeters, we expect to be able to achieve

$$\sigma_{Had}/E \lesssim 40\%/\sqrt{E}.$$

The total radial thickness of the calorimeter active volume, including structural elements and signal cableways (see section 5.1.3) is 57 1/4 in.

5.1.2 Transverse Segmentation

The division of the CC into eight readout segments in the radial direction has already been mentioned above. All eight are also subdivided in ϕ and

z to give fully projective readout towers.

i) ϕ-segmentation. Each of the 32 modules in each layer is divided into two readout segments in ϕ. Thus, $\Delta\phi = 2\pi/64 \simeq 0.1$. The 32-fold modularity was chosen so that with $\Delta\phi \simeq 0.1$, all readout pads would touch an edge of a module to simplify the readout connections.

ii) z-segmentation. For reasons of economy, equal-z rather than equal-rapidity segmentation was chosen. This allows all readout pads at a given depth in the CC to be of equal size. Readout pads have increasing size in z, with increasing depth, thus giving projective geometry as seen from z = 0. This affords the further advantage that the capacitance (and hence electronic noise) is the same in all towers at a given depth. A size is chosen such that at the inside radius of the CC (which subtends a rapidity interval $\Delta\eta = 2.4$) the average rapidity interval covered by a pad is $\Delta\eta = 0.1$ (i.e., Δz = 88 in./24 = 3.67 in.). The variation in rapidity segmentation is then from $\Delta\eta \simeq 0.12$ at $\eta = 0$ to $\Delta\eta \simeq 0.07$ at $\eta = \pm 1.2$.

The exception to the transverse segmentation described above is in the third EM layer, where typical electromagnetic showers are at the peak of their longitudinal development. Throughout this layer the transverse segmentation is increased four-fold. Tests and simulations show[4] this improves the location of shower position and hence also the rejection of accidental γ/hadron overlaps mimicking the electron candidates. The total number of EM towers in the 32 EM modules is

$$N_{EM} = 32\left[24_z \times 2_\phi + 24_z \times 2_\phi + 46_z \times 4_\phi + 22_z \times 2_\phi\right] = 10368 \text{ channels.}$$

In the hadronic sections, fewer towers fit in ±44 inches due to the greater radius. A similar calculation yields 3,584 hadronic channels for a total CC channel count of 13,952.

5.1.3 Module Construction

As mentioned above, the CC consists of 96 separate modules, each of full length, arranged in three concentric layers with no through-going cracks. All 96 modules sit in a common liquid-argon cryostat.

A primary design goal was to minimize the dead space and dead mass in the calorimeter system. This required that the CC design have minimum support structures between modules. Figure 5.6 depicts the design chosen, in which each module is contained in a box structure whose sidewalls are thin perforated stainless steel sheets. The front wall and back wall are somewhat heavier gauge stainless and the endplates are again heavier. The table in Fig. 5.4 has the radial dimensions of the modules. The perforations allow free passage of argon vapor and liquid. Electrical connections are made at the plate and readout board edges. Notches in the plates and readout boards provide passages for the wires. At the radial termination of a tower the wires are attached to a PC board running the length of the module which brings the signals through the module endplates as sketched in Fig. 5.6. After installation of the modules into the cryostat, the exposed PC board ends carrying all the signals will be connected to ribbon cables[5] and brought to the top of the cryostat. (A similar system provides high voltage to the resistive surfaces of the readout boards.) Cryostat and installation details are discussed in later sections.

Construction of modules will proceed as follows: starting from the heavy back wall, plates, readout boards, and PC signal boards are laid up in a

stack, with argon gaps maintained by insulating spaces attached to the readout board. Wires are attached and high voltage tests are performed throughout the stacking procedure to avoid extensive restacking in case of shorts. The front and side walls, preassembled into a U-shaped trough, are now placed over the completed stack and pressed down on the stack to assure uniform gaps. After final electrical tests the module walls are welded together, forming the box described earlier. Calculations show that such a structure can be entirely supported from its end plates. For example, EM modules (which weigh ~3/4 ton) can be end-supported with ≤0.050-in. deflection at the center with sidewalls of only 0.030 in. Allowing for such side walls, reasonable intermodule gaps, and fabrication/assembly tolerances, a dead region between active areas in adjacent EM modules of ≤0.25 in. can be maintained. Thirty-two such gaps comprise 4% of the entrance face of the calorimeter. The identification and measurement of electrons will be degraded in these gaps, but the energy will be measured since all gaps are centered on the active areas of the hadronic modules behind. Hermetic coverage will therefore <u>not</u> be comprised by the intermodular gaps.

In the hadronic and leakage modules (3-5 tons in weight) somewhat heavier module walls are required; larger gaps between the modules here are insignificant, due to the size of hadronic showers, and the fact that the gaps are behind the active area of the EM modules, which are about one absorption length thick.

<u>Signal Considerations</u>. The capacitance of the CC readout towers is given in Table 5.1. The electronic noise is proportional to this capacitance;[6] expressed in terms of equivalent electron charge,

$$N_e = 4.1 \times 10^3 / nf$$

for a single-FET preamp input stage. The signal for a minimum ionizing particle, for example, depends on the total energy deposit in the tower, the liquid argon sampling fraction, and the energy deposit per observed electron charge in liquid argon which is 52.8 eV.[7] Table 5.1 also shows the energy deposit of a single minimum ionizing particle in each CC tower. Signal-to-noise ratios ranging from > 4:1 to >20:1 can be inferred.[8] The leakage section towers have the lowest ratio, but minimum ionizing particles should still be observable. In the EM and hadronic compartments there is also a noise contribution from uranium radioactivity.[9] This is also listed in Table 5.1 and is seen to be the dominant noise component[10] in the EM layers and comparable to electronic noise elsewhere.

Signal processing is discussed in more detail in section 5.5 below.

5.1.4 Cryostat Construction

The CC array is housed in a single vacuum insulated cryostat, consisting of a double-walled, cylindrical stainless steel vessel. The main design goals and constraints were:

i) 40 psia maximum internal pressure, i.e. 25 psi maximum pressure difference.

ii) relatively thin inner cylindrical walls and end walls to preserve the advantages afforded by hermetic uranium-liquid argon calorimetry.

iii) Construction technique compatible with the array installation method chosen (and discussed below).

Figures 5.3 and 5.7 show overall layouts of the vessel and give some overall dimensions. We discuss some of the salient features below.

i) Forces due to the weight of the array and liquid argon are transfer-

red directly down through the cryostat walls to the base which is rigidly fastened to the central iron "keel" of the toroidal magnet. The forces are taken through the insulating vacuum on low thermal conductivity feet designed to accommodate the thermal contraction of the inner vessel.

ii) The inner vessel is cylindrical but eccentric relative to the beam line to provide space at the top for ullage, for cooling coils, and for routing signal cables from the array ends to the signal feed throughs near the top of the vessel (see Fig. 5.7). The total vessel volume is 10,200 gallons; the volume of liquid argon contained during operation is 4300 gallons.

iii) The vent line (4-in. diameter) comes through the vessel at the top-center and projects vertically up through a small notch in the magnet halves where they meet at the centerline. Other cryogenic services (small-diameter insulated lines, sensor readout cables, etc.) come out of the CC space between the end and central parts of the magnet iron.

iv) The end wall forces would result in unacceptably thick walls if the full span were covered with self-supporting plate. Several features of the present design have been selected to minimize the endwall thickness.

   a) An inherent feature of the CC geometry is the inner cylinder, which provides significant support for the end walls.

   b) A second cylindrical tube, between the EM and hadronic sections (seen in Fig. 5.3) further reduces the wall thickness, especially that part near the ends of the EM section. Monte Carlo studies (see Fig. 5.2) show that for energy deposited partly in

CC and partly in EC, it is dead mass (such as walls) adjacent to the CC electromagnetic section which is most damaging to the energy resolution.

c) The end walls of the inner and outer vessels are further minimized by allowing them to be in mechanical contact through low heat loss supports. In order to have this mutual support maintained after thermal contraction of the inner vessel (~1/8 in. at each end), the cryostat assembly will be done so that at room temperature the inner and outer walls preload each other through the supports.

Assembly of the CC module array is done from the cryostat ends which are both open at this stage of installation. The modules are inserted with a counter-balanced sliding-beam hoist attached to the building crane. The idea is shown schematically in Fig. 5.8. Modules are installed in the manner of building a circular arch, with the three layers built from the outside to the inside up to the midplane. At this point a temporary mandrel is inserted to support the top half until the arch is completed, at which point it is self-supporting. As the modules are installed they are fastened to one another with small brackets attached to the end plates for longitudinal stability.

After the array is complete and the signal, high voltage, and control sensor cabling installed, the inner cylindrical walls are inserted and the ends are welded on. The vessel walls are designed to accommodate several unweld/reweld procedures in case repairs or reconfigurations of the array are required in the future.

5.1.5 CC Cryogenics

The overall cryogenic system is discussed below in section 5.4. Here we present the design for the internal cryogenic circuits in the CC. Two aspects of operation, cooldown and maintenance, need to be considered separately.

Cooldown. We have designed for a 100-hour cooldown proceedure. Removing the heat contained in the room-temperature array is the determining factor. Because the CC is effectively a densely packed nest of horizontal cylinders, natural convection is poor. Heat conduction along the uranium plates plus radiation from the outer layer are not sufficient to achieve a 100-hour cooldown (the average heat transfer is equivalent to about 40 kW). Therefore a blower and closed loop circulation system will be used in conjunction with some baffles around the array to force argon gas to flow between the absorber plates during cooldown. Calculations show that a small amount of gas, blown in at relatively high velocity through small orifices can stimulate sufficient flow within the cryostat to achieve the necessary heat transfer.[11]

The cooling is effected by means of LN_2 coils in the top of the cryostat, as seen in Fig. 5.3. These coils are fed by two separate LN_2 circuits, one servicing the main set of coils in the center, the other servicing the two auxiliary coils to the sides. Both circuits are in operation during the cooldown.

Maintenance. After cooldown the cryostat is filled with liquid argon to the level indicated in Fig. 5.3. The auxiliary coils are at this point immersed in liquid and shut off. Maintainence of the full vessel (~1.5kW heat load) can be handled by the main coils alone. In fact, for ease of control, it may be advisable to subdivide the main coil into two or more separate circuits and run only one of these during normal operation with a full vessel.

Other small coils are to be used to intercept directly the known heat leaks. Examples are inner vessel supports at the bottom and the spacers between inner and outer end walls. Presently, it appears that only the bottom supports could be sources of bubbles that could enter the array itself. Calculations show that these will constitute a $\lesssim$ 0.5 kW leak. The approximately 14,000 signal wires also constitute a heat leak of $\simeq$ 0.5 kW. It is expected that as a result a stable gas volume will develop in each of the four signal feedthrough ports seen at the top of the vessel in Fig. 5.7, providing a warm feedthrough for all the signals and other cables. The remaining 0.5 kW is divided between endwall spacers, pipes, and radiation. The cryogenic operation of all the calorimeters is discussed further in section 5.4.

5.2 THE END CAP CALORIMETERS

Calorimetric coverage of the angular region between 5° and 50° in both the forward and backward direction is provided by two mirror image 250 ton end cap calorimeters (EC). These devices are liquid argon calorimeters with a plate structure consisting of a mixture of copper and uranium plates. The angular region between 32° and 50° as shown in Fig. 5.10 is shadowed by the CC. The region between 5° and 32° has an unobstructed view of the interaction products. The electromagnetic section of the calorimeter is 20 radiation lengths (X_0) in depth and is expected to yield a $12\%/\sqrt{E}$ resolution for photons and electrons. The hadronic section of the calorimeter (plus the electromagnetic section) is 8.9 absorption lengths (λ_0) thick at 5° and should allow a hadronic resolution of $40\%/\sqrt{E}$. A central hole in the plate structure is tapered from front to back to match the 5° cone necessary to allow particles to reach the end plug calorimeter (PC). The outer dimension of the plate structure is also tapered from front to back to minimize material. The cross section and side view of this plate structure and cryostat are shown in Figs. 5.9 and 5.10 along with the surrounding muon iron and proportional drift tubes planes.

5.2.1 Transverse and Longitudinal Mechanical Modularity and Support Structure

There are three functionally distict longitudinal sections in the EC. There is an electromagnetic section with 0.079-in. thick uranium and copper plates, a fine hadronic section with 0.197-in. thick uranium and copper plates, and a coarse hadronic section with 0.787-in. thick copper plates. In order to keep the weight of each longitudinal section of the plate structure below the 50-ton experimental area crane capacity the fine hadronic

section is split into two modules. The parameters of each module are given in Table 5.2.

The sizes of uranium plates that can be produced by available rolling mills dictate that each uranium disc layer be assembled from 16 individual plates each subtending 22.5° of azimuthal angle ϕ (see Fig. 5.11). The size and number of the uranium plates needed for the end caps are given in Table 5.3. The copper disc layers will be assembled from eight plates each covering 45° in ϕ. In order to minimize cracks the calorimeter will be constructed in 45° ϕ segments each of which is six cells thick (See Fig. 5.14 and section 5.2.2). The electromagnetic and hadronic modules will be assembled from 45° ϕ segments with each successive six-cell thick ϕ segment rotated with respect to the preceeding modules. This arrangement is shown in Fig. 5.13. Each of the modules is therefore four ϕ segments thick. The weights of the modules are given in Table 5.2.

Each ϕ segment is pinned together by two sets of four 3/4-in. diameter hollow stainless steel tubes positioned at two different radii from the beam. These tubes line up with tubes in the other ϕ segments at different depths in a given module so that bolts can be inserted through four 45° ϕ segments in the assembly of the electromagnetic and hadronic modules. The rotations of the ϕ segments shown in Fig. 5.13 is chosen to insure that no cracks between ϕ segments line up for the full depth of a module. Thirty-two ϕ segments are used in each of the four modules (electromagnetic, fine hadronic I and II, and coarse hadronic modules) in this essentially crack-free design.

Each of the modules assembled from these ϕ segments is an independent structure that can be handled by the crane in the experimental area. Each of these large donut-shaped structures is seated in a cradle mounted on a cart which rolls on removable rollers into the cylindrical cryostat discussed in

section 5.2.6. The modules are shown mounted on this cart in Figs. 5.10 and 5.11. They are individually dropped into place on the cart with the copper plates at the bottom of the donut-shaped module resting on the stainless cradle. The modules are stabilized against forward and backward tipping by attaching them to the cradle.

5.2.2 Longitudinal Cell Segmentation and Readout Structure

The basic cell structure for both the electromagnetic and hadronic parts of the EC is shown in Fig. 5.14. Each cell in the electromagnetic and fine hadronic sections consists of a uranium plate, argon gap, a copper clad G10 readout board with a pad structure etched or routed on each side, argon gap, copper plate, argon gap, second G10 readout board, and a final argon gap. This cell structure is then repeated to achieve the desired thickness. The hadronic leakage section has the same cell structure except that all plates are copper. The thickness of gaps and the thickness of plates appropriate to each longitudinal section of the calorimeter are given in Table 5.4. In a given longitudinal section of the calorimeter the copper plates are the same thickness as the uranium plates in order to optimize density, cost, and compensation (equality of electron and hadron pulse heights).

The readout used in the EC is provided by copper-clad double-sided G10 board positioned between each copper and uranium plate as shown in Fig. 5.14. These G10 readout boards have identical structure on both sides (see section 5.2.4). The pad structure is covered with a thin mylar sheet coated with a resistive layer (resistance of the layer $\sim 10^6 \Omega$/square) which is held at high voltage with respect to the grounded metallic plates. The mylar sheet isolates the amplifiers from the high voltages and eliminates the need for blocking capacitors.

The charge drifting in the argon gaps on both sides of a given board induces signals on the pads. These signals are transported to the periphery of the detector by leads on the same side of the board. Table 5.5 gives the details of the longitudinal ganging that is planned for the EC. This ganging in depth gives longitudinal readout segments of 2.5, 2.5, 5.0, 10.0 X_0 in the electromagnetic modules, 7.9 X_0 and 1.9 λ_0 in the first fine hadronic module 2.3 and 3.3 λ_0 in the second fine hadronic and the coarse hadronics modules respectively. This longitudinal ganging is schematically shown in Fig. 5.15.

5.2.3 Transverse Segmentation and Readout Structure

Pad structures which are routed or etched into the 1/16 in. copper clad G10 readout boards mentioned in the previous section provide the desired transverse readout segmentation in each longitudinal segment of the calorimeter. The transverse segmentation is $\Delta\eta = \Delta\phi = 0.1$ in all longitudinal segments except the third electromagnetic one (see Fig. 5.15 and 5.16a) This granularity is also maintained in the fine hadronic module II and the coarse hadronic module.

The third depth segment (Fig. 5.16b) in the electromagnetic module which extends from 5 to 10 X_0 is more finely subdivided than any other section since it is used to determine the positions of photons and electrons. The segmentation is chosen in this section such that no pad in the area unshadowed by the central calorimeter has a size greater than 1.57 in.×1.57 in. This is achieved by maintaining a $\Delta\eta = \Delta\phi = 0.1$ segmentation out to a polar angle of 10° (radius of 12 in. from the beam). Between 10° and 25° a transverse segmentation of $\Delta\eta = \Delta\phi = 0.05$ is maintained. Beyond 25° the $\Delta\eta = \Delta\phi = 0.1$ segmentation is resumed. With this finely segmented layer positioned at shower maximum we expect to determine positions of electromagnetic particles

to an accuracy of 0.6 in./$\sqrt{E(GeV)}$ plus a constant term that should be of order of 0.1 in.

In all the various longitudinal readout segments the 0.015-in. wide signal leads are brought out on the same side of the boards as the pads and run radially to edge connectors at the periphery of the modules. Longitudinal ganging then takes place at that point with mass termination cables that transport the approximately 12,000 signals of each endcap to the preamplifier electronics mounted on the cryostat. The liquid argon is excluded from the vicinity of the lead package by appropriate spacers and the lead package positions are varied from board to board to prevent any spacers from lining up through the full depth of a module. The readout pad configuration for each successive cell in depth in the calorimeter is different because of the projective geometry employed in the segmentation. The readout plane in a given gap is constructed from 16 identical G10 boards each subtending 22.5° of azimuth. There will be 96 different types of boards needed in the construction of an endcap in order to produce the proposed tower structure shown in Figs. 5.15 and 5.16. These board types will be produced by computer controlled router techniques or by standard photography and etching techniques. In all, 3072 boards will be needed for the end caps.

5.2.4 Cryostat and the Cryogenic System

A cylindrical dewar (see Figs. 5.10 and 5.11) with an outer vessel 205 in. in diameter and 96 in. in length and an inner vessel of 196 in. in diameter and 83 in. long contains the entire EC and provides vacuum thermal insulation for the liquid argon inventory. The dewar is designed and will be built to ASME Code for 25 psig with an external vacuum, in the insulation region including the 10 psig hydrostatic head of the liquid argon.

Access to the dewar's volume for insertion of the detector is from the rear. When access is required, four small welds on the conical pipe need to be ground off and three flanges on the cryostat vessel must be disconnected. The inner cold vessel flange has a welded seal that must to be ground off. The other two flanges are conventional O-ring seals.

While the rear walls of the dewar are 3.5 in. thick, care was taken to insure that the upstream end of the dewar be thin to maintain good energy resolution of the electromagnetic section. A set of thin windows 100 in. in diameter has been incorporated into the front walls of the dewar to accomplish this objective as well as to prevent degradation of the missing p_T measurement by loss of shower energy in thick walls. The cold vessel window is trumpet shaped, constructed from 1/2-in. thick Inconel 718. There will be a tensioning bellows in both the conical warm and cold cones (see Fig. 5.10) to keep the window always in tension. The outer warm vessel window is torispherical, constructed from 1/4 in. thick S.S. 304. The flat front inner end wall which supports the thin window is 3-in. thick S.S. 304. The inner and outer cylindrical shells are 5/8 in. thick while the outer flat walls are 1/2 in. thick, all S.S. 304. However, these relatively thick structures are hidden behind the central calorimeter; Monte Carlo calculations suggest that they have no serious impact on the missing p_T measurements, see Fig. 5.2. The inner shell has five 3-in. I-beams to carry the load of the liquid argon. Eight cylindrical 6 in. ports are placed on top of the dewar for cables. One eight inch port is provided for cryogenic relief.

The detector will roll on rails mounted in the inner cold vessel. These rails and the inner vessel are supported by G10 spacers to the outer vessel. The heat loss through these spacers will be approximately 50 W. The heat loss of the entire dewar is approximately 1 kW. The major contributors (80%) to

the heat loss are the cables coming out of the dewar. Fifty kilowatts of refrigeration will be needed to cool the vessel and its contents (200 tons of detector) in 100 hours. This refrigeration is supplied by liquid N_2 flowing through a heat exchanger (1-in. diameter tube 260 ft long) mounted at the top of the cryostat as shown in Figs. 5.10 and 5.11. The cryogenic system is discussed in section 5.4. The flow rate of the LN_2 will be regulated by the pressure of the argon gas in the dewar. This pressure will be maintained at 5 ±0.5 psig. The liquid argon flow will be controlled by a level indicator and temperature indicator. The liquid level will be controlled to ±1/8 in. With these controls the liquid argon density will be uniform to 1% over the detector volume. The density profile will be maintained constant, to 0.2% during operation.

In the cryostat there are volumes from which the liquid argon will be excluded to limit the argon inventory and to minimize radiation lengths before the EM sections. At the present time we anticipate as an exclusion technique for the latter use of thin perforated S.S. 304 containers filled with 10 mm Macrospheres glass balls. According to our information Macrospheres are non permeable and will not contaminate the argon. The effective density of these devices will be 0.58 g/cm^3. In filler volumes, aluminum or G10 can be used for example around the plate structure. The volume of liquid argon inventory is about 5000 gal per EC.

5.2.5 Assembly Procedure

After the cart with a full module load is inserted into the cryostat the cryostat will be sealed in the following sequence. The rear cold wall is bolted to the cryostat and a seal weld is done around the periphery. The conical pipe is inserted into the cryostat and welded at the front and back to

the cold vessel. The warm end walls are bolted on and the warm conical pipe is inserted and sealed at the back and welded at the front. During the insertion of the loaded cart into the cryostat the cable bundles which are already attached to the feedthrough plates (which seal the cable ports) are grappled from the outside of the cryostat and fitted into place in the cable port. After the cryostat is sealed it is rolled from the assembly point in the assembly hall onto the 5-ft wide "keel" which forms part of the lower segment of the rectangular central iron toroid.

5.2.6 Detector Capacitance and Signal/Noise

The detector's segmentation and ganging described in the preceding sections give rise to different signal-to-noise ratios for different sections of the endcaps As a measure of the signal we take the charge produced by a minimum ionizing particle in a given readout segment of the detector. Since dE/dx for a minimum ionizing particle in liquid argon at the boiling point (1 atmosphere) is 2.114 MeV/cm and an electron-ion pair is produced per 52.8 eV of energy deposit, we expect approximately 4×10^4 electrons/cm of minimum ionizing track in liquid argon.

The amplifier design that has been chosen for the DO calorimeter (see section 5.5) has an incoherent noise of approximately 4100 electrons per nf of detector capacitance. In the approximation that this noise is linear with capacitance, worst case signal-to-noise ratios can be calculated for the various sections. The capacitance of a given pad with its attendant lead varies from pad to pad in a given readout section, but in general, the worst case is found to be the large pads at the outside perameter of the modules. The capacitances, however, are relatively constant over a board since the larger pads at the outer perimeter have the shortest leads while the smallest pads near

the beam hole at the center of the module have the longest leads. For those small pads the leads dominate the capacitance. Table 5.6 tabulates the worst case capacitances and the expected signal-to-noise ratios for each longitudinal readout segment. Uranium noise, discussed in section 5.1, is also tabulated.

5.3 PLUG CALORIMETER

The small angle region, with angles below 5°, is an important one for two reasons.

1. Calculations show that missing-p_T studies will have a large background from particles lost down the beam hole unless measurements with good resolution are made down to about 1° (see Fig. 3.1).
2. A large part of rapidity phase space is represented by angles below 5°--about one third of the total useful rapidity range lies in this interval.

Point 2 has several consequences. Two of the most important are the following:

a) Many events will have significant or dominant energy contributions from the outgoing particles in this angular range.

b) The typical event will have on the average 10 to 15 particles between 1° and 5° of each beam (and about 10 more particles within 1° of each beam). The p_T vectors of these particles must be measured with sufficient accuracy to avoid having these particles contribute a large uncertainly to the missing p_T in an event.

5.3.1 Longitudinal Cell Structure

In order to obtain optimum energy resolution for hadrons, we use a cell structure with the same thicknesses for all cells from front to back of the plug calorimeter (PC). We also wish to make the average density as large as possible, to obtain minimum transverse shower size (since we are already driven by practical considerations to use tower sizes larger than dictated by shower size). High average density is also esirable in order to make the

structure as compact as possible longitudinally, since the total longitudinal space available for the entire detector is limited.

To make the density as high as possible, all metal plates are of uranium, and we have chosen a design which reduces the thickness of readout boards and of liquid argon to the minimum values which will still give satisfactory signal-to-noise ratio. Finally, the individual uranium plate thickness is chosen to be as large as possible consistent with preservation of compensation (rough equality of hadron/electron pulse height); we estimate that 0.236 in. uranium thickness will be satisfactory.[13]

The cell structure we have chosen is shown in Fig. 5.18. It uses 0.236 in. uranium, 0.079 in. of G10 in two layers, with the leads brought out between the layers, and 0.98 in. of LAr. The cell thickness is 0.413 in. and corresponds to approximately 2.0 X_0 and 0.064 λ_0. We use 142 cells, for a total thickness of nine λ_0.

Figure 5.17 shows the arrangement for readout from individual tower pads. A G10 board with etched pads and with leads on the back reads the signal from a 0.098-in. LAr gap. The lead goes to one edge of the board, as in the EC. There the pads from several successive cells are ganged in depth; for each tower there are six depth groups, with one readout circuit for each such group. For the 352 towers indicated on Fig. 5.18 there are thus 2112 readout channels.

It is relatively easy to obtain a good signal-to-noise ratio for the PC towers, since particle energies of interest at these angles are relatively high and since pad area and pad capacitance are relatively small. For towers of 25 cm^2, a typical four-tower section of EM calorimetry in the PC will have a total amplifier plus uranium noise of about 40 MeV, and a forty-tower array

of hadron calorimetry would have a total amplifier plus uranium noise equivalent of about 600 MeV. For a particle at a typical PC angle of 60 mrad, p_T values of interest start at perhaps 6 to 10 GeV/c, corresponding to laboratory energies of about 100 GeV. For electrons of that energy the energy resolution will be of order 2 GeV; and for a hadron jet of 100 GeV it will be of order 4 GeV. We thus see that for the cell structure shown in Fig. 5.19, amplifier noise will not be a substantial contributor to energy resolution.

We are thus able to use the compact high-density design, giving showers of minimum possible transverse size and giving an endplug of minimum possible overall length.

It can also be noted that the estimated signal-to-noise ratio for minimum ionizing particles traversing a single readout unit is about 4:1 in the worst case, and more typically 6:1 for thicker units. Thus it will be quite feasible to see muons or other minimum ionizing particles, for calibration and monitoring purposes.

In addition to the 352 towers indicated in Fig. 5.19 and Table 5.7 one LAr layer of more finely segmented pads will be intalled at 6 X_0, just after the third cell and before the fourth uranium plate. In this layer each normal pad in rings 2 through 10 (see Table 5.7) will be subdivided in four, in order to localize EM showers more sharply, and to assist in identification of isolated electrons. This layer would not be needed for good energy resolution. The 1408 readouts from this layer will increase the total number of channels per PC to 3520. They will not initially be instrumented electronically pending examination of the electron identification possibilities below 5°.

5.3.2 Transverse Segmentation

For this small angle region, transverse segmentation and tower size are constrained by two opposing factors.

i) One wants small $\Delta\eta$ (pseudo-rapidity) intervals, so that the p_T uncertainty for a particle due to angular resolution will not greatly exceed the p_T uncertainty due to energy resolution. This implies $\Delta\eta \leq 0.05$.

At small angles, the radial size of a tower, Δr, measured perpendicularly from the beam line, is related to $\Delta\eta$ by $\Delta\eta = \Delta r/r$. For the plug calorimeter, located at $z \approx 190$ in., the $\Delta\eta \leq 0.05$ condition gives $\Delta r \leq 0.17$ to 0.87 in. (for $\theta = 1°$ to $5°$).

ii) Towers of the size indicated above would be much smaller than shower sizes for hadrons with energies of interest for the endplug. These energies will range up to hundreds of GeV over the entire angular region up to 5°; near 5° we are also interested in energies down to a few tens of GeV. For hadron showers with energies 50 GeV or more, shower sizes in a compact uranium/liquid argon array will be of order several cm diameter for 2/3 to 3/4 containment.[14] Thus, for efficient and economical segmenting, with good matching to shower size, one would like $\Delta r = 1$ to 2 in.

These requirements (i) and (ii) are incompatible, particularly at the smaller angles. This results in our choosing $\Delta\eta$ to be 0.3 for the smallest angles, decreasing to 0.15 for angles near 5°. Thus, particles at the smallest angles will have an angular contribution to p_T-uncertainty which is relatively large. Below about 2° there are three rings of segments; the innermost two are useful principally for shower containment and as guard rings. The

outermost rings, similarly, are needed to give good containment of cascades from hadrons which impact the outer limit of the fiducial region.

The ϕ subdivision is matched to the $\Delta\eta$ segmentation. Towers are roughly square if $\Delta\phi$ is equal to $\Delta\eta$. We have chosen the ϕ segmentation as $\Delta\phi = 0.20$ (32 intervals in 2 π). This is well matched to the $\Delta\eta$ range 0.15 to 0.25 in the PC. The segmentation derived from these considerations is described in Table 5.7.

5.3.3 Module Construction and Assembly

Figures 5.19 and 5.20 show front and side sectional views of a PC unit. The cryostat cross-section is circular with a 64 in. overall outside diameter, fitting into the 68-in. square hole in the EF muon toroid. It is a double-walled vacuum-insulated stainless steel pressure vessel with thin (0.25 in.) torispherical front walls and flat rear walls. A double-walled inner cylinder surrounds the beam pipe and is discussed below. The net liquid argon volume of the each PC is approximately 300 gallons.

The uranium plates are octagons, 50 in. wide. At present we cannot obtain uranium plates as wide as 50 inches. Each cell will therefore use two narrower plates, fastened to each other side-by-side.

The uranium and G10 plates are held together by a number of tie rods. At the center of the array one uranium plate is replaced by a 1 in. thick S.S. 304 plate which projects beyond the uranium plates on the sides. A cradle supports the array from the sides and below and is attached to this central steel plate. The array can be supported from projections on the sides of the steel plate and, with a special cantilevered stand, can be lifted and inserted into the open cryostat from the rear.

Figure 5.22 shows a beam pipe passing through the plug calorimeter; it is

a pipe of 3-in. diameter at the front end and 8-in. diameter at the rear. The larger diameter rear section is needed to accommodate beam position monitors. The plug calorimeter is located at the maximum possible z, just ahead of the low-beta quadrupole, so as to provide the best possible angular resolution at small angles.

The inner radius beam-hole walls of the cryostat are inserted from the rear, after the calorimeter has been inserted into the cryostat. The beam-hole walls (pipes) are then welded to the cryostat front walls and rear walls.

The beam pipe at the front is 1.5 in. outer radius. With clearance provided for the cryostat beam-hole pipes, for vacuum, and for the uranium plates (including thermal contraction effects), the uranium starts at the radius of about 2.7 in. At the first uranium plate (at 203 in.) this corresponds to an angle of 13 mrad.

5.3.4 Electronic and Cryogenic Services

Figures 5.10 and 5.20 indicate that signal leads and cryogenic connections are brought through the rear wall of the cryostat through ports which make upward right-angle bends before terminating at flanges. The argon vapor and liquid interface in these ports and providing warm feedthroughs for the signals. As in the EC and CC, preamplifiers are mounted in shielded boxes are mounted directly on the feedthrough port flanges to minimize pickup noise.

5.4 CRYOGENIC CONSIDERATIONS

Refrigeration for system cooldown and operation, and for argon storage and purification, is provided by the vaporization of liquid nitrogen. A 20,000 gallon nitrogen dewar filled from commercial sources stores and delivers the refrigeration required. A 20,000 gallon argon dewar supplies argon to the calorimeter and can store the inventory when any calorimeter is not operational. A purifier is provided to maintain the purity of the argon as may be required. System piping, automated control, special vent features, and safety instrumentation and interlocks protect against the asphyxiation hazards of cryogens spills in confined spaces.

5.4.1 General Considerations

The schematic for the cryogenic services is shown in Fig. 5.21. The liquid argon cryostat of the calorimeter will be located some thirty-five feet (10.7 m) below grade in the experimental hall. The calorimeter cryostat will not support the added pressure of 22 psig that would be required to lift liquid argon from the calorimeter to a surface storage dewar.

A commercial 20,000 gallon liquid argon dewar of standard design can be placed in a confined area without creating an oxygen deficiency hazard greater than class 0.[15] Thus, the system inventory dewar can be located in an alcove off the assembly hall, at roughly the elevation of the calorimeter itself. The dewar will be filled from piping extending to the surface, and,allows the reliable movement of liquid argon to and from the calorimeter by pressure transfer.

A liquid nitrogen dewar on the surface will supply refrigeration to a condensing coil within the argon dewar to eliminate boiloff losses. The same

liquid nitrogen supply system will provide refrigeration for the calorimeter liquid argon.

The calorimeter is refrigerated by liquid nitrogen with an extended surface condensing coil in the gas volume above the liquid argon level. The flow of liquid nitrogen will maintain a constant pressure in the calorimeter. The boiloff nitrogen is vented to the surface in vacuum insulated vent piping to prevent water condensation. The calorimeter is cooled from room temperature by condensing argon gas at constant pressure. Liquid argon can be transferred from the dewar to expedite the process, the boiloff recondensed by the heat exchanger. A larger exchanger significantly increases capacity for cooldown.

The storage dewar and the calorimeter piping will be sized to permit the transfer of the entire liquid argon inventory in less than eight hours, allowing the calorimeter to be conveniently emptied before it is moved to or from the assembly hall/collision hall.

A purifier will be provided to remove electronegative contaminants (chiefly oxygen) from the liquid argon. The purifier may be required to prepare the initial inventory of argon for use, and to maintain its purity during initial operation of the calorimeter. The value of the argon inventory ($60,000) may require the purifier be used to clean up the argon after an inadvertent contamination as well.

A sump will be provided below the level of the cryostat pit so that, in the event of an accident, spilled liquid cryogens will flow from the area of spillage to the sump with minimum vaporization. The sump will be actively vented to the surface and is part of the air-exchange system of the experimental hall. In the event of a major spill, the sump collects the cryogen with minimum boiloff and the quiescent liquid is leisurely pumped from the sump to

the surface after dealing with other immediate after-effects of the accident. This sump system will ensure that the asphyxiation hazards of even a large catastrophic spill are minimized. The sump will have a capacity of 20,000 gallons, and consist of a minimum wall area subbasement below the pit, lined with a sheet metal skin supported from the concrete walls of the subbasement by a layer of insulating foam. Spillage is similarly drained from the collision hall and assembly halls by means of a conduit in the floor lined with insulation to reduce heat transfer from the concrete to the fluid.

5.4.2 System Details

5.4.2.1 The Calorimeter Cryostat. The various calorimeter cryostats can be cooled in 100 hours using refrigeration heat exchangers provided in the top of the vessels. To achieve this cooldown rate the refrigeration system must have a capacity of approximately 100 kW. This corresponds to a vaporization of 10 gal/min. of liquid nitrogen. Cooldown can begin after the cryostat volume is properly pumped and purged to argon. As cooldown proceeds, makeup argon will be provided by gas transfer to the cryostat. It may be necessary to provide direct cooling for the cryostat inner vessels via separately valved nitrogen lines.

After the calorimeters have been cooled, they are filled with liquid argon from the storage dewar. At a transfer rate of 40 gpm, each calorimeter can be filled in 8 hours. Flashing and final heat capacity removal will limit cooldown to the maximum condensing capacity. When full, the cooldown portion of the heat exchanger is valved off, and the operation portion of the heat exhanger regulates the cryostat pressure.

The normal operation refrigeration requirements of the calorimeters are currently estimated to be less than 2000 watts each. This heat load will

require the vaporization of 10 gal/hr of liquid nitrogen. A small flow of gaseous nitrogen to the heat exchanger vent stack ensures that it is purged at all times.

Cooldown is an inherently gradual procedure, and interlocks and automated control systems can make it an easily monitored process. The approximately 60,000 gallons of nitrogen required by cooldown is readily provided by transfer from and periodic refill of the system nitrogen dewar. Valving and bayonet disconnects at the detector platform are provided to permit the system to be detached from the piping manifold and moved after cooldown.

The calorimeters are filled with liquid argon only after they are in position on the platform, either in the assembly hall, or in the collision hall. The liquid inventory is removed before the calorimeters are moved. Operating personnel will monitor the fill procedure closely, and all others will be excluded from the area. When all calorimeters have been filled, the pressure in the supply dewar is lowered to that of the calorimeters, so that unexpected or deliberate overpressure in a calorimeter allows liquid transfer to the dewar. Emergency electrical power is provided to maintain valve actuator controls, instrument readout and system control electronics during power outage.

A calorimeter is emptied by raising the pressure in the cryostat 1-2 psig above that of the storage dewar. This is facilitated by the use of a heater, after stopping nitrogen flow to the heat exchanger in the calorimeter. The fill/empty line into the bottom of the calorimeter can be positioned to ensure that all but a few liters of liquid can be exhausted this way.

The calorimeter is thermally insulated by a vacuum jacket and nitrogen cooled supports. The vacuum vessel provides a diagnostic and a competent first line of defense against inner vessel failure and leakage. The added

heat load from a complete failure of the vacuum vessel does not exceed a few kilowatts and will not endanger the inner vessel. The cooldown heat exchanger can readily handle this added heat load while the inventory is deliberatly transferred back to the storage dewar. Specific relief vent piping common to hydrogen and helium (air condensing) systems are not required.

Monitors are placed near all critical valves and piping bayonets which alarm upon cryogen leakage. The large flow rates used during cooldown and fill/empty procedures require that care is used when starting either process to ensure that no piping connections are leaking. Flow measurement on the cryogen flow lines automatically trip line shutoff valves at the sources to guard against uncontrolled flow in the case of line rupture or other excess flow conditions.

5.4.2.2 Inventory Dewar The system argon dewar will hold the entire argon inventory and be installed in an alcove off the assembly hall at an elevation similar to that of the calorimeter. The dewar alcove will contain the purifier subsystem and much of the cryogenic service valving and control instrumentation. The alcove will be walled off from the assembly hall so that it is of independent ODH classification at all times. A vertical shaft will extend from the alcove to the surface to provide a passageway for the piping runs to and from the surface. The shaft should be sufficiently large in cross-section to expedite the piping installation work.

The argon dewar will be of standard 65 psig design with conventional control piping and instrumentation. A vaporizer will be provided so that a clean source of backfill and makeup gas is available during purging and cooling of the calorimeter. A heat exchanger coil will be installed inside the vessel to refrigerate the contents of the dewar with liquid nitrogen. Piping runs from the dewar to the surface include an argon fill line, a liquid

nitrogen supply line and a gaseous nitrogen vent line. The dewar reliefs are ducted into the vertical shaft, which will also provide the draft for the ODH ventilation and purge of the experimental hall.

5.4.2.3 System Piping. Piping chases are provided in the building to accommodate piping runs from the argon dewar alcove to the collision hall and to the experimental hall. One and one half inch ID vacuum jacketed lines are adequate for the calorimeter liquid nitrogen and liquid argon lines. Separate vacuum lines for insulation and pump and purge will be provided.

Special connections provide for the connecting of the cryogen lines from the piping chases to the platform. The connections that terminate the fixed piping runs from the dewar to the assembly and collision halls are located in recesses in the edges of the pit. A third connection set is installed on the platform and from it lead the piping runs to the calorimeter on the platform. The calorimeter connections become adjacent to the fixed connections in the pit recess when the platform is in the assembly or collision position. Removable bayonet "u-tubes" join the two, and interlocks prevent the subsequent movement of the platform while the u-tubes are in place.

A vent pipe is provided above the collision and assembly positions to vent the nitrogen exhaust, and to provide emergency vent relief of the cryostat vacuum space.

Differential pressure instrumentation is installed at respective ends of each cryogen piping run so that leaking or rupture of the piping is detected and the cryogen flow automatically valved off.

5.4.2.5 Argon Purifier. A continuous argon purifier providing a means to remove the highly soluble, electronegative oxygen and nitrogen impurities to the level of immeasureable and tens of ppb respectively, has been designed and tested.[1] Liquid argon as supplied by vendors has been successfully used

directly, repeatedly, and over long periods without purification.[3] The scale of the D0 detector is, however, judged to be large enough and complicated enough, in terms of contaminent sources, to warrant the provision of purification.

The system will be sized to allow in five days a single pass purification of impurities occurring at the 100 ppm level in 20,000 gallons of liquid argon. The approach would treat liquid argon by warming it for room temperature purification by a counter-flow stream of treated argon gas, that, with the help of some nitrogen temperature refrigeration, is returned as liquid argon to the original source.

5.4.2.5 System Vacuum Station. A utility vacuum station is provided to rough out the calorimeter insulating vacuum space and the argon vessel itself. This station will consist of a blower and mechanical (liquid sealed) forepump having an effective capacity of 500-1000 cfm at 0.1 mm, and ultimate pressure of 3×10^{-3} torr.

After the mechanical pump has roughed a vacuum to 10 mm, a booster blower is used to increase the system capacity at lower pressures. A turbomolecular pump of similar capacity is provided for attaining high vacuum after rough vacuum is achieved in the calorimeter insulating vacuum.

5.4.2.6 Emergency Sump and ODH Safety. If 800 gallons of liquid argon (or 583 gallons of liquid nitrogen) were spilled in the pit and vaporized, the gas would displace all of the air in the pit. The resultant hazard to personnel working in the pit is obvious. A larger spill from a major structural failure of the cryostat, would present a great asphyxiation hazard to anyone in the experimental hall unless passive systems are provided to minimize the effects of such a spill.

Splash containment and gutters are provided on the calorimeter platform

to minimize vapor generation and channel the liqid cryogen spilled in a major structural failure of the calorimeter to a conduit along one edge of the pit floor. The conduit leads to a sump below the level of the pit which has 20,000 gallon capacity. The sump is a "subbasement" whose walls are lined with sheet metal which is supported off the concrete with a thin layer of foam or wood. A cubic pit 15 feet on a side has sufficient volume for the entire liquid argon inventory. The conduit is positioned so that cryogen spillage from valve packings, bayonets, etc., or actual rupture of the cryogen piping, especially at the connection boxes, is channeled to the sump.

Analysis[4] has shown that for even a very large spill of 120 gpm (three times the normal fill rate or 12 times the cooldown nitrogen flow rate, or equivalent to the flow through a two inch diameter hole from the cryostat) a system of conduits and sump provides a credible defense against the attendant asphyxiation and freeze hazards. The spilled cryogen flows down the conduits, of about 1 square foot cross-section and sloped at 1° toward the sump. The liquid and dense vapor entering the sump readily displace the air in the sump.

The analysis shows that, for example, in the first two minutes about 35 gallons of spilled argon is vaporized (only 15% of the total spilled) in the conduits and by the cooling of the sump. After the spill ceases, the argon in the sump becomes quescient with boiling loss of less than 5 liquid gpm. The cryogen is later pumped to the surface for disposal after the immediate effects of the incident are managed.

During the spill, the heavy vapor (specific gravity 1.4 at room temperature) in the sump must be lifted to the surface with a high capacity high head blower. The initial rate of vapor generation (at 100°F) is about 1800 cfm, falling in time.

The considerations of Oxygen Deficiency Hazard Safety for the experimen-

tal hall indicate that a hierarchy of ambient pressures in the area is desireable. The collision hall should be maintained at the same pressure as the accelerator tunnel to minimize air exchange between the two. The assembly hall should be a positive pressure with respect to the collision hall, and the counting rooms, elevators, and stairwells at a positive pressure with respect to the assembly hall. The emergency sump should be at a pressure below that of the collision hall.

The vent shaft above the argon dewar serves as the ventilation shaft for the sump. The normal building ventilation exhausts up this shaft so that incidental low-level cryogen spillage vapor is swept out at all times. Protective barriers exclude all personnel from the shaft.

Oxygen sensors in the pit and near the ceiling of the collision hall and the assembly hall, low temperature sensors below the calorimeter, flow alarms associated with the piping and dewar already discussed, etc. will activate an emergency purge system which increases the ventilation rates as required by a major cryogen spill. The purge rate required may be as high as six times the rate for all anticipated upset conditions; at no time should the O_2 concentration fall below 18% in habitable areas.

Care must be taken to ensure that no "dead spaces" remain in corners, elevator shafts, etc. Emergency power, redundant ventilation system control circuits and interlocks, indicator panels and activation buttons, and audible and visible alarms, are provided to ensure personnel safety.

Safety interlock systems and the purge ventilation system are periodically tested by the building personnel to ensure the highest availability and reliability of the personnel protection system provided.

5.5 ELECTRONICS FOR THE LIQUID ARGON CALORIMETER

The use of liquid argon as a unity gain ionization chamber to sample EM and hadronic shower development offers unique advantages in maintaining the calibration of the energy response of the calorimeter. At the same time one is faced with having to measure minute signals, over a large dynamic range. Furthermore, the high interaction rate expected at TeV I, requires new solutions to avoid pile-up in measuring the correct signal amplitudes.

The output signals are best measured in electron charges "e" and range typically from 50,000 to 500,000 e's for muons in various parts of the calorimeter and up to $\approx 6\times10^8$ e's for 500 GeV electromagnetic or hadronic showers. If an accuracy of 10% is desired for single muon signals, a dynamic range of 10^5 is required. This dynamic range can be reduced to $\leq$20,000 by judicious longitudinal segmentation.

The calorimeter parameters used are:

Electrons collected per MeV of energy in argon:	20,000
Fraction of energy in argon in the EM calorimeter	0.15
Fraction of energy in argon in the Hadron calorimeter	0.05
EM calorimeter resolution	$0.12/\sqrt{E}$
Hadron calorimeter resolution	$0.40/\sqrt{E}$
Total number of cells	44,000

The electronics for the readout of the DO calorimeter is described in the following, with special attention to noise and pile-up problems.

5.5.1 The Charge Sensitive Preamplifier

The basic circuit for a low noise charge sensitive preamplifier[19] is shown in Fig. 5.22. A junction field effect transistor (JFET) is used at its input as the lowest noise device available. The open loop gain of the

amplifier is given by $G = -ig_m/(\omega C)$, its input impedance, with the feedback capacitor C_F, by $r_{in} = (g_m)^{-1} \times C/C_F$. Shown across the input is also a calorimeter cell, of capacitance C_A. The output voltage of the preamp is given by $V_{out} = -Q/C_F$ where Q is the charge collected in the calorimeter cell.

Defining e_n as the input voltage noise density of the FET in $V/\sqrt{Hz}$, the input noise charge density is $e_n \times (C_A + C_{par.})$, where the parasitic capacitance is usually negligible. With typical values of $e_n \geq 10^{-9}$ $V/\sqrt{Hz}$ and for C_A up to 10,000 pF, this can result in input equivalent charge noise of up to 10^5 e's (depending on signal shaping), clearly an unsatisfactory situation. Matching the calorimeter cell to the preamp via a step-up transformer of optimum ratio results in the noise charge being proportional to the square root of the capacitance. Input noise equivalent charges of $\approx$ 69,000 e's have been obtained for a cell capacitance of 50 nF and short shaping times.[20] This result scales to 31,000 e's noise for 10 nF. Recently, very low noise FET's have become available. In addition, n FET's can be used in parallel, resulting in a $\sqrt{n}$ noise reduction. Finally, longer integration times can be used at TeV I. With the signal processing to be described later and with 10 nF across the input, we have measured noise charge of 41,000 e's for several hundred amplifiers using a single 2SK147 (Toshiba) FET and of 30,000 e's for two FET's in parallel. We feel this solution to be simpler, more reliable, less expensive than using coupling transformers, and is very well suited to the proposed detector. Figure 5.23 gives the complete schematic of the preamplifier, for a single input FET, as appropriate for the majority of the calorimeter sections.

An important difference with respect to conventional designs, is the calibration input which injects a test charge via a precision resistor, rather than the traditional capacitor. This method is chosen because it is not

possible to obtain few pF capacitors with better than ≈ 10% accuracy. Selecting or measuring over 44,000 capacitors would be a rather hopeless enterprise, with many mistakes likely. Resistors in the 100-500 kΩ range are easily available with 0.1 to 0.02% accuracy and excellent temperature coefficient and long term stability. The noise due to such a resistor across the input is quite negligible for the present application. This has been calculated and has been measured for the preamps used in the DØ calorimeter test in summer 1984. Test pulses of well defined areas are required for absolute calibration. Relative calibration to better than 0.1% of the 44,000 channels in the entire calorimeter can be obtained by using a stable pulser. Corrections for different cell capacitances and signal cable resistances, necessary because of the finite open loop gain and bandwidth of the preamp, are in the 1% range and can be established to better than 0.1%.

Calibration pulses will be distributed to the preamp calibration inputs in a manner to allow testing for "stuck" multiplexers in addition to gain monitoring. In addition to an initial calibration of the various cells of the calorimeter for capacitance and cabling resistance effects, test charges will be injected in an appropriate set of different cells.

5.5.2 Signal Processing

To achieve the noise performance mentioned above, as well as to avoid pile-up, some form of signal-shaping is necessary. A sharp cutoff is necessary at low frequencies to remove the 1/f noise as well as to reject AC noise and microphonics effects in the detector. Since the total noise contribution is proportional to the square root of the bandwidth, an upper cutoff is necessary, although not as sharp as at low frequencies. A single RC integration is quite sufficient in general. Pile-up can be minimized by fast

baseline return, at the expense of signal amplitude and therefore added noise, or by baseline sampling just before beam crossing. We choose to use the latter, since it is ideally suited to the collider operation and allows multiple event buffering to ease trigger deadtime problems. Figure 5.24 shows the idealized set up to the sampling stages, of which several hundred channels have been tested and were used in our first beam test. Baseline and signal sampling consists of two follow/hold modules, which are switched to hold at times t (just before beam crossing) and $t' = t + \tau$. The difference between the two samples, obtained with a single op-amp and four precision resistors is a d.c. voltage proportional to the collected charge. This circuit will be referred to in the following as BLS for Base Line Subtractor. The response of the circuit in Fig. 5.24 can be easily computed. The resistance R_I is the preamp input impedance, $\approx 21\ \Omega$. C_A is the gap capacitance chosen as 7000 pF as in the test setup, therefore $R_I C_A \approx 150$ ns. C_F is 22 pF and $RC_F = 400\ \mu s$. Finally, $R_2 C_2 = 50\ \mu s$ and $R_3 C_3 = 0.3\ \mu s$.

The (Laplace transform of the) output voltage in terms of the input charge is given by

$$V(s) = [Q(s)/C]\times[a/(s+a)]\times[s/(s+b)]\times[s/(s+c)]\times[d/(s+d)]$$

with $a=1/R_I C_A$, $b=1/RC_F$, $c=1/R_2\ C_2$ and $d=1/R_3 C_3$. For a charge Q injected in a short time (<0.15 μs), the output voltage as a function of time, in terms of Q/C="1", is given by

$$V(t) = \text{"1"}\times -a^2 d/(b-a)/(c-a)/(d-a)\times\exp(-at) - abc/(a-b)/(c-b)/(d-b)\times\exp(-bt)$$
$$-adc/(a-c)/(b-c)/(d-c)\times\exp(-ct) - ad^2/(a-d)/(b-d)/(c-d)\times\exp(-dt)$$

$V(t)-V(t-\tau)$ is plotted in Fig. 5.25 for $\tau=2.7\ \mu s$ in order to visualize the error due to the baseline subtraction technique for closely spaced signals. An "undershoot" of ≈ 1.5% of the peak value is evident at times greater than 2 μs, returning to zero with a time constant of ≈ 50 μs. As we will

argue later, this tail does not affect significantly the accuracy with which signals of interest are measured. The effective pole introduced by the double sampling after the 50 μs differentiation can also be cancelled by using instead the difference $V(t)-\alpha\times V(t-\tau$ where α depends mainly on R_3C_3 and τ. In this case $\alpha \approx 0.985$ resotres the baseline to within 0.1% of the signal before the next beam crossing. Low-frequency rejection, however, is no longer 20 dB per decade but becomes a constant -26 dB at low frequencies. We will soon have test results to decide whether this is acceptable. (To avoid confusion we emphasize that the signal of Fig.5.25 is <u>not</u> an actual signal anywhere in the circuits. It is however a convenient way to represent the residual baseline error for a second (or more) pulse following the one shown).

5.5.3 Pile-up

We assume in the following that the inelastic cross section is 50 mb, the luminosity is 10^{30} $cm^{-2}s^{-1}$ and the neutral plus charged multiplicity is 12 particles per unit of rapidity. These assumptions correspond to one interaction per ≈ 6 crossings. Since the detector is subdivided in 0.1 rapidity intervals and 64 azimuth sectors we expect in average $9\times12/(6\times10\times64) = 0.03$ particles per crossing in a 3×3 tower array, each particle corresponding to an E_T signal of 300 MeV.

With pulse shape given in Fig. 5.25 we compute that the r.m.s. error in measuring signals in any detector element is 1% of 300 MeV or $\alpha_{pile\text{-}up}(E_T)=3$ MeV, a quite negligible value compared to other sources of noise (see Table 5.1). In this case, α 0.985, restores the base-line to within 0.1% of the signal before the next bunch crossing.

5.5.4 Frequency Response

The frequency response of the circuit in Fig. 5.23 is given by

$$(|V(\omega)|/C)\times ad\omega^2/\sqrt{\{(\omega^2+a^2)(\omega^2+b^2)(\omega^2+c^2)(\omega^2+d^2)\}}$$

and that of the BLS by $|\exp(i\omega t)\times[1-\exp(-i\omega\tau)]| = 2\sin(\omega\tau/2)$, where τ is the time interval between the two samplings. The combined result is shown in Fig. 5.25. Note the very large rejection of low frequencies, better than -100 dB at 100 Hz, and better than -50 dB at 1000 Hz. This frequency response can be used to compute the input charge noise, from a knowledge of the input voltage noise density e_n. We in fact reverse the procedure and from the measured noise we obtain e_n=1.2 nV/$\sqrt{}$Hz for the type 2N4861 FET(Fig. 8 of Ref. 5.20), e_n= 0.55 nV/$\sqrt{}$Hz for a type 2SK147 FET, and 0.39 nV/$\sqrt{}$Hz for two such transistors in parallel.

5.5.5 Electronic Noise and Energy Resolution

We discuss explicitly in the following the example of the CC. Table 5.1 gives some parameters of a typical tower of the central calorimeter. If we require 0.1 of the muon signal as a least count, the range of 16,000 to 1 is necessary to measure electrons of $\approx$ 200 GeV.

From Table 5.1 we can evaluate the total electronic noise in the energy measurements of hadronic and EM showers in a single tower, given in Table 5.8 together with the r.m.s resolution for various energies.

From Table 5.8 it is clear that the electronic noise in a nine tower array does not seriously affect the accuracy of measuring a local energy deposit. More relevant to the overall performance of the detector is the r.m.s. noise in measurements of the energy deposited in a major fraction of the calorimeter, for instance in one eighth of the CC. From Table 5.8 we obtain an electronics r.m.s noise for one eighth of the central EM calorimeter

of 105 MeV and for the hadronic one, of 900 MeV. Likewise, for the entire CC, one has an electronic r.m.s noise of 300 MeV for the EM section and of 2.5 GeV for the hadronic section.

5.5.6 Energy Trigger Signals

In addition to precise measurements of the collected charge, the calorimeter electronics must provide fast signals for trigger generation. Trigger signals will be obtained from the preamp outputs by hard differentiation ($\approx$ 250 ns) and mild integration($\approx$ 150 ns, provided by the calorimeter capacitance or by additional filtering) producing pulse shapes peaking at $\approx$ 250 nsec after beam crossing. The measured trigger signal from test preamps is shown in Fig. 5.27. Because of the increased bandwidth and loss in peak amplitude, the electronic r.m.s. noise for these signals is estimated to be $\approx$ 2 times larger than the values given in Table 5.8. Since trigger signals will be generated for clusters of $\approx$ 10 towers, the r.m.s. electronic noise in the trigger signals is estimated to be $\approx$ 50 MeV for the EM calorimeter and 600 MeV for the hadron calorimeter per tower cluster.

5.5.7 Analog to Digital Conversion of Calorimeter Signals

It appears at present that 14 bit analog to digital converters are necessary to cover the range of interest. Assuming that we can build converters able to operate in 4 μs, including multiplexer and buffer settling times, and that a total digitizing time of 256 μs is acceptable (for an average trigger rate of 400 Hz and double event buffering at the BLS, this implies a dead time of 1%), each digitizer can serve 64 channels. Thus some 700 ADC's are necessary for the whole calorimeter. Since the above speed might not be

easy to achieve, we prefer to plan at present in terms of more ADC's and multiplexing only 32 channels. Preliminary design and testing of some ideas for these ADC's prove that the latter goal is easily and economically achievable.

5.5.8 Location of Electronics Elements

The best location for the various electronics circuits is dictated by several criteria, such as noise consideration, number of lines connecting detector and computers, ease of maintenance and/or emergency repairs and perhaps experience and taste.

Noise considerations require the charge sensitive preamps to be clustered around the signal feedthroughs on the cryostat walls, in well shielded enclosures. The preamps do not have differential outputs, in order to control size and power dissipation, therefore reasonably short runs of twisted pairs should be used between preamp outputs and BLS inputs. Thus, the BLS circuits will be located inside the detector platform. The output of the BLS are DC voltages which upon a recognition of a trigger can be held for milliseconds. If the ADC's were also in the interaction hall, digital transmission to the computers would be possible at reasonable high speeds and over few lines.

From the common experience of several systems operating in this way we prefer to transport the analog signal to a safe area where the ADC's are located. The main advantages of this approach is to limit the necessity for beam off access for repairs to analog circuits only, which are known to be much more reliable than complex digital circuits such as ADC's, crate controllers, data transfer buses, etc. One additional advantage of locating all digital electronics at the end of a well buffered, differential analog transmission system, is to reduce the noise from switching circuits from feeding

into the very sensitive electronics. There remains, of course, the problem of transporting over 44,000 signals over 200-300 ft distances, with low noise and adequate bandwidth. Since the analog signals are d.c. it is particularly easy to time multiplex them before transmission. We plan to multiplex 16 signals into a twisted pair driven differentially, with a differential peak signal of 20 V. From previous experience the noise at the receiving end can be maintained below 0.1 mV, corresponding to a dynamic range of 200,000 to 1, well beyond requirements.

With this scheme 44,000 analog signals can be transported with 172 ribbon cables, each containing 16 twisted-flat pairs.

5.5.9 Organization of the Electronics for the Calorimeter

In order to facilitate installation, debugging, and repair of all the electronics in the interaction hall, we envision the following structure for the collection of the calorimeter signals. Preamps are grouped in sets corresponding to integer multiples of towers and connected to cards containing the same number of BLS channels. These cards also produce the tower energy sum trigger signal. Groups of 16 BLS cards are time multiplexed via a crate backplane into one card containing the differential linear driver for analog transmission to the safe area "counting room." The trigger signals, after adding groups of towers are also transmitted to the counting room, without multiplexing, of course. For further discussion see the chapter on the trigger. A block diagram of these functions is shown in Fig. 5.28.

A high level of modularity is envisioned for all the electronics to be installed in the interaction hall. Preamps will be small hybrid circuits mounted on sockets in mother boards with power distribution, test signals, and

related switches. The BLS boards likewise will be mother boards with each BLS channel being either a hybrid or a miniature printed circuit on sockets.

In the movable counting house each ribbon cable, carrying $16 \times 16 = 256$ signals is connected to a card containing differential receivers, multiplexers and 8 (or 4) ADC's. A crate of 16 of these cards receives and digitizes 4096 signals. A crate controller card collects the digital results, subtracts offsets and normalizes the gains with a 16 (or 24) bit parallel multiplier. The results (after empty channel suppression) are finally unloaded into the lines carrying digital information to the dual ported memories of the level 2 trigger processing systems.

SECTION 5.1 REFERENCES

1. Tests have been made with thermosetting polymer thick film inks made by Acheson Colloids Co., Port Huron, MI. These inks are screen printable and resistances approaching 1 MΩ/square are readitly achieved . Thermal shock tests have been performed.

2. H. Gordon et al., Nucl. Instrum. Methods **196**, 303 (1982);
   O. Botner et al., Nucl. Instrum. Methods **196**, 314 (1982).

3. C. W. Fabjan et al., Nucl. Instrum. Methods **141**, 60 (1977).

4. P. Mockett, Proceedings of the 1983 SLAC Summer School.

5. Prototype tests have used cables of this type made by W. L. Gore & Assoc., Flagstaff, AZ.

6. V. Radeka, IEEE Transactions on Nucl. Science **NS-24**, 293 (1977).

7. The energy deposit per observed electron charge is twice the Ar ionization energy, because on <u>average</u> the induced signal is the result of the drift of ionization electrons over <u>half</u> the gap. See W. J. Willis and V. Radeka Nucl. Instrum. Methods **120**, 221 (1974).

8. The calculated values of signal and noise assume electronics with integration time constant 0.3 μs and sampling time 0.6 μs. See section 5.5.

9. R. Johnson, "Signal Processing for Uranium-Liquid Argon Calorimeter, DO note 55, 1/20/84 (unpublished).

10. A factor 2 suppression of uranium noise (due to positive potential difference between uranium and resistive layer) is assumed in Table 5.1. An additional factor 2 may be achieved by coating the uranium plates but this has not been taken into account here. Suppression factors given here are the results of tests by the SLD collaboration and were kindly provided by D. Hitlin (private communication).

11. Another application of this idea is described in R. Watt and F. Barrera, "Large Argon Calorimeter Cooling," a SLAC memo to A. Langford, April 10, 1981.

12. O. Botner et al., R807 internal note 263 and Physica Scripta **23**, 556 (1981).

13. Fermilab experiment E609 (private communication).

14. W. Selove et al., Proceedings of the Fermilab Calorimetry Workshop (1975).

15. An Oxygen Deficiency Hazard Class 0 index is assigned a region where the asphyxiation fatality probability of a lone individual does not exceed 10^{-7} per hour.

16. H. Zaklad, A Purification System for the Removal of Electronegative Impurities fro Noble Gases, LBL, April 1971.

17. R. Watt, private communication.

18. Updated Analysis of the Effects of a Large Liquid Argon Spill at the DO Detector, Cryogenic Consultants, Inc., Report 593-105, July 31, 1984, unpublished.

19. V. Radeka, IEEE Trans. Nucl. Sci. **NS-21** no. 1, 51 (1974).

20. W. J. Willis and V. Radeka, Nucl. Instrum. Methods **120**, 221 (1974).

TABLE 5.1 Central Calorimeter Parameters

Layer		No. Cells per Tower	No. Towers per Layer	Cap.(nf) per Tower	RMS Electronic Noise(MeV)/Tower**	RMS Uranium Noise(MeV)/Tower	Total RMS Noise(MeV)/Tower	Muon Signal (MeV)/Tower
EM	#1	3	1536	0.33	0.56	1.9	3.0	14
	#2	3	1536	0.36	0.61	2.0	2.1	14
	#3	10	5888	0.33	0.56	1.9	2.0	46
	#4	16	1408	2.7	3.4*	5.4	6.4	74
Fine Had.	#1	15	1152	3.5	9.4*	13.	16.	150
	#2	35	1024	13.	35.*	25.	43.	350
	#3	30	768	17.	46.*	29.	54.	300
Coarse Hadr.	#1	20	640	17.	71.*	-	71.	300

* Assume 2-JFET input stage
** Positive potential on uranium relative to resistive layer

TABLE 5.2
Longitudinal and Transverse Mechanical Modularity of the DØ End Caps

	EM Module	Fine Hadron Mod I	Fine Hadron Mod II	Coarse Hadron Mod.	Totals
*Number of Cells	24	24	24	24	96
Number of Uranium Discs	24	24	24	0	72
Number of Copper Discs	24	24	24	24	96
Outer Discs Diameter	163.35"	159.84"	149.60"	118.11"	
Beam Hole Diameter Coverage	13.56"	16.87"	20.37"	24.67"	
Weight (lbs) U	27,600	65,800	56,600	0	150,000
Cu	13,100	30,900	26,600	63,600	134,200
Total	40,7000	96,700	83,300	63,600	290,100
Thickness (cm)	36.5	50.9	50.9	61.4	199.5
(in.)	(14.37)	(20.0)	(20.0)	(24.17)	(78.54)
Radiation Lengths (X_0)	19.9	47.3	47.3	34.4	148.9
Interaction Lengths (λ_0)	.96	2.31	2.31	3.37	8.89
Number of Longitudinal Readout	4	2	1	1	8

* See section 5.2.3 for discussion of cell structure

TABLE 5.3
DO End Caps
Uranium Plate Requirements

Section	Number	Size Trapedsoid W1×W2×j×t (in.)	Weight/Plate Segment (lbs)	Total Weight (lbs)
EM	192	32.19"×2.47×74.70"×0.079	69.54	13,352.33
EM	192	32.19"×2.60×74.39"×0.079	69.51	13,346.73
EM	192	32.19"×2.72×74.08"×0.079	69.46	13,336.99
EM	192	32.19"×2.85×73.76"×0.079	69.42	13,328.82
FHI	192	31.12"×3.05×70.54"×0.2	163.90	31,469.53
FHI	192	31.12"×3.23×70.10"×0.2	163.74	31,437.90
FHI	192	31.12"×3.40×69.66"×0.2	163.52	31,395.24
FHI	192	31.12"×3.58×69.22"×0.2	163.33	31,359.60
FHII	192	29.12"×3.65×64.03"×0.2	142.68	27,399.97
FHII	192	29.12"×3.96×63.24"×0.2	142.25	27,312.88
FHII	192	29.12"×4.13×62.81"×0.2	142.01	27,266.55
FHII	192	29.12"×4.31×62.37"×0.2	141.78	27,222.14
	2304			388,223.92
				144.11 tons

20% rejection ≈ 2765 plates ≈ 173 tons

TABLE 5.4
Longitudinal Cell Structure - End Cap Calorimeter

Electromagnetic Module Cell Structure	Material	Length (mm)	X_0	λ_0
	Cu	2	0.140	0.0132
	Ar	2	0.014	0.0024
	G10	1.6	0.008	0.0030
	Ar	2	0.014	0.0024
	U	2	0.625	0.190
	Ar	2	0.014	0.0024
	G10	1.6	0.008	0.0030
	Ar	2	0.014	0.0024
		15.2 mm	0.837 X_0	0.0402 λ_0

Sampling fraction = 20.7%

Fine Hadronic Module I & II Cell Structure	Material	Length (mm)	X_0	λ_0
	Cu	5	0.350	0.0336
	Ar	2	0.014	0.0024
	G10	1.6	0.008	0.0030
	Ar	2	0.014	0.0024
	U	5	1.560	0.0176
	Ar	2	0.014	0.0024
	G10	1.6	0.008	0.0030
	Ar	2	0.014	0.0024
		21.2 mm	1.982 X_0	0.0963 λ_0

Sampling fraction = 9.3%

Coarse Hadronic Module Leakage Cell Structure	Material	Length	X_0	λ_0
	Cu	20	1.399	0.1325
	Ar	2	0.014	0.0024
	G10	1.6	0.008	0.0030
	Ar	2	0.014	0.0024
		25.6 mm	1.436 X_0	0.1403λ_0

Sampling fraction = 3.3%

TABLE 5.5
Longitudinal Readout Ganging - Endcap Calorimeter

	Readout Segment	Distance** from Detector Center (cm)	# of Cells	Length* (cm)	X_0	λ_0	Thickness (cm) Ar	U	Cu	G10
EM	1	153	3	4.56	2.51	0.1206	2.4	0.6	0.6	0.96
Module	2	158	3	4.56	2.51	0.1206	2.4	0.6	0.6	0.96
	3*	163	6	9.12	5.02	0.2412	4.8	1.2	1.2	1.92
	4	172	12	18.24	10.04	0.4824	9.6	2.4	2.4	3.84
			24	36.48	20.08	0.9648	19.2	4.8	4.8	7.68
Fine Hadronic	5	193	4	8.48	7.93	0.37	3.2	2.0	2.0	1.28
Module I	6	202	20	42.40	39.64	1.93	16.0	10.0	10.0	6.40
			24	50.88	47.57	2.31	19.2	12.0	12.0	7.68
Fine Hadronic Module II	7	247	24	50.88	47.57	2.31	19.2	12.0	12.0	7.68
Coarse Hadronic Module	8	301	24	61.44	34.44	3.36	9.6	-	48.0	3.84
Totals	8		96	199.7	149.7	8.95	67.2	28.8	76.8	26.88

*Does not include intersegment and intermodule distances required for bolting structures.
**Does include estimates of intersegment and intermodule distances of 0.25 in. and 1 in. respectively.

TABLE 5.6 Transverse Pad Configuration - End Cap Calorimeter

Module	Longitudinal Readout Section	θ Region	η Region	Minimum Pad Size	Maximum Pad Size	Worst Case Capacitance (pf)	Ur*** Noise (e^-)	Amplifier Noise (e^-)	Worst Case Signal** Noise	# Pads
EM Module	1	5°→53.9°	3.13→0.68	1.4×1.4	17.8×27.3	4400	2.2×10^4	1.8×10^4	3.5/1	1536
	2	5°→53.0°	3.13→0.70	1.5×1.5	18.4×28.1	4500	2.2×10^4	1.8×10^4	3.5/1	1536
	3*	5°→52.2°	3.13→0.71	1.6×1.6	18.9×29.0	9400	4.6×10^4	3.8×10^4	3.0/1	3456
	4	5°→49.1°	3.13→0.78	1.7×1.7	18.2×25.7	17000	8.5×10^4	6.9×10^4	3.5/1	1536
Fine Hadronic Module I	5	5°→46.0	3.13→0.86	1.8×1.8	19.4×27.5	6000	3.0×10^4	2.4×10^4	3.5/1	1472
	6	5°→44.7	3.13→0.89	1.9×1.9	19.1×25.5	28000	14.5×10^4	11.5×10^4	3.5/1	1472
Fine Hadronic Module II	7	5°→56.5	3.13→1.11	2.3×2.3	17.7×21.4	26000	15.3×10^4	10.6×10^4	4.0/1	640
Coarse Hadronic Module	8	5°→34.0°	3.13→1.19	2.8×2.8	13.0×14.5	7300	2.0×10^4	2.9×10^4	11/1	544
										12192

* $\Delta\eta = \Delta\phi = 0.05$ for $10° \leq \theta \leq 25°$

** Signal = minimum ionizing particle at normal incidence to the argon gap.
Noise includes uranium radioactivity noise for an integrating time of 600 ns.

*** Uranium noise is calculated from the empirical formula σ_{noise} (meV) = $K\times\sqrt{A\tau}/\sqrt{2}$ where τ = 600 ns sampling time, A = area of largest pad in a given section in in.^{2} and K is proportionality constant = 0.1. This formula takes into account radioactivity from both sides of the uranium plates and operation of the uranium plate at positive high voltage with respect to the resistive layer.

TABLE 5.7 Transverse Segmentation Tower Geometry at z = 540 cm*

Θινλσ	η	θ (deg)	r (cm)	Δη	Δ-r(cm) at z=540 cm	Δ r-φ (cm)
	2.85	6.62	62.68			
11				0.15	8.8	11.4
	3.00	5.70	53.90			
10				0.15	7.5	9.8
	3.15	4.91	46.36			
9				0.15	6.5	8.5
	3.30	4.22	39.89			
8				0.15	5.6	7.3
	3.45	3.64	34.32			
7				0.15	4.8	6.3
	3.60	3.13	29.53			
6				0.17	4.6	5.3
	3.77	2.64	24.91			
5				0.20	4.5	4.4
	3.97	2.16	20.39			
4				0.23	4.2	3.6
	4.20	1.72	16.20			
3				0.25	3.6	2.8
	4.45	1.34	12.61			
2				0.30	3.3	2.2
	4.75	0.99	9.34			
1				0.30	2.4	1.6
	5.05	0.73	6.92			

* 540 cm is 1.5 λ_0 into calorimeter.

TABLE 5.8

	Total Noise, MeV Equivalent in 3×3 Towers	1 GeV Shower rms res. (MeV)	10 GeV Shower rms res. (MeV)	100 GeV Shower rms res. (MeV)
EM	40	120	379	1200
Hadronic	350	400	1265	4000

FIGURE CAPTIONS - CHAPTER 5

5.1 Cross-section for missing p_T vs. missing p_T. The solid line is for uranium-liquid argon energy resolution and EM/hadron response equal to 1. The dotted line is for iron-liquid argon energy resolution and EM/hadron response of 1.4.

5.2 Effect of beam hole and dead area shown in the inset. The ordinate is the rms missing p_T normalized to that for a 0.5° (η = 5.5) hole effect (σ_0). The dotted line is the effect of increasing the beam hole size to the value on the abscissa. The horizontal bars show the effect of that rapidity interval in the dead region of calorimetry. The study used p_T = 50 GeV jets.

The inset shows the calorimeter model used for a M simulation. The dotted area indicates dead region. Radial lines delineate regions isolated for study. The calorimeter and dead region had a uniform absorption length of 20 cm and a radiation length of 1.3 cm. The dead region was 10 cm thick.

5.3 Side and end sections of the complete CC. The notes indicate the cryostat wall thicknesses and other relevant dimensions. Also shown are the heat exchangers, the mutual support of the cryostat end walls and the insulating supports at the bottom. One leakage module, near the top, is omitted to accommodate the present position of the main ring bypass.

5.4 End view of a typical CC module showing wall dimensions, radial dimensions of the 3 layers, and details of the cell structure.

5.5 Plan view of a readout board typical of all layers except EM layer #3 where there are 4 times as many pads per board. Details show the interpad gap, the layered structure of the board and the edge notches to provide relief for the jumpers which gang the pads into tower.

5.6 Sketch of a typical module showing the perforated walls and the slot for bringing the ganged signals out. Although not to scale the drawing shows the correct proportions for a leakage model.

5.7 Side and end views of the CC. Overall dimensions are given. The vent pipe and signal feed-through ports are illustrated. Shielded boxes containing the preamplifiers are shown mounted directly on the feed-through ports.

5.8 Schematic presentation of the method to be used for inserting modules into the cryostat.

5.10 Cross-section view of the EC cryostat and plate array.

5.11 Side view (section) of the EC cryostat and plate array.

5.12 Arrangement of plates and readout boards for the EC.

5.13 The assembled module of plates for EC showing the azimuthal rotation scheme.

5.14 Cell structure for the EC.

5.15 Segmentation pattern of EC in the r-z plane.

5.16 Segmentation pattern of EC in the r-ϕ plane: (a) shows the pattern in EM layers 1, 2, and 4 and hadronic layers 1 and 2; (b) shows the segmentation in the third EM compartment.

5.17 The uranium-liquid argon cell structure for the plug calorimeter.

5.18 The transverse segmentation of the PC readout boards.

5.19 Front view of the PC cryostat and plate array.

5.20 Side view (section) of the plug calorimeter.

5.21 DO Cryogenic System flow schematic.

5.23 Basic configuration for a FET input charge sensitive preamplifier.

5.24 Circuit diagram for the charge sensitive preamplifier. The input protection diodes are 50 A surge rectifiers.

5.25 Equivalent circuit of a signal shaping system up to the double sampling stage.

5.26 Equivalent signal shape after filter, double sample and difference, illustrating the error in base-line measurement for 50 μsec differentiation and 0.6 μsec interval between the samples.

5.27 Equivalent frequency response of the filter and BLS circuit.

5.28 Calorimeter trigger signal from prototype test (80 MeV total input).

5.29 Block diagram of the calorimeter electronics organization in the interaction hall.

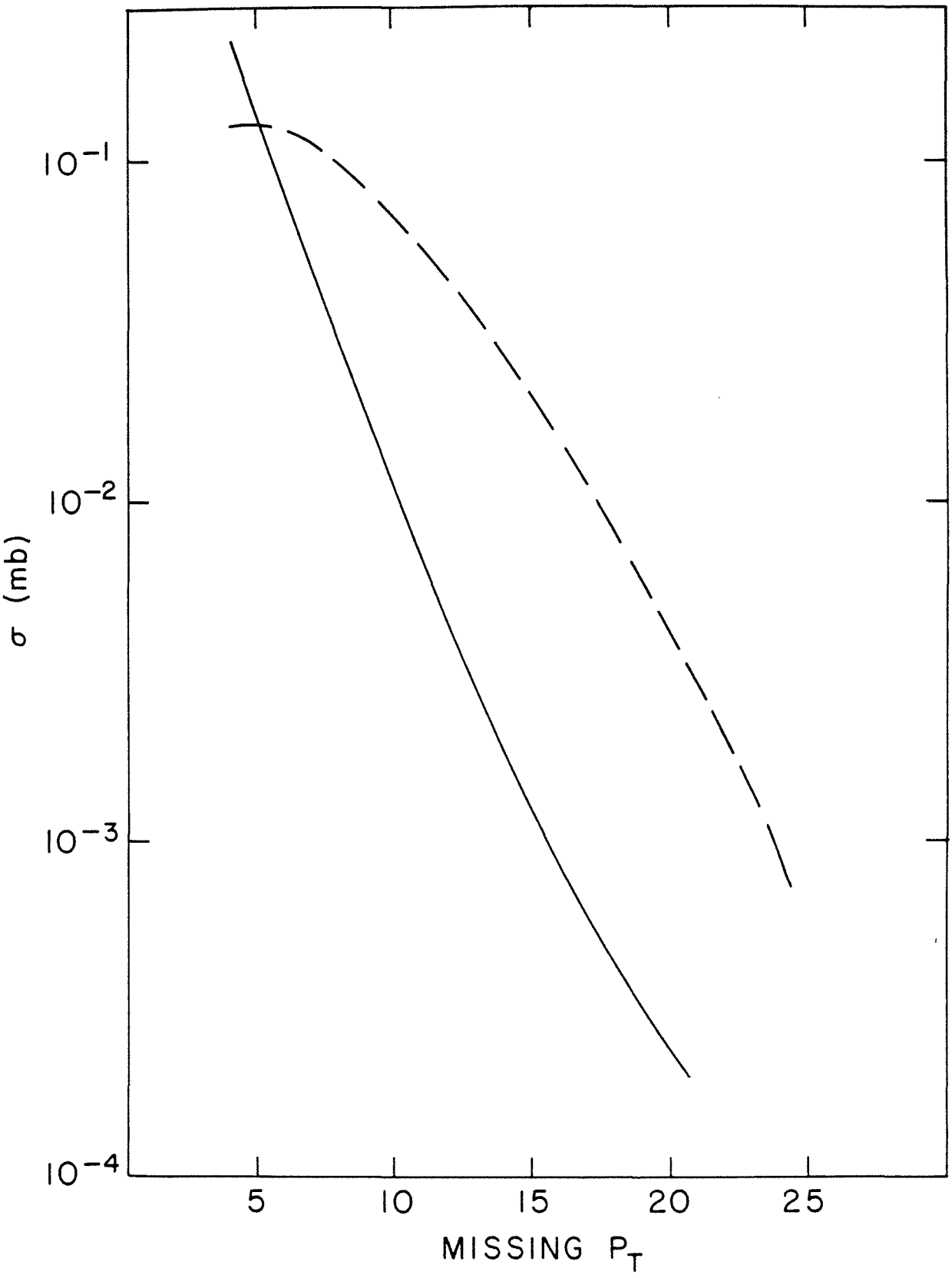
10^{-1}
10^{-2}
10^{-3}
10^{-4}
σ (mb)
5
10
15
20
25
MISSING P_T

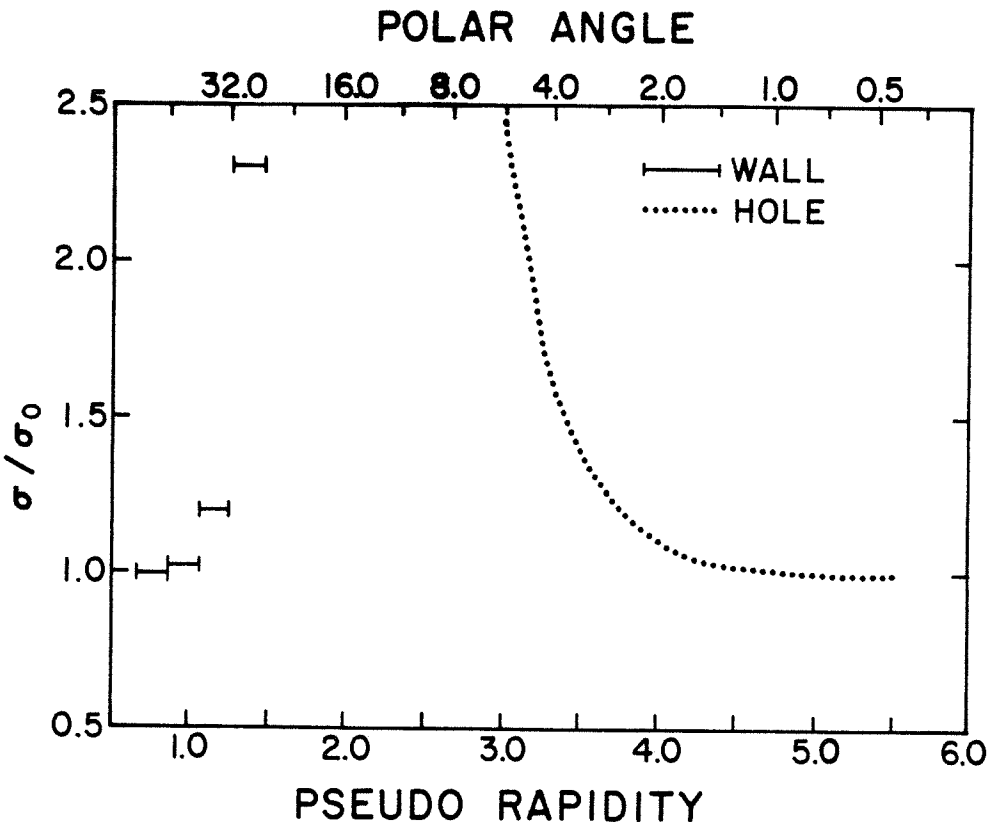
POLAR ANGLE
32.0
16.0
8.0
4.0
2.0
1.0
0.5
2.5
2.0
1.5
1.0
0.5
σ / σ0
WALL
HOLE
1.0
2.0
3.0
4.0
5.0
6.0
PSEUDO RAPIDITY

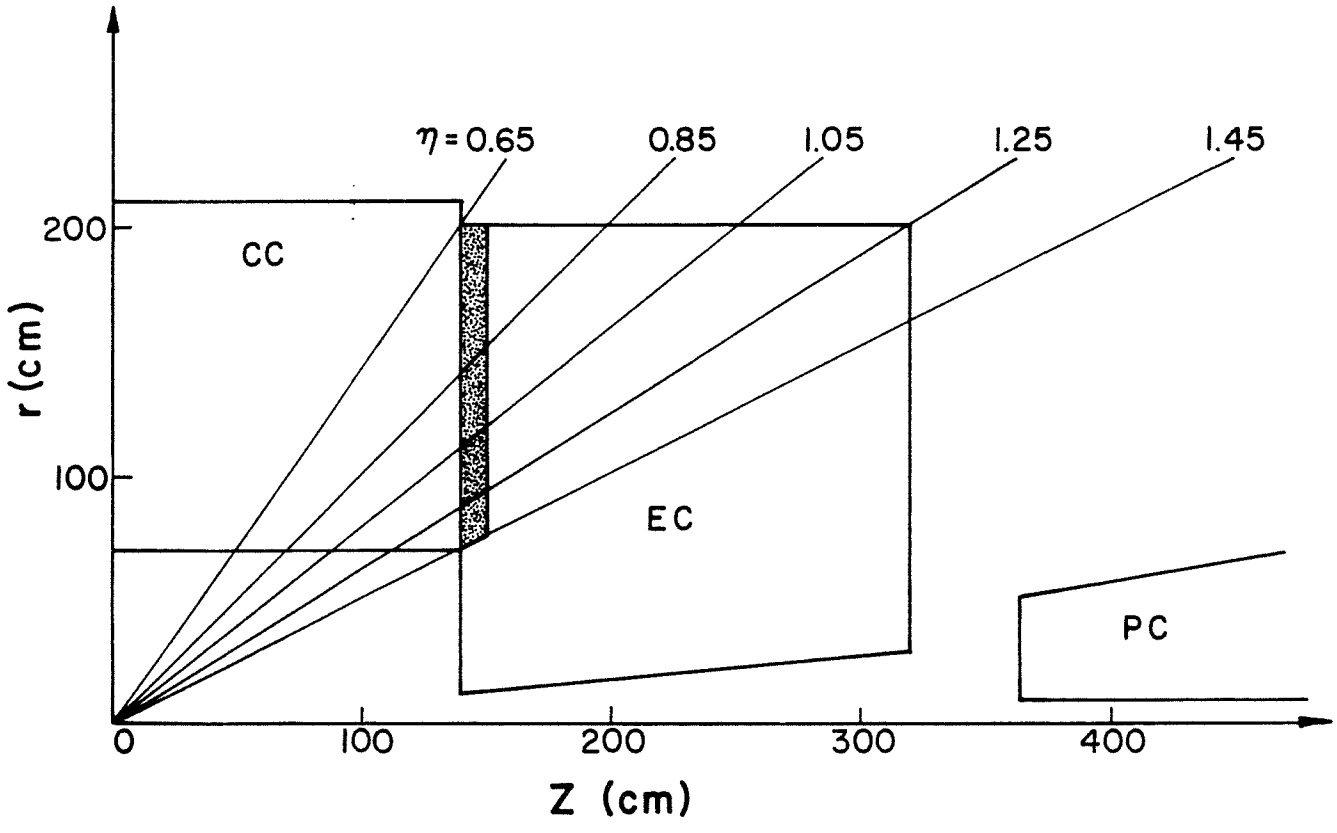
η = 0.65
0.85
1.05
1.25
1.45
200
100
r (cm)
CC
EC
PC
0
100
200
300
400
Z (cm)

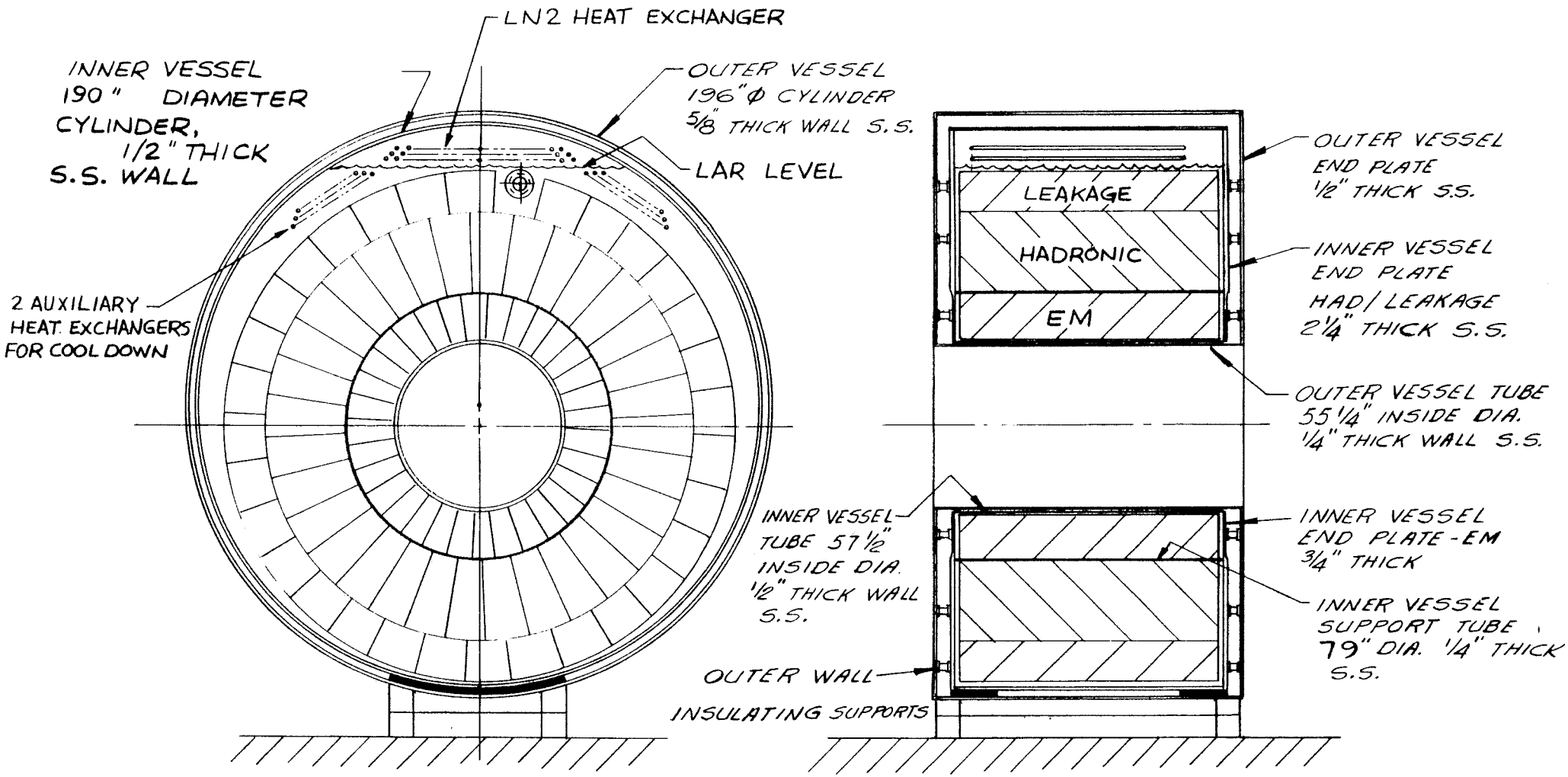

CENTRAL CALORIMETER
CROSS SECTION

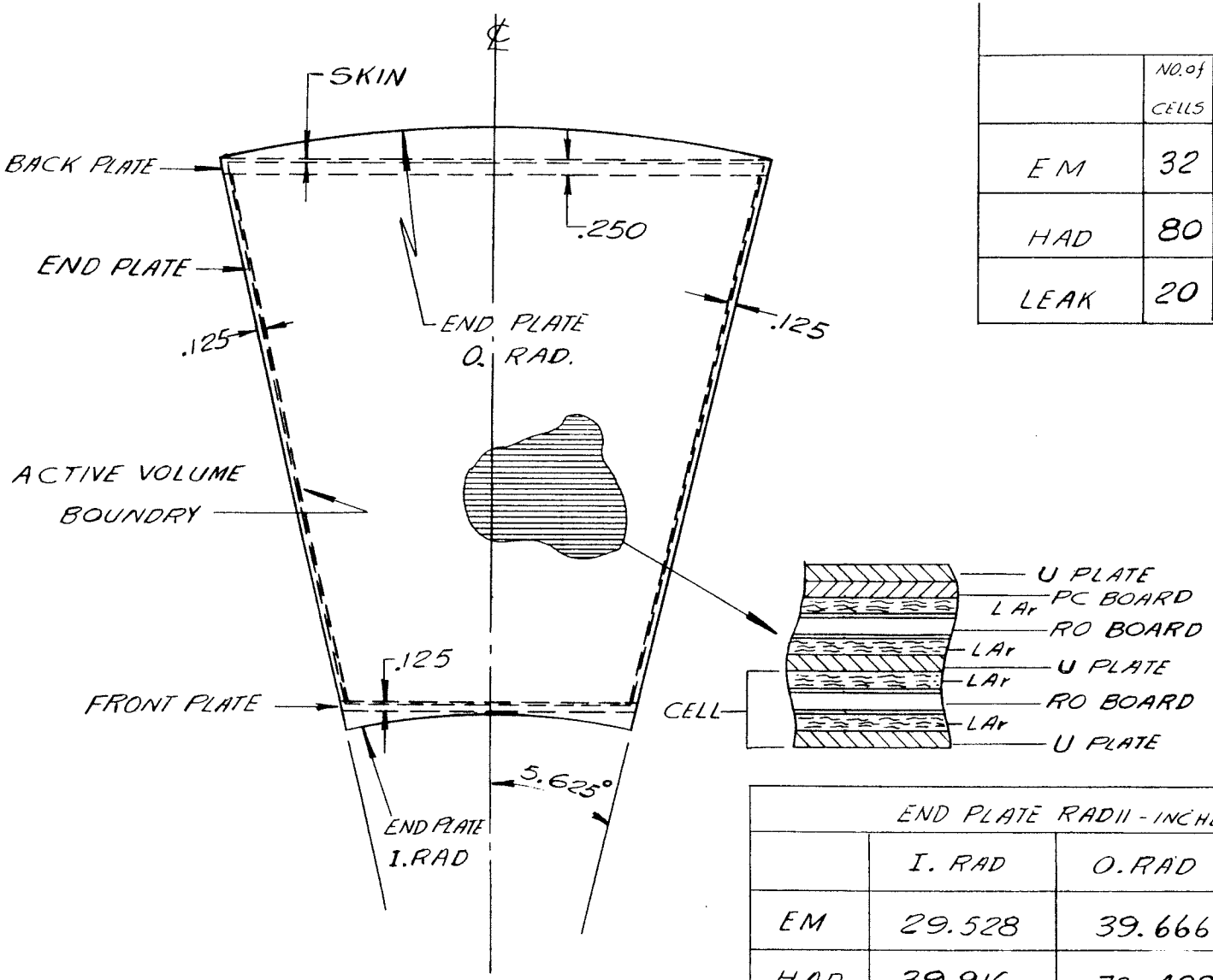

THICKNESS (INCHES						
	NO. of CELLS	U	L Ar	G-10 RO	PC	PC BOARDS AFTER CELL #
EM	32	.079	2x.063	.063	.194	3, 6, 16, 32
HAD	80	.197	2x.063	.063	.194	15, 50, 80
LEAK	20	CU .5"	2x.063	.063	.194	20

END PLATE RADII - INCHES		
	I. RAD	O. RAD
EM	29.528	39.666
HAD	39.916	72.498
LEAK	72.498	87.430

READOUT BOARD

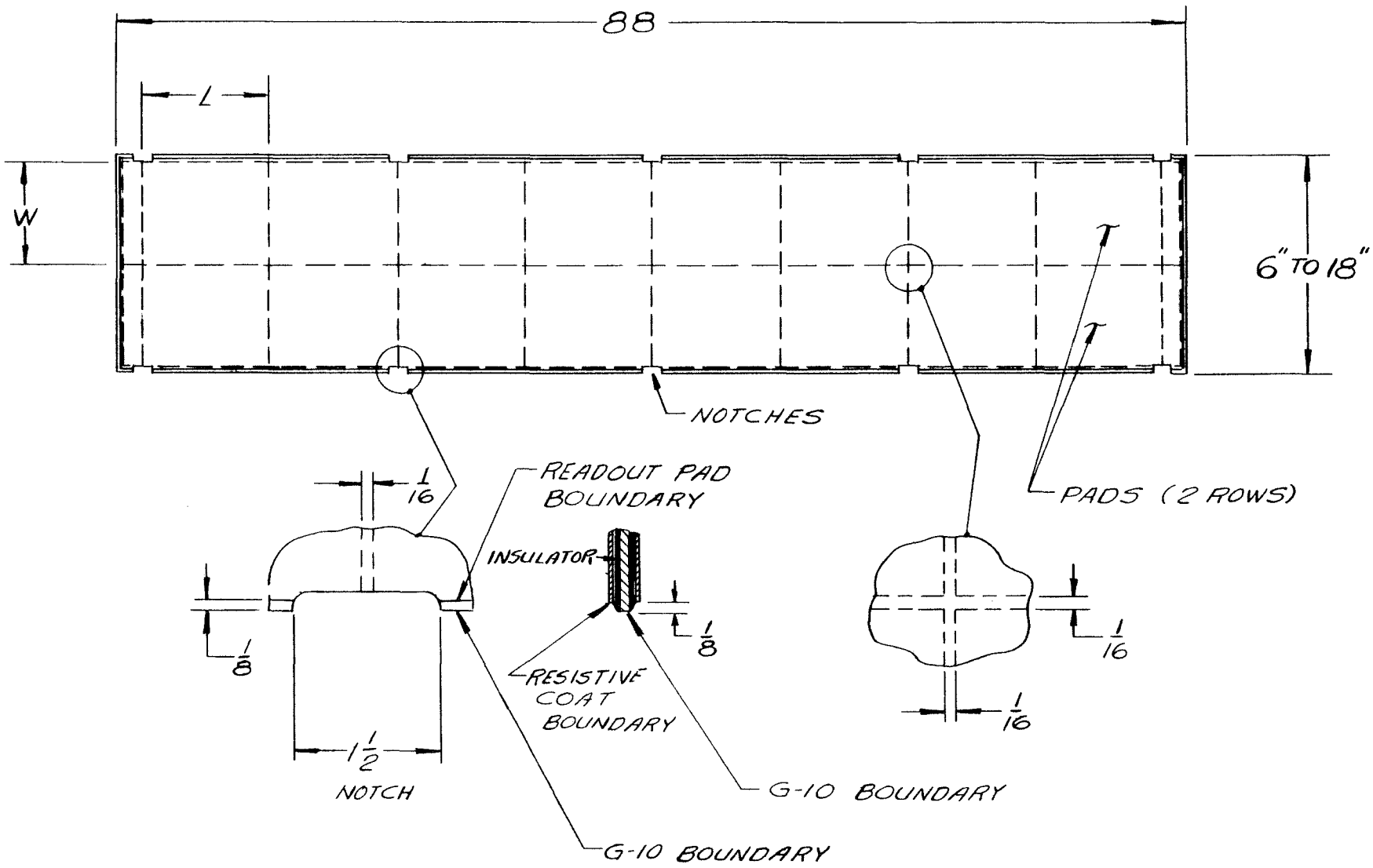

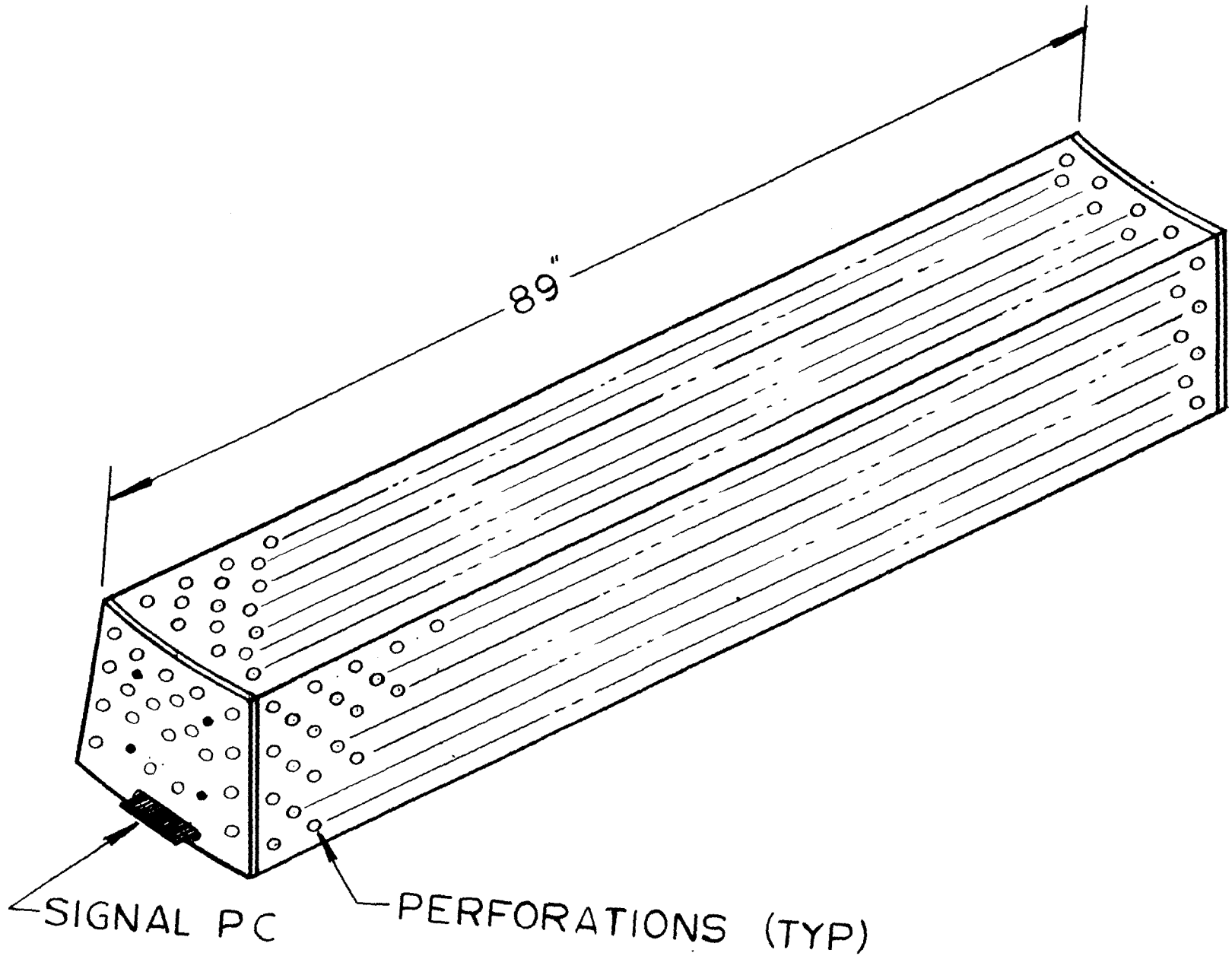

LEAKAGE MODULE

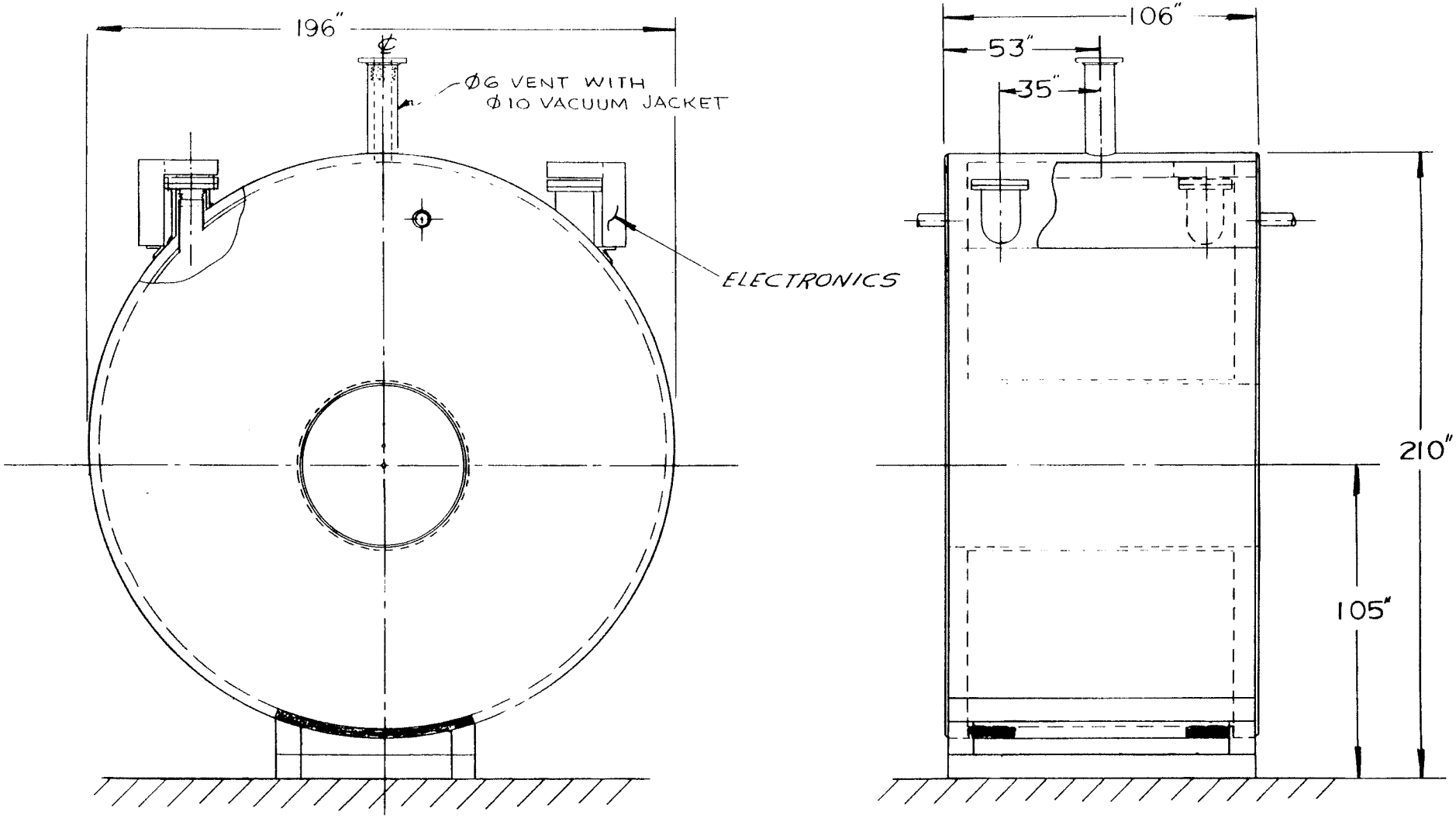

CENTRAL CALORIMETER

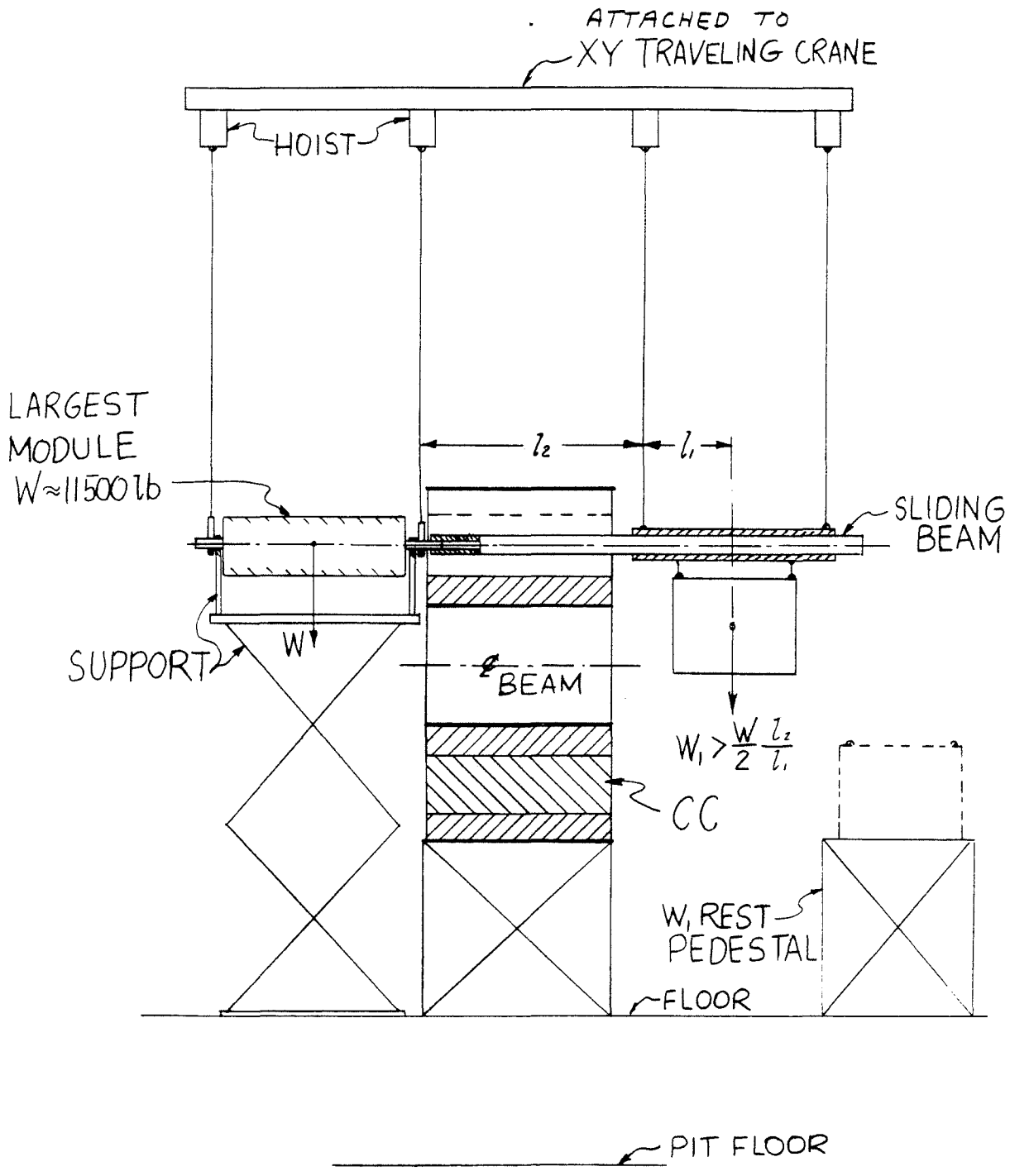

SCALE : 1/50

ASSEMBLY OF CENTRAL CALORIMETER

C. Fe

P.D.I

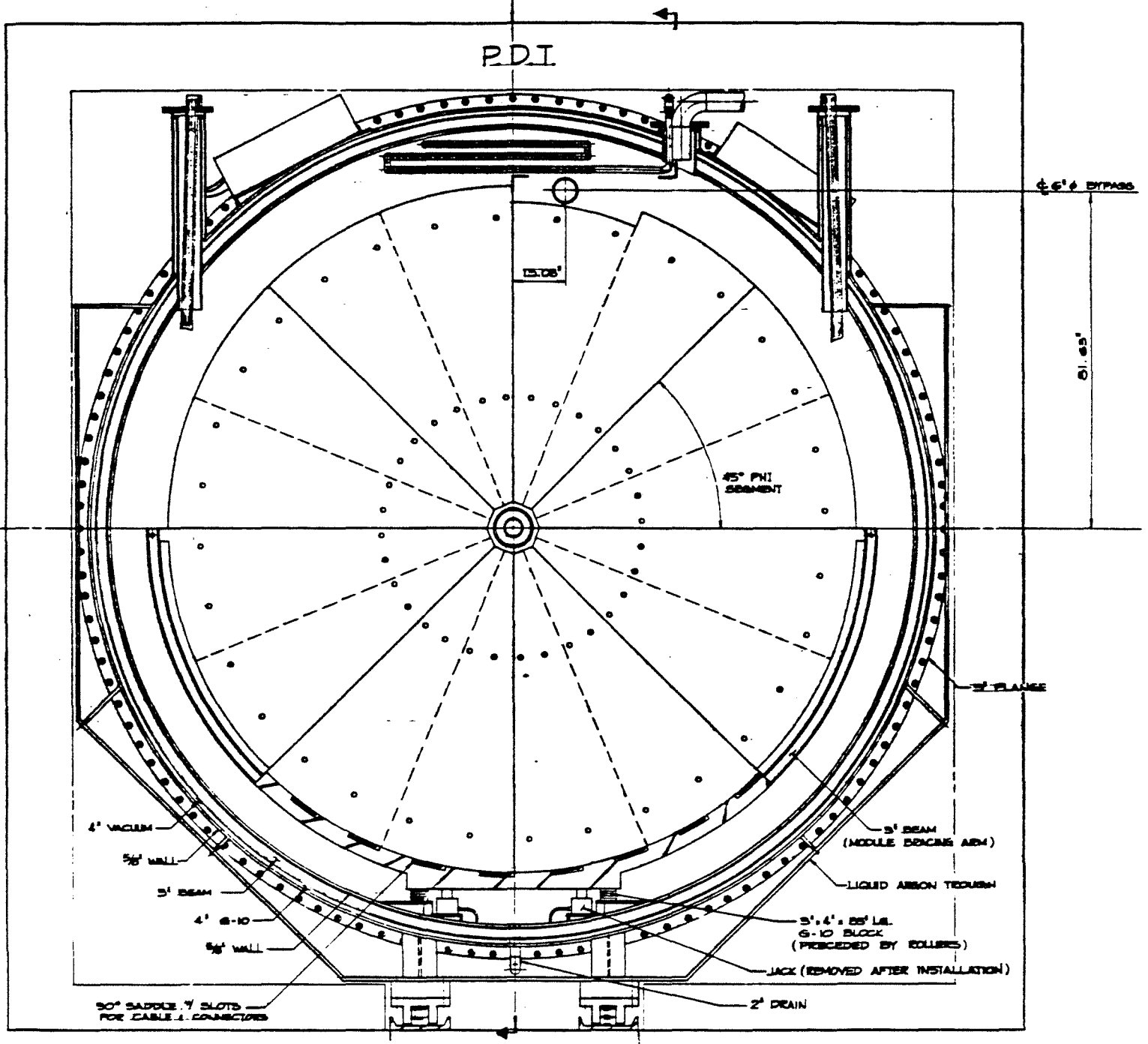
15.08°
45° PHI SEGMENT
4" VACUUM
5/8" WALL
3" BEAM
4" G-10
5/8" WALL
90° SADDLE, 4 SLOTS FOR CABLE & CONNECTORS
3" BEAM (MODULE BRACING ARM)
LIQUID ARGON TEDLAR
5", 4" x 88" LG. G-10 BLOCK (PRECEDED BY ROLLERS)
JACK (REMOVED AFTER INSTALLATION)
2" DRAIN

C. Fe

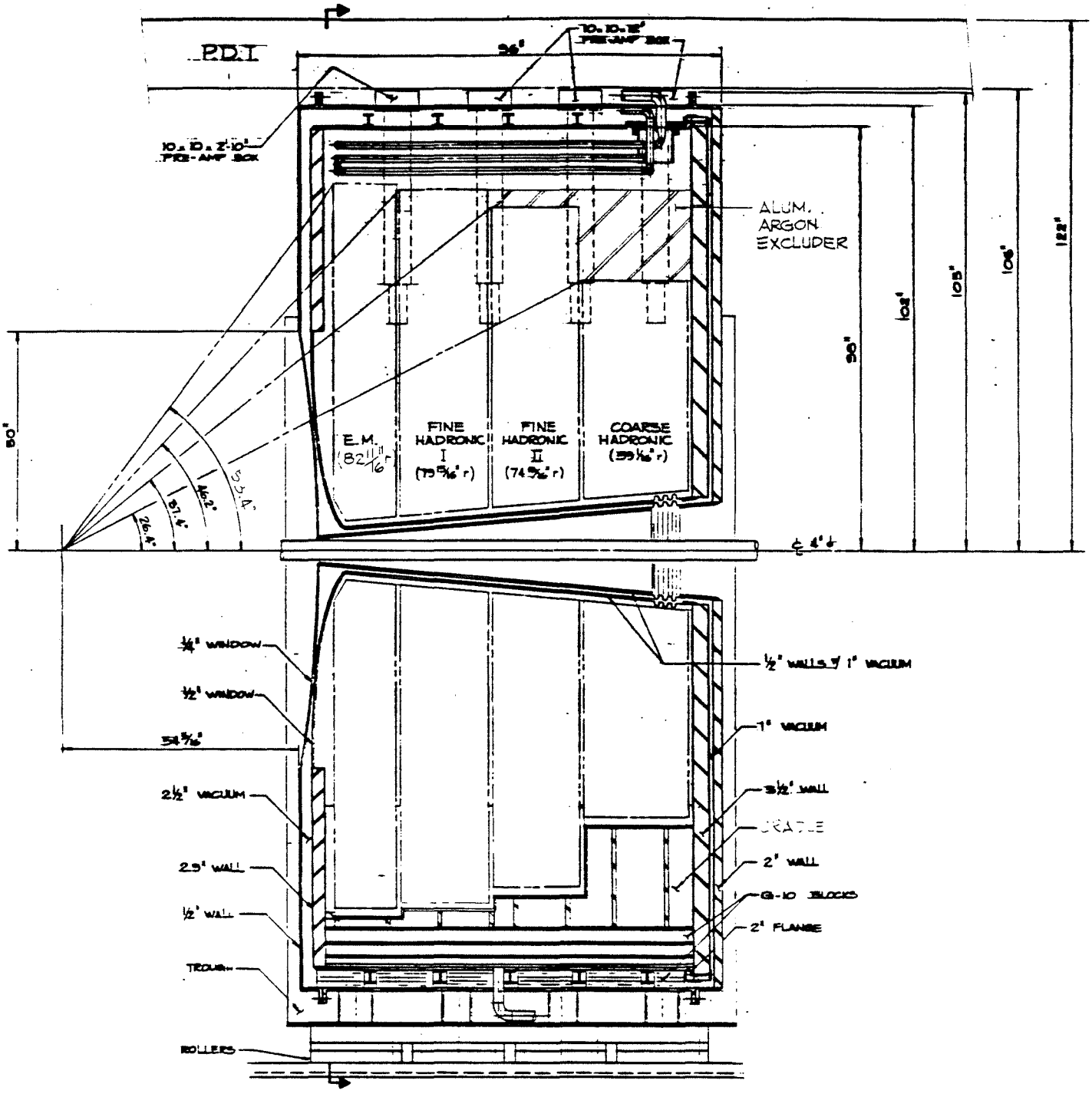
PDI
36"
10 x 10 x 2'-10"
PRE-AMP BOX
ALUM. ARGON EXCLUDER
E.M. (82 11/16" r)
FINE HADRONIC I (79 5/16" r)
FINE HADRONIC II (74 5/16" r)
COARSE HADRONIC (59 1/16" r)
80"
90"
102"
105"
108"
122"
¢ 4"
26.4°
37.4°
46.2°
53.4°
1/4" WINDOW
1/2" WINDOW
54 5/16"
2 1/2" VACUUM
2.5" WALL
1/2" WALL
TROUGH
ROLLERS
1/2" WALLS & 1" VACUUM
1" VACUUM
3 1/2" WALL
CRATE
2" WALL
G-10 BLOCKS
2" FLANGE

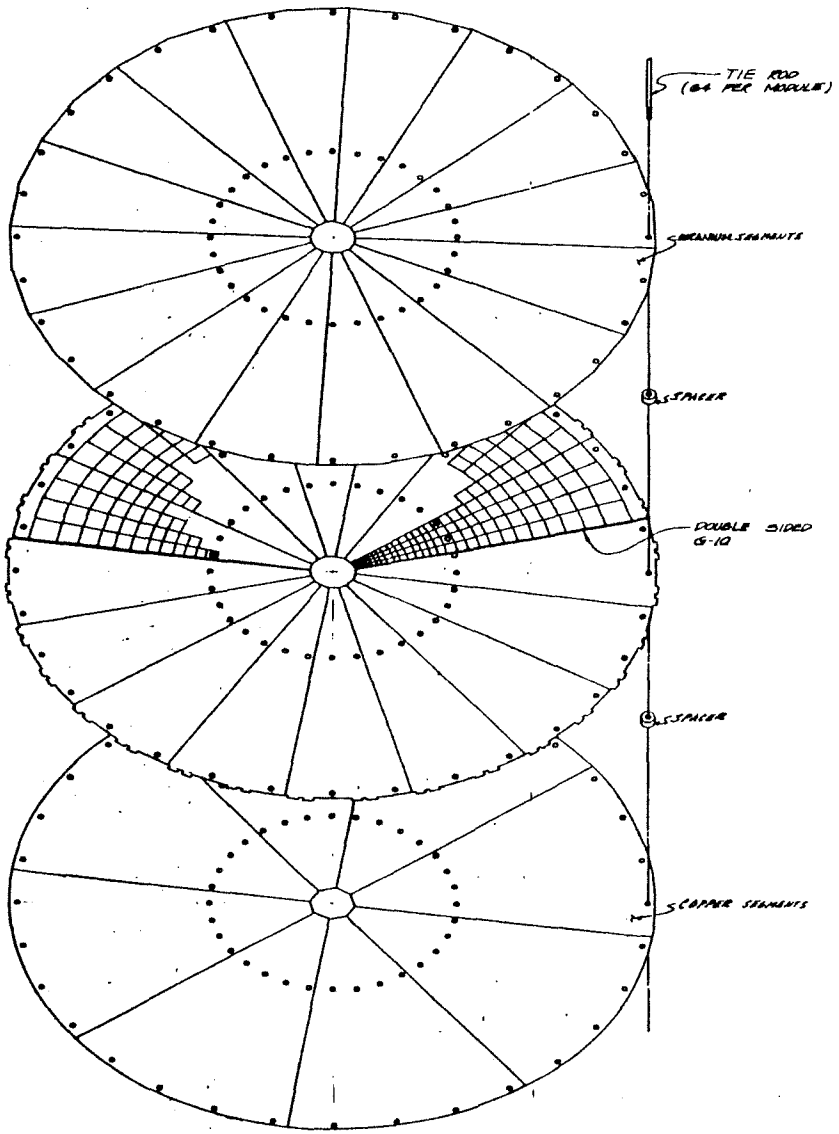

TYPICAL CELL CONSTRUCTION

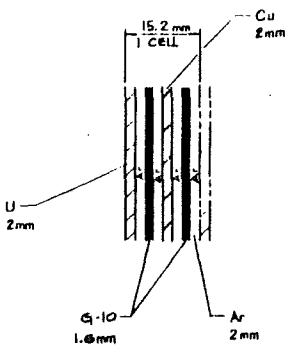

ELECTROMAGNETIC
(24) CELLS

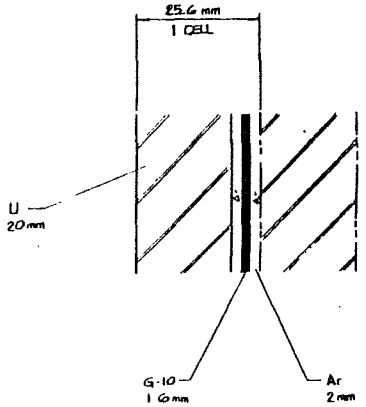

COARSE HADRONIC
(24) CELLS

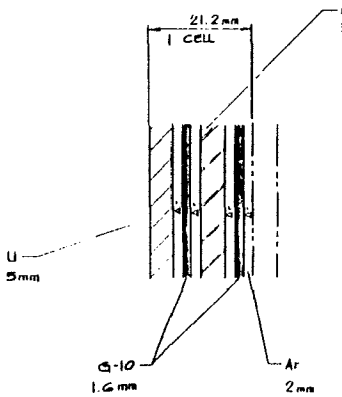

FINE HADRONIC
(48) CELLS

ITEM NO.	PART NO.	DESCRIPTION OR SIZE	QTY. REQ.

PARTS LIST

UNLESS OTHERWISE SPECIFIED: FRACTIONS ± | DECIMALS ± | ANGLES ±

1. BREAK ALL SHARP EDGES 1/64 MAX.
2. DO NOT SCALE DWG.
3. DIMENSIONING IN ACCORD WITH ANSI Y14.5 STD.
MAX. ALL MACHINED SURFACES

DESIGNATOR | DRAWN | CHECKED | APPROVED | USED ON | MATERIAL

FERMI NATIONAL ACCELERATOR LABORATORY
UNITED STATES DEPARTMENT OF ENERGY

SCALE: NONE | FILMED | DRAWING NUMBER | REV

DØ END CAP CALORIMETER
MODULE ASSEMBLE

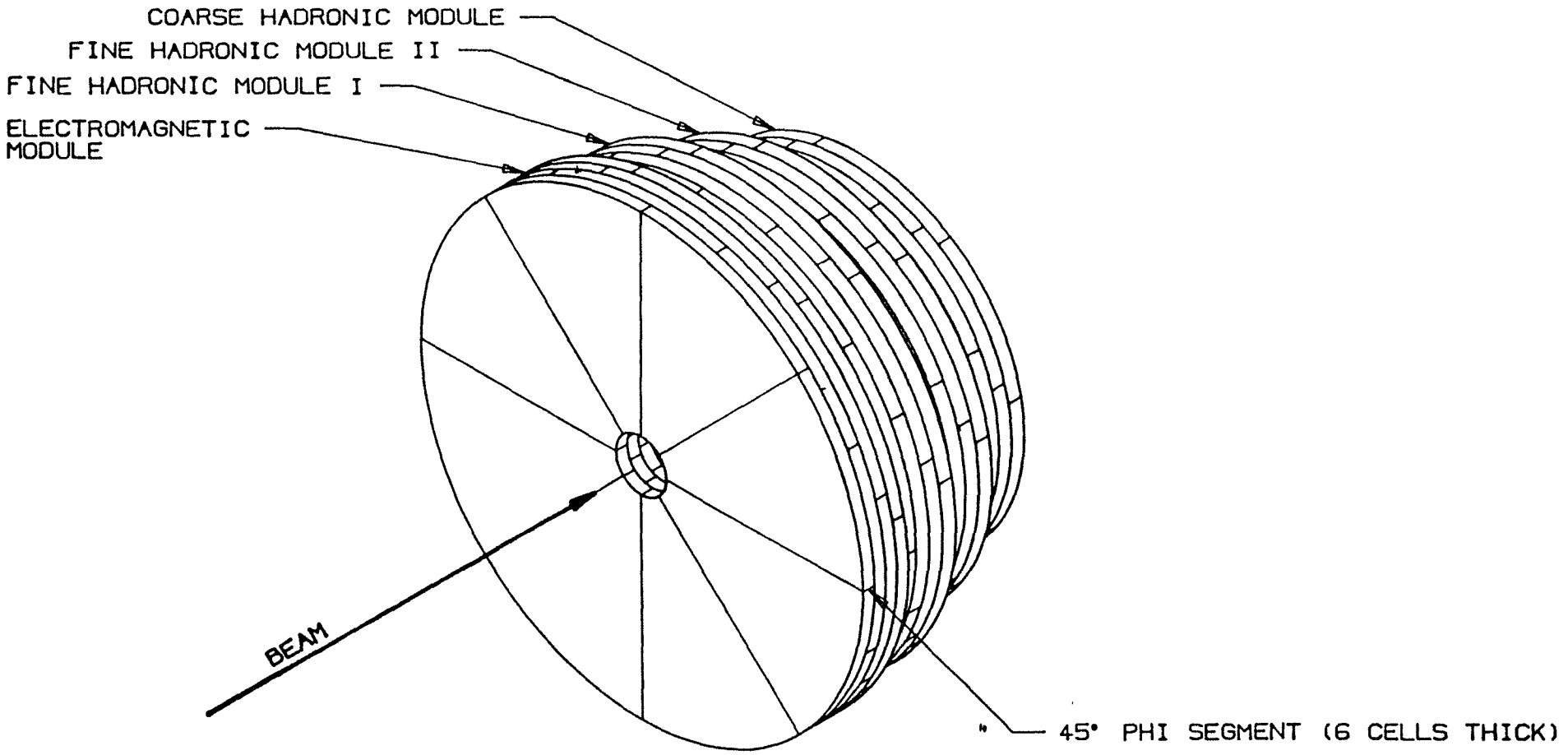

Fig.

LONGITUDINAL CELL STRUCTURE

DØ END CAP

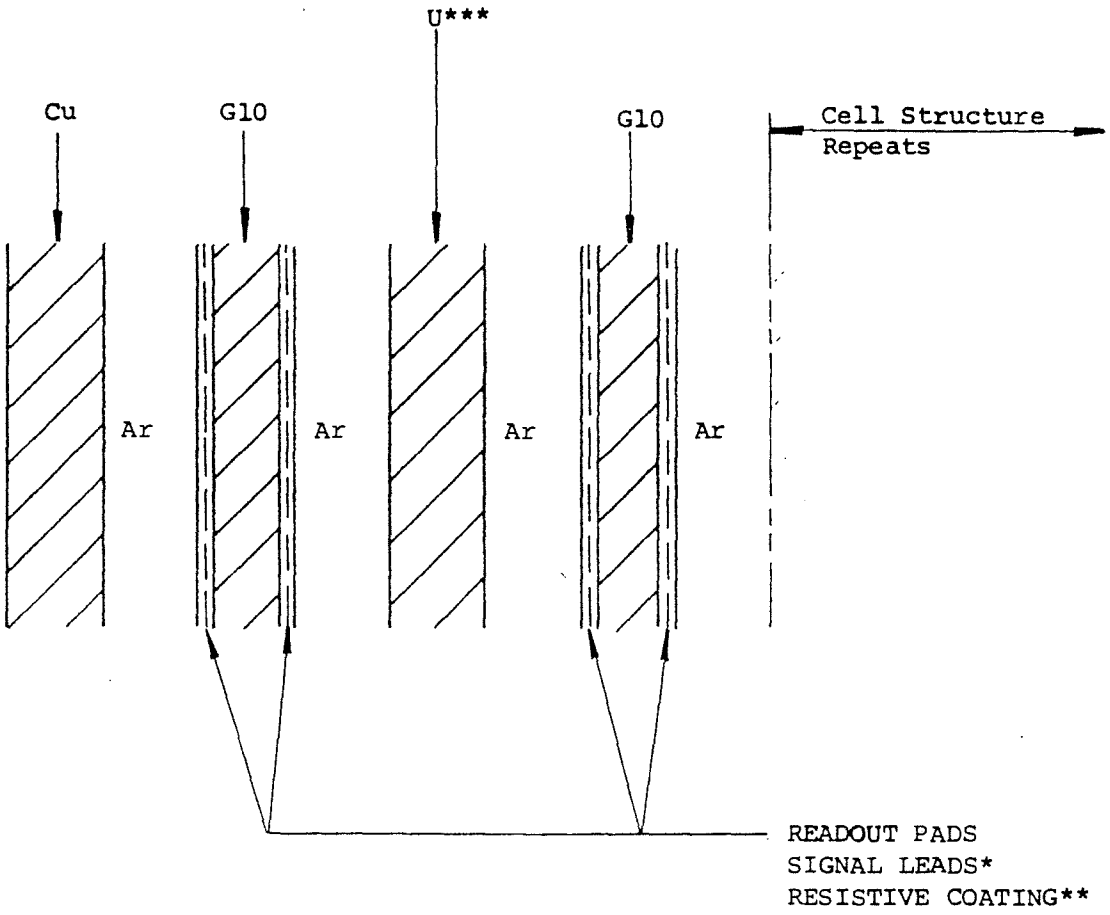

* Leads on the same side of G10 Boards as Pads

** Resistive Coating of graphite-chromium oxide mixture on thin mylar covering pads structure. Held at negative high voltage relative to the ground of the metal plates.

*** The coarse hadronic leakage section of the end caps have only copper plates.

SCHEMATIC SIDE-VIEW OF READOUT SEGMENTATION
END CAP CALORIMETER

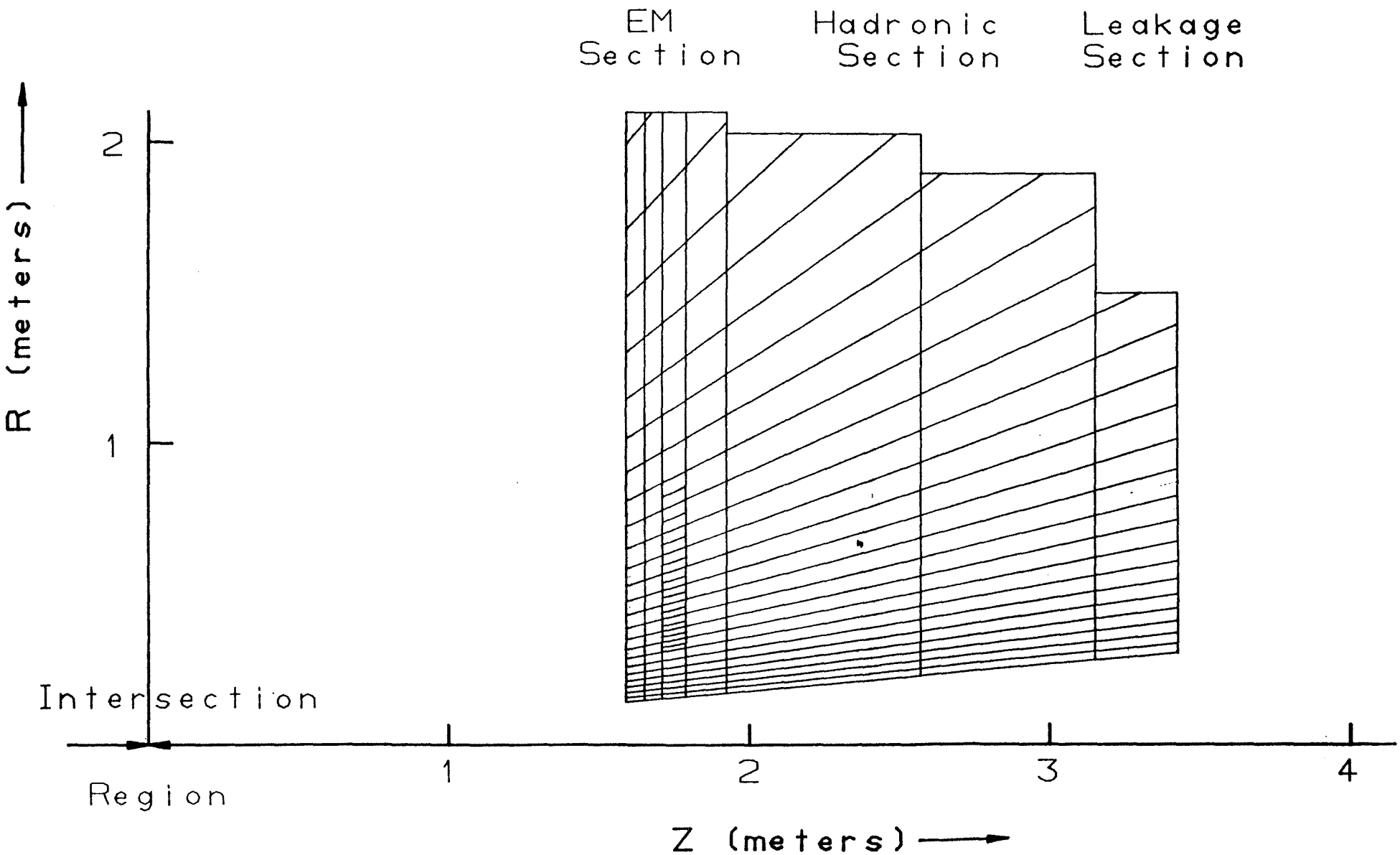

SCHEMATIC END VIEW OF PAD SEGMENTATION
FRONT FACE OF ELECTROMAGNETIC SECTION 1

$\Delta\eta = .1 \qquad \Delta\phi = .1$

INNERMOST EM PAD 1.5cm X 1.5cm

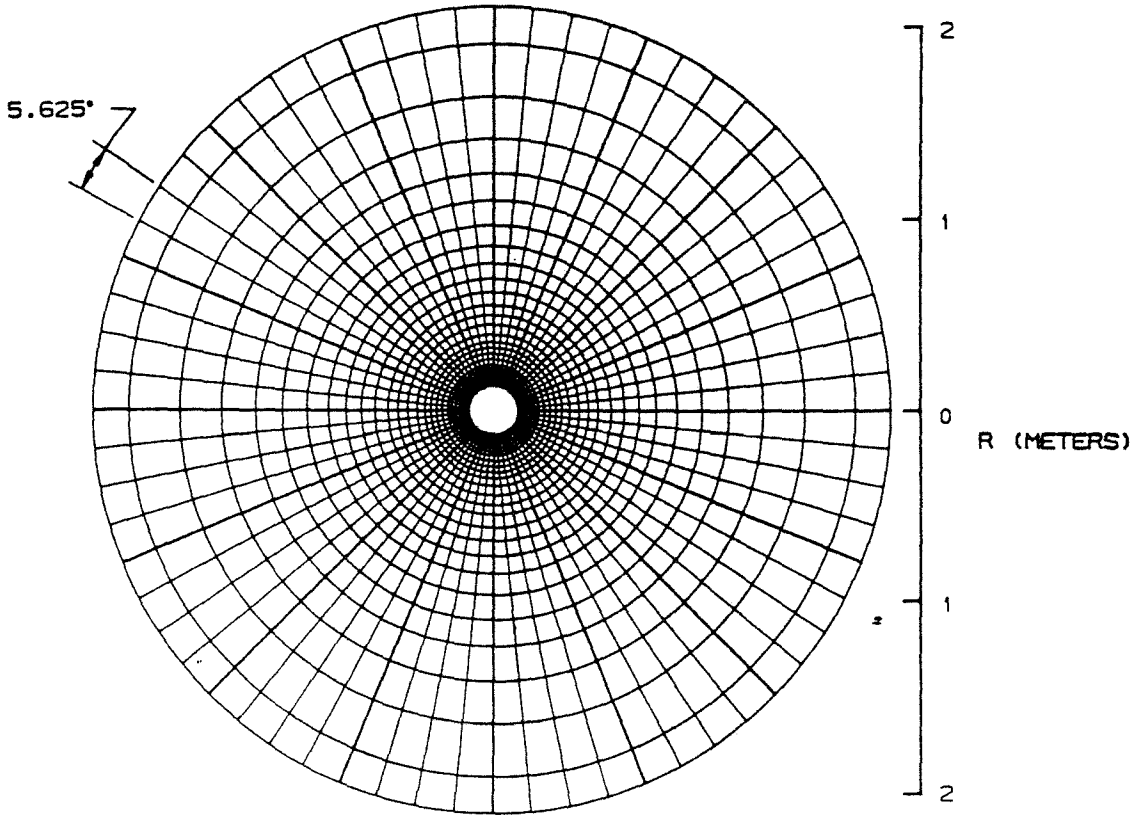

8. SCHEMATIC END VIEW OF PAD SEGMENTATION
FRONT FACE OF ELECTROMAGNETIC SECTION 3

FROM 10° TO 20° Δ = .05 Δ = .05
ALL ELSE Δ = .1 Δ = .1
INNERMOST EM PAD 1.5cm X 1.5cm

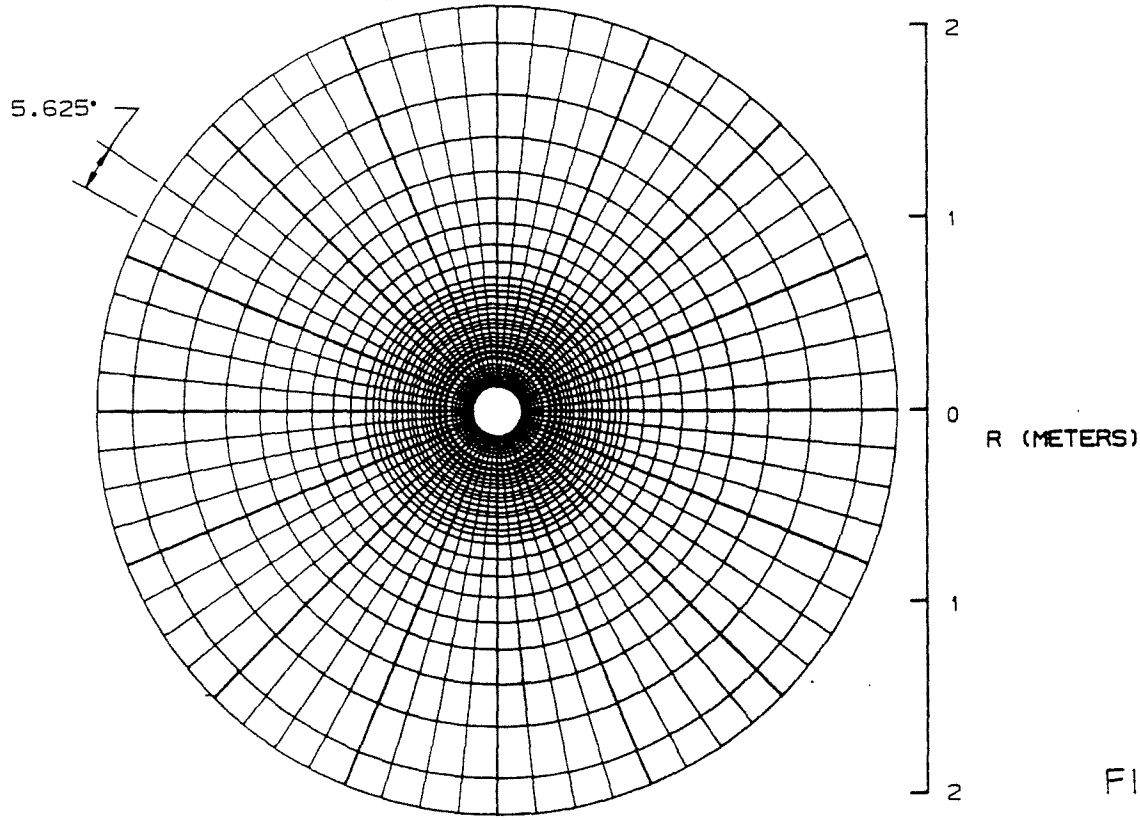

FIG. 5.16

84/10/11 16.09.51 96115

FERMILAB ENGINEERING NOTE | | Dø | PC-1 | 02.

PLUG CALORIMETER | WK, WS

CELL STRUCTURE

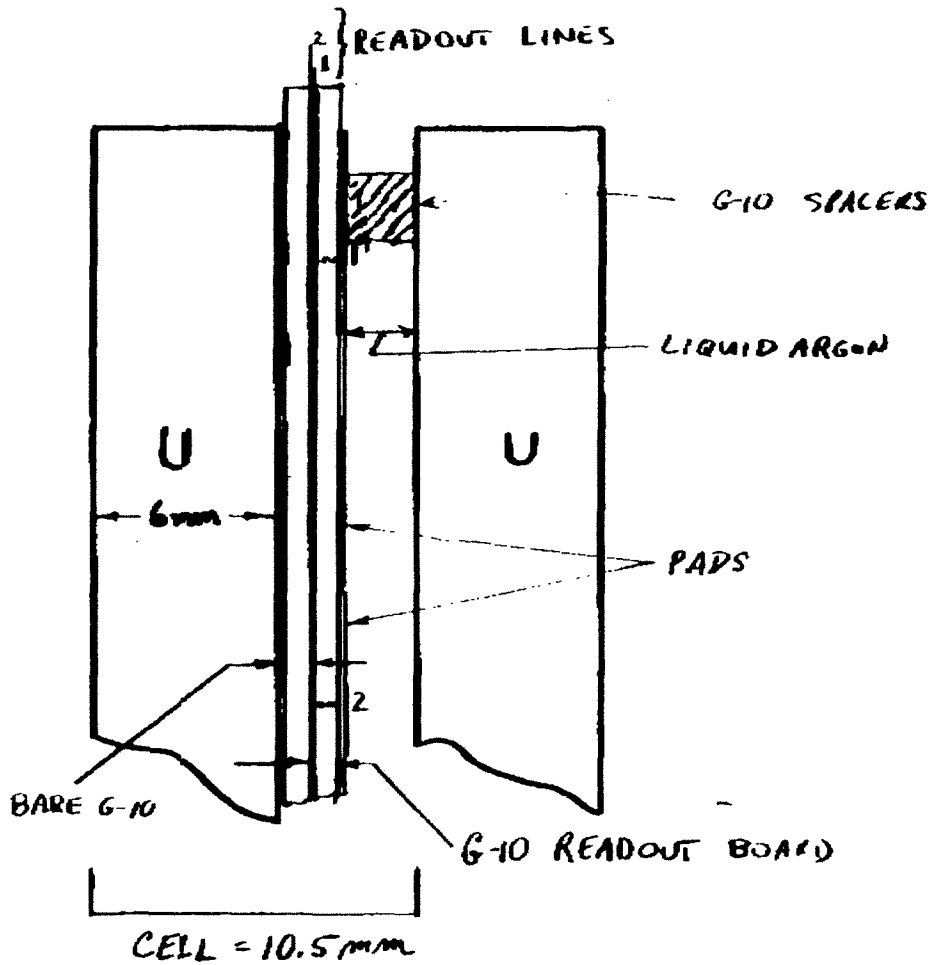

END PLUG
FRONT VIEW

PC-1-01

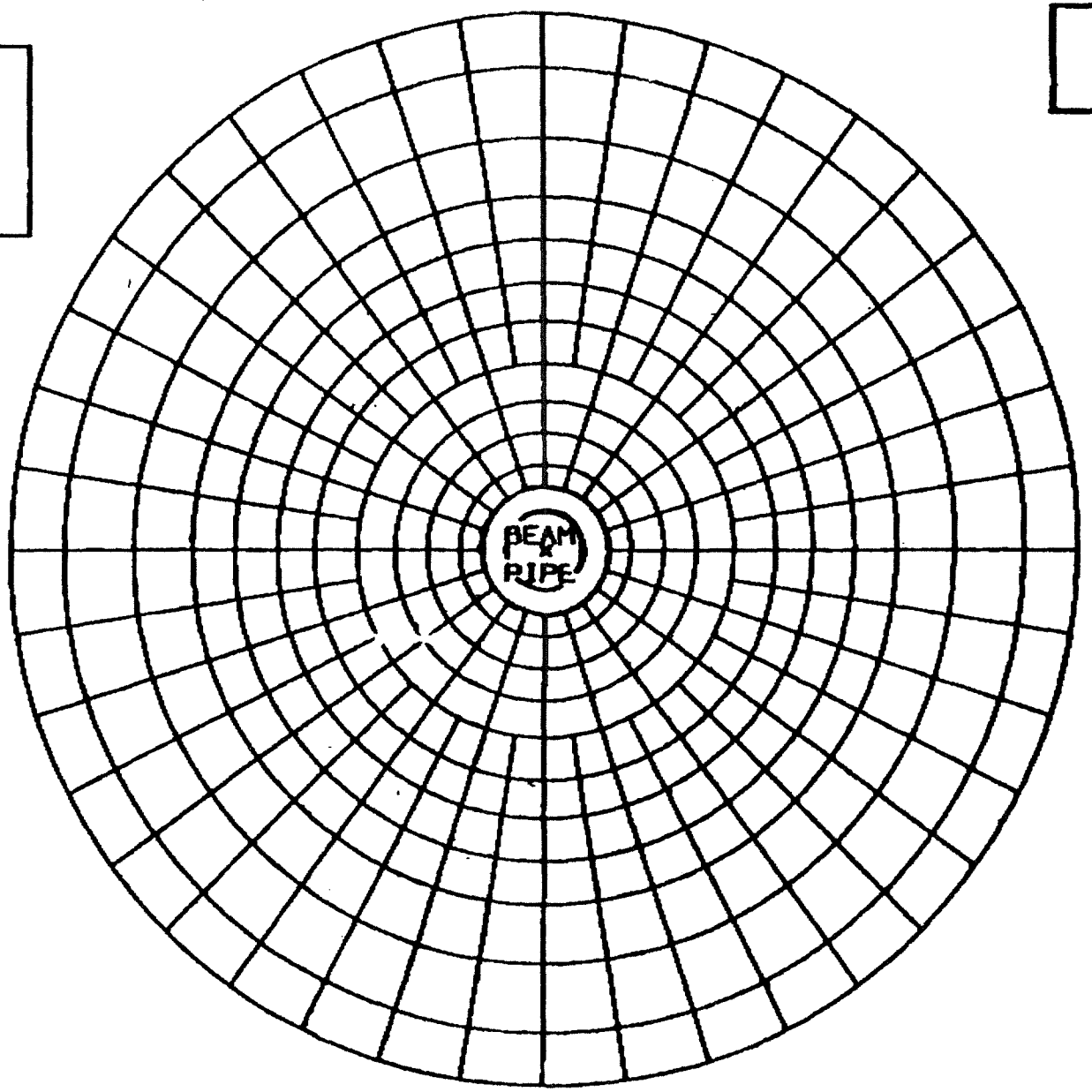

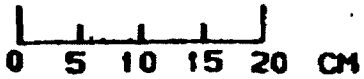

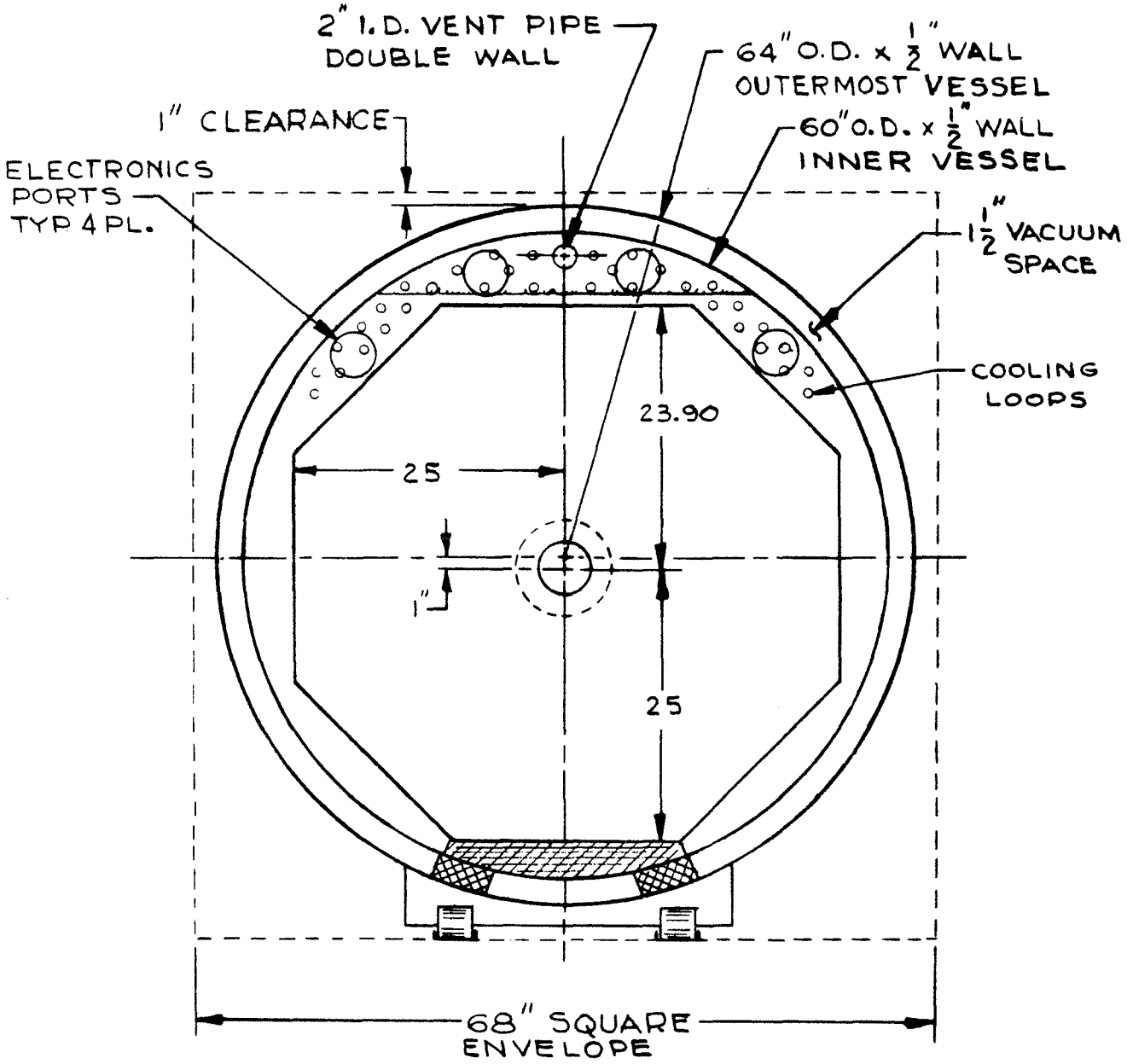

FRONT VIEW SECTION

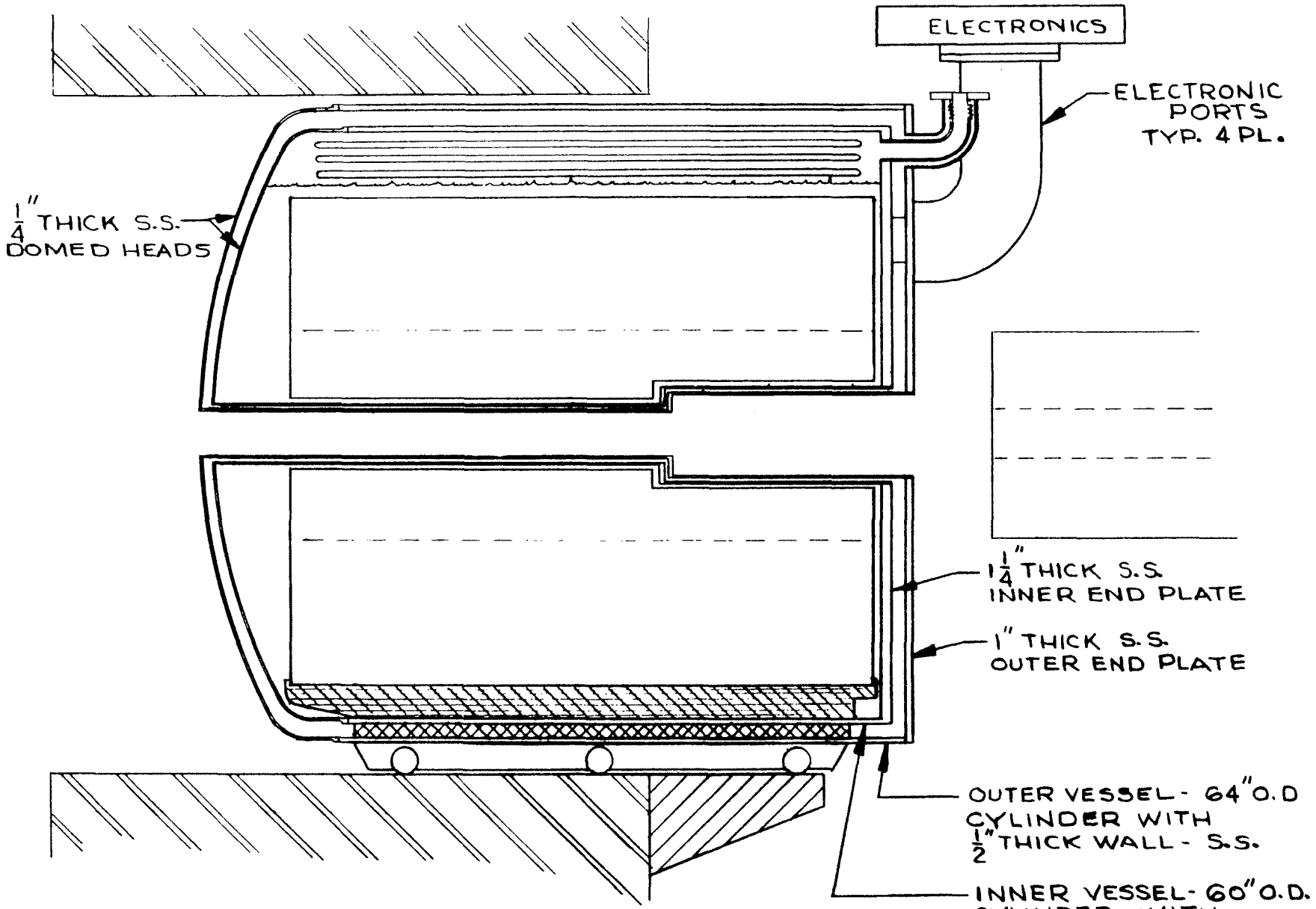

PLUG CALORIMETER
SIDE VIEW SECTION

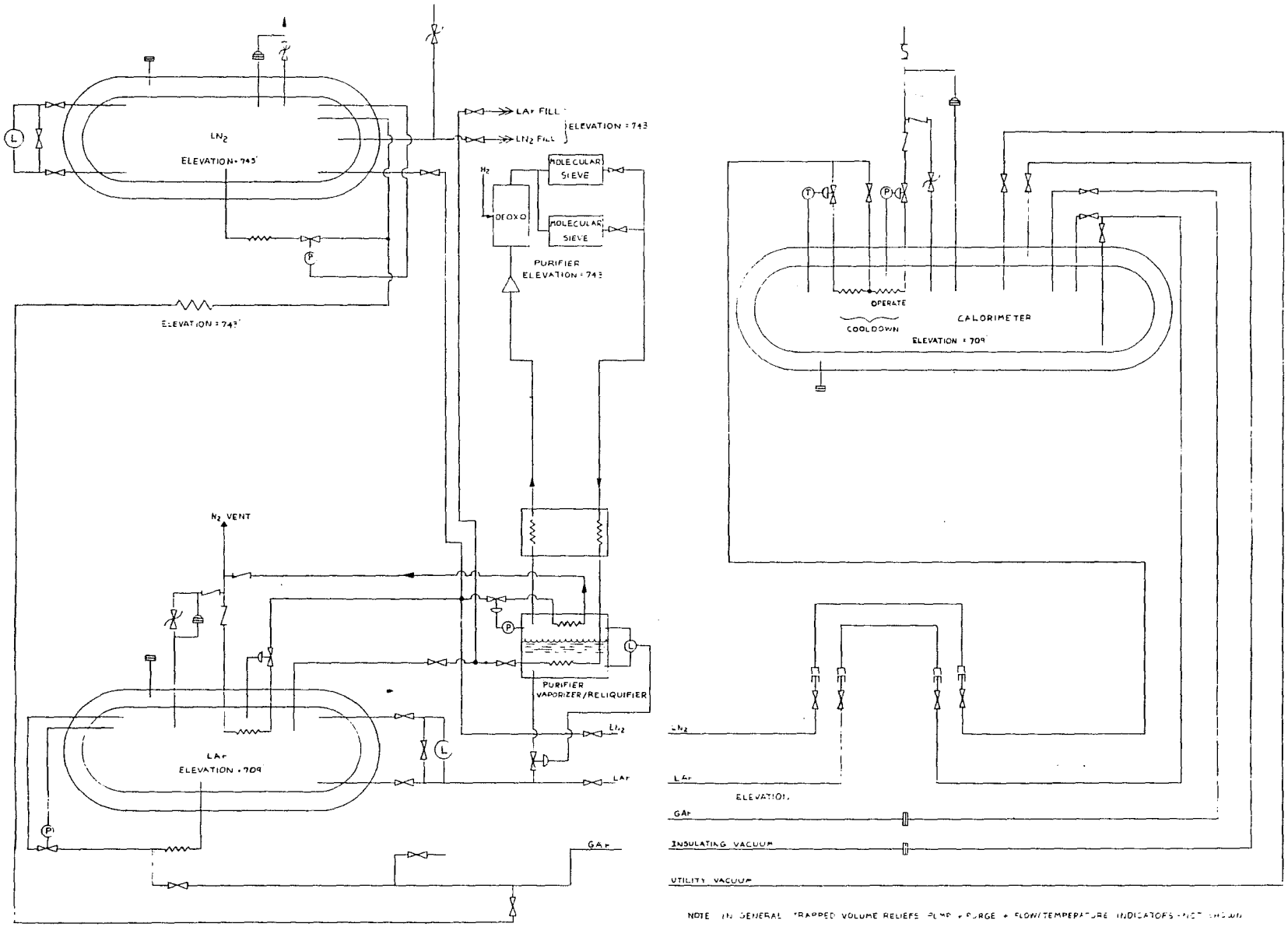

NOTE: IN GENERAL, TRAPPED VOLUME RELIEFS, PUMP + PURGE + FLOW/TEMPERATURE INDICATORS NOT SHOWN.

REV.	BY	DRAWN / APPD	DATE / DATE

ITEM NO.	PART NO.	DESCRIPTION OR SIZE	QTY. REQ.

PARTS LIST

UNLESS OTHERWISE SPECIFIED			DESIGNATOR	E P SMITH	5-11-64
FRACTIONS	DECIMALS	ANGLES	DRAWN	P E CALAHAN	5-11-64
±	±	±	CHECKED		
1. BREAK ALL SHARP EDGES 1/64 MAX.			APPROVED		
2. DO NOT SCALE DWG.			USED ON		
3. DIMENSIONING IN ACCORD WITH ANSI Y14.5 STD. MAX. ALL MACHINED SURFACES			MATERIAL -		

FERMI NATIONAL ACCELERATOR LABORATORY
UNITED STATES DEPARTMENT OF ENERGY

D-0 CRYOGENIC SYSTEM FLOW SCHEMATIC

SCALE	PLANO	DRAWING NUMBER	REV.
NONE			

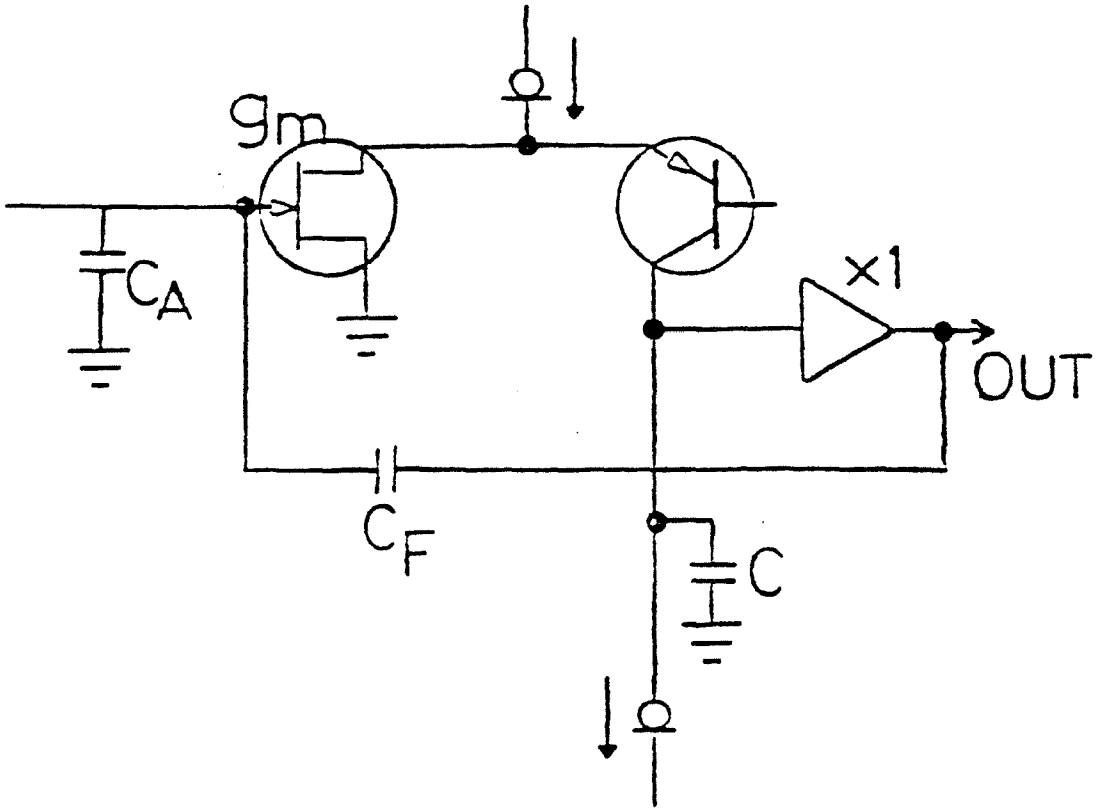
gm
CA
CF
C
x1
OUT

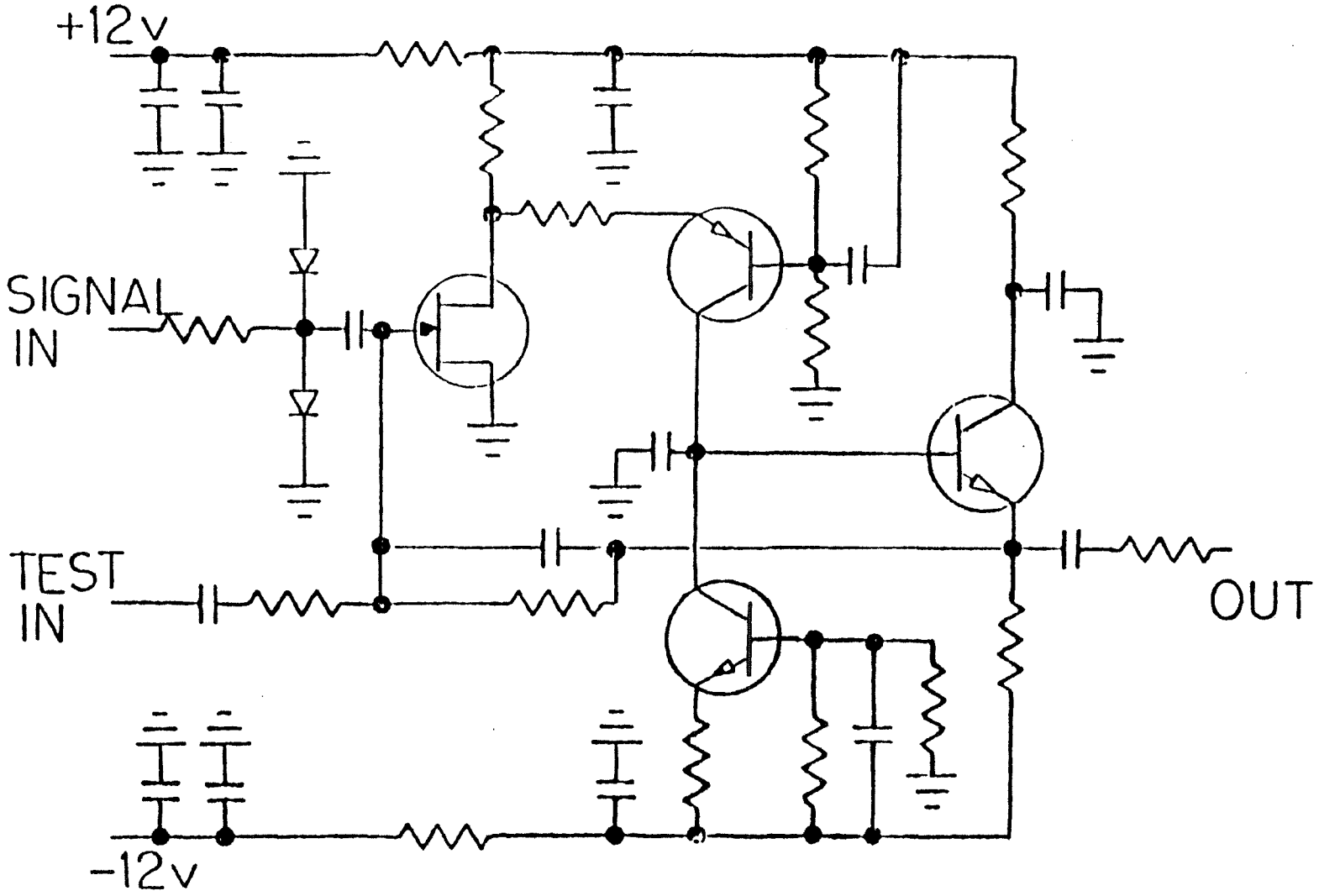
+12v
SIGNAL
IN
TEST
IN
OUT
-12v

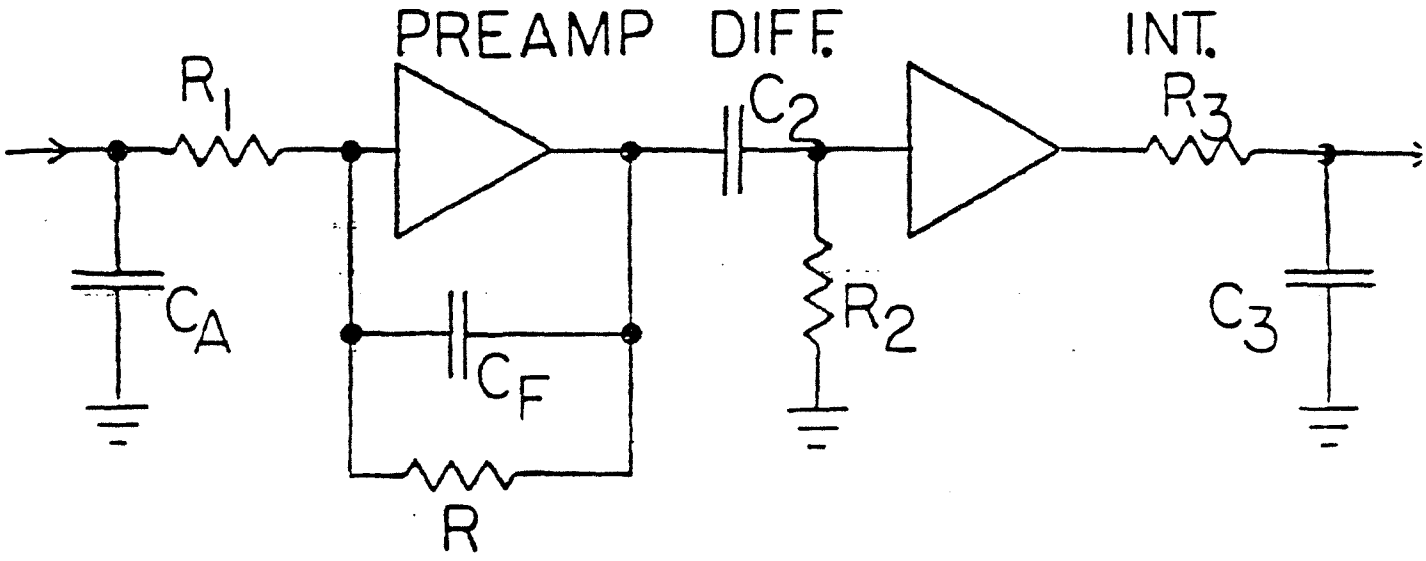
PREAMP
DIFF.
INT.
R1
C2
R3
CA
CF
R2
C3
R

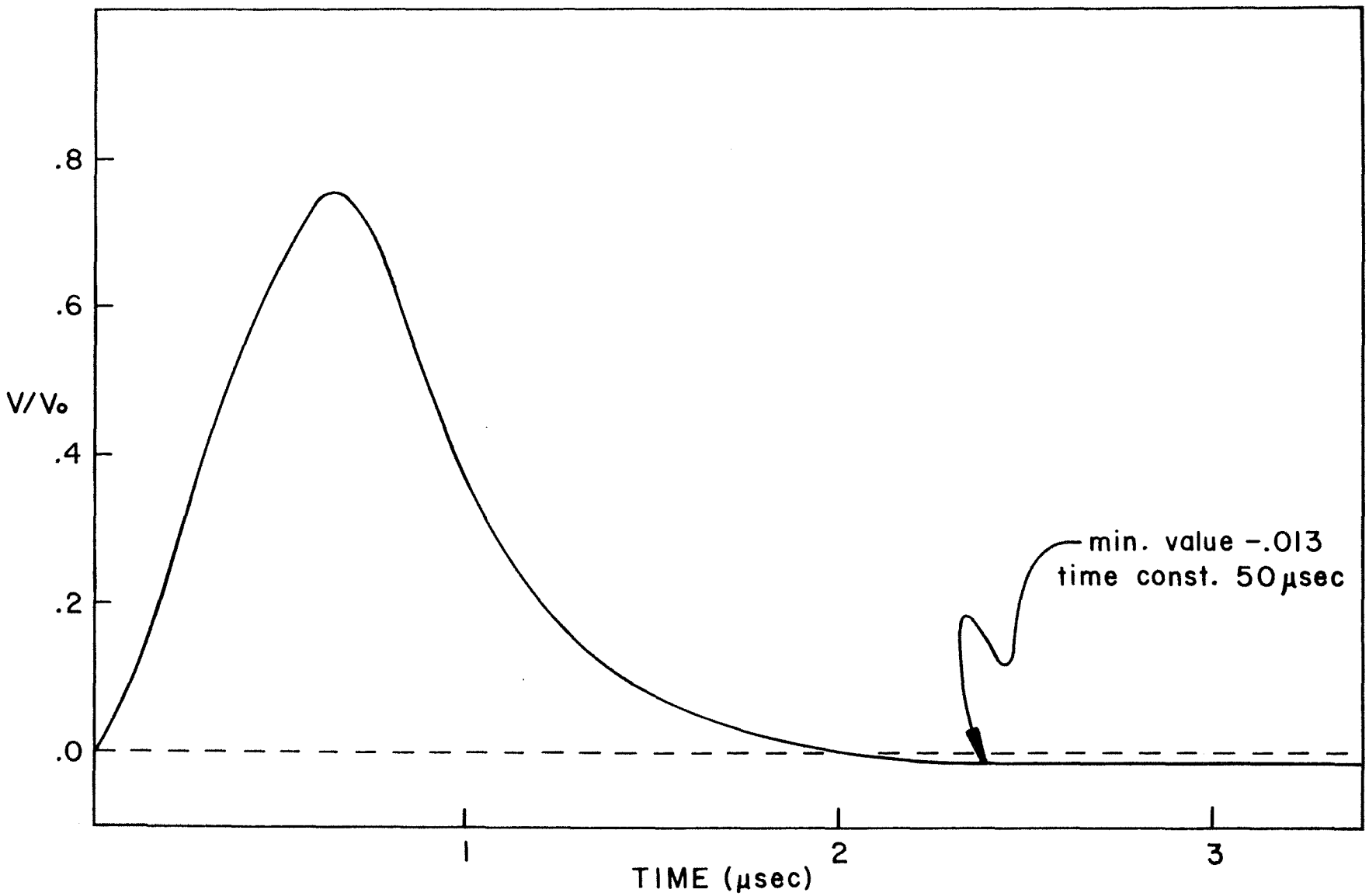
.8
.6
V/Vo
.4
.2
.0
min. value -.013
time const. 50 μsec
1
2
3
TIME (μsec)

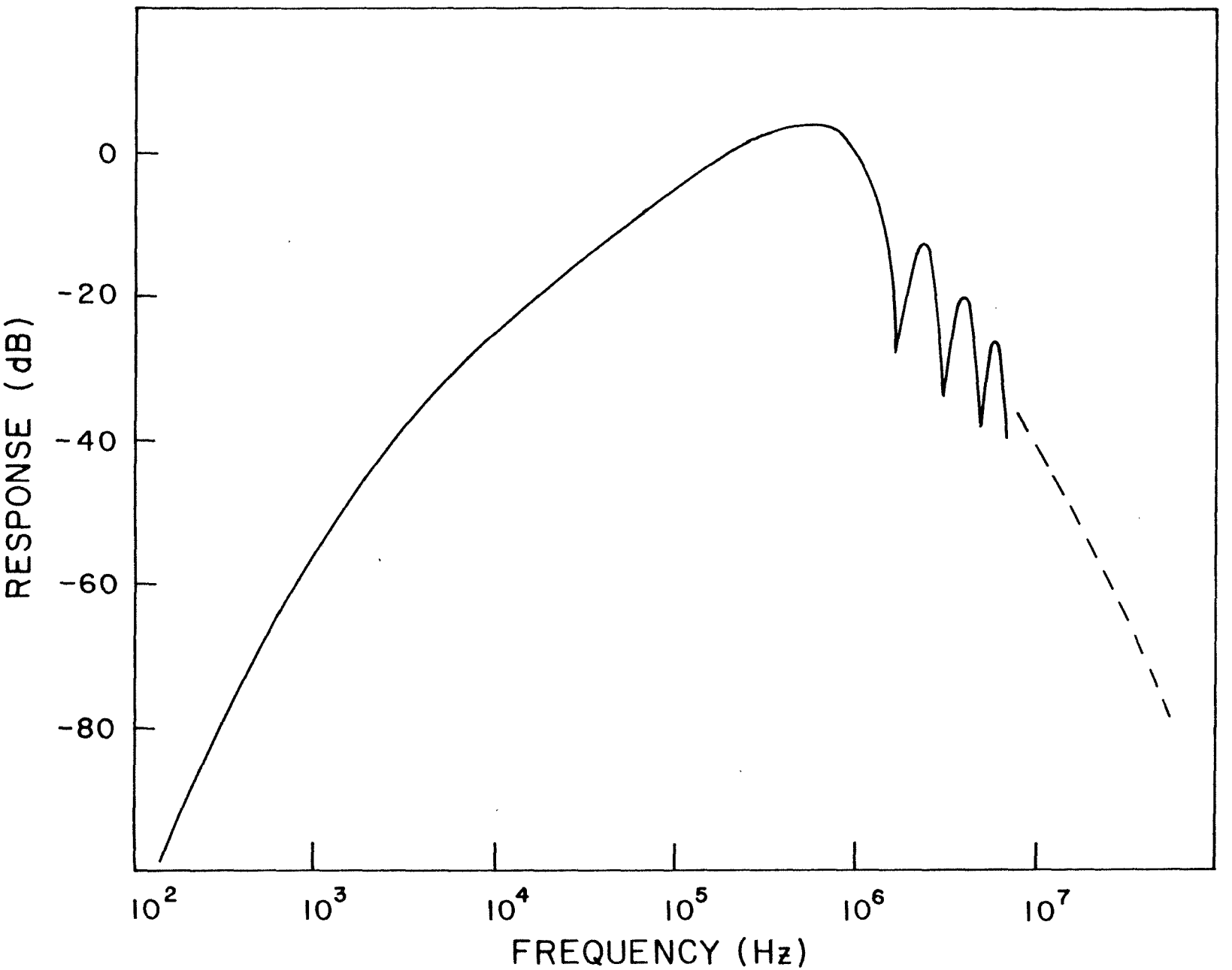
0
-20
-40
-60
-80
RESPONSE (dB)
10^2
10^3
10^4
10^5
10^6
10^7
FREQUENCY (Hz)

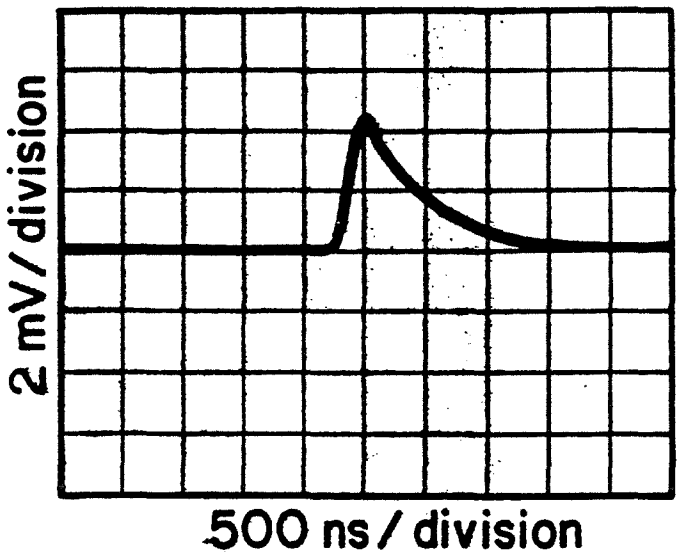

Liquid Argon Chamber Preamplifier Trigger Output for 80 MeV Total Energy Input.

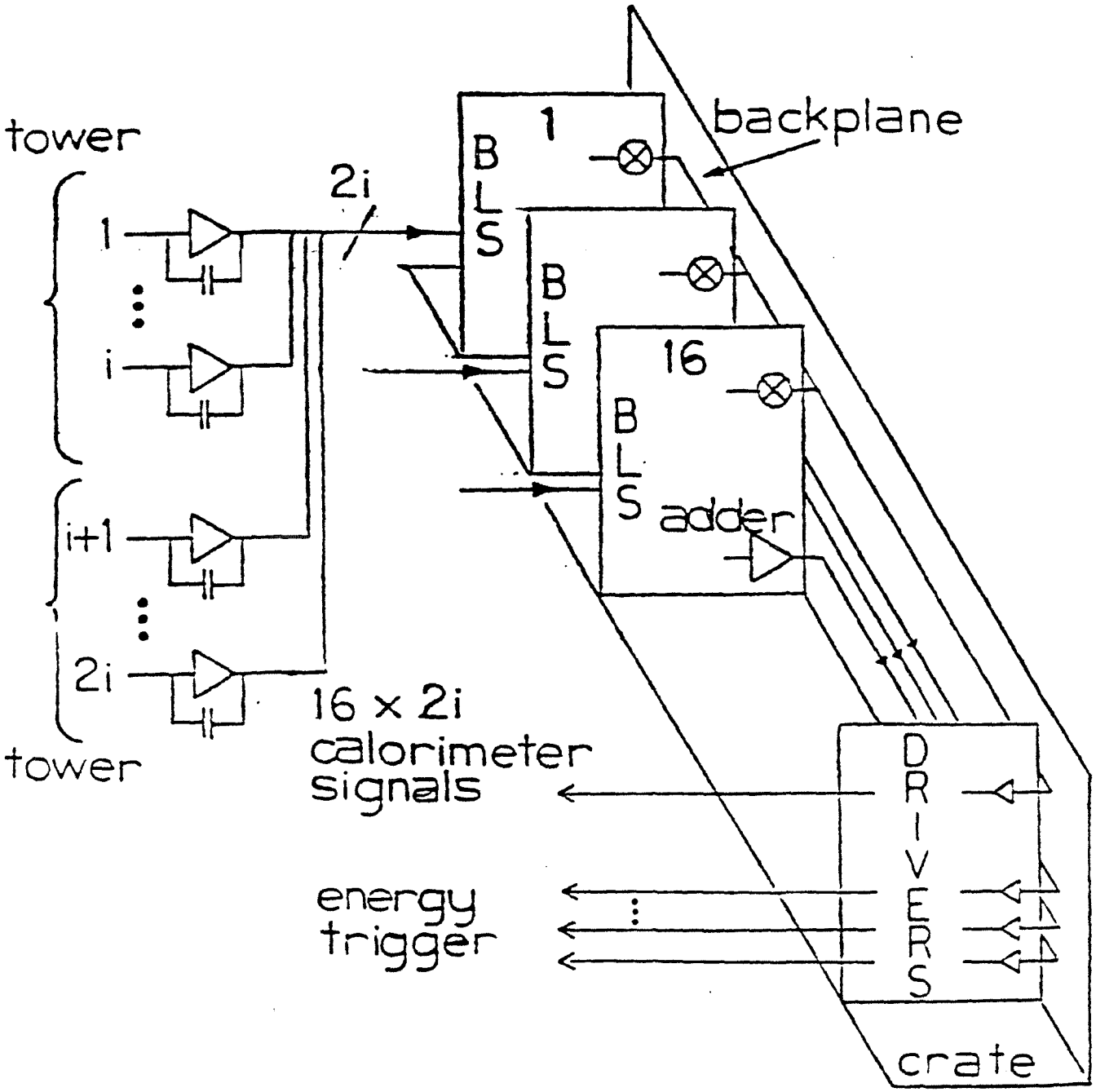
tower
1
i
i+1
2i
tower
2i
16 x 2i
calorimeter
signals
BLS
1
BLS
BLS
16
adder
backplane
DRIVERS
energy
trigger
crate

6. THE MUON DETECTOR

6.1. INTRODUCTION

In Chapter 2 we presented the physics justification for measuring leptons--both electrons and muons--as well as possible. In this chapter we describe a muon detector optimized to accomplish these goals within reasonable financial and space limitations.

The DØ experiment will study leptons from fundamental hard scattering processes at and beyond the electroweak regime, implying $p_T \gtrsim 50$ GeV/c for muons of interest. Since angles down to ~11° are covered, this implies the need to separate muons from hadrons at momenta $p \gtrsim 260$ GeV/c. It was decided to scale the depth of material such that the punchthrough probability is approximately independent of angle, and depends only on p_T.

An elevation view of the detector is shown in Fig. 6.1. Drift tubes before and after the magnetized absorber provide the trigger as well as track information. Vertex tracking for off-line analysis comes from the central tracking chambers described in Chapter 4.

There are three basic design criteria:

1. The iron must be thick enough to absorb showers effectively.
2. The $\int$Bdl coupled with the tracking granularity must provide momentum measurement errors smaller than multiple scattering up to at least 260 GeV/c. The transverse magnetic kick of the magnetized steel varies from about 0.6 GeV/c at 90° to about 0.9 GeV/c at 11°, the angular range of full muon coverage.
3. Occupancy in any muon tracking detector element must be low.

The result of optimizing the design to meet these criteria is a detector with 3820 tons of steel magnetized to 20 kG instrumented by 12,720 drift tubes. The criterion of having a momentum measurement constant in p_T implies a lever arm scaling as $1/\sin\theta$, while constant punchthrough, as a function only of p_T, implies an absorber thickness scaling as $\sim \ell n(1/\sin\theta)$. The final design is 13.3 λ_0 deep at 90° and 18 λ_0 at 11°. The punchthrough probability per incident track, throughout the detector, is then 0.3% at p_T = 15 GeV/c and 2% at p_T = 40 GeV/c.

As the angle drops below 11° it becomes increasingly difficult to satisfy these scaling requirements. Muon measurements are no longer attempted and the transition to the plug calorimeter (described in Chapter 5) is made.

6.2. MAGNETIZED TOROIDS

6.2.1 Basic Design Parameters

The overall view of the muon detector is shown in Figs. 6.1, 6.2, and 6.3. The muon detector is divided into a central portion (CF) and forward and backward end-sections (EF). There is a central magnetized yoke and two end-cap magnetized yokes, with their corresponding coils which form the central and end toroids respectively.

The basic parameters for these toroids are summarized in Table 6.1.

6.2.2 Steel Design

The iron yokes will be assembled from 10-in. thick grade 1020 low carbon steel. There is the possibility that some iron from the old S.R.E.L. Cyclotron, now at Brookhaven National Laboratory, might be available. In this case this high grade (somewhat radioactive) iron will be used for part of the yoke. The S.R.E.L. pieces could be used for the yokes of either of the two end-caps with a minimum of machining, or for the central yoke.

The central yoke has a rectangular cross section, and is composed of one long bottom base and two C-shaped clam-shells, as is shown in Fig. 6.3. These will be assembled from blocks weighing no more than 50 tons each. The end-cap yokes also have a rectangular cross section.

6.2.3 Coil Design

In order to gain the maximum momentum resolution for a given weight, the steel will be excited above 19.5 kG. This high excitation level requires the use of water-cooled coils. To save power, relatively low current density will be used for the copper conductor. The conductor was chosen to keep the total

power below 500 kW. The conductor chosen has a square cross section of 1.6 in. × 1.6 in. with a cooling hole of 0.6-inch diameter. The design current is 2000 A.

There will be 32 coils of 10 turns each for the central toroid and 16 coils of 8 turns each for the end-cap toroids. All are one layer coils and their heights are 16 and 13 in. respectively. Both coil sets will cover 55% of the inner surface of their toroids, and the remaining open surfaces will be used for mounting proportional drift tubes and the end-plug calorimeter. The total amount of copper will be 120 metric tons. The 1.6-in. copper conductors can be bent and brazed together, and will be insulated with thermal-curing epoxy fiberglass tape. All coils proposed here are removable and can be prefabricated for quick installation during magnet assembly.

With the total power of 442 kW for the coils and some power for the bus bars and leads, one 500 kW power supply will be used, and all coils will be connected in series. To reduce the electrical noise to the calorimeter preamplifiers, a regulated transistor power supply will be used.

6.2.4 Magnetic Flux Calculations

The calculated flux distributions for the central and end-cap toroids are shown in Figs. 6.4 and 6.5, respectively. At 2000 A, the flux inside the straight part of the central toroid is 20.0 kG uniformly across the yoke width. The stray field at the location of the main ring beam is 9 Gauss. This can be easily shielded with soft iron sheets around the main ring beam pipe.

The flux distribution in the end-cap toroid is slightly less uniform as shown in Fig. 6.5. The flux in the straight sections next to the window is fairly uniform but the flux at the corner is decreasing rapidly in the radial

direction. It will be necessary to do flux mapping for all toroids at the 5% level. The flux integrals along straight rays coming from the vertex will be obtained by induction loops embedded in the iron.

The magnetic field inside a 15 in. diameter hole for a main ring beam penetration of EF, is about 550 Gauss without any shielding. This field could be reduced to less than 0.1 Gauss with a magnetic shield of 1 cm thick mild steel and 0.5 cm thick mu-metal.

6.2.5 Assembly of Toroids and Detector Support System

The toroids will be assembled in place on the detector platform, 39 ft wide by 45 ft long, in the D0 assembly hall. The completed toroids and platform then form the skeleton on which the active detector elements are mounted. The platform I-beam weldment must hold the base of the toroids about 104 in. above the floor. It must also distribute the 4700-ton load of the assembled detector onto the heavy-duty rollers that will enable the detector to roll in and out of D0. This platform will be assembled first, and then the toroids on top of it. Figure 6.6 shows one stage of the assembly.

The arrangement and assembly of the 10-in. steel slabs of the toroid will be chosen to minimize machining and welding. Tolerances are important at the mating machined surfaces crossed by lines of magnetic flux and at some reference surfaces. Since the assembled toroids and platform form the structure for all further detector assembly, it is important that this assembly procedure be straightforward and rapid.

6.2.6 Maintenance and Access

The central toroid will be built with a clam-shell structure enabling the two halves to separate horizontally. The end-cap toroids will slide parallel to the beam over the low beta quads. The plug calorimeter, mounted on rails in the hole of the end iron, will stay fixed in position, while the end iron moves under it. This will allow the end-cap calorimeter to be moved away from the intersection point into the place vacated by the retracted end-cap toroid. Full access to the end-cap calorimeter and to the central tracking chambers and central calorimeter will then be possible. The maintenance on the toroids and muon chamber system itself should be minimal. The muon chambers will clamp rigidly (and reproducibly) to the toroids thus allowing removal, repair, and alignment procedures to be simple and quick.

6.3. MUON PROPORTIONAL DRIFT TUBE SYSTEM

6.3.1 Muon Proportional Drift Tubes (PDT)

The instrumentation to register charged particles exiting the iron serves two functions. First, relatively crude but fast position correlations are needed to satisfy the first level trigger requirements. In particular, a rough p_T cut must be easily obtained from the bend angle in the steel. After the first level selection, coordinate digitization must provide precise locations and bend angles for further analysis. Since the first level trigger requires a decision between beam crossings, the size of a drift tube is limited to about 4 in. In all locations, as discussed in Chapter 7.2, this size is well matched to the first level "road" size requirements. This is accomplished by scaling the lever arm approximately as $1/\sin\theta$.

Many designs exist which provide accurate drifting over 4 in dimensions. Drift chambers with simple box structure cells have been built[1] which gave excellent test beam resolution (300 microns) and were self supporting in sizes up to 13 ft × 13 ft. The cell cross section used was 3 in. × 1.5 in. with a single central wire and no field shaping. Planes of crossed cells were bonded together to give rugged units with fixed relative alignment. The major problem with this design was the fact that the electron drift velocity was not saturated, leading to time dependent drift velocities different for each tube and an effective system resolution of 1 mm. We propose a similar cell, 4 in.×1 in., with an added electrode for field shaping which will solve this problem. The intermediate voltage electrode yields a reasonable drift distance vs. time relation over a wide variety of voltages even for this asymmetrical cell as is discussed later in this section.

Crossed planes are extremely difficult to use within the moving table. They are also difficult to fit within the tight constraints on space between CC and CF. For this reason we have adopted a vernier pad readout[2] of cathode induced pulses. This scheme, illustrated in Fig. 6.7, employs cathode pads cut into a series of connected triangular wedges. The charges collected from two such nested wedge pads can be used to determine the coordinate along the wire, modulo the wedge length, as described below. In our design there are two such cathodes, one above and one below the wire. One has wedge length equal to the full length and determines which of the smaller wedge segments is to be used for the precise coordinate determination. The Charpak group has obtained a resolution of 1.9 mm (FWHM) for a 30 cm. wedge length.[3] Other advantages of this solution are a reduced wire count and the elimination of ambiguities inherent in crossed plane hodoscopes. Our proposed solution produces space points. The pad solution, as contrasted with current division on the anode wire, puts all connections at one end, which greatly eases problems of space and access. The induced signals on the tapered pads can be digitized with a slow multiplexed ADC system similar to the liquid argon calorimeter ADC system.

Prototype vernier pad cells have been constructed and tested in a test beam and, more recently, using cosmic rays. The cosmic ray test stand consists of triggering scintillators, and small-cell crossed plane, tracking PDT's. A schematic of a test cell is shown in Figure 6.7a. The approximate vernier pad charge sharing which is expected[4] is described as follows:

With reference to Fig. 6.7a, let L, W be the length and width respectively of the vernier pad, split into sides A and B by a straight diagonal line. An anode wire is placed at height, a, above the pad, and has a charge, Q_0; y is the distance along the PDT cell that one wants to measure. The

angles θ_1 amd θ_2 are defined by:

$$\tan \theta_2 = W/2a$$

$$\tan \theta_1 = yW/La.$$

The induced image charge on the pad is split between the two sides:

$$Q_A \simeq Q_0/\pi \ (\theta_2 - \theta_1)$$

$$Q_B \simeq Q_0/\pi \ (\theta_2 + \theta_1).$$

From this:

$$\frac{Q_A - Q_B}{Q_A + Q_B} = \Delta Q \simeq \theta_1/\theta_2 \simeq 2y/L.$$

ΔQ is only approximately linear in y if the boundary between A and B is a diagonal straight line. Clearly this boundary can be designed to produce linearity. If the pad amplifiers are dominated by noise then the error in ΔQ scales as $1/\theta_2$. This consideration favors a large cell aspect ratio.

The test PDT was operated with 50% argon/50% ethane. The cell size was 1 in×4 in with "I" beam field shaping. The wire was 50μm gold plated tungsten. The PDT was operated in proportional mode and the expected wire signal was ~2μA. The capacitances were 70 pF/m for the wire and ~300pF/m for each pad signal.

In the tests the gas gain was set by defining the wire-to-pad voltage to be 2.8 kV. Then the gas saturation was studied by raising the wire and pad voltage together. The results, shown in Fig. 6.8, imply gas saturation for $\lesssim$ 2 kV. We chose 3 kV to be safe. The resulting drift time vs. position and incident angle are shown in Fig. 6.9. Clearly saturation of the drift velocity was achieved as expected from electrostatics calculations. The resolution, as shown in Fig. 6.10, is 1 mm FWHM, a reasonable result which was limited by the alignment of the test chambers.

Using the cosmic ray test setup, a prototype PDT with a triangular cathode pad array has been evaluated. The cathode pads are 12 in. long. Figure 6.11 shows the difference of the amplified pad signals (normalized to the sum) as a function of position along the PDT traversed by the cosmic ray. The resolution achieved so far is ± 5mm, primarily limited by amplifier noise pickup due to inadequate shielding. Longer prototypes, with two sets of pad arrays (Fig. 6.7b) are under test. By using long pads as well as short pads, the need for charge division on the PDT anode wire is eliminated. All electronics can thereby be set on one end, simplifying nesting and cabling.

In the design described here each detector plane will consist of a double layer of PDT cells offset by one-half cell to eliminate the left-right ambiguity of a single drift wire. It is necessary to minimize the construction cost and assembly time of this two electrode PDT. We are currently investigating the possibility of using an aluminum extrusion for the basic cell walls and an inexpensive plastic insert with copper tape vernier pads for the intermediate electrode as shown in Fig. 6.12a. A special end extrusion, as shown in Fig. 6.12b, would provide the mechanical alignment of the two planes of offset cells. It would also allow accurate wire positioning for a multi-cell, 2-plane module, and would complete the three dimensional structural rigidity of the assembly.

The final configuration and design of the muon PDT's will be determined after extensive Monte Carlo runs using ISAJET with the results from our Spring 1984 test run. The test run measured hadron punchthrough in an array of absorbers and magnetized iron comparable to the calorimeters and iron in the detector. A description of the results of that test is in section 6.4.2.

6.3.2. PDT Front End Electronics

One fast signal from the wire and four separate slow signals from the pads, two from the top and two from the bottom, must be processed. The wire presents a large signal but needs high bandwidth readout to achieve the required time resolution. The pads need very low noise readout to preserve y resolution, but do not require large bandwidth since their information is not used in the first level trigger.

An overview of the front-end electronics is shown in Fig. 6.13 for 16 PDT's. The multiplexed signals from 64 PDT's are routed through line drivers to the ADC system. There are four analog signals from the wedges and two time to voltage converted (TVC) outputs since double-hit capability is provided on each PDT wire. In addition, the address of each PDT wire which received a hit is passed to the first level trigger system.

A portion of the analog board which processes the signals from the wedges of one PDT is shown in Fig. 6.14. Each pad is connected to a low noise, charge sensitive amplifier. This integrated charge is presented to a shaping network which produces a psuedo-Gaussian pulse with a FWHM of approximately 5 μS. A sample/hold circuit stores the magnitude of the pad charge until such time as the information is read out. No information is lost in this scheme. The multiplexed ADC system accesses the pad data via a series of analog switches. By multiplexing the data in this manner the cable requirements for the PDT system is reduced by a factor of 64.

The fast wire signals require more sophisticated signal processing, while the slow analog data is relatively inexpensively logged. The wire is connected to a broadband preamplifier and a fast shaping and line driving network. The shaping network clips the signal very short (20 nsec) in order to achieve

good two hit separation. At this point the wire signals are transmitted on a short cable to a separate, but locally situated, fast board.

A portion of the 16 channel fast board which processes the signals from 4 of 16 PDT wires is shown in Fig. 6.15. The signals are first discriminated and brought up to logic level. From here they are routed to two subsections on the board. On one section signals are latched, then priority encoded hit addresses are passed to the first level trigger system described in section 7.2. The other section of the board contains 16 time to voltage converters (TVC's) with two hit capability. The dual hit TVC for one of 16 PDT's serviced by the fast board is shown in Fig. 6.16.

A two-hit TVC is chosen because of the measured δ ray problem as seen in our test beam data. Note that all signals are in analog form, and interface easily to the calorimeter analog readout. Hence both the muon and calorimeter systems achieve a high level of standardization. We will use a simple subset of the calorimeter ADC system with 10 bit instead of 14 bit ADCs and a faster cycling time since the muon system is multiplexed by 64 rather than 16. One crate of ADC's with 256 inputs would process signals from 4096 PDT's. ($64\times256/4$). Hence the entire PDT system will require about 3 ADC crates.

We are investigating hybrid circuits and quasihybrids to replace some of our multiple component subsystems. If they prove cost effective they will be used.

6.3.3 Chamber Placement and Coverage

The purpose of the muon drift tube system is:

to permit triggering on single muons above a selectable minimum transverse momentum with an acceptable trigger rate,

to reduce of cosmic ray muon triggers to an acceptable level,

to provide an off-line momentum resolution close to the multiple scattering limit,

to provide almost hermetic coverage of muon detection down to a minimum polar angle (11°),

and to provide a signature of muons above a certain minimum p_T in areas where, for engineering reasons, the coverage is impaired.

These requirements are based on the physics goals of reasonable momentum resolution for most muons, combined with accountability for as many muons as possible in interesting events. Knowledge of the transverse momentum carried by the muon(s) is necessary to infer the missing momentum possibly due to neutrinos in such events. Good muon accounting is also required to be able to study interesting multilepton events.

Chambers are arranged in three major shells: the inner planes CMA (Central Muon, plane A) and EMA (End Muon, plane A) cover the inner surfaces of the major steel pieces. Their purpose is to measure a (short) track segment prior to the steel. This segment improves the momentum resolution of muons of lower energy by remeasuring the muon direction after the muon has undergone multiple scattering while traversing the central calorimeters. This segment also extends recognition of muon tracks that have been seen outside of the steel, but which may have been lost in the central tracking chambers because they were embedded in a hadron jet.

The next planes, CMB and EMB, cover the outside of the major steel pieces. CMB and EMB provide a short track segment which points at the outermost layers, CMC and EMC. The CMB-CMC and EMB-EMC pairs provide an accurate track angle determination to determine the muon momentum.

The following sections describe in detail the different portions of the muon chamber system. The integrated layout is shown in Figs. 6.1, 6.2, and 6.3. These figures show an ideal, hermetic detector. It is recognized that as engineering design of services (cables, cryogenics, supports) becomes more

specific, some chambers may have to be reduced in size or split in various ways. The effect on the physics of each such change will be evaluated by Monte Carlo simulation.

6.3.3.1 The Central Inner Layers. The central A layers (CMA) are assembled in 4-layer modules, each of which covers one-quarter of an inside face of the toroid. The top and side modules will be supported by precision rails on the steel, located between the CF coils. The top chambers are bisected to allow insertion and retraction of the modules in a situation where the actual support points cannot be reached. While one will probably survey the chamber locations after each move, they are expected to return with sufficient accuracy to their previous locations.

6.3.3.2 The Central B Layers. The central B layers cover the central iron and the outer edges of the end iron and are attached to CF. They split along a line parallel to and above the beam line when CF clamshells open.

The central B layers will form a mechanical, pre-aligned unit with the central C layers, which will mount on the outside of CF. This reduces the necessary number of alignment constants. CMB and CMC each consist of three decks.

The bottom B layer is interrupted by the roller tracks for the central iron, CF. Since all PDT wires run parallel to the magnetic field lines for optimum resolution, this segmentation does not increase the wire count. It does, however, increase the number of different types of modules. The bottom B layers will fit in slots created by an "H" shaped support member under the roller tracks in order to minimize any holes in the coverage.

6.3.3.3 The Central C Layers. The C layers consist of three planes. As mentioned above, the top and side face CMC planes are attached to their

corresponding B layers, and form mechanical units with them. The bottom C chambers are segmented by the support beams and nestle between them.

A particularly difficult place to cover is the edge of the "sidewalk", where the end iron (EF) approaches closely to the concrete. This leaves little lever arm for muon tracking. With the arrangement shown in Fig. 6.1 we assure that each muon passes at least through a set of more narrowly spaced planes, enough to tag the presence of a potentially high p_T muon. If this tag exists in a interesting event, this event will have to be discarded. The procedure is equivalent to a small loss in luminosity for those events, which is far better than having some events contaminated with unknown momentum muons.

6.3.3.4 The End Inner Planes. The end inner planes (EMA) are made from two double planes, spaced by five inches, and forming a pre-aligned unit. The chamber layout pattern is shown in Figs. 6.1 and 6.17. The layout is constrained by the narrow space allowed for this set (24 inches minus 6 inches for a cable gap and 3 inches for the EF coil, leaving 15 inches for the chamber assembly.) This lack of space makes overlapping impractical; consequently there are small cracks between adjacent sub modules. The cracks in one plane are covered by the chambers in the other plane as seen in Fig. 6.17.

The outer size of the EMA planes is constrained by the desire to leave a 6 m gap for cable passage between the planes and the CF coil ends.

6.3.3.5 The End B Planes. The EMB planes are constructed from two double planes, spaced by 14 in. This spacing is constrained by the need not to exceed the length of the table, and to allow table removal without interfering with the low beta quadrupoles. The spacing of these planes is needed to allow accurate pointing to the EMC planes in the presence of higher chamber occupation at the smaller angles.

Figure 6.18 shows the layout of individual modules. There are two "frames" of chambers, an inner frame and an outer frame. This division eliminates the need to have wires run from small angles to large angles. The congested small angle region (inner frame) is kept separate from the cleaner outer region. It will be easy, for instance, to trigger only on wires in the outer frame initially, until the detector is better understood.

All planes overlap by a small amount. This helps not only to avoid cracks in the muon coverage, but also affords an easy way of aligning modules to each other using event or cosmic ray tracks.

6.3.3.6 The End C Planes. The EMC planes consist of one double layer of proportional drift tubes. Each plane is again arranged in two frames, an inner frame and an outer frame. The two frames are placed at different distances along the beam, the outer one being closer to the interaction region as shown in Fig. 6.19.

The reason for this is two fold. First, the end wall of the collision hall has large air duct openings along each side for almost the full height. There are also personnel access stairwells ending there. Secondly, by placing the outer frame closer to the vertex, one regains some of the long lever arm coverage in the 40° to 50° polar angle region. At the same time, the lever arm beyond 20° is still sufficient out to the largest p_T values one can expect.

Because of the interference with the low beta quadrupoles, it is difficult for the EMC planes to be attached to, and moved with, the main body of the experiment. The EMC chambers may have to move on a separate rail carriage. The ideal solution is to telescope them into the main body of the detector.

6.3.3.7 Wire Count and Dimensions. Table 6.2 lists all chamber dimensions and wire counts. The totals are:

Central chambers	8280
End chambers	4440
	12720

In summary, in the bend coordinate we will have 4 points before the steel and 6 points after the magnetized steel. In the non-bend coordinate it will be sufficient to read the pads on only half the chambers. This gives, in the non-bend coordinate, 2 points before the steel and 3 after. Clearly, if it proves necessary, additional analog boards could be obtained to instrument more of the pads. Therefore, the total number of analog channels required per PDT is 4 (2 slow analog for pads [4 on only 1/2 the chambers] and 2 hit TVC's) for a total channel count of 50648. Table 6.3 lists some of the physical parameters of the chambers.

6.3.4 Alignment

It is necessary to know the position of each wire in the muon PDT system to an accuracy better than the expected spatial resolution (0.3 mm transverse to the wire, a few mm along the wire.) There are also large areas where the muon tracks traverse the planes at angles near 45°. In those locations the position of the plane normal to its surface must be known with almost the same accuracy. This implies extremely flat plane construction, and minimal plane deflection under its own weight.

One has then the task of surveying each module to the required accuracy. This effort is hampered by four factors: the four major parts of the apparatus could be moved fairly frequently; most of the apparatus is hidden from view once it is assembled; and the fact that the act of turning on

the toroid excitation current will create forces likely to change the mechanical relationships between major pieces of equipment. In addition, the dimensions of the detector are so large that thermal expansion can lead to shifts of the order of 1 mm per 10°C.

On the positive side, there are a few design features which will enable us to achieve the surveying goals stated above:

(1) The muon momentum is measured by comparing the angles of the track before and after passage through the iron. If both the inner and outer chamber sets are mounted on the same piece of yoke then motion of the support does not affect momentum resolution. In addition, the support points can be chosen to line up on both sides, eliminating thermal expansion effects.

(2) As much as possible, pre-aligned chamber modules will be installed. These modules will be pre-surveyed relative to their support references. If mounted on surveyed supports (such as precision balls or rails), the modules should be very close to the calculated positions.

(3) The layout should be arranged to provide a small amount of overlap between adjacent modules, so that muon tracks from events and cosmic rays can be used for final alignment verification, and for precision alignment. There is a small fraction of muon tracks that will pass through modules belonging to both the end system and the central system, or through modules mounted on the iron, and those that are trapped under the calorimeters or in the table. The final alignment of those depends crucially on the availability of a fairly sophisticated cosmic ray muon trigger. This trigger is expected to run whenever the accelerator is off, but the toroid will have to be energized to maintain all dimensions as in the running condition. The cosmic ray trigger will have a momentum cut in addition to requiring the track to pass through the general area of the vertex.

6.3.5 Chamber Gas Leaks and Safety

We assume a leak rate of 1 standard ft^3 per hour (scfh) per module. This leak rate totals 5600 scf per day for the 232 modules. The total gas escaping is equivalent to seven gas cylinders per day. Assuming perfect mixing with the air in the collision hall, and inflammability when one part of chamber gas is mixed with two parts or less of air, this quantity of escaping gas must be mixed with 11,000 scf of air per day. The collision hall volume is $40 \times 40 \times 65$ ft^3 = 104,000 scf. Therefore the air in the collision hall must be replaced with fresh air at least once every 9.3 days.

A leak rate this large would place no additional burden on the ventilation system. Moreover, keeping the average leak rate per module well below the 1 scfh assumed will be a design and fabrication goal. Additionally, adequate ventilation will be provided even in the more inaccessible parts of the detector for gas safety as well as electronics cooling.

6.4. DETECTOR PERFORMANCE

6.4.1 Hadronic Punchthrough

A hadron induced event in a neutrino detector at Fermilab,[5] shown in Fig. 6.20, graphically illustrates the need for many absorption lengths (λ_0) of material, in this energy range. More quantitatively, Fig. 6.21 shows the punchthrough probability from CERN experiment WA1[6] as a function of depth for various energies. Clearly, at 90° and $p_T \simeq 50$ GeV/c, one needs more than 12 λ_0 to achieve 1% punchthrough probability. It is worth mentioning that CDF[7] in B0 has only ~ 6 λ_0 at 90° where the production of massive new particles would be kinematically favored to occur. By comparison, the UA1 experiment has found it necessary to go from 6 λ_0 depth to 9 λ_0 depth[8] in order to study isolated muonic decays of the $W^{\pm}$ and the Z^0.

As seen from Fig. 6.21, the effective attenuation length is weakly dependent on momentum. This dependence was used to scale the depth of steel at various angles to maintain roughly constant punchthrough probability with p_T. For our thickness, the punchthrough probability, at all angles, is $\simeq$ 0.3% at $p_T \simeq 15$ GeV/c and $\simeq$ 2% at $p_T \simeq 40$ GeV/c.

To set the scale for the punchthrough problem one compares $\pi^{\pm}$ yields[9] to $\mu^{\pm}$ yields from $W^{\pm}$ decays in Fig. 6.22. Punchthrough alone is not enormously suppressed at 13 λ_0 depth, and buries the $W^{\pm}$ signal. In order to extract a clean signal at p_T values at and beyond the electroweak regime, one needs to track the particle which exits the magnetized iron. A muon will undergo multiple Coulomb scattering in the uranium calorimeter and magnetized iron. In one dimension, it will scatter by $\Delta p_T^{MS}/p_T$, with $\Delta p_T^{MS} = 14\text{MeV}\sqrt{L/L_{rad}}$. For example at $p_T = 35$ GeV/c at 90°, the mean scattering angle will be 6.8 mrad. In contrast, a hadronic shower remnant will have a transverse momentum

set by typical hadronic interactions, $\langle p_T^h \rangle \simeq 350$ MeV/c. A crude estimate of the rejection factor due to only one angle cut is then,

$$\text{rejection} \simeq \frac{\Delta p_T^{MS}}{\langle p_T^h \rangle} = \frac{\langle n \rangle m_\pi}{\sqrt{s}}$$

where $\langle n \rangle$ is the mean multiplicity $\simeq 1.6$ ℓn s, $\sqrt{s} = \sqrt{2 m_p p_T}$ at 90° and the secondaries are assumed to be pions produced at rest in the c.m. This factor is $\simeq 0.019$ at $p_T = 35$ GeV/c.

This rejection power was better quantified by using data from a fine-grained calorimeter[5] (see Fig. 6.20). At 35 GeV/c the rejection factor is 25 for a one dimensional rejection, based only on exit angle. The p_T dependence of this rejection factor is rather modest as indicated by the expression given above. A similar rejection factor can be obtained from a cut on the exit position of the track. A Monte Carlo evaluation of this factor[10] for 2 independent exit coordinates is compatible with being equal to the angle factor squared. Finally, UA1[11] with 2 independent position and angle cuts, has a Monte Carlo result scaled to 13 λ_0 at $p_T = 35$ GeV/c which gives a joint rejection factor $(20)^4 = 1.6 \times 10^5$.

In the DØ case, there exist position and angle cuts on the exit track in the non-bending plane. In the bending plane, the vertex and the 3 drift tube stations lead to one constraint. A conservative estimate is shown in Fig. 6.22, using a rejection factor from only 2 of the 3 cuts. Clearly the residual punchthrough background given by the Coulomb telescope is well below the $W^{\pm}$ signal. At $p_T = 35$ GeV/c the total rejection factor due to 13 λ_0 of absorption and the 2 cuts is $\simeq 7 \times 10^3$. For comparison, non-interacting punchthrough is completely negligible: $e^{-13} = 2.3 \times 10^{-6}$ for a rejection of 4.3×10^5.

6.4.2 Punchthrough Test

Tests were conducted during April and May of 1984 in the NW test beam at Fermilab. The hadron punchthrough at depths of 7 and $14\lambda_0$ was measured at momenta of 10, 25, 50, 100, and 150 GeV, with a close simulation of the muon detection system proposed. The rejection power of the Coulomb telescope was determined by simultaneously measuring muons. This data is being used in conjunction with Monte Carlo jet events to optimize the PDT layout in the DO detector. The resulting program will answer questions of muon pattern recognition, required redundancy in the presence of δ rays and hadron punchthrough from jets, and the efficiency/rejection power of various trigger schemes.

The layout of the muon test is shown in Fig. 6.23. The incident particle is tagged by 5 sets of PWC's and 2 scintillators. These detectors simulate the central tracking detectors. The beam track tagging was followed by 50 in of lead which roughly simulates the ULA calorimetry of the DO detector. Particles exiting this $7\lambda_0$ of material are detected in 2 stations of PDT, A and B.

Following the A and B stations, there is approximately $7\lambda_0$ of magnetized iron which approximates the DO toroids. Tracking behind the iron is done in 3 more PDT stations, C, D, and E. Triggering the system requires that a beam particle penetrate to the CF scintillators between station D and E. Additional material then follows, with a final set of "μtag" counters.

The system redundancy and cell size were better than the DO detector design, so that the effects of a reduced number of detection planes, or a larger cell size in the PDT, could be simulated off-line.

The lead and iron were periodically retracted for "straight through" runs to align the central tracking PWC to the A, B, C, D, and E PDT stations. At present this alignment is known to approximately 1 mm FWHM. With this align-

ment one achieves a $\Delta p/p$ for muons (defined using the "μtag" counters in Fig. 6.23) of $\sigma/p \sim 0.24$. This result, scaled as $(B_0 \sqrt{L})^{-1}$ to the DO field and steel length, agrees with the design estimates of $\Delta p/p$ given in section 6.4.4. Thus, this crucial muon parameter is confirmed.

Using the μtag counters to define a muon, the distribution of position and multiplicity for muons are shown in Fig. 6.24 for the 150 GeV data set. A hit is defined if an adjacent cell time check sum is valid. Clearly, at both 7 and $14\lambda_0$ depth approximately 15% of all muons have a hit multiplicity > 1. Presumably this is due to accompanying δ rays, muon bremsstrahlung, or electron recoil showers. We are in the process of extracting the position and angle dependence of these extra hits for input to the Monte Carlo. Clearly, for the DO muon system to be efficient, enough redundancy needs to be provided to find muon tracks in the presence of these extra tracks. Note that these hits are fairly tightly collimated with respect to the muon direction. This fact confirms the need for a 2-hit TVC system as described in section 6.3.2 for a 5 cm drift distance if the efficiency is to be kept > 90%.

6.4.2.1 The Coulomb Telescope. A prime consideration in the design of the system is to maintain spatial resolution for the muons consistent with their multiple scattering radius of uncertainty as discussed in section 6.3.2. This is needed to insure maximal rejection against hadrons. The hadron shower is contained in approximately $\pm \lambda_0$ transversely, while the muon is in a cone whose angle scales as 1/p.

The 150 GeV data are shown in Fig. 6.25 with the requirement that there be a hit in A and B within a radius of 1 cm with respect to the incident beam ($R_{min}^{AB} < 1$ cm). This cut passes ≥ 95% of the μtag events. Plotted in Fig. 6.25 is the maximum radius of hits in the stations downstream of the iron,

R_{max}^{CDE}. Clearly the muons are contained within a radius < 2.5 cm at least 90% of the time. The loss is due to δ rays as discussed above.

The $\overline{\mu tag}$ events are a mixture of muon leakage events and real hadron showers. As seen in Fig. 6.25, there is a peak at small R_{max} whose width is consistent with the multiple scattering of a 150 GeV muon. In order to estimate the background due to hadrons, $\overline{\mu tag}$ events were selected with $R_{min}^{AB} > 1$ cm, and normalized to the data with $R_{min}^{AB} < 1$ cm in the region with $R_{max}^{CDE} > 5$ cm. The resulting curve is shown in Fig. 6.25.

Of the 150 GeV triggers, 30% are $\overline{\mu tag}$ events, 11% have $R_{min}^{AB} < 1$ cm, and 1% have $R_{max}^{CDF} < 2.5$ cm. Of these only 1/2000 are not obvious muon leakage. Hence the hadron rejection factor (using Fig. 6.25) is ≥ 30,000. This data confirms the estimates from section 6.4.1 of a rejection factor ≥7100.

6.4.2.2 Hadron Punchthrough. A major goal of the DØ muon detector is to study muons in a jet environment.

Shown in Fig. 6.26 are the multiplicity and position distributions of $\overline{\mu tag}$ events at 150 GeV. At $7\lambda_0$ (station A) and $14\lambda_0$ (station C) depths, the most probable multiplicity is 1. It is instructive to compare these data with those shown in Fig. 6.26 for muons where the high multiplicity tail is absent.

Also shown in Fig. 6.26 is the distribution in position at $7\lambda_0$ and $14\lambda_0$ depths. The cross-hatched spike at $7\lambda_0$ is due to noninteracting hadrons in station A. This effect is a bias due to our trigger which selects late developing showers. Note that this spike has the same shape as the muon data in Fig. 6.26. Subtracting this bias, one has a shape which can be approximated by a Lorentzian line shape with $\Gamma \simeq 10$ cm at $7\lambda_0$ and $\Gamma \simeq 24$ cm at $14\lambda_0$, showing the growth of the transverse shower width with depth. The increase in size of the shower in the C, D, and E stations is consistent with approximately 100 mrad mean angle of the hadronic shower particles.

The distribution of multiplicity, position, and angle of shower particles is a necessary input to a realistic Monte Carlo simulation of the DØ muon detector. As shown in Fig. 6.27, between 50 and 150 GeV there is little momentum dependence of these variables. At 50 GeV there is a substantial muon contamination to these data as indicated by the spike at multiplicity = 2 due to muons with a δ-ray. The μtag events were used to subtract this background from the 50 GeV/c data. The resulting multiplicity and position distributions, as seen in Fig. 6.27 are only weakly dependent upon momentum.

6.4.3 Muons from Decay and Heavy Flavors

Decays from $\pi \to \mu\nu$ and $K \to \mu\nu$ are, in principle, a major source of background to prompt muons from sources due to electroweak bosons and heavy flavor decays. As discussed in Section 7.2, decays are the dominant background for a low-p_T trigger cut at $p_T \simeq 5$ GeV/c. In the electroweak regime of p_T, one uses a model of meson production[9] which is shown in Fig. 6.22. The decay reduction factor for pions is roughly $Rm_\pi/p_T(c\tau)_\pi$ which favors a compact detector design. The DØ detector has a cylindrical space, R = 70 cm, for tracking and transition radiation detection for electrons. At larger radii the dense uranium liquid-argon calorimeter provides a minimal decay distance. The yield of decay muons is shown in Fig. 6.22 and compared to the cross section for electroweak decays, $W^\pm \to \mu^\pm\nu$. Note that for $p_T > 5$ GeV/c, the dominant source of background muons comes from K-decays, not π-decays.

In Fig. 6.22, no reduction factor has been imposed for decay "kinks." To set the scale for cuts, at $p_\mu = 30$ GeV/c, a $\pi \to \mu\nu$ decay has a 1 mrad kink, and a $K \to \mu\nu$ decay has an 8 mrad kink. The central tracking resolves angles to ≃ 1 mrad; hence, substantial reduction factors are available. For isolated

muons from $W^{\pm}$ or Z°, powerful topological cuts are available. The UA1 experiment,[12] with a less compact geometry, shows that $W^{\pm}$ and Z° can be easily extracted from this background. Note also that a yield which falls as e^{-bp_T}, when smeared by a Gaussian resolution with standard deviation σ, is increased by a factor $\exp((b\sigma)^2/2)$. As inspection of Fig. 6.22 shows, at $p_T \simeq 30$ GeV/c the slope is $b \sim 8$ GeV $^{-1}$. Given a resolution $dp/p = 0.18$ as discussed in Section 6.4.4, this implies a factor $\exp((b\sigma)^2/2) \simeq 1.4$ which is quite tolerable.

Another background is due to the production of jets containing heavy flavors which decay semileptonically. The yield for muons from this source, as evaluated by the ISAJET Monte Carlo,[13] is shown in Fig. 6.22. The yield is comparable to that for decays in the regime $p_T \simeq 30$ GeV/c. As with decay backgrounds, powerful topological cuts[12] exist which can be used to separate electroweak and heavy flavor muons.

6.4.4 Muon Momentum Resolution

The effects contributing to muon momentum resolution can be divided into those associated with multiple Coulomb scattering, and those associated with measurement errors. The contributions to the relative momentum resolution due to multiple scattering are independent of the momentum, whereas the relative contributions due to measurement errors scale with the momentum; hence the former are important at low momenta, while measurement errors dominate at large momenta and ultimately determine the maximum momentum at which a sign determination can be made.

Where multiple scattering dominates, $dp_T/p_T = dp/p$ varies as $1/\sqrt{L}$ where L is the depth of steel traversed. At low momentum, the resolution in p_T at $\phi = 0^{\circ}$ is only slightly dependent on θ; there is a 40% variation from 90° to 11°.

In analyzing the contributions to the muon momentum resolution, we must distinguish two situations, depending upon whether a track segment in the chambers between the calorimeter and the steel is measured, case A, or is missing, case B. In the former case (A), the vertex information from the central tracking chambers may not be necessary, but measurement errors in the chambers between the calorimeter and the iron contribute to the momentum resolution. In the latter case (B), the vertex information is necessary; the degradation of this information due to vertex measurement errors and multiple scattering in the calorimeter contributes to the momentum resolution. In both cases, multiple scattering in the iron and measurement errors in the chambers outside the iron give additional contributions to the momentum resolution.

We will discuss the contributions to the relative momentum resolution due to different types of measurement errors and multiple scattering separately, at fixed momentum. Subsequently, we will present the total relative momentum resolution vs p_T at selected angles, for representative values of the measurement errors. The geometry of the chambers, is taken as discussed in section 6.3. (z is along the beams.) The field magnitude in the iron is taken as 20 kG, with a direction assumed constant over the full extent of each quadrant of the square. Energy loss in the iron is neglected. The transition between the central and end iron systems has been taken to be at $\theta = 40°$, independent of ϕ; thus the central-end iron corners are not treated in detail.

Figures 6.28 through 6.30 show resolution calculations for a momentum of 100 GeV/c. Figure 6.28 presents the angular dependence of the relative momentum resolution per 1 mm measurement error in the "bend plane" (z direction for the central iron, either x or y for the end iron), associated with one set of

chambers beyond the iron. The contributions to the resolution due to "non-bend plane" measurement errors (y direction) is independent of the momentum, and is more than 100 times smaller than the results shown in Fig. 6.28.

The bottom curves in Fig. 6.29 show the contribution due to errors in the x-location (z-location for the ends) of the chamber planes; this is relevant to the alignment and flatness requirements for these chambers. The contributions due to "bend-plane" measurement errors and chamber plane location errors associated with the planes between the calorimeter and the iron (relevant for the momentum resolution for case A) have a similar angular dependence. The contribution to the relative momentum error due to vertex postion errors in the z-direction (relevant for case B) varies from about 0.4%/mm to 4.6%/mm as θ varies from 10° to 90° (at ϕ = 0° and p = 100 GeV/c).

The top curves in Fig. 6.29 show the multiple scattering contribution to the relative momentum resolution, due to both the steel and the calorimeter. The steel alone contributes about 80% of the total.

Figures 6.30 shows, for case A, the total relative momentum resolution vs p_T, for various angles. The resolution is computed assuming 1 mm bend plane errors in each of 2 sets of chambers outside the iron, and 1 set inside the iron. In addition, an error of 1 mm in perpendicular plane location was included for each set. The lower sets of curves shown in Figs. 6.30b and 6.30c at low momenta correspond to the resolution achievable in case A when information is available from the chambers between the iron and the calorimeter.

For p_T below the measurement error limit the resolution is dominated by multiple scattering. In this regime 2 types of topologies, corresponding to cases A and B defined above, can be identified. For muons in jets, the central track match will often be obscured, (case A) in which case one really has only a line at $13\lambda_0$ and a short line at $7\lambda_0$. In this situation $(dp_T/p_T)_{jet}$ =

± 0.19 (at $\theta = 90°$, $\phi = 0°$), which is essentially $\Delta p_T^{MS}/\Delta p_T^B$. For case B only the central track must be available (which requires isolated muons) but it is smeared by the 230 radiation lengths in the calorimetry. In this situation, (dp_T/p_T) isolated $= \pm 0.27$ (at $\theta = 90°$, $\phi = 0°$). Note that what is quoted here is the FWHM/2.36, whereas the resolution curves in fact have a Gaussian piece with additional long tails on the high momentum side.

We conclude that the system described here will measure muon momenta well through the physically interesting region of transverse momenta ($p_T \lesssim$ several hundred GeV/c) and will enable identification of muons even in the difficult environment of hadronic jets.

REFERENCES CHAPTER 6

1. S. Aronson, private communication, BNL E734.
2. D. F. Anderson et al., CERN EP/84-01.
3 J. Allison et al., "Diamond shaped cathode pads for the longitudinal coordinate from a drift chamber."
4. G. Fischer et al., Nucl. Instru. and Methods **100**, 515 (1972).
5. E594 Collaboration, private communication.
6. S. Iwata, DPNU-3-79
7. CDF Design Report, 1981.
8. CERN/SPSC/82-51.
9. I. Hinchcliffe and R. Kelly, CDF-83.
10 A. Grant, Nucl. Instrum. Methods **131**, 167 (1973).
11. CERN/SPSC/78-19.
12. UA1 CERN-Preprint 83-39. Replace with Phys. Lett publication(s).
13. F. E. Paige, BNL 30805.

TABLE 6.1 Parameters of Magnetized Toroids

	CF	EF	Total
Steel			
Inner Half Width	122 in	34 in	
Outer Half Width	164 in	164 in	
Length	304 in	60 in	
Weight	2070 ton	2×875 ton	3820 ton
Coil			
Current	2000 A	2000 A	
Field	20.0 kG	19.5 kG (at inner edge)	
Number of Coils	32	16×2	
Turns each Coil	10	8	
Conductor Cross Section	1.60×1.60 in^2	1.60×1.60 in^2	
Hole Diameter	0.60 in	0.60 in	
Resistance of each Coil	2.2 mΩ	1.0 mΩ	
Overall Size of each Coil	16 in high 45 in wide 310 in long	13 in high 136 in wide 63 in long	
Total Resistance	70 mΩ	16×2 mΩ	102 mΩ
Total Voltage	140 V	32×2 V	202 V
Total Power	280 kW	64×2 kW	408 kW
Total Weight	83 ton	19×2 ton	120 ton
Total Length	19000 ft	4300×2 ft	27600 ft
Water, Number of Paths	1/Unit Coil	2 Unit Coils in Series	
	32	8×2	
Δp/Path	200 PSI	200 PSI	
Flow/Path	10 gal/min	11 gal/min	
Total Flow	320 gal/min	88×2 gal/min	500 gal/min
Temperature Rise	4.5° C	3.3° C	

Table 6.2. The Muon Proportional Drift Tube Modules

Module	# of modules	# of decks	Wire length (in.)	Module width (in.)	# wires per module	Total wires	Module wt.(lb.)	Description & Shape
CMA1	12	4	120	152	152	1824	1520	Central, top & sides, 1/2 length, 1/2 width
CMA2	2	4	120	100	100	200	1000	Central, below CC
CMA3	4	4	120	88	88	352	880	Central, below EC
CMB1	12	3	168	236	177	2124	2500	Central outside iron, top & sides
CMB2	2	3	204	232	174	348	3000	Central, below CF
CMB3	4	3	204	32	24	96	400	Central, below CF
CMB4	4	3	204	92	69	276	1200	Central, below CF
CMC1	12	3	228	264	198	2376	3800	Central outer shell, top & sides
CMC2	2	3	228	200	150	300	2900	Central outer shell, bottom
CMC3	4	3	228	128	96	384	1850	Central outer shell, bottom
					Total # wires	8280		

Table 6.2 continued

Module	# of modules	# of decks	Wire length (in.)	Module width (in.)	# wires per module	Total wires	Module wt. (lb)	Description & Shape
EMA1	16	2	152	84	42	672	550	Inner end chambers
EMB1	8	4	142	72	72	576	900	End chambers outside EF
EMB2	10	4	174	116	116	1160	1700	End chambers outside EF
EMB3	2	4	126	116	116	232	1250	End chambers outside EF
EMB4	4	4	174	72	72	288	1100	End chambers outside EF
EMB5	4	4	204	72	72	288	1300	End chambers outside EF
EMC1	10	2	174	120	60	600	900	Outer end chambers at z = 322 in.
EMC2	2	2	142	120	60	120	750	Outer end chambers at z = 322 in.
EMC3	4	2	174	76	38	152	600	Outer end chambers at z = 322 in.
EMC4	8	2	216	88	44	352	800	Outer end chambers at z = 382 in.
					Total # wires	4440		
					Grand Total	12,720		

TABLE 6.3 Chamber Boundaries, Angles, and Pseudorapidities

Chamber:	CMA	CMB	CMC	EMA	EMB	EMC (inner)	EMC (outer)
Minimum x,y in center	107 in	167 in	220 in	34 in	34 in	112 in	68 in
Maximum x,y in center	119 in	175 in	228 in	119 in	216 in	228 in	156 in
Minimum z	-152 in	-236 in	264 in	158 in	239 in	322 in	382 in
Maximum z	152 in	236 in	264 in	173 in	264 in	327 in	387 in
Minimum θ, in center	36.6°	37.3°	40.8°	11.6°	7.7°	19.0°	10.0°
in corner	46.4°	47.2°	50.7°	16.2°	10.8°	26.0°	14.0°
Maximum θ, in center	133.6°	132.8°	129.3°	35.7°	40.7°	35.1°	22.1°
in corner	143.4°	142.7°	139.2°	45.5°	50.5°	44.8°	29.8°
Minimum η, in center	11.1	1.09	0.99	2.29	2.70	1.79	2.44
in corner	0.85	0.83	0.75	1.95	2.36	1.47	2.10
Maximum η, in center	1.11	1.09	0.99	1.13	0.99	1.15	1.63
in corner	0.85	0.83	0.75	0.87	0.75	0.89	1.32

FIGURE CAPTIONS - CHAPTER 6

6.1 Elevation view of the DØ detector showing muon chambers.

6.2 Top view of the DØ detector showing muon chambers.

6.3 Cross section through the central portion of the DØ detector showing the muon chambers.

6.4 Calculated magnetic flux distribution for the central toroid.

6.5 Calculated magnetic flux distribution for the end-cap toroid.

6.6 Assembly scenario for CF.

6.7 Test PDTs (a) short prototype (b) long prototype

6.8 PDT test cell results: high voltage I beam scan.

6.9 PDT test cell results: Drift time vs. position for various angles with approximate electrostatic potentials shown below.

6.10 PDT test cell results: Spatial resolution in drift coordinate.

6.11 PDT test cell results: Spatial resolution in pad current division coordinate.

6.12 Concepts for PDT extrusions: (a) cross section (b) end extrusion

6.13 Front end electronics overview.

6.14 Analog board.

6.15 Fast board.

6.16 Fast board detail showing dual hit TVC.

6.17 Layout of inner end (EMA) muon chambers.

6.18 Layout of outer end (EMB) muon chambers.

6.19 Layout of outer end (EMC) muon chambers.

6.20 Typical event in Fermilab E594 with 100 GeV π^- incident.

6.21 Punchthrough probability from CERN WA1 as a function of depth.

6.22 Comparison of $\pi^{\pm}$ yields, $\mu^{\pm}$ yields from decays and heavy flavors, $\mu^{\pm}$ from W decay, and punchthrough per incident hadron.

6.23 Muon beam punchthrough test setup.

6.24 150 GeV μtag data from test.

6.25 150 GeV Data: μtag and $\overline{\mu\text{tag}}$ data from test.

6.26 150 GeV $\overline{\mu\text{tag}}$ test data: multiplicity and spatial distribution of accompanying particles.

6.27 Comparison of $\overline{\mu\text{tag}}$ test data at 50,100,150 GeV.

6.28 Relative momentum resolution per unit displacement in the "bend plane" (in % per mm) vs. θ, for three ϕ angles as labeled, for p = 100 GeV/c.

6.29 Top: Relative momentum resolution due to multiple Coulomb scattering in the iron and calorimeter (in %) vs θ, for three ϕ angles as labeled. Bottom: Relative momentum resolution per unit displcement perpendicular to the chamber planes (in % per mm) vs θ, for three ϕ angles as labeled, for p = 100 GeV/c.

6.30 (a) Relative momentum resolution vs p_T at $\theta = 10°$. The variation with ϕ is negligible, as is the effect of a case A topology.

(b) Relative momentum resolution vs p_T at $\theta = 50°$. The curves are labeled by ϕ. The lower curves at low momenta correspond to the case A topology.

(c) Relative momentum resolution vs p_T at $\theta = 90°$. The curves are labeled by ϕ. The lower curves at low momenta correspond to the case A topology.

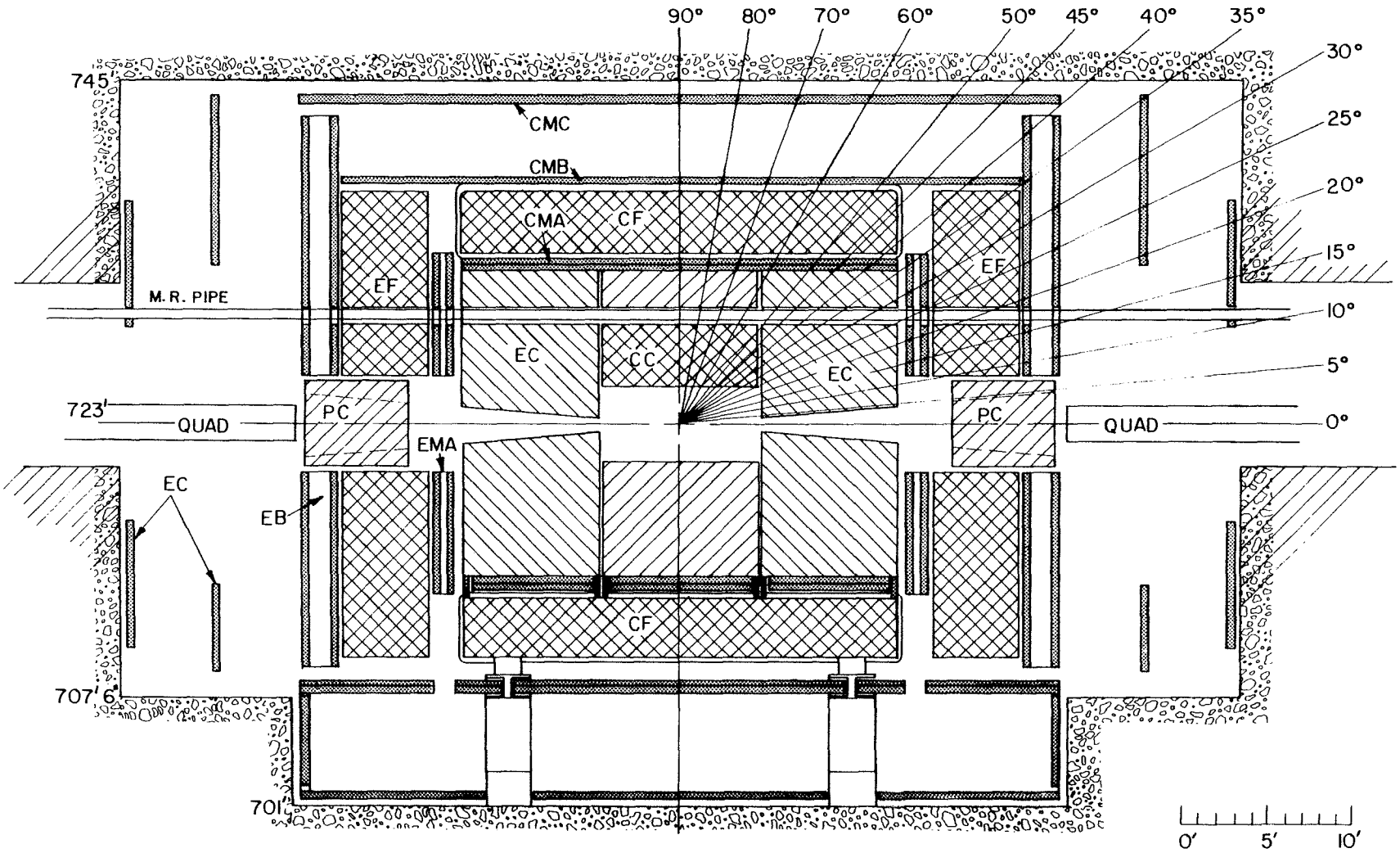

ELEVATION OF DETECTOR

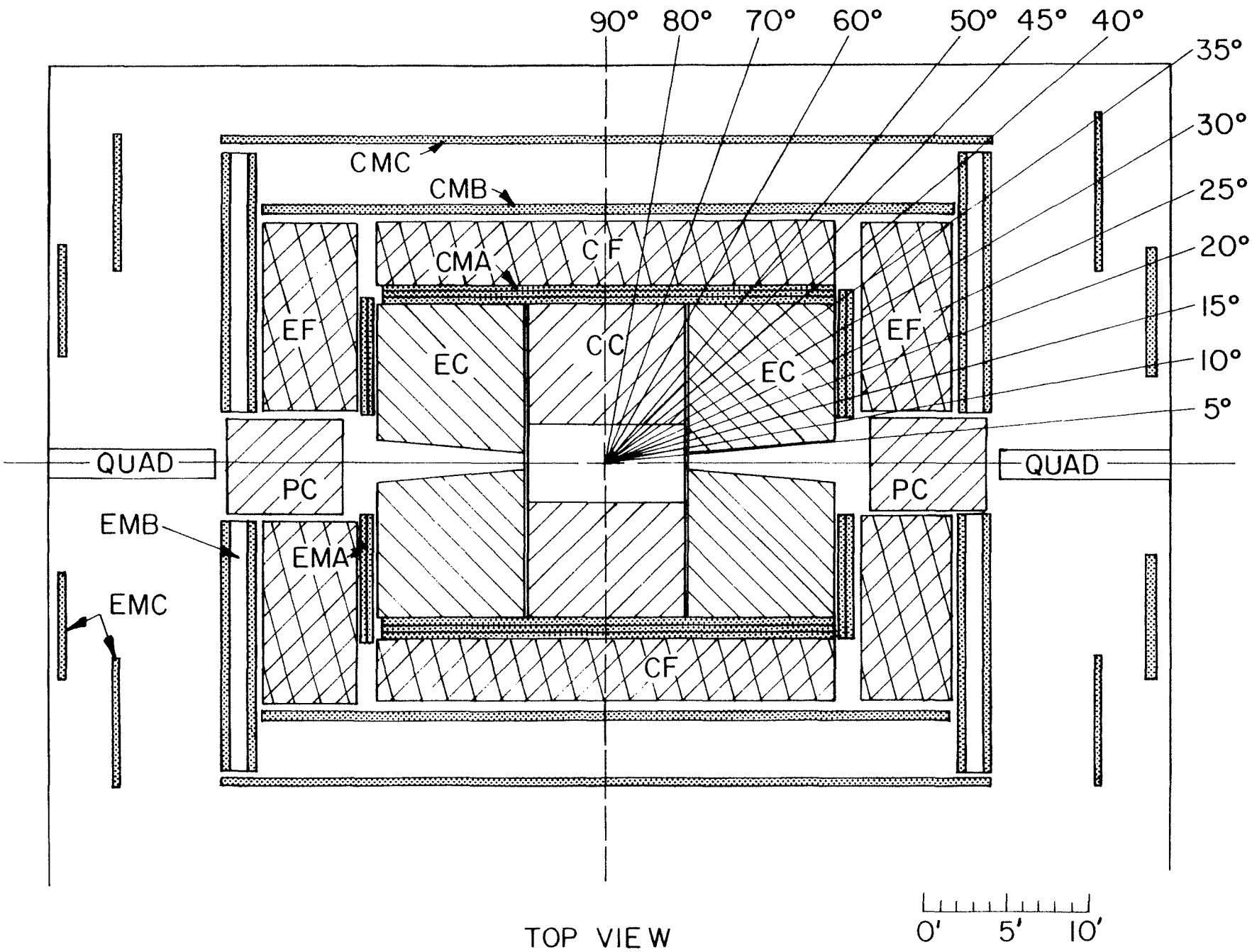
90°
80°
70°
60°
50°
45°
40°
35°
30°
25°
20°
15°
10°
5°
CMC
CMB
CMA
CF
EF
EC
CC
EC
EF
QUAD
PC
PC
QUAD
EMB
EMA
EMC
CF
0'
5'
10'

TOP VIEW

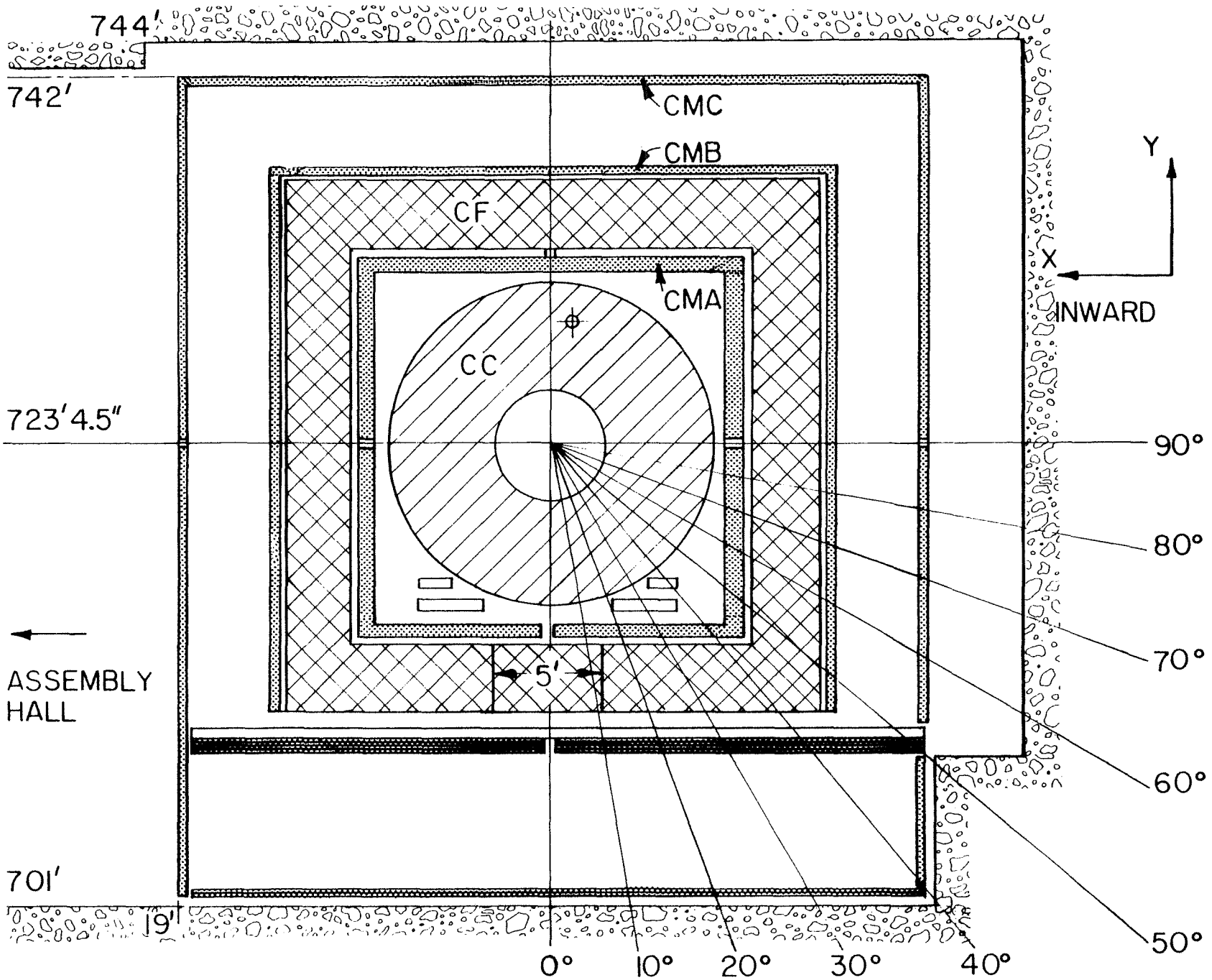
744'
742'
723'4.5"
701'
19'
CMC
CMB
CF
CMA
CC
5'
Y
X
INWARD
ASSEMBLY HALL
90°
80°
70°
60°
50°
40°
30°
20°
10°
0°

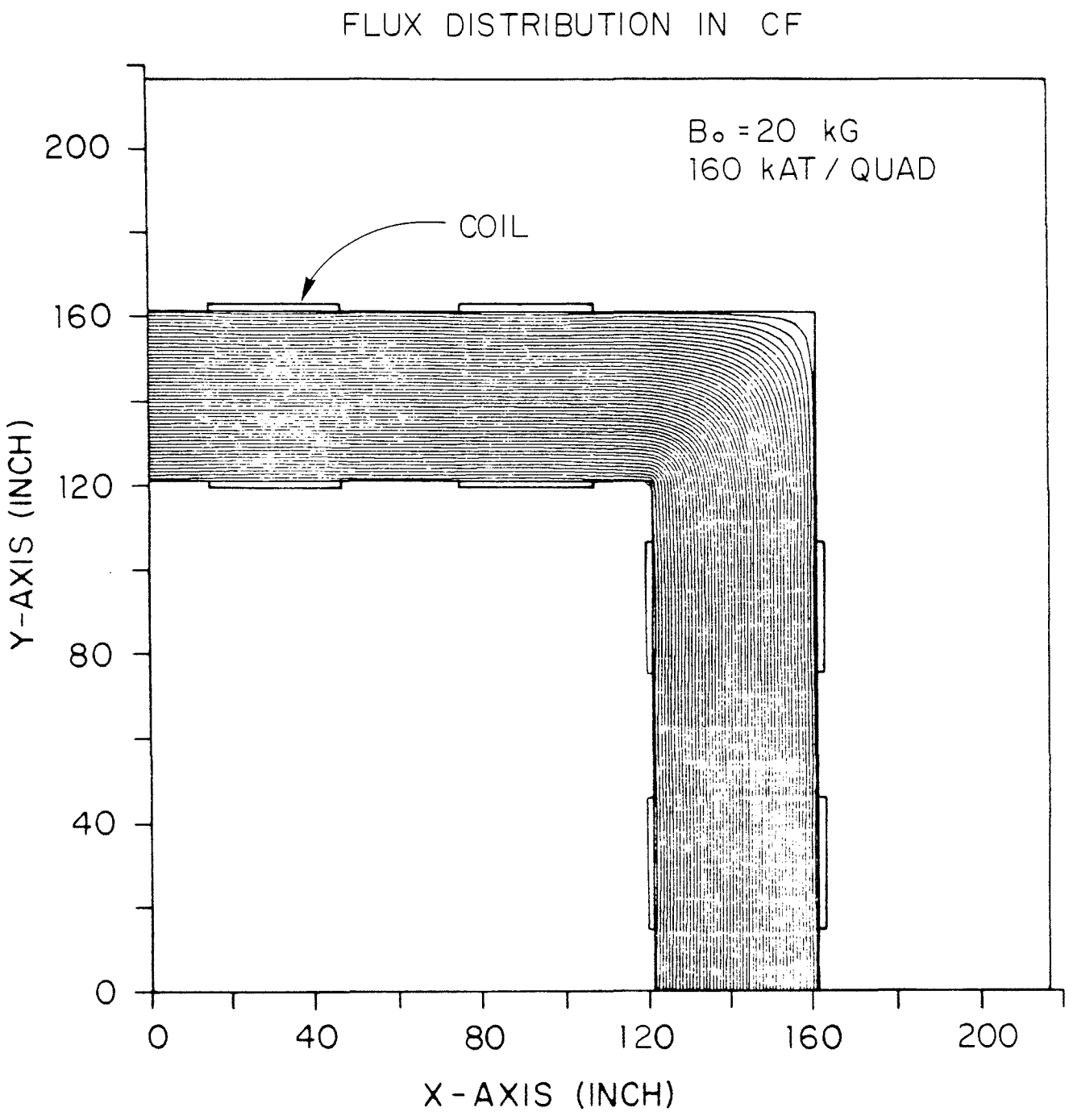
FLUX DISTRIBUTION IN CF
B_o = 20 kG
160 kAT / QUAD
COIL
200
160
120
80
40
0
Y-AXIS (INCH)
0
40
80
120
160
200
X-AXIS (INCH)

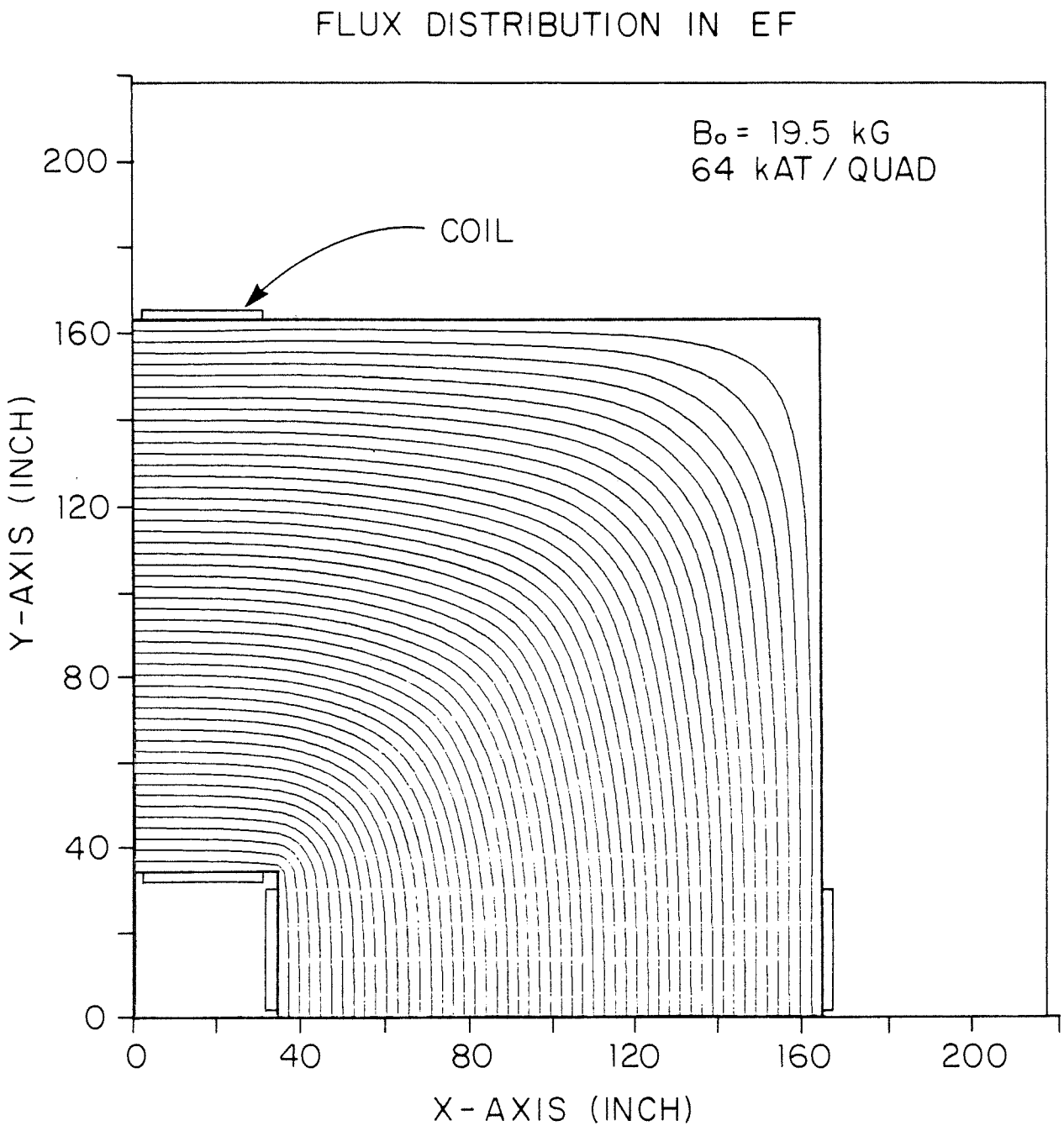
FLUX DISTRIBUTION IN EF
B_o = 19.5 kG
64 kAT / QUAD
COIL
200
160
120
80
40
0
Y-AXIS (INCH)
0
40
80
120
160
200
X-AXIS (INCH)

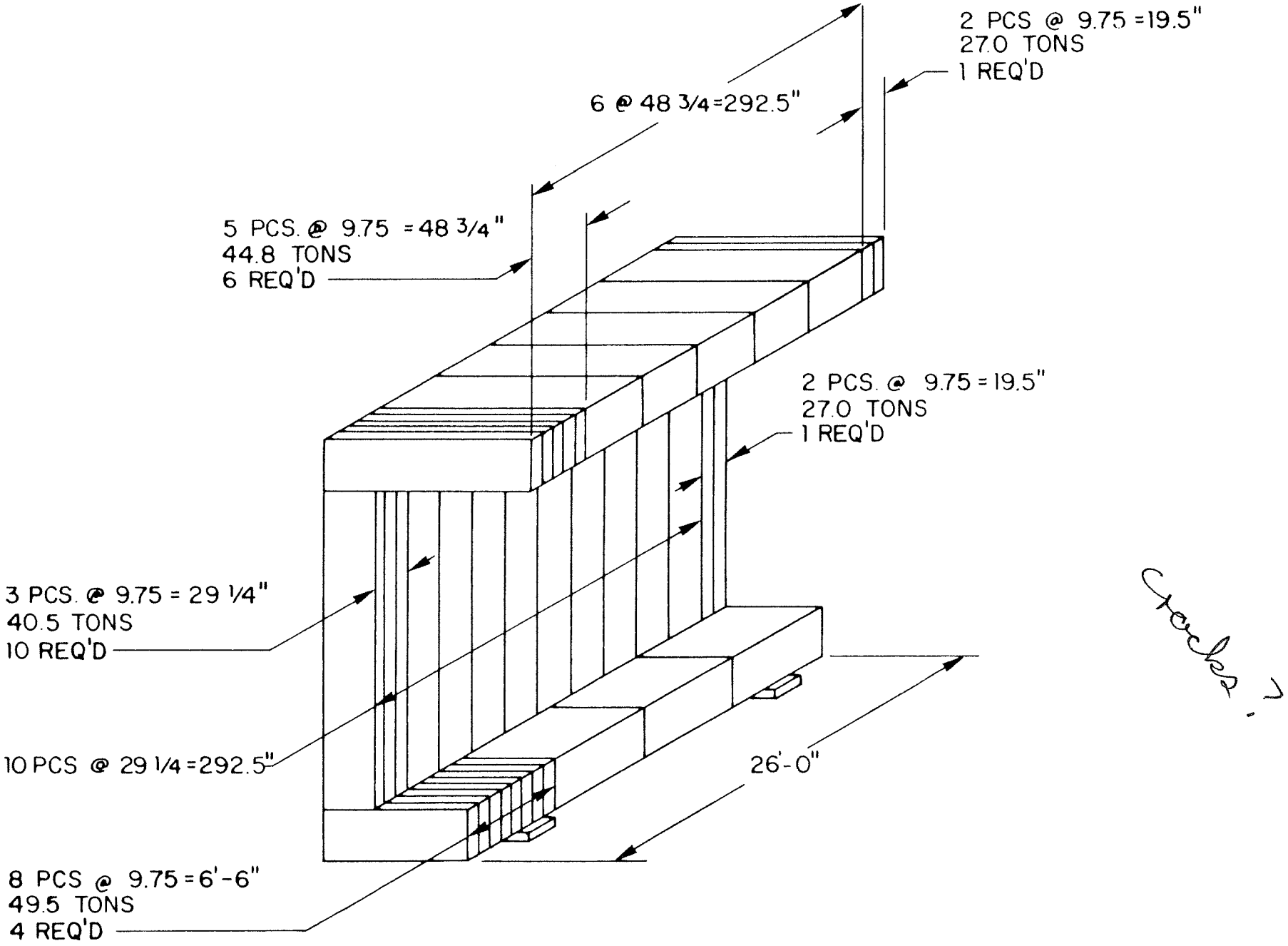

ASSEMBLY SCHEME OF CF YOKE

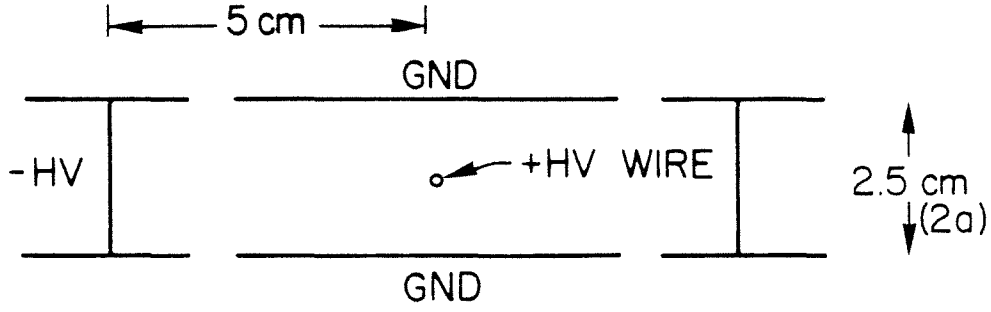
5 cm
GND
-HV
+HV WIRE
2.5 cm
(2a)
GND

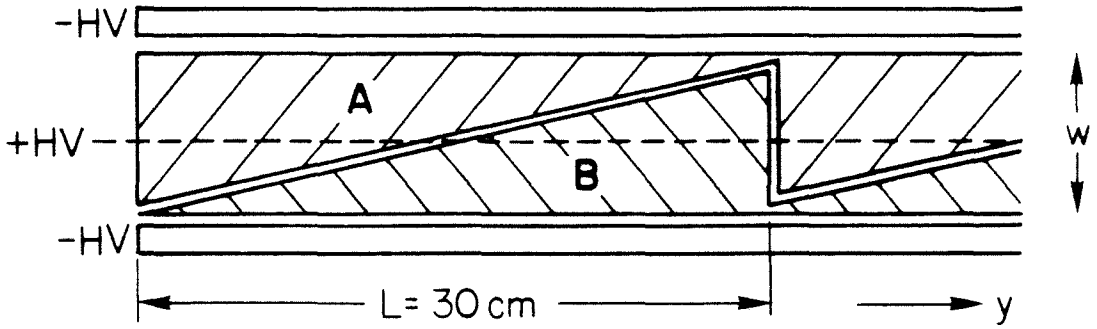
-HV
A
+HV
B
w
-HV
L= 30 cm
y

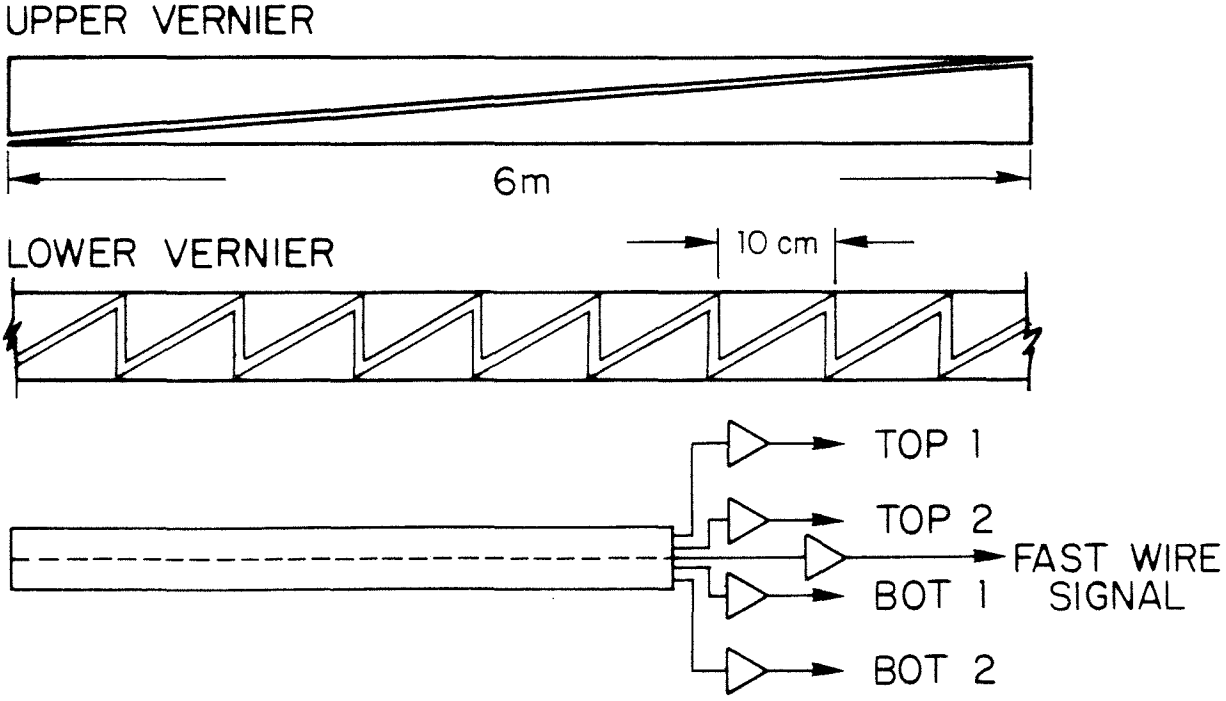
UPPER VERNIER
6m
LOWER VERNIER
10 cm
TOP 1
TOP 2
FAST WIRE
SIGNAL
BOT 1
BOT 2

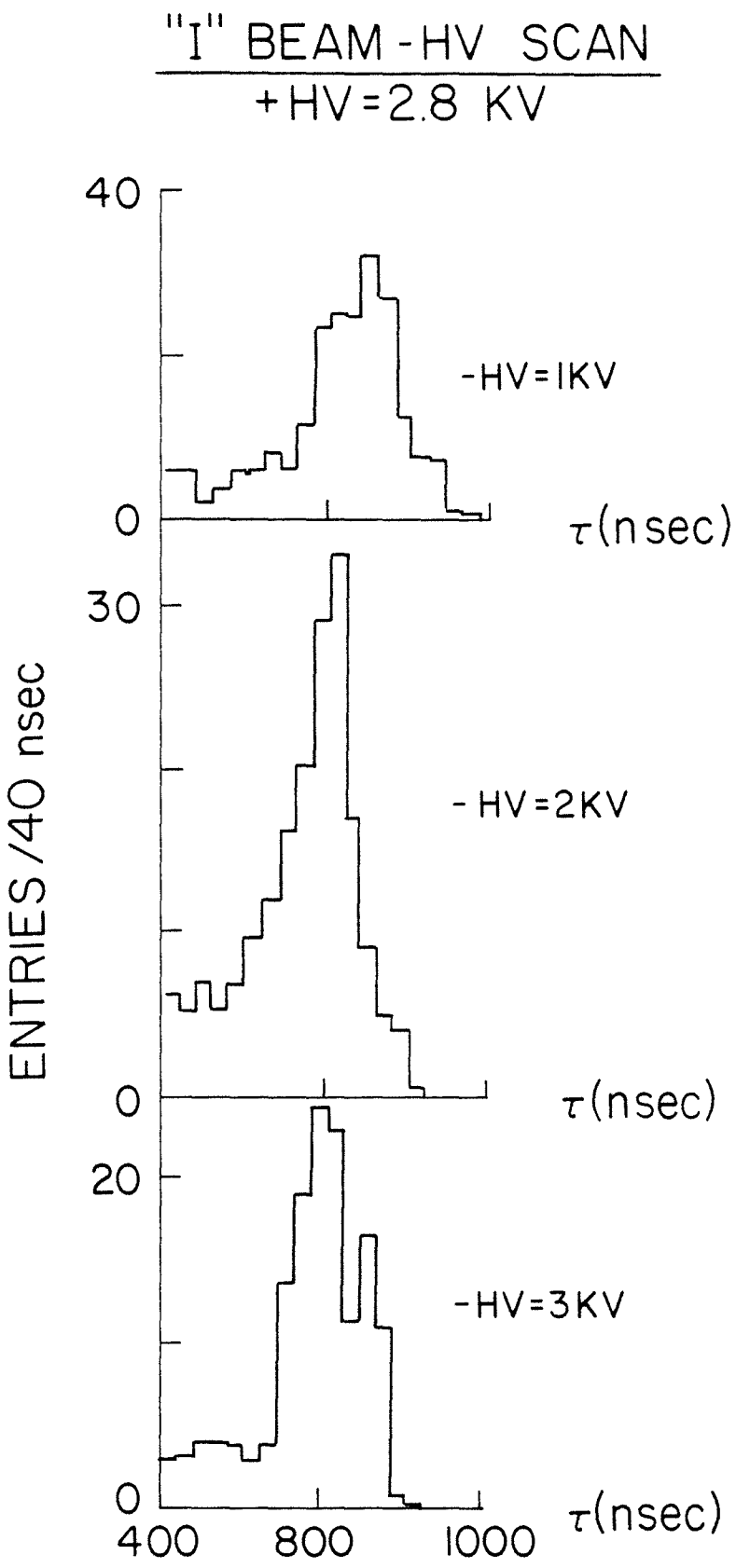
"I" BEAM - HV SCAN
+HV = 2.8 KV
ENTRIES /40 nsec
40
0
-HV = 1KV
τ(nsec)
30
0
- HV = 2KV
τ(nsec)
20
0
-HV = 3KV
τ(nsec)
400
800
1000

$z(\tau)$ TEST PDT CELL

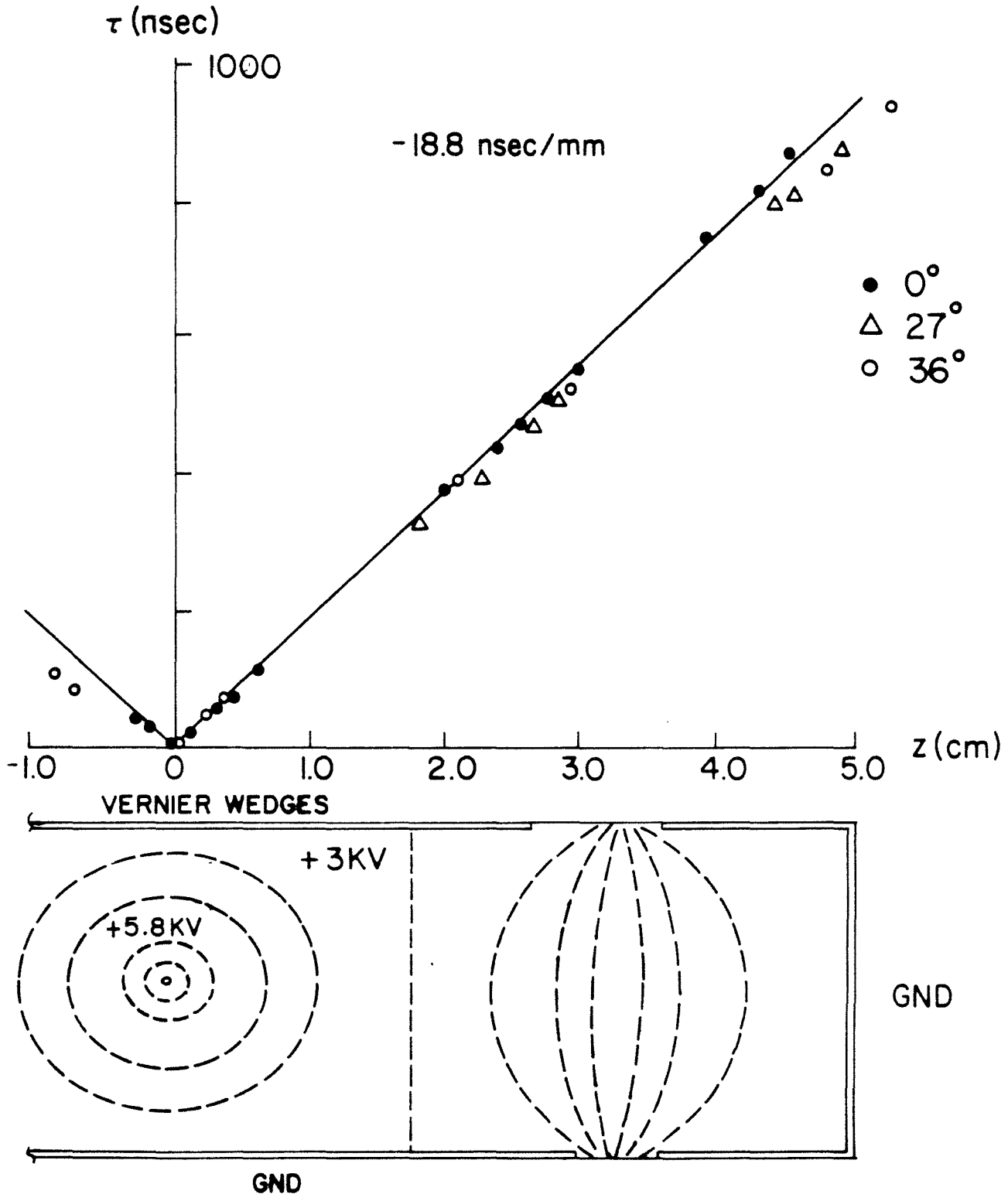

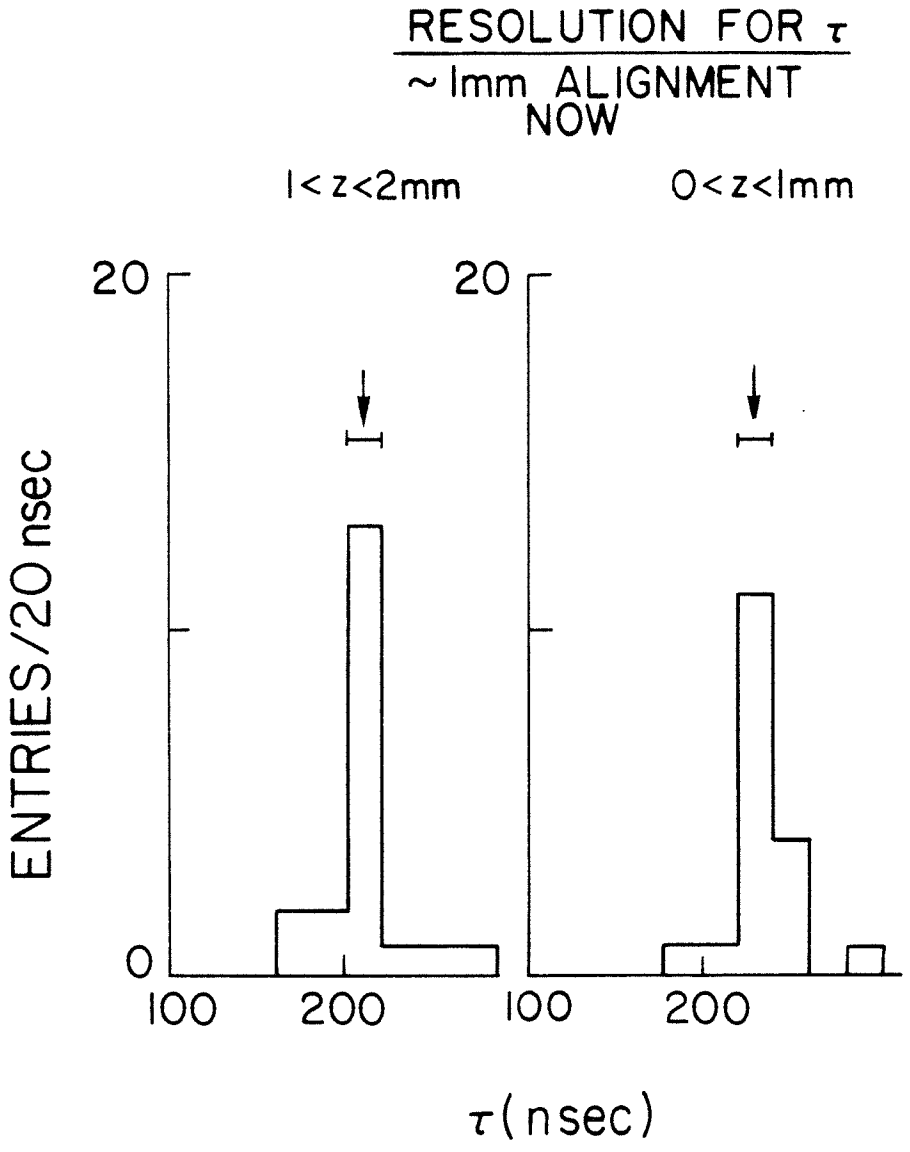
RESOLUTION FOR τ
~ 1mm ALIGNMENT
NOW
1< z<2mm
0<z<1mm
20
20
ENTRIES/20 nsec
0
100
200
100
200
τ(nsec)

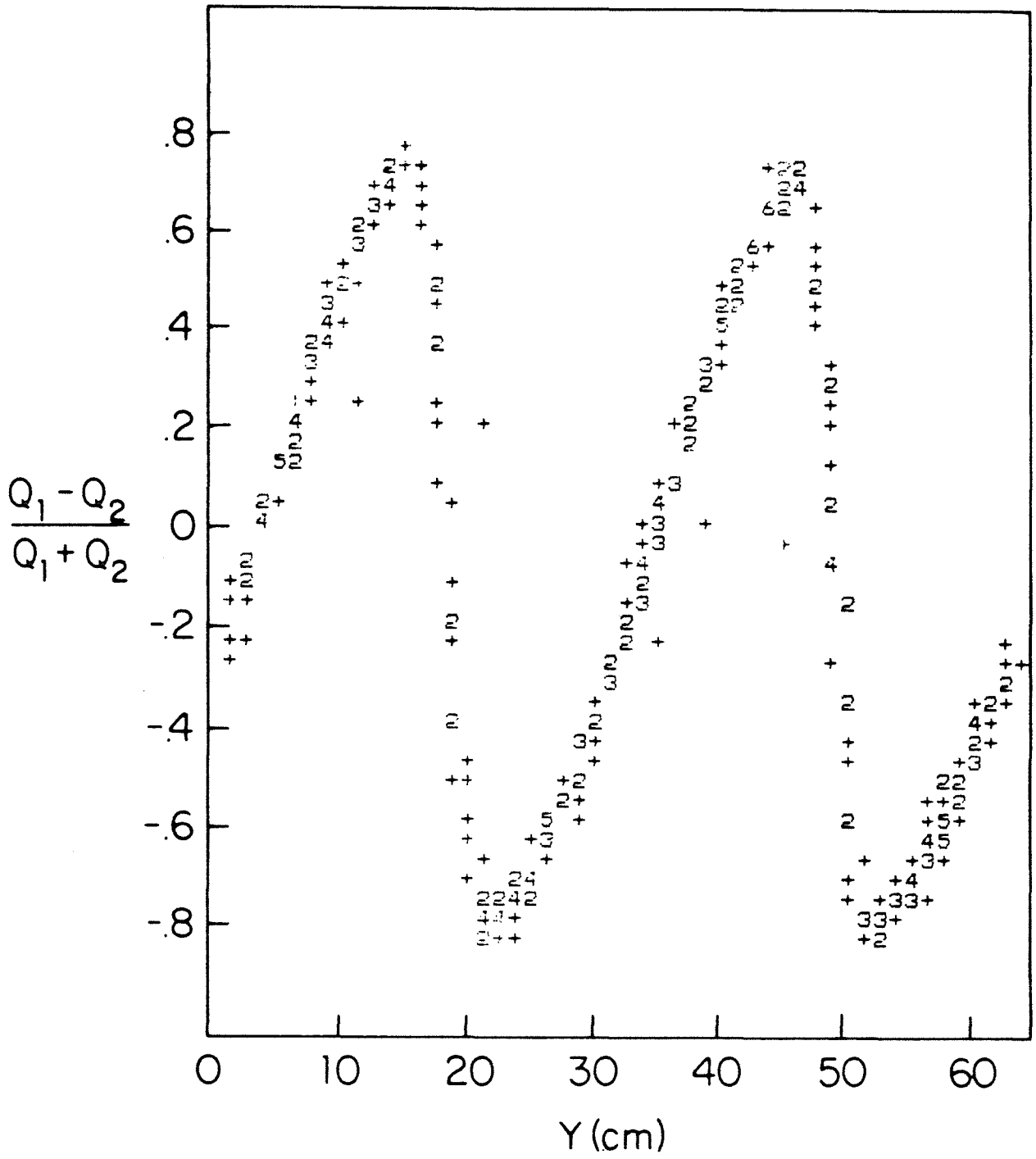
$\frac{Q_1 - Q_2}{Q_1 + Q_2}$
.8
.6
.4
.2
0
-.2
-.4
-.6
-.8
0
10
20
30
40
50
60
Y (cm)

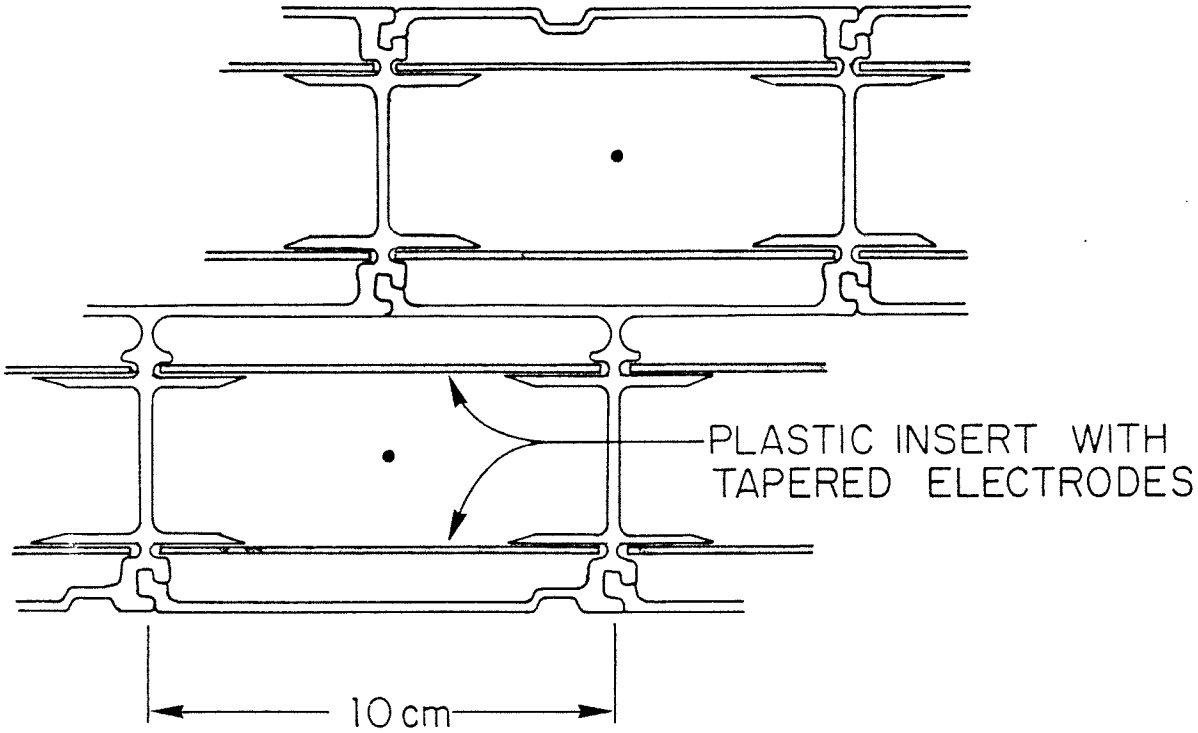

a.) INTERLOCKING EXTRUDED CELLS

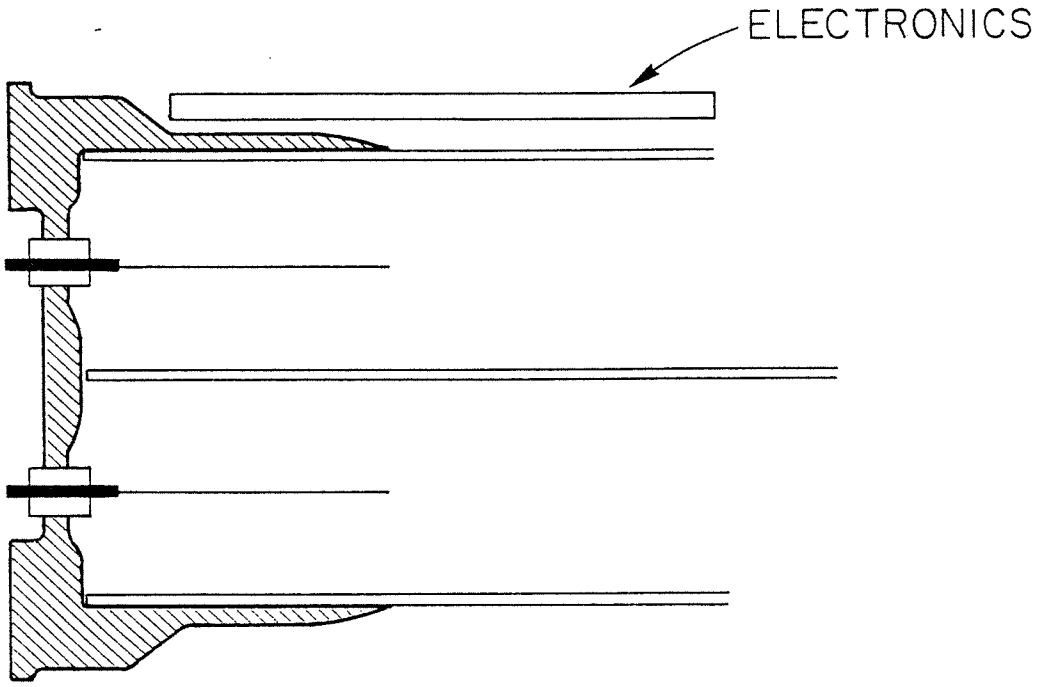

b.) END EXTRUSION

FRONT-END ELECTRONICS
(Portion for 16 of 64 PDTs)

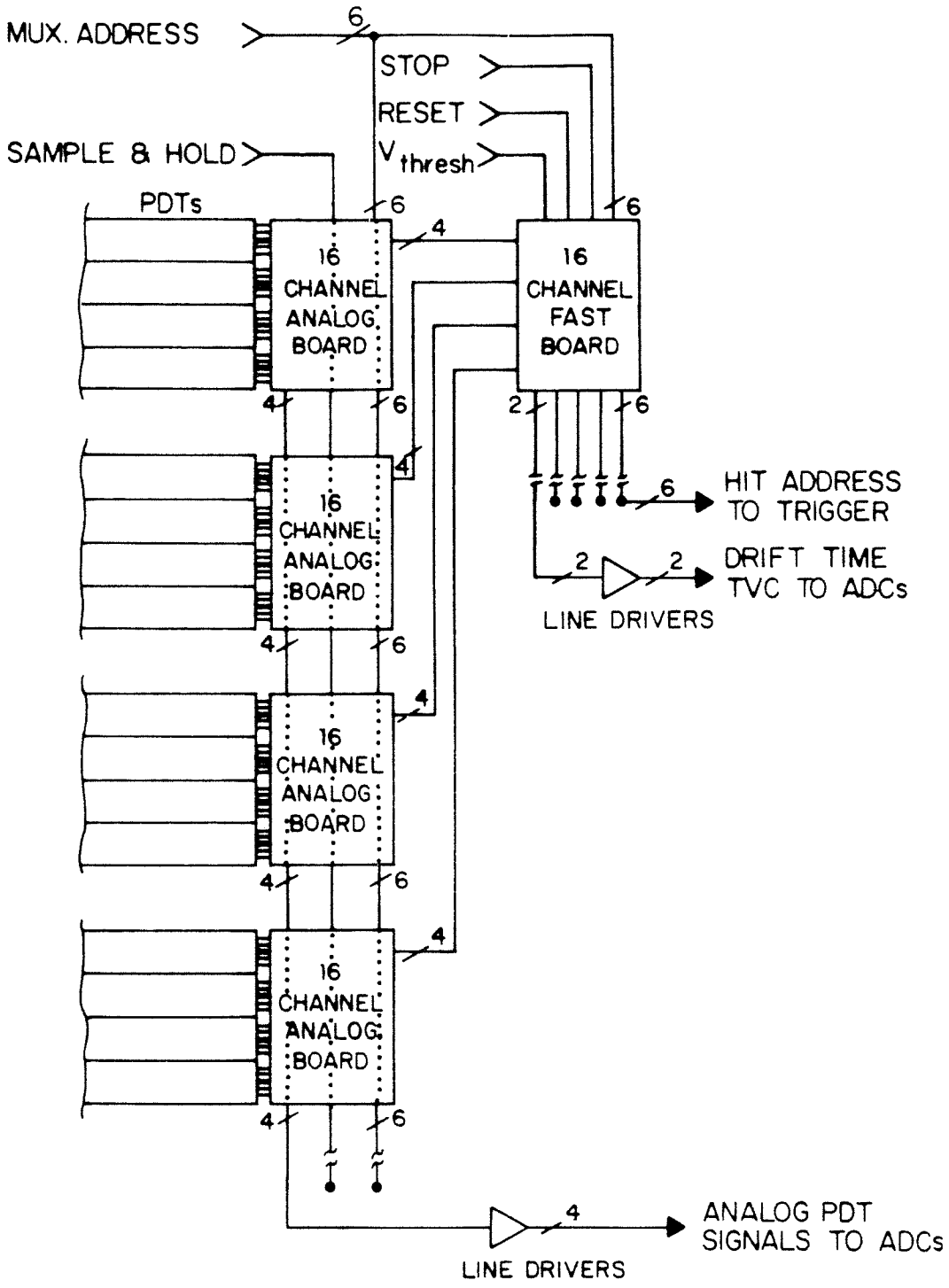

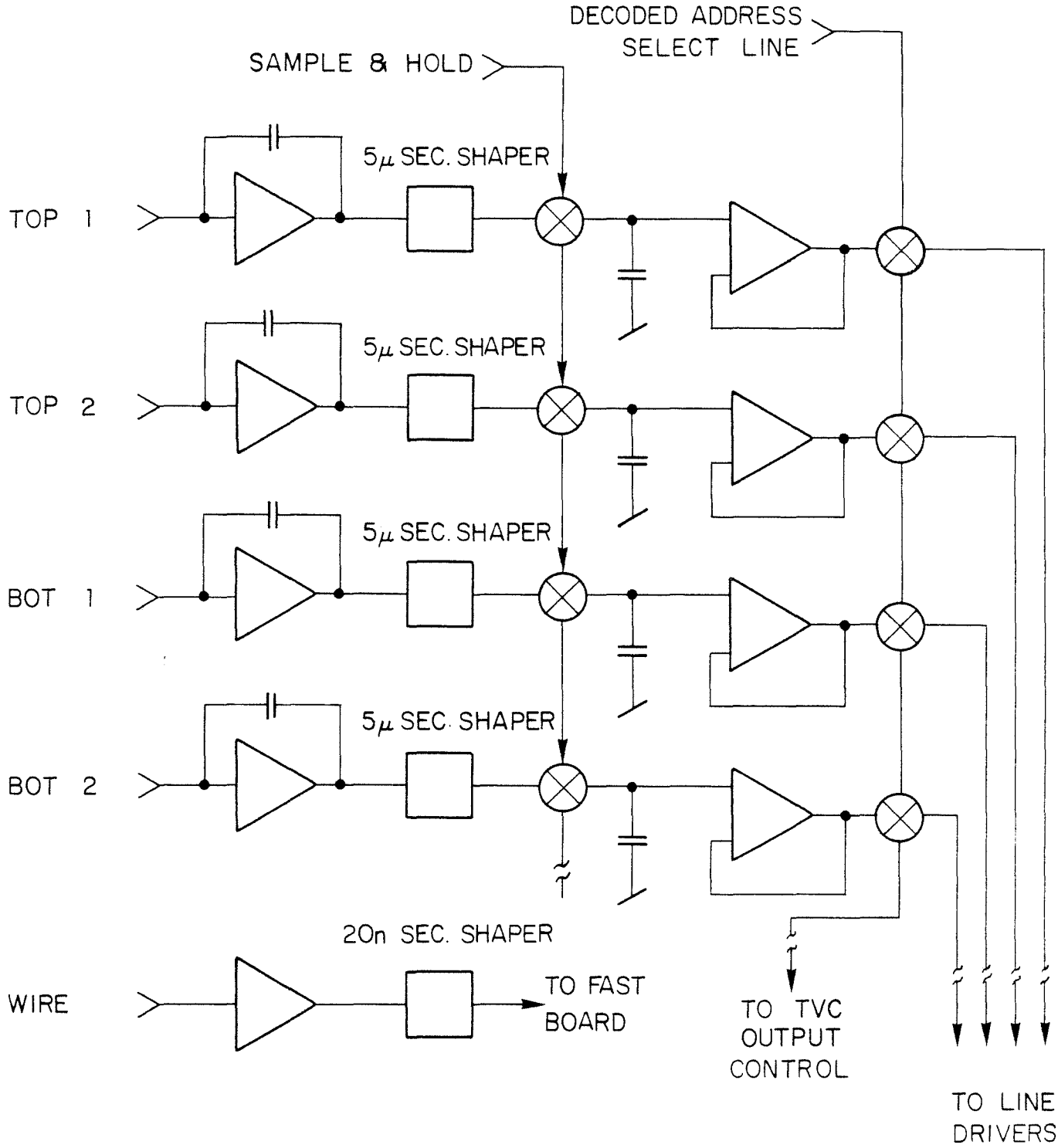

ANALOG BOARD

(Portion for 1 of 4 PDT)

FAST BOARD (PORTION FOR 4 OF 16 PDTs)

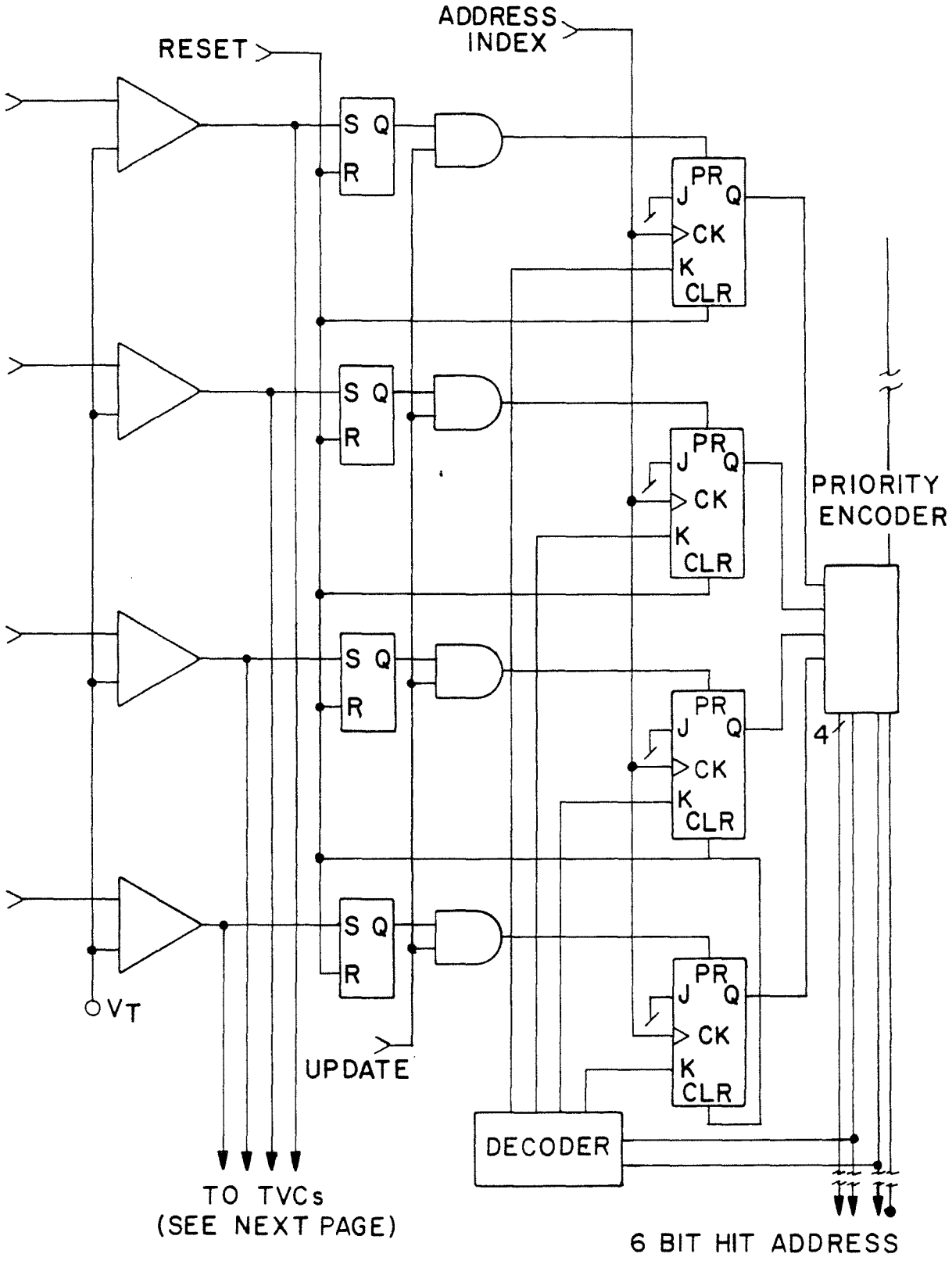

FAST BOARD (CONTINUED)
(Dual Hit TVC for 1 of 16 PDTs)

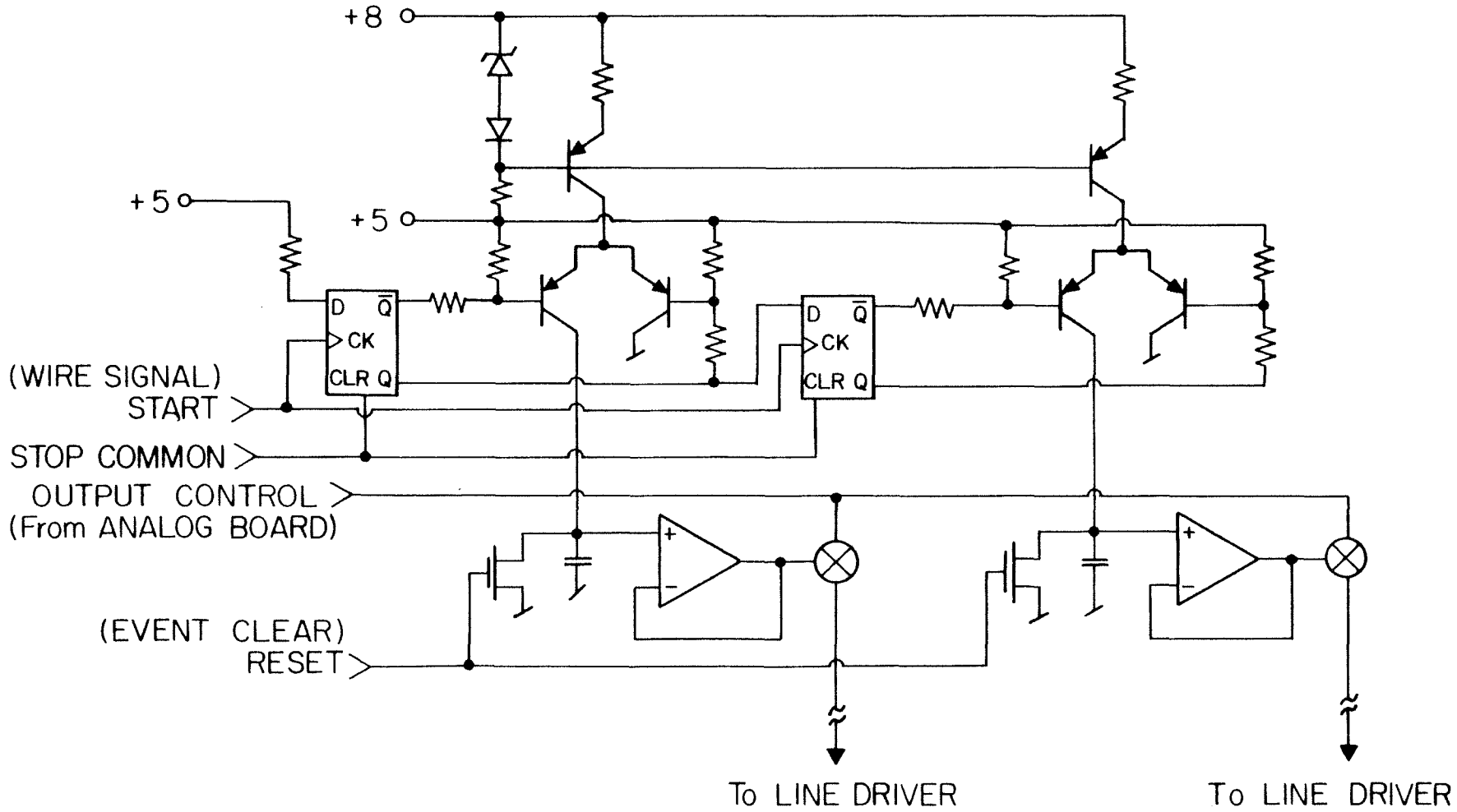

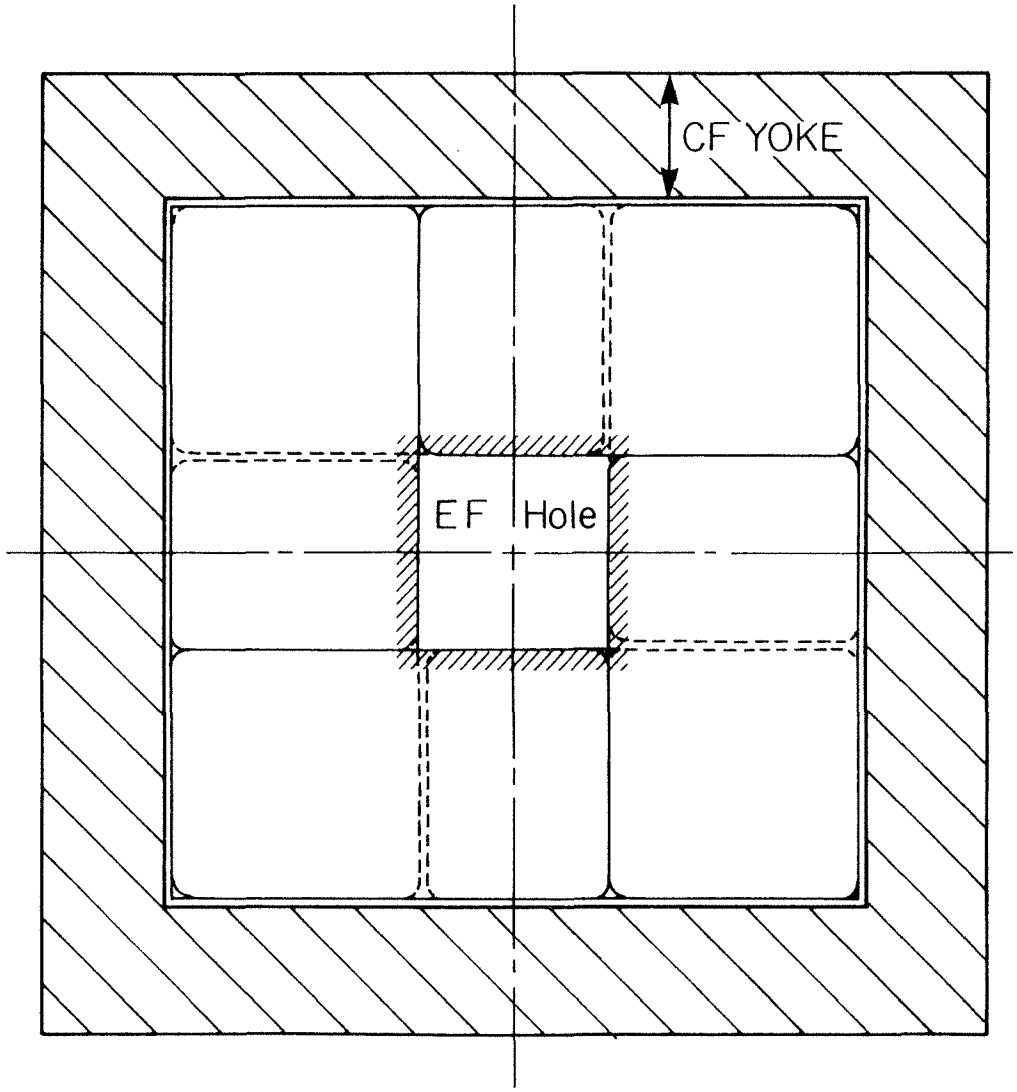

ARRANGEMENT OF EMA PLANES

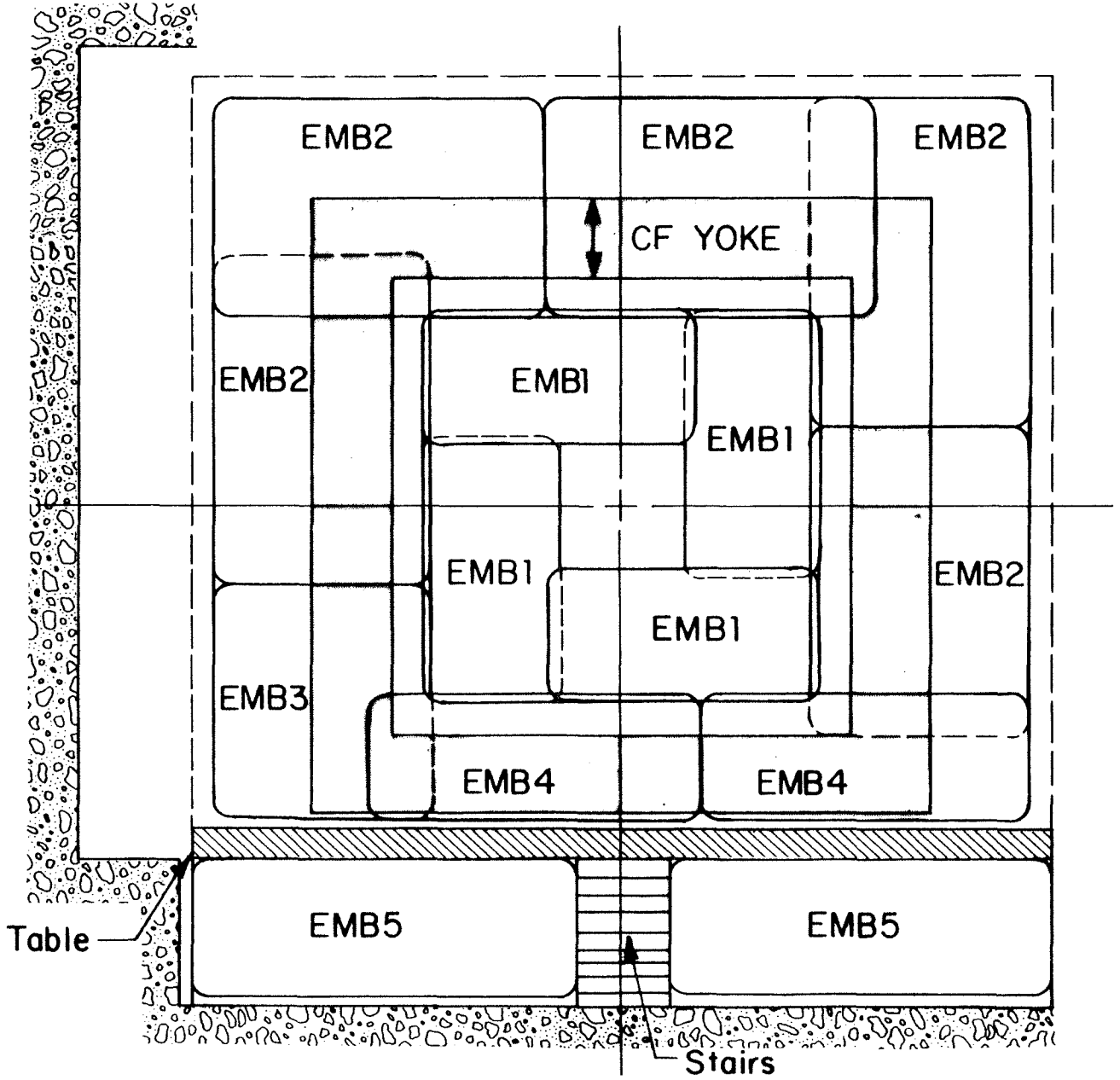

ARRANGEMENT OF EMB PLANES

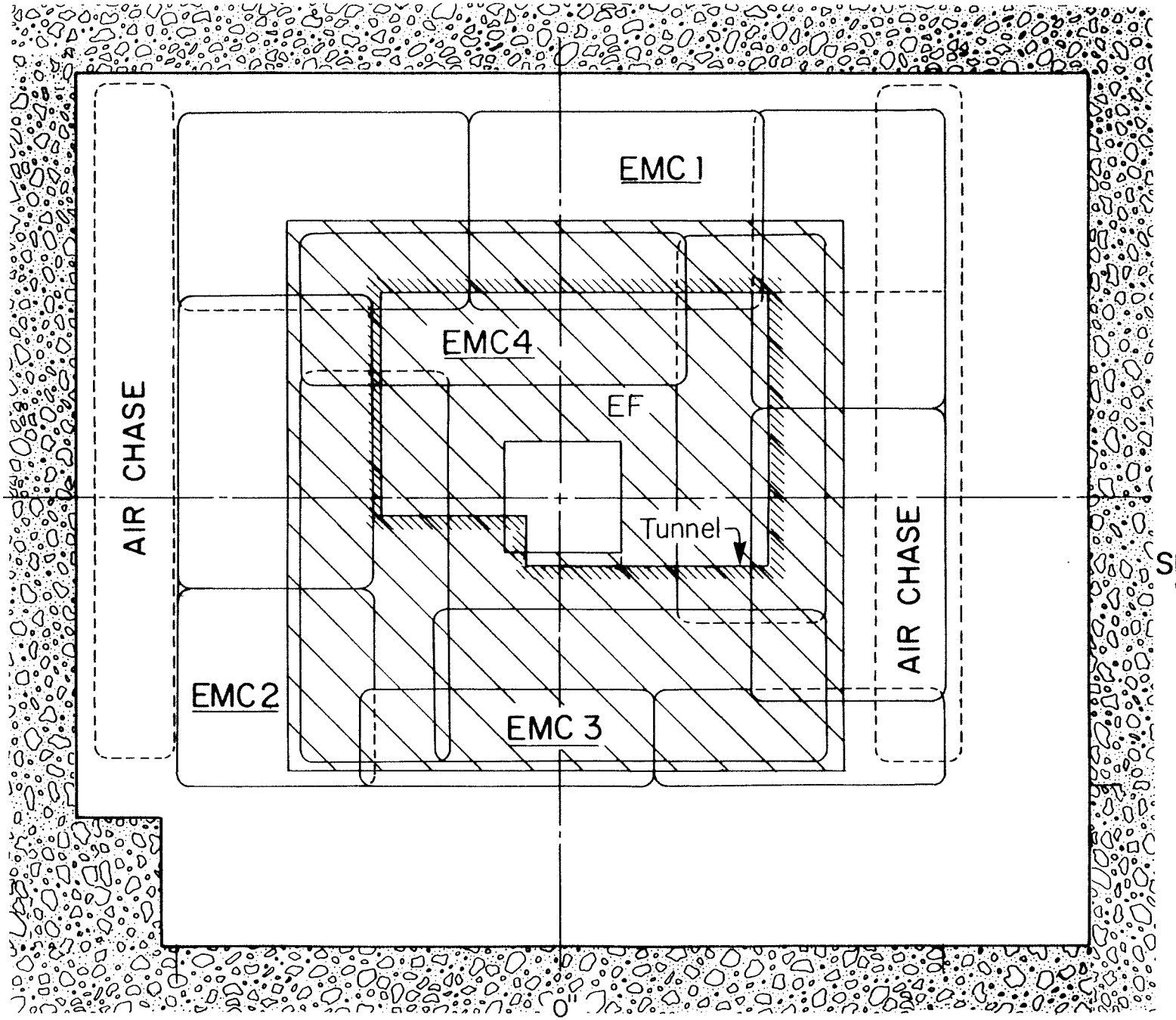

ARRANGEMENT OF EMC PLANES

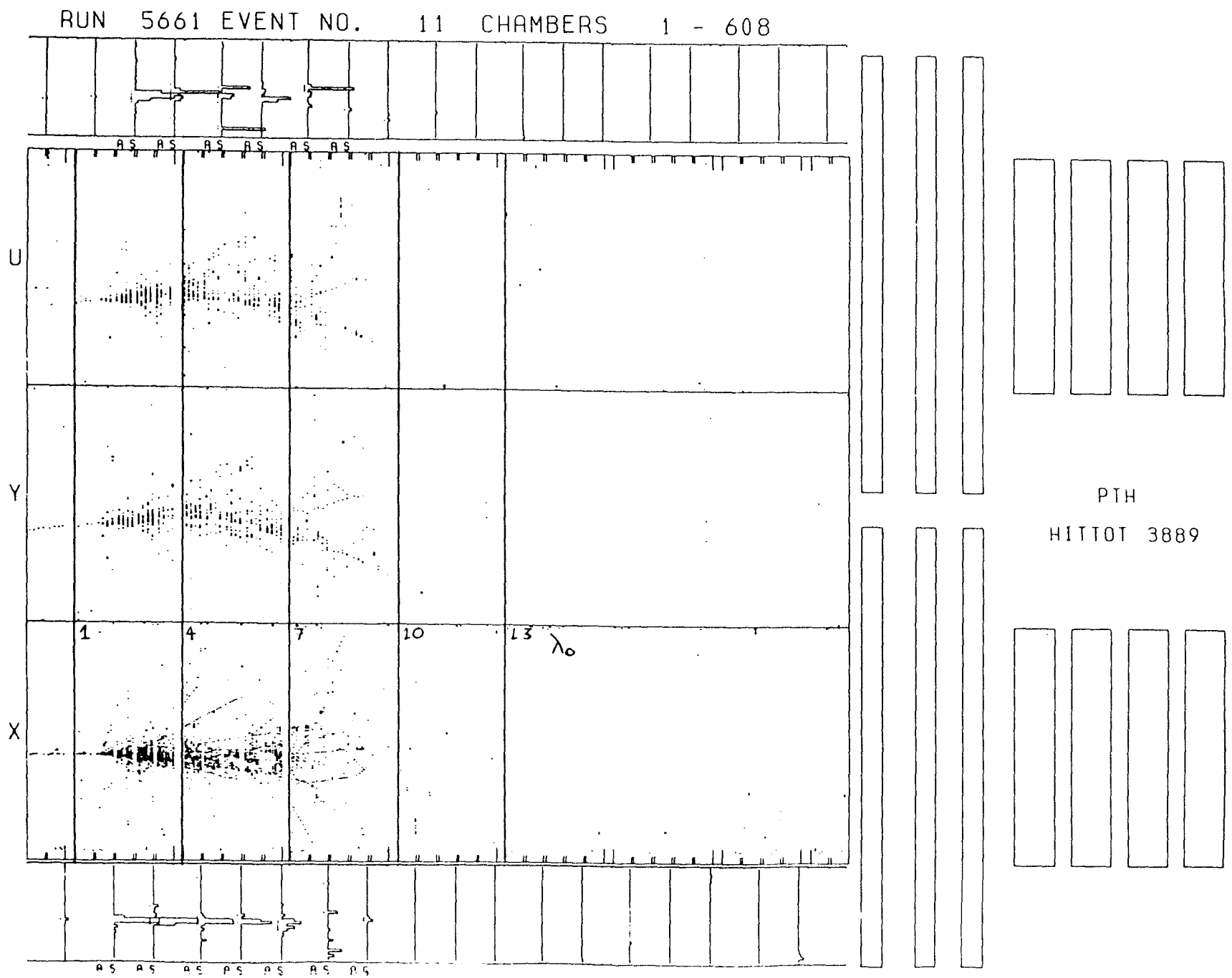
RUN 5661 EVENT NO. 11 CHAMBERS 1 - 608
U
Y
X
1
4
7
10
13
λ_o
PTH
HITTOT 3889

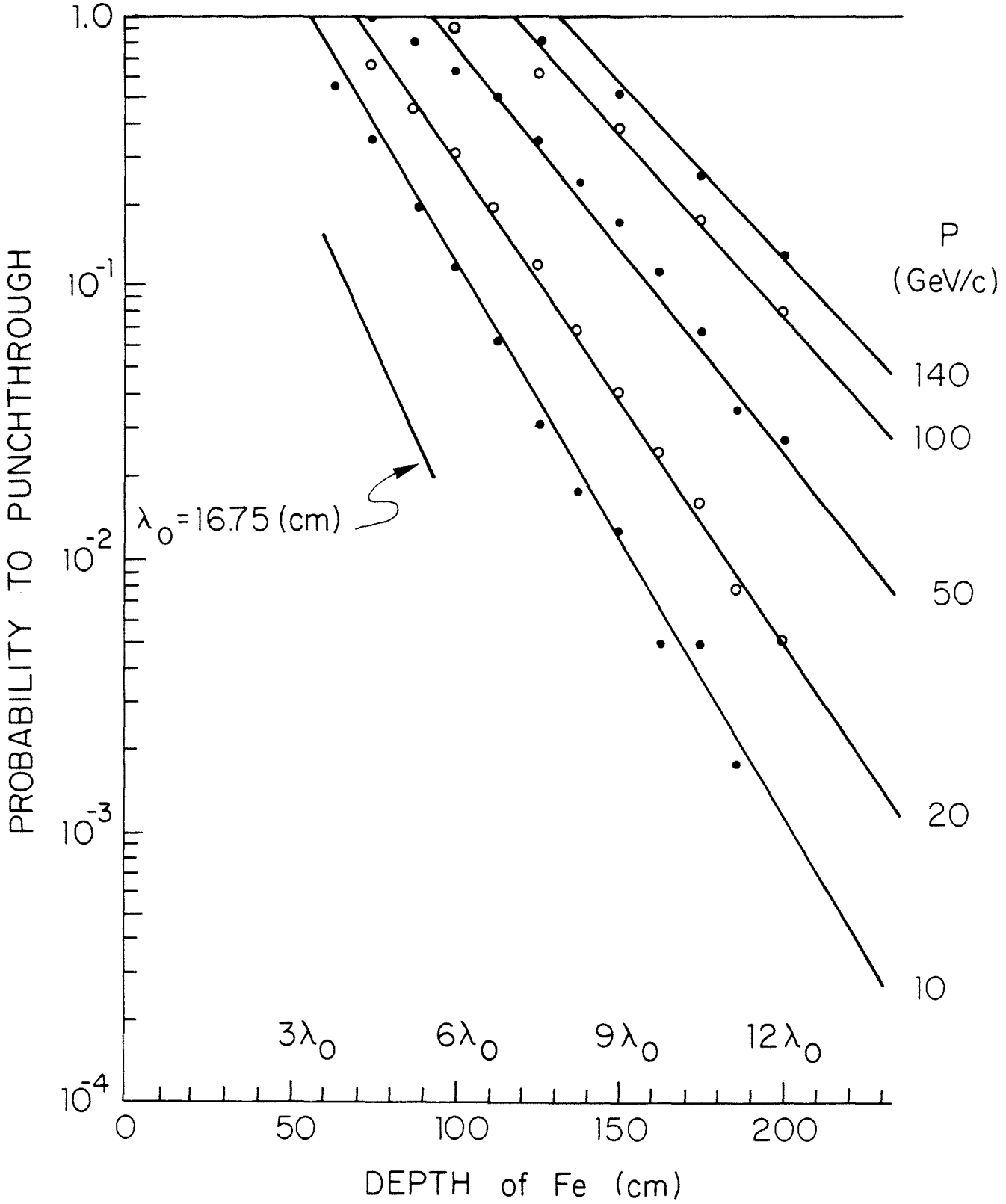

WA1 PUNCHTHROUGH DATA

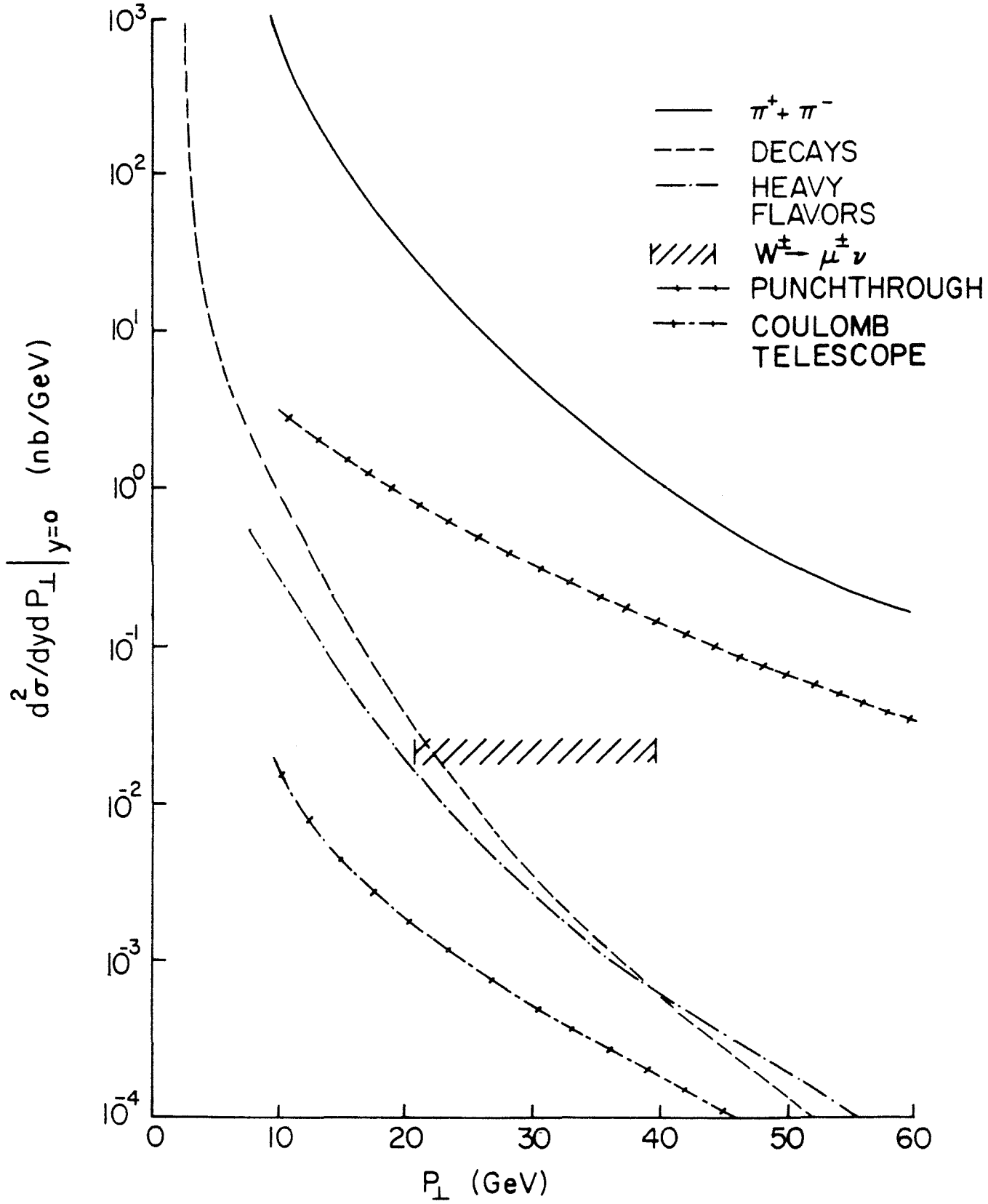
$\pi^+ + \pi^-$
DECAYS
HEAVY FLAVORS
$W^\pm \to \mu^\pm \nu$
PUNCHTHROUGH
COULOMB TELESCOPE
$d^2\sigma/dy\,dP_\perp\big|_{y=0}$ (nb/GeV)
10^3
10^2
10^1
10^0
10^{-1}
10^{-2}
10^{-3}
10^{-4}
0
10
20
30
40
50
60
$P_\perp$ (GeV)

MUON BEAM TEST SETUP

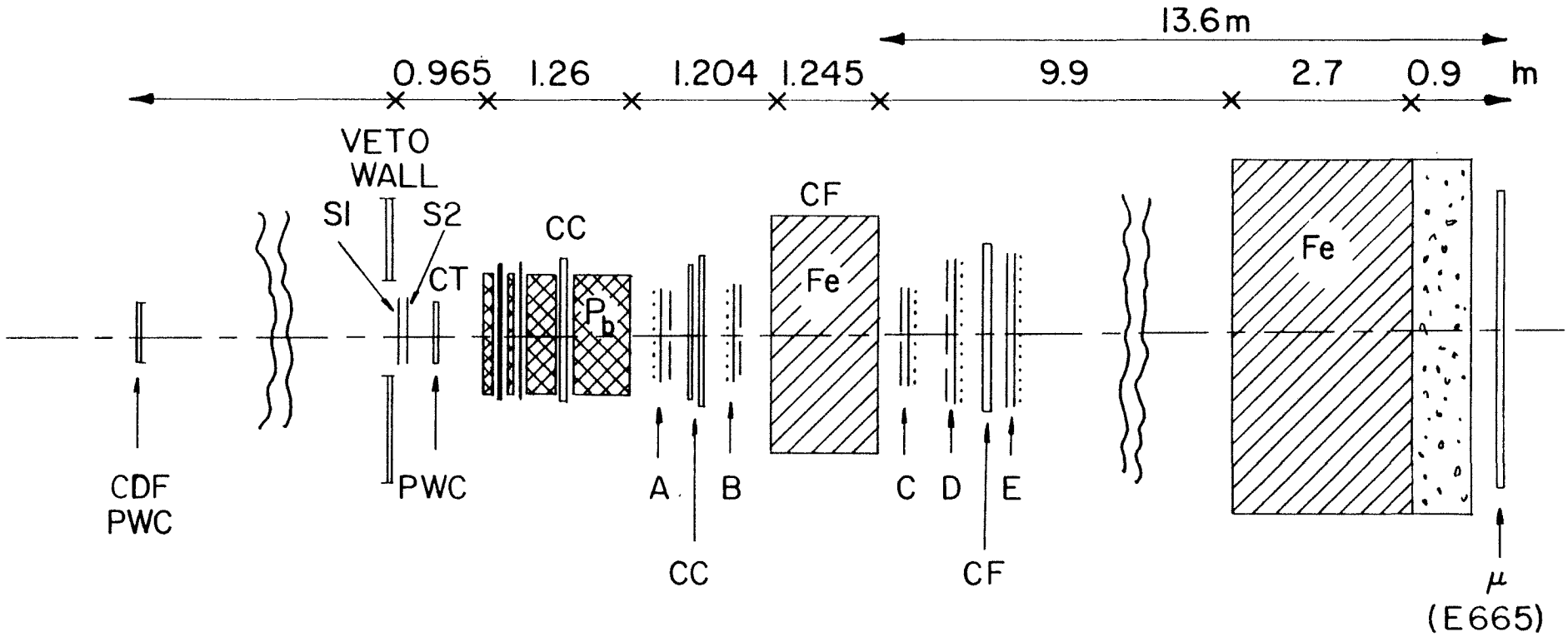

MODE BEAM = $SI \cdot S2 \cdot \overline{V}$

TRIGER = $BEAM \cdot CC \cdot CF$

		SI,S2	PWC	A,B	CC	C	D,E	CF	μ
DETECTOR	(cmW)	7.8	6.4	17.8	25.4	35.6	73.7	63.5	80
SIZE	(cm H)	7.8	6.4	20.3	25.4	35.6	35.6	35.6	80

150 GeV μ TAG DATA

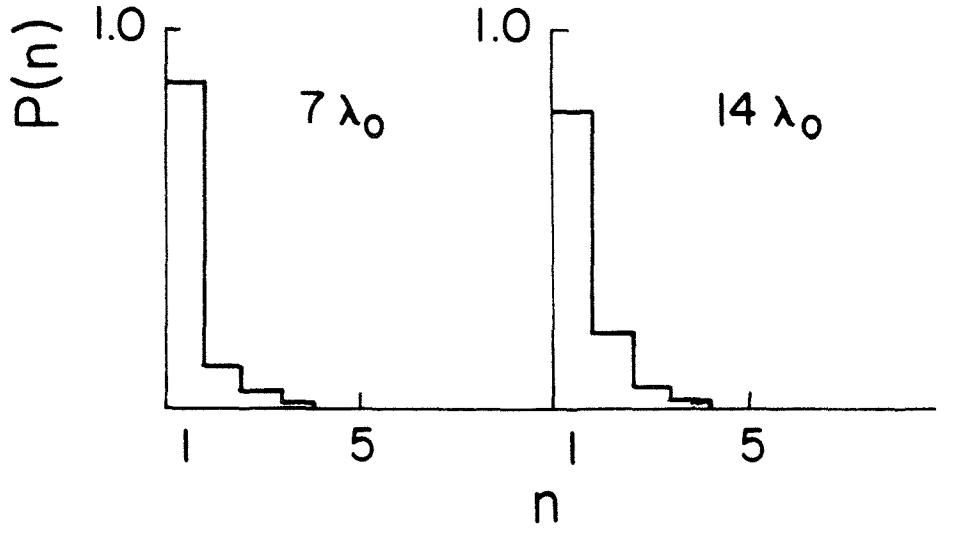

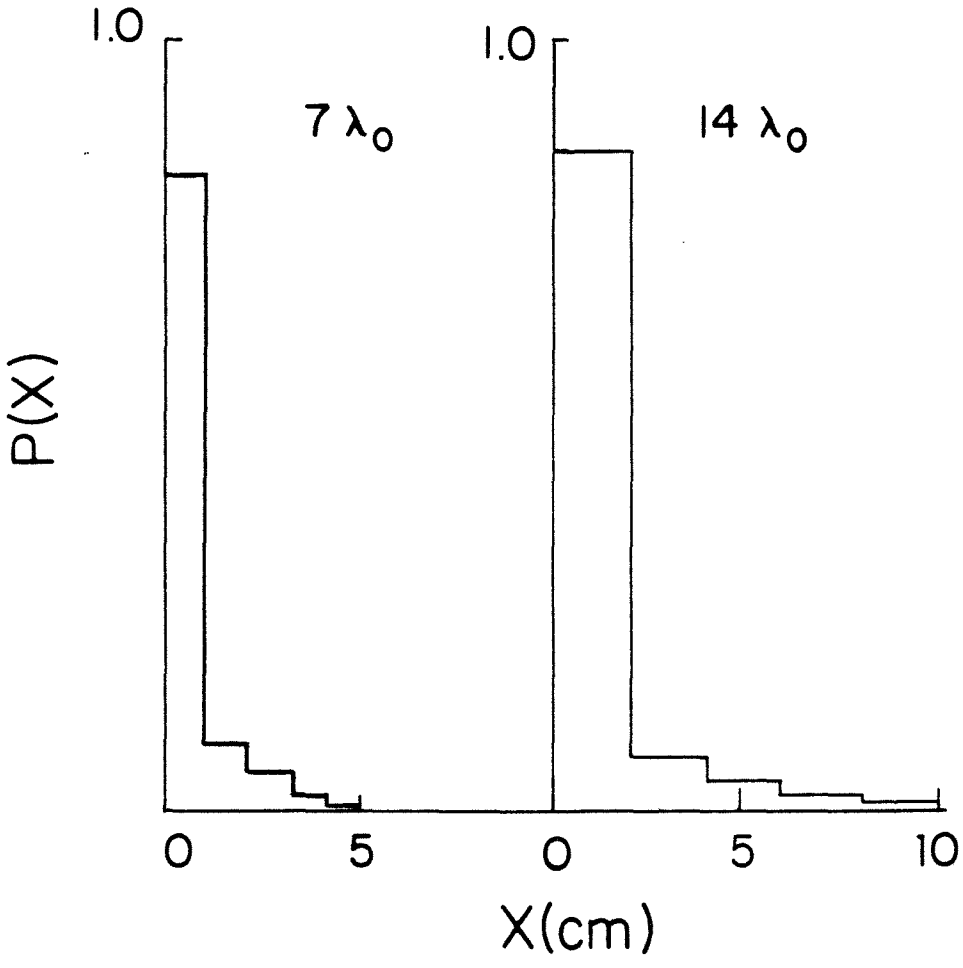

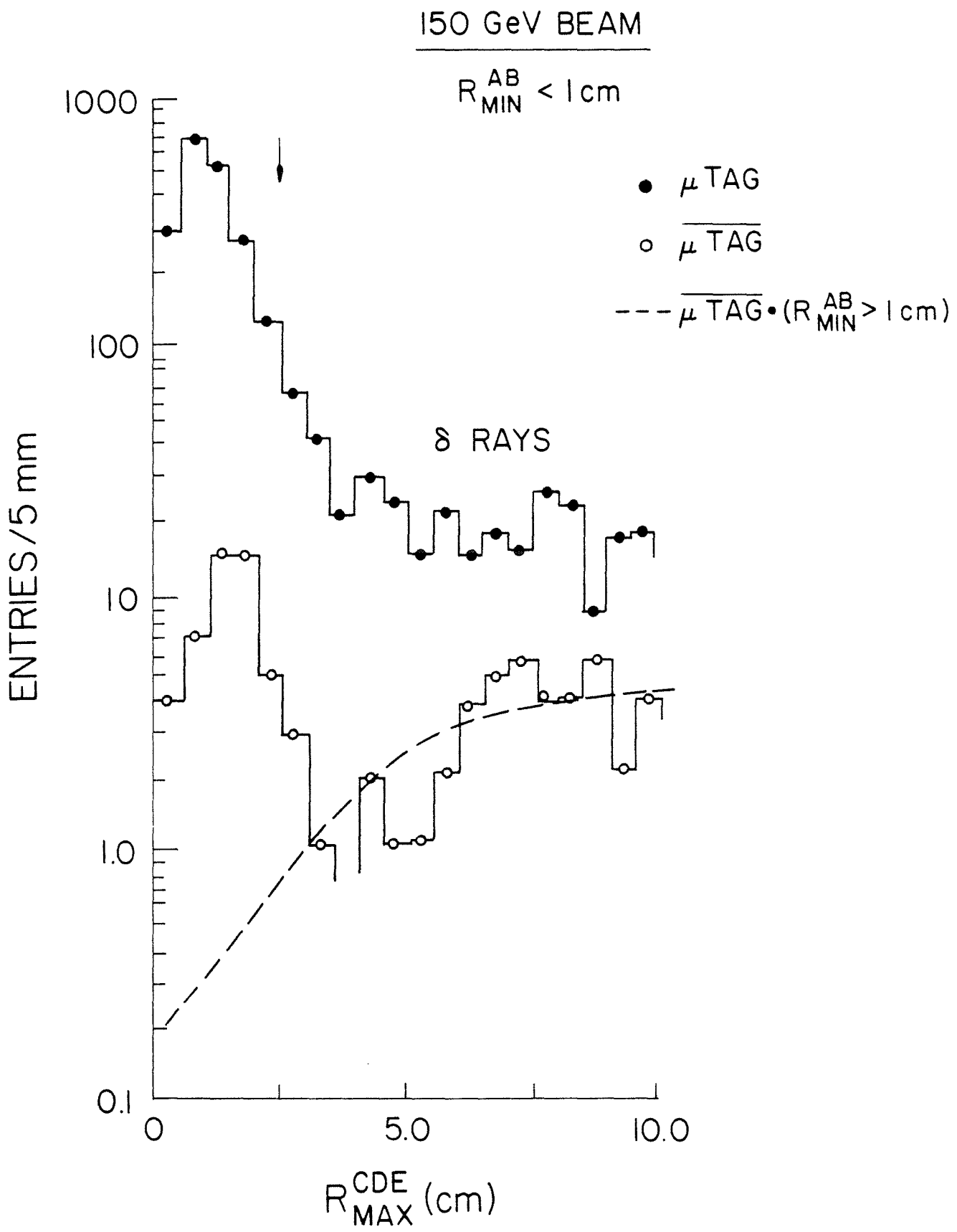
150 GeV BEAM
$R^{AB}_{MIN} < 1$ cm
μ TAG
$\overline{\mu\ TAG}$
$\overline{\mu\ TAG} \cdot (R^{AB}_{MIN} > 1\ cm)$
δ RAYS
1000
100
10
1.0
0.1
ENTRIES/5 mm
0
5.0
10.0
R^{CDE}_{MAX} (cm)

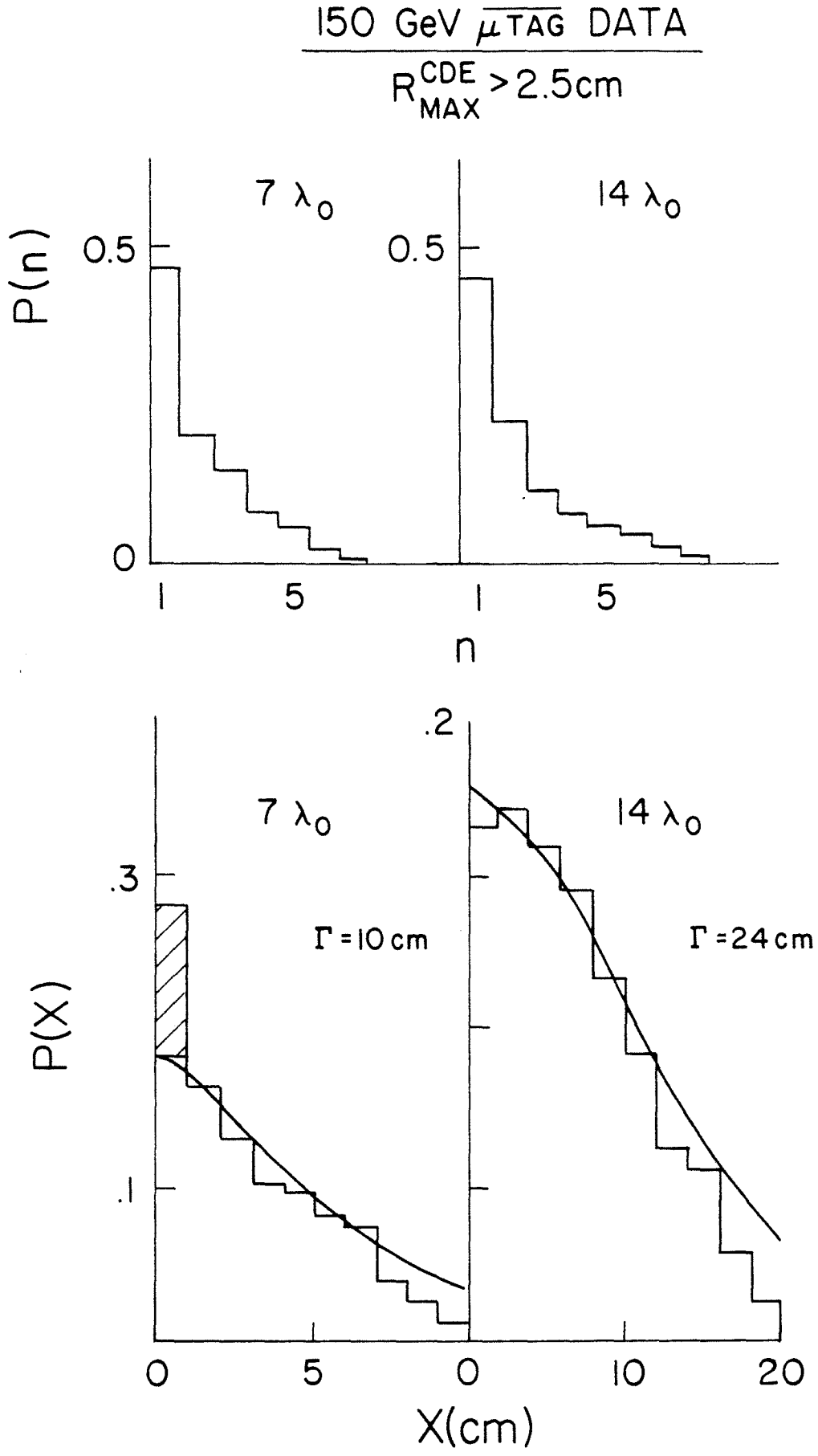
150 GeV $\overline{\mu TAG}$ DATA
$R_{MAX}^{CDE} > 2.5cm$
7 λ_0
14 λ_0
P(n)
0.5
0
1
5
n
.2
.3
.1
P(X)
$\Gamma = 10\,cm$
$\Gamma = 24\,cm$
0
10
20
X(cm)

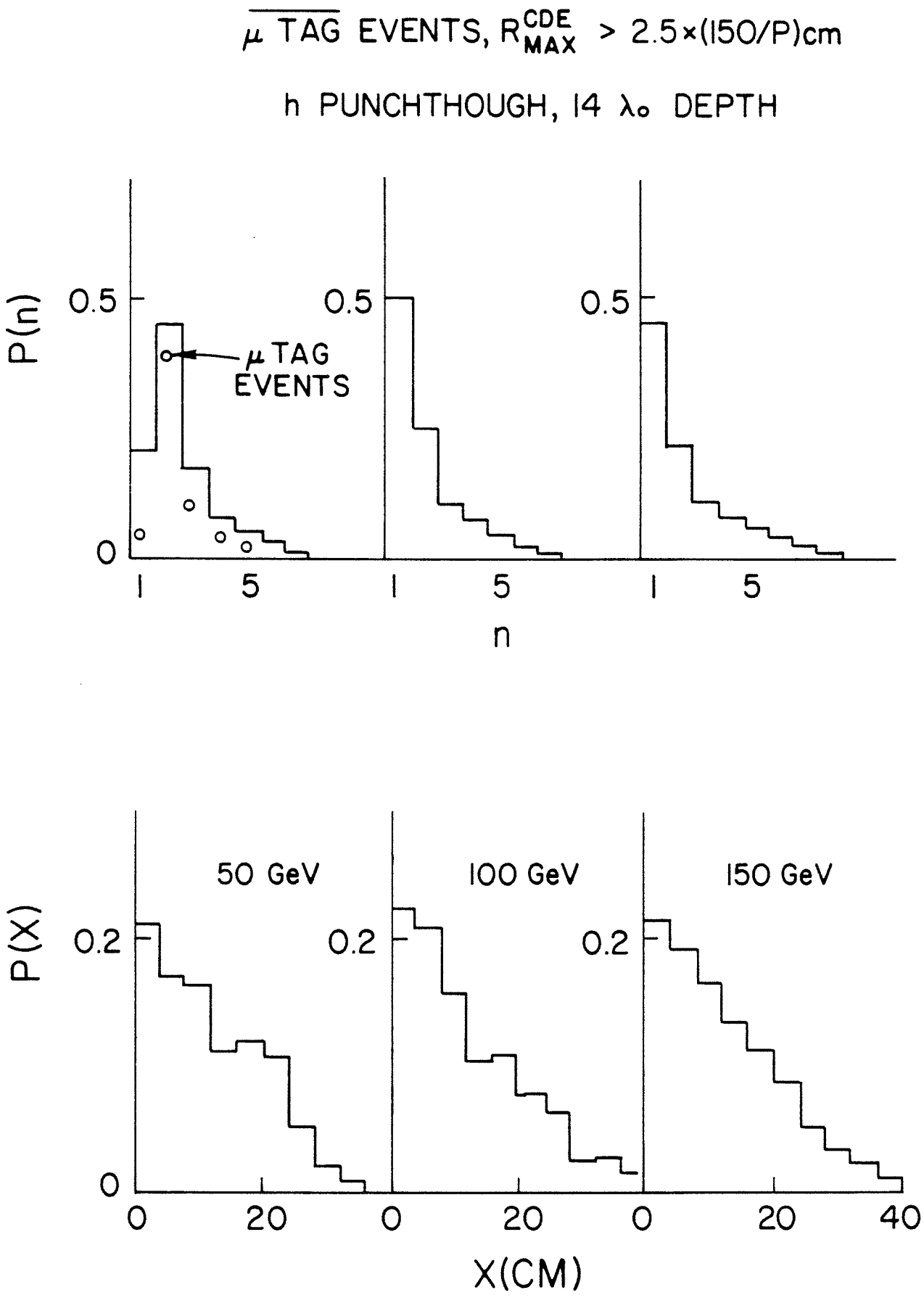
$\overline{\mu}$ TAG EVENTS, R^{CDE}_{MAX} > 2.5×(150/P)cm
h PUNCHTHOUGH, 14 λo DEPTH
P(n)
0.5
0.5
0.5
0
μ TAG EVENTS
1
5
1
5
1
5
n
P(X)
50 GeV
100 GeV
150 GeV
0.2
0.2
0.2
0
0
20
0
20
0
20
40
X(CM)

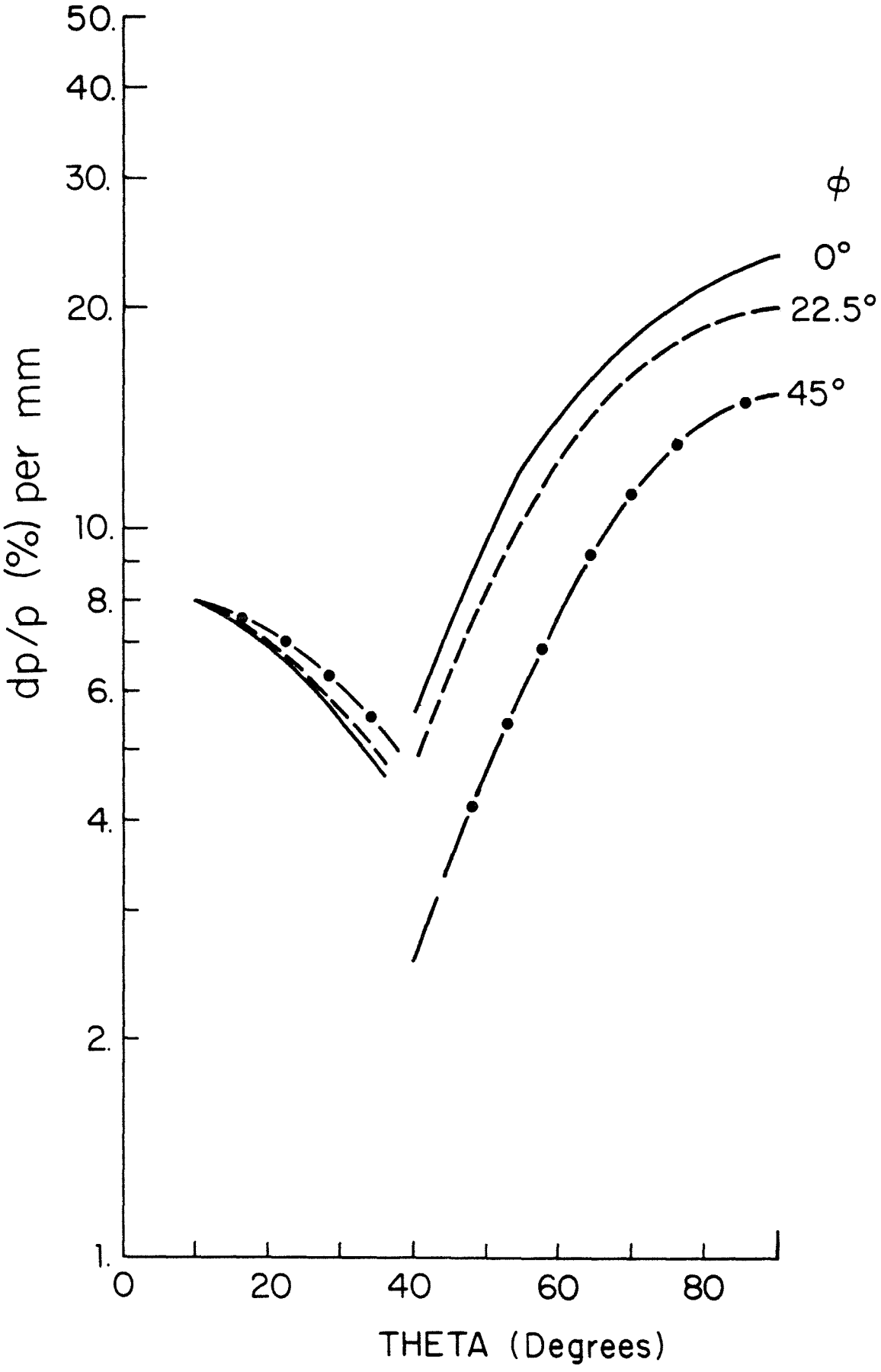
50.
40.
30.
20.
10.
8.
6.
4.
2.
1.
dp/p (%) per mm
0
20
40
60
80
THETA (Degrees)
φ
0°
22.5°
45°

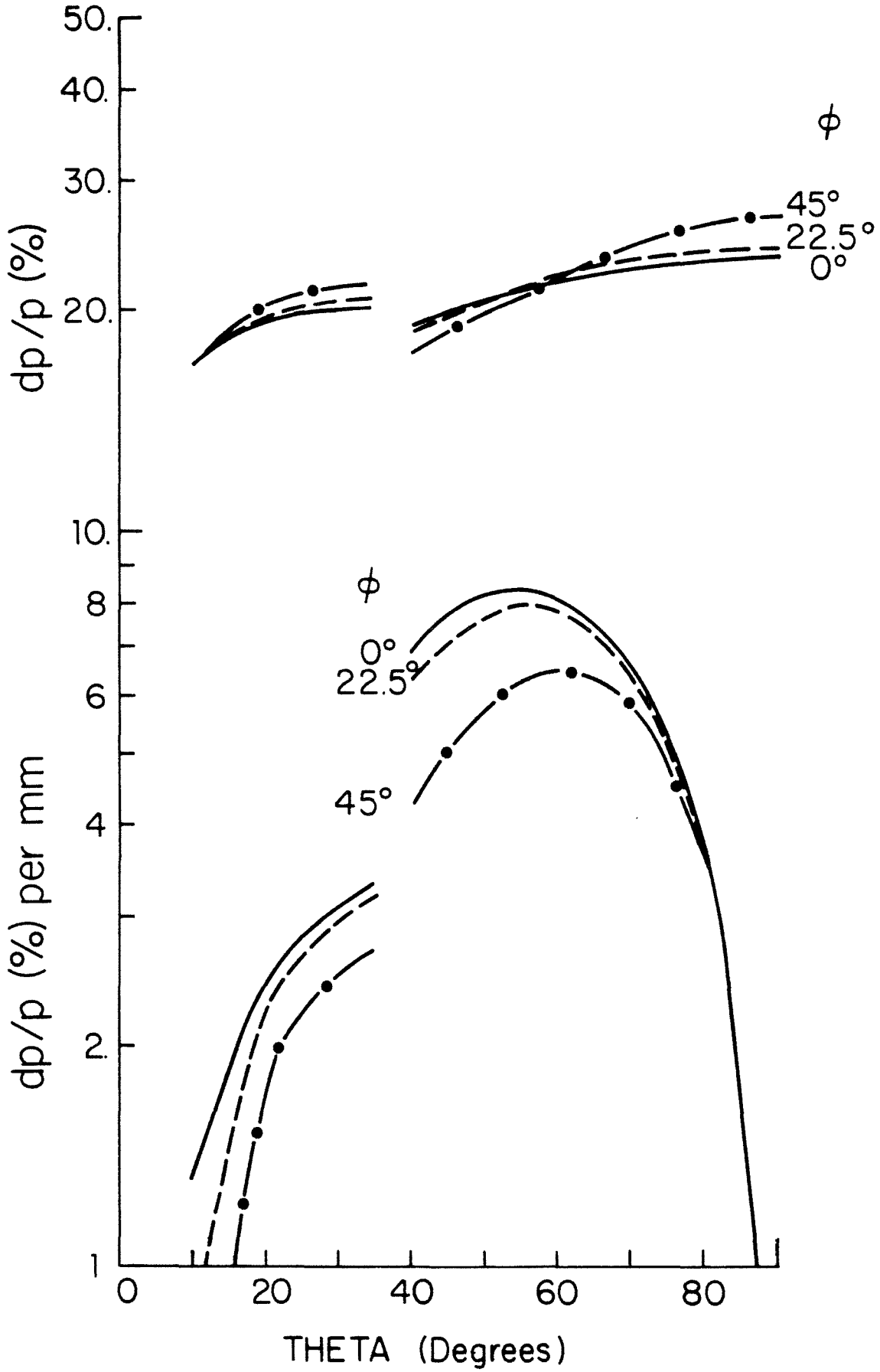
50.
40.
30.
20.
10.
8
6
4
2.
1
dp/p (%)
dp/p (%) per mm
φ
45°
22.5°
0°
φ
0°
22.5°
45°
0
20
40
60
80
THETA (Degrees)

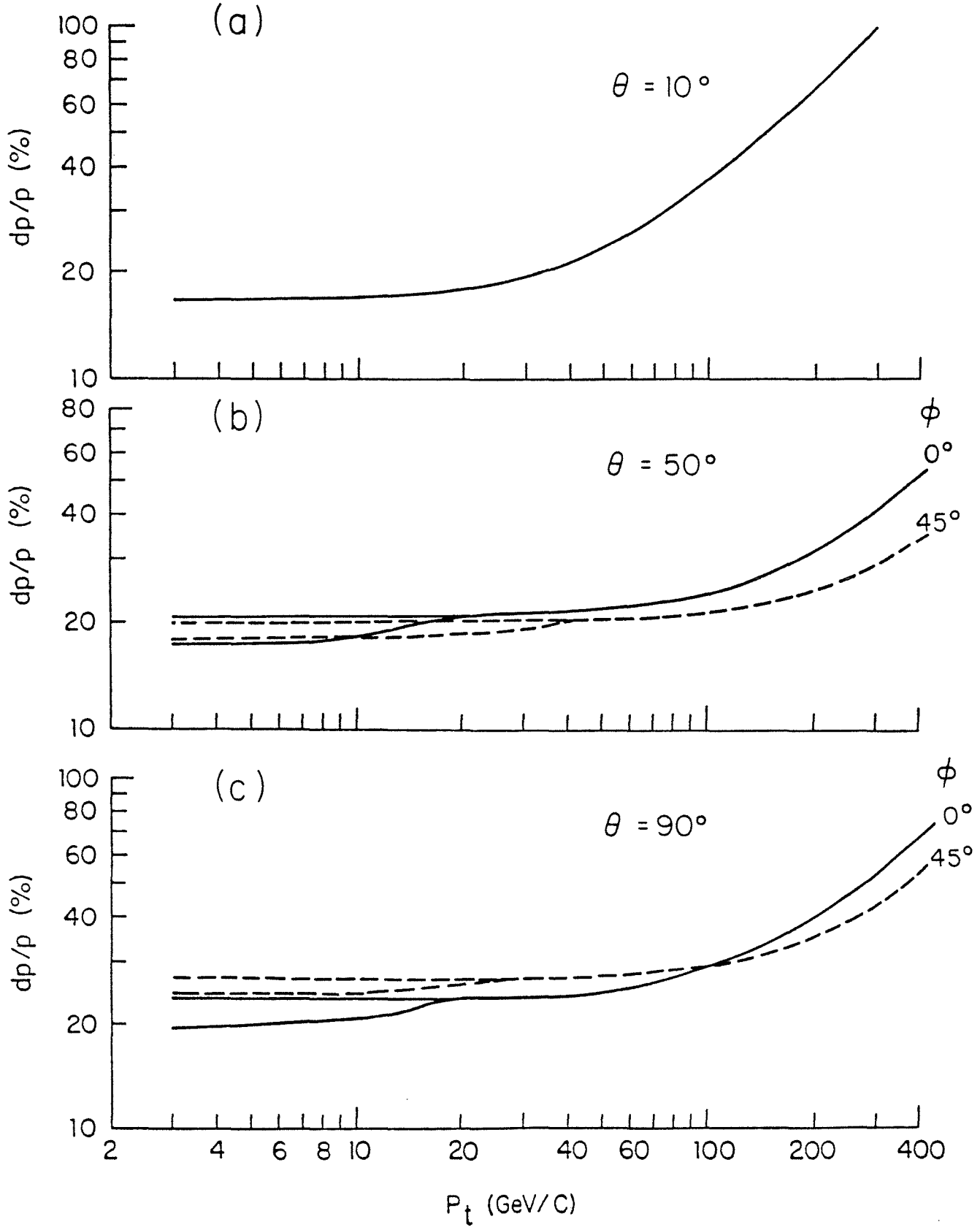
(a)
θ = 10°
(b)
θ = 50°
φ
0°
45°
(c)
θ = 90°
φ
0°
45°
dp/p (%)
100
80
60
40
20
10
2
4
6
8
10
20
40
60
100
200
400
Pt (GeV/C)

7. TRIGGER SYSTEMS

The interaction rate at nominal luminosity is $R_I \simeq 50$ kHz. The task of the trigger system is to provide incisive selections of events on the basis of physical criteria. To accomplish this goal, the trigger electronics is designed as a multi-level system. This architecture is chosen to reduce the deadtime of the trigger. The lowest level, level 0, selects beam-beam interactions using scintillation counters on a ~100 nsec time scale. Level 1 then selects the interactions of interest using conventional trigger logic on a few μsec time scale using some specific limited analog information from the calorimeter and muon PDTs. Finally, level 2 selects the final data to be logged on the time scale of ~2 msec using detailed algorithims operating on the complete event record. The level 2 trigger is described in more detail in Chapter 8.

7.1 LEVEL ZERO TRIGGER

The level 0 trigger is assumed to consist of three items:

1. A timing signal giving the beam-crossing time derived from the accelerator clock. This would set the zero time for all the TDC's in the system.
2. Signals from scintillator walls placed upstream and downstream of the detector covering the aperture of the tunnel. These would supply a veto to the trigger to discriminate against beam halo and background particles produced by interactions outside the beam crossing region.
3. Timing signals from scintillators covering the endplug calorimeters. These counters, triggering on the beam jets accompanying any interaction of interest, would provide the timing signals from which the position of the interaction within the interaction diamond would be determined. With care, the uncertainty in the timing difference of the two ends can be limited to Δt = 200 psec. This translates into a position resolution of

$$\Delta x = c\Delta t/2 = 3 \text{ cm.}$$

This distance will be encoded as a three bit number and passed on to the level one trigger. These scintillators will serve the added important function of monitoring the luminosity. Careful attention to the timing will be needed to maintained sensitivity to multiple interactions in a single crossing. The extent of the interaction diamond (σ = 28 cm) should help in properly counting this class of events.

7.2 LEVEL ONE TRIGGERS

In this discussion we assume a luminosity of 10^{30} cm^{-2} sec^{-1} and a total cross-section of 100 mb giving an interaction rate of 100 kHz. The problem that the level one trigger must solve is how to reduce this trigger rate by a factor of >200 without sacrificing any "interesting physics" in the process. The level one trigger is assumed to introduce no dead time. That is, it must make all decisions in the time between beam crossings. We have also anticipated the need of a "level 1.5" trigger which would not satisfy this criterion, if certain parts of the detector such as muon PDT time signals or TRD hit encoding will not be able to provide the needed information in the limited inter-bunch time. When appropriate trigger requirements are met, the system will wait an additional 10 or 20 μsec for this information to arrive. The additional dead time introduced by this wait will be minimal because the level 1 trigger requirements will have reduced the candidates to a small number. The collider is expected to start with three bunches each of protons and anti-protons which would imply a time between crossings of 7 μsec. In anticipation of the time when the number of bunches will be doubled, we have made all our designs with the assumption of a 3.5 μsec time between crossings. In actuality this means that the level one trigger must make its decision in 1.9 μsec with the remaining 1.6 μsec being lost to the charge collection time in the liquid argon calorimeter and to the inevitable cable delays. This short time scale affects our trigger design in a fundamental way: all decisions must be made in a global way without resort to iterative or serial techniques.

7.2.1 Calorimeter Trigger

The triggers to be discussed here are all derived from analog information read in from the calorimeters. A number of important questions must be

addressed if optimum use of this information is to be made at the trigger level:

1. Trigger Segmentation. Current understanding of the underlying physics processes at high energy as well as the experience at CERN indicate that it is highly useful to arrange the trigger in projective towers pointing to the interaction vertex weighted by sin θ. In the absence of other constraints, the logical tower size would be set by the size of the smallest jet (in angular extent) that would be encountered or the smallest tower size, whichever is larger. The finite size of the interaction region complicates this simple argument. We have performed Monte Carlo studies of this question[1] and have arrived at the following conclusions:

   a) For electromagnetic (EM) deposition a reasonable choice of tower size in azimuthal angle and pseudo-rapidity is $\Delta\phi = 11.25°$ and $\Delta\eta = 0.2$.

   b) For hadronic energy (H) the choice can be coarser by a factor of two in both variables, $\Delta\phi = 22.5°$ and $\Delta\eta = 0.4$.

This choice results in $32\times50 = 1600$ EM trigger towers and $16\times25 = 400$ H trigger towers.

2. In order to minimize amplifier noise in the ULA, the integrating times should be as long as possible, of the order of microseconds in our case. This precludes the use of these signals for the fast trigger and dictates that we use instead a "fast out" derived from the amplifier signals by differentiating the signal with a time constant of 200 nsec. The increased amplifier bandwidth in the signal introduces noise. Our "hard-wired" tower structure assumed above helps in this respect since the noise adds stochastically and the signals add in

phase. In Chapter 5 the noise was estimated at 13 MeV for a single tower, 40 MeV for a 10 tower trigger signal, and about 0.9 GeV for the full detector. This contributes to the E_T smearing at the trigger level but at this level does not represent a serious problem.

3. Electronic and Hadronic Subdivision. One of the principal advantages of a uranium calorimeter is its uniform response to deposited hadronic or electromagnetic energy. There is, therefore, no clearly defined boundary between the EM and H sections. It is, nevertheless, useful from the trigger viewpoint to make such a division. We wish to identify electrons and photons in the presence of hadronic energy and therefore all the towers are assumed to consist of two longitudinal sections: the first 20 radiation lengths or one absorption length will be called the EM section and the renmainder will be the H section.

We note that for purposes of the first level calorimeter trigger we emphasize good measurements of transverse energy, missing vector momentum, and jets.

In order to estimate rates for our various triggers we have relied on the results of UA1 and UA2 and on Monte Carlo simulations of our detector exposed to events generated by ISAJET. Our principal conclusions to date are the following:

1. The Total Transverse Energy E_T Trigger. A threshold of 75 GeV on this variable will reduce the trigger rate to about 50 Hz. A curve derived from our Monte Carlo is shown as Fig. 7.1. It shows the trigger rate as a function of threshold cut. The events were generated with the expected distribution along z (the beam direction) but sin θ was computed as though the events were all produced z = 0. It is clear that this trigger by itself would bias against a large class of

interesting events such as electrons from W decays. It will, however, be useful in conjunction with other criteria, such as activity in the muon or EM sectors.

2. Missing Transverse Momentum (MP_T). The UA1 experience has shown the value of being able to calculate the missing transverse momentum. One of the advantages of a ULA calorimeter is its improved energy resolution and hence its improved transverse momentum resolution. This resolution is ultimately limited by real physics such as missing energy carried away by neutrinos. We have attempted to estimate these effects in Fig. 7.2, showing the trigger rate vs. the threshold of the Mp_T cut for our detector exposed to ISAJET generated events. To achieve a trigger rate of 5 Hz we require a trigger threshold level of about 10 GeV/c. We should note here that the MP_T trigger will also be used together with other criteria as was the case of the E_T trigger.

3. Jet Trigger. At $\sqrt{s}$=2000 GeV, the dominant source of jets is expected to be from two jet events. The expected trigger rate of our "jet trigger" vs. the jet threshold is shown in Fig. 7.3. A rate of 50 Hz can be achieved with a threshold setting of 20 GeV.

4. Electron-Photon Trigger. A requirement that E_T in an EM trigger tower exceed 15 GeV will reduce the trigger rate to about 100 Hz.[3] This rate is almost wholly due to π^0 showers, according to our ISAJET simulations. For a 20 GeV threshold, the rate is about 15 Hz. We have included provisions in the trigger to sharpen the distinction between EM and H energy by using the H section as a veto for the EM.

7.2.2 Muon Level One Trigger

The task of the muon trigger is to select muons from a background of cosmic rays, decays, and hadronic punchthrough. This selection ideally should be only on the basis of the p_T of the muon and not on the angle θ. The ability to trigger on muons over the full angular coverage depends upon the thick uranium and iron to control both punchthroughs and decays, combined with an adequate lever arm and granularity in the muon chambers to measure the bend angle.

Punchthrough and decay rates were estimated from Monte Carlo minimum bias events generated using ISAJET and from the test beam data discussed in Section 6.4.2. The total charged hadron yield and muon decay rate for $10° < \theta < 170°$ ($|y| < 2.4$) is given in Fig. 7.3 as a function of p_T. Punchthrough at these low p_T values is quite small, as discussed in section 6.4.1. Muon rates from various sources which exit the steel are shown in Fig. 7.5. Clearly decays are the dominant source of muons at this low p_T. The rate rises exponentially with θ which makes small angle triggering difficult. In Fig. 7.6 are shown the rates in the central tracker, in layer A, after the calorimetry and in layer B outside the iron as evaluated by Monte Carlo. Typically, the rate in the A PDT layer is $\simeq$ 20X the rate in the B layer. The raw beam-beam trigger rate of muons exiting the steel for all angles is estimated to be 50 Hz. This rate is predominately at small angles (Fig. 7.6) and necessitates a trigger which calculates p_T and utilizes the sharp p_T cutoff seen in Fig. 7.4.

The rates for decay and punchthrough are discussed in sections 6.4.3 and 6.4.1 respectively. The trigger rate is dominated by π and K decays which occur at a rate ~5 KHz per unit of rapidity. Most of the decay muons do not penetrate the iron. This cut on momentum leads to a muon rate outside the

toroids which depends exponentially on θ, as seen in Fig. 7.5. This rate would easily saturate data taking and must be reduced by the level 1 trigger.

The elements available to a trigger scheme are, z_v = vertex location, A = muon chamber coordinate inside the steel, and B,C = coordinates outside the steel. For CF the trigger coordinates are z while for EF they are x. Basically, at the low p_T appropriate to triggering, z_v is masked by the ~230 X_0 of calorimetry and A has too short a lever arm to offer much p_T discrimination. The trigger then relies on B and C with resolution 5 cm (10 cm cell with left-right ambiguity broken using adjacent shifted cells) and a lever arm between station B and C sufficient to set a p_T cutoff which will control the trigger rate.

A Monte Carlo program has been written to study the trigger in detail. Effects included are detector geometry, energy loss, multiple scattering, and magnetized iron magnetic bending. For the central detector, a charged particle loses ~2.2 GeV in CC and 1.9 GeV in CF for a total average range cut of 4.1 GeV which leads to a cut $p_T \gtrsim 2.8$ GeV. For the forward-backward detectors the numbers are similar, which leads ($\theta > 10°$) to a cut $p_T \gtrsim 1.0$ GeV.

These cuts imply that the raw beam-beam rate into the central muon chamber is ~0.02 Hz per unit of rapidity. Clearly, the trigger need only be stringently applied in the forward-backward detectors. Figure 7.7 shows the $(x_B \cdot x_C)$ coincidence matrix for $\theta \sim 20^0 \pm 6^0$ for all events which pass through EF. In this figure and those which follow, p_T is generated uniformly from 0 to 10 GeV. The locus for fixed p_T, in the absence of z_v source size, energy loss, and multiple scattering would consist of two straight lines due to μ^+ and μ^-. Multiple scattering smearing is the dominant effect. Figure 7.8 shows the same events, but with the restriction $p_T > 5$ GeV. Clearly, it is

possible to remove the low p_T muons that exit EF by requiring this $x_B \cdot x_C$ coincidence.

A summary of the rejection power of the B • C coincidence is shown in Fig. 7.9 for $\theta \sim 90°$, 20°, and 12°. At a fixed C cell of 5-cm width, the distributions of B cells for various p_T bands are shown. Recall that for fixed p resolution the p_T resolution goes as $\sim 1/\theta$. However, improved lever arm, thicker steel, and improved vertex viewing angle alleviate this problem somewhat. Clearly at wide angles a cut at $p_T = 4$ GeV easily gives full efficiency for $p_T > 5$ GeV and zero efficiency for $p_T < 3$ GeV. This situation persists down to $\theta \sim 20°$, although the trigger bands are more compressed. Finally, at $\theta \sim 12°$ the matrix is still more compressed, and will leak very slightly for muons with $p_T \sim 3$GeV.

Assuming that $p_T \geq 3$ GeV, then the level 1 trigger rate does not exceed 0.04 Hz per unit of rapidity, or a beam-beam trigger rate at level 1 of 0.2 Hz. As described elsewhere (section 6.3.2), the PDT front-end electronics will supply fast priority encoded latch addresses. Beyond this level, commercial electronics will be used. First, a valid hit in adjacent cells (8-bit addresses) will be generated (5-cm width). These addresses will be passed through a commercial downloaded trigger matrix. All octants of CF and quadrants of EF detectors can trigger in parallel. The level 1 muon trigger decision will be available ~1.5 μsec after beam-beam crossing, at which point it is made available to the full level 1 trigger AND/OR network.

7.2.3 Muon Level 1.5 Trigger and Cosmic Rays

Cosmic ray level 1 muon triggers are a potential problem due to their high rate. They are also of great use for muon PDT chamber alignment and continuous monitoring of the performance of the entire detector.

In order to study the cosmic ray triggers, a Monte Carlo program was written. Cosmic ray muons were generated as $dI/d\Omega \simeq I_0 \cos^2\theta$ where I_0 is the vertical flux. I_0 was distributed as $E^{-\gamma}$ with $\gamma \sim 0.5$ for $E \sim 1$ GeV which is the CF range cut. Using $I_0 = 10^{-2}cm^{-2}sec^{-1}sr^{-1}$, the rate in CF layer C (top quadrant) is $R_{CF} \simeq I_0 A\Delta\Omega \simeq 88$ kHz.

Given a drift time of 1 μsec, and an interaction rate of $R_I = 50$ kHz the accidental rate is ~4400 Hz. A range cut of ~1 GeV is imposed by requiring a hit in the A layer since minimum bias events have few hits ($\lesssim$ 1% of R_I). The Monte Carlo predicts that this cut reduces the rate to 1400 Hz.

Applying the $z_B \cdot z_C$ correlation trigger, discussed in section 7.2.2, further reduces the rate to 308 Hz. This surprisingly small reduction factor is due to the $\cos^2\theta$ zenith angle distribution of cosmic rays, which is much less favorable than a distribution that is flat in this variable. Requiring further that $z_V = 0$ and that a point in z_A lie on the trajectory results in an additonal reduction factor of ~4, to a rate of 78 Hz.

Cosmic rays arrive randomly within the 1 μsec time window. Beam-beam muons have adjacent layer times $T_1 + T_2 = (d \pm \alpha a)/v_0$ where d = 5 cm, a = layer separation, and α = tangent of muon angle with respect to the tube normal. Using the latch hits to estimate α one can impose $T_1 + T_2 =$ constant to 100 nsec. This time check sum cut reduces the rate down to 8 Hz. This means one has a level 1 trigger rate of 8 Hz cosmic rays and 0.2 Hz beam-beam.

Additional cosmic ray suppression can be gained by requiring the muon to pass through the beam region in the non-bendplane within the limits imposed by multiple scattering. The limits are illustrated in Fig. 7.11. The factor gained thereby is ~0.067 giving a rate of 0.5 Hz (cosmic) and 0.2 Hz (beam-beam). This last criterion cannot be applied at level 1 as it requires the position information from the long wavelength pads which will be available no sooner than ~5 μsec after beam crossing.

7.3 FAST TRIGGER LOGIC

The schematic diagram for the level 1 trigger is shown in Fig. 7.12. In this section, we follow the signals from the detector through this logic.

7.3.1. Level One Trigger Input Signals

There are two types of input signals to the level one trigger system: primary and secondary. The primary inputs change value with each beam crossing and the secondary inputs are adjusted when necessary using the level one trigger control computer. The primary and secondary inputs are listed in Tables 7.1 and 7.2. They include all of the possible detector parts that could contribute to the trigger. All of the primary input signals originate from front-end electronics (e.g., liquid argon calorimeter preamplifiers, muon proportional tubes, etc.) near the detector and are brought through the shield wall on cables to the level one trigger electronics which is located on the control room side of the shield wall.

In this discussion we confine our attention to the liquid argon calorimeter signals and follow them through the trigger processor. Other information such as muon track addresses enter trivially at the inputs to the intermediate latches. We form three separate combinations of these signals: EM, which is a sum in depth of the electromagnetic sections of the calorimeter; H, which is a sum in depth of the hadronic sections; and the total which is the sum of the two. For the EM section the number of signals in azimuthal angle and pseudo-rapidity will be $32 \times 50 = 1600$ and for the other two it will be $16 \times 25 = 400$.

7.3.2 Differential Line Receiver and Gated Integrate and Hold Circuits

The trigger tower signals are transported from the front-end electronics on twisted flat cable to the differential line receiver circuits in the level one trigger. These signals are true differential signals to avoid noise problems with ground loops. The signals are in the form of pulses and are the sum of hard differentiated preamplifier outputs (Fig. 7.13). After the differential line receivers the signals are integrated and held until the next beam crossing. This enables the rest of the first level trigger electronics to work from stable levels and not pulses. Immediately before a beam crossing all the gated integrator circuits are reset to zero. The outputs of the gated integrator circuits go to the sin θ weighted circuits, and the trigger tower ADC circuits. This part of the trigger system also includes a set of test pulsers. There is a test pulser connected to the input of every gated integrate and hold circuit. The test pulsers are used to verify the proper operation of the first level trigger.

7.3.3 Trigger Tower ADC Circuits

Each of the 2000 trigger tower signals is converted to an 8-bit digital number by a separate ADC. These ADCs are set to have a full scale range of 127.5 GeV. They complete the analog-to-digital conversion in a few micro-seconds. The digital outputs of these ADCs are put in the level one trigger data block which is passed from the level one trigger to the event buffer when the detector is digitized. Because the level one trigger data block has a fixed structure the second level trigger has quick access to information about energy distribution in the detector without having to unpack all the data from the main data acquisition readout. The outputs from these ADCs are not used in making the level one trigger decision.

7.3.4 Sin θ Weighted Circuits

The sin θ weighted circuits convert the input trigger tower signals from a voltage that is proportional to deposited energy to a voltage that is proportional to the transverse component of the deposited energy. These circuits initially assume that the vertex of the interaction is in the center of the diamond and they use a value of sin θ based on this. The fast timing information from the luminosity counters discussed above provides the location of the interaction point with an accuracy of a few centimeters. The sin θ weighted circuits use this information in calculating the correct E_T values for the deposited energy. This can be important as sin θ can vary by a factor of two if extreme values of the interaction point are used. The outputs of the weighted circuits are used by the E_T, p_T, and jet finder circuits.

7.3.5 E_T Trigger Circuits

Separate E_T triggers are formed for the electromagnetic, for the hadronic, and for the total E_T signals. First of all the sin θ weighted trigger tower signals are added and then converted to an 8-bit digital number with a fast ADC. Each of these numbers is used as one input to a set of 32 digital comparators. The other input to each comparator is an 8-bit digital number which is preset by the control computer. The outputs from these sets of digital comparators are used as inputs to the AND/OR network. In this way there are 32 separate E_T thresholds for the electromagnetic, for the hadronic, and for the total energy triggers. The digital outputs of the ADCs are also put in the output data block of the level one trigger which is passed from the level one trigger to the event buffer when the detector is digitized.

7.3.6 Missing Transverse Momentum Trigger

A missing momentum (MP_T) trigger is formed for the total energy signal. Each trigger tower signal weighted by sin θ is then weighted by sin ϕ and cos ϕ to form the x and y projections in the $\theta = 90°$ plane. The total p_x and p_y signals are formed by adding the contributions from each trigger tower. The p_x and p_y signals are then digitized by 8-bit fast ADCs. The result is two 8 bit numbers representing the p_x and p_y of the event. These two numbers together form a 16 bit address to a look up table PROM. The data in the PROM represent p_ϕ and $|p|$ where

$$p_\phi = \tan^{-1}(p_y/p_x) \text{ and } |p| = \sqrt{p_x^2 + p_y^2}$$

The p_ϕ data are passed on as part of the data block generated by the level one trigger. The $|p|$ is used as one of the inputs to a set of 32 digital comparators. the other inputs to the comparators are separately preset by the control computer. The outputs from these digital comparators are used as inputs to the AND/OR network. This once again gives 32 separate thresholds for Mp_T. Each one can be used as part of a separate specific trigger formed in the AND/OR network. The $|p|$ data are also put in the data block that is generated by the level one trigger.

7.3.7 Jet Finder

Jets are found separately in both the electromagnetic and total energy signals. The trigger tower signals weighted by sin θ are added 2×2 to form cluster signals. The cluster signals are overlapping; that is, there are either 1600 or 400 trigger tower signals and 1600 or 400 trigger cluster signals. The cluster signals represent the transverse energy deposited in an area of $\Delta\phi = 22.5°$ and $\Delta\eta = 0.4$ for electromagnetic signals and an area of $\Delta\phi = 45°$ and $\Delta\eta = 0.8$ for the total signal. This represents a reasonable

compromise between jet size and resolution. Our Monte Carlo studies show that these areas are large enough that a substantial fraction of the energy of any jet will fit in some cluster signal. The cluster signals are then searched to find the jets. A cluster signal is examined by comparing it to a decreasing ramp threshold. For a cluster signal to qualify as a jet it must not be vetoed at the time that it crosses (becomes greater than) the threshold ramp. If a cluster signal has more energy than an adjacent neighbor then it vetoes that adjacent neighbor from qualifying as a jet. As the ramp crosses some low energy limit (~ 5 GeV) a low energy limit veto becomes active to inhibit any cluster signal with an energy below the low energy limit from qualifying as a jet. In this way the jet finder circuits locate all of the local energy maxima in the detector above the low energy limit. Figure 7.14 summarizes the operation of this circuit and illustrates the operation of the jet finding algorithm on a sample energy deposition pattern. The output of the jet finding circuits is a 1600 line EM jet bus, a 1600 line EM jet bus with a hadron veto, and a 400 line total energy jet bus. Again everything must be done globally because of the short time to make the trigger decision. The outputs of the jet finders are used by the jet counters, the 2D spatial correlators, and the jet stack builder. The jet stack builder places the address of every cluster that has qualified as a jet in the output data block of the first level trigger.

7.3.8 Jet Counters

The electromagnetic and total energy jets are counted separately using the same type of circuit. The jet counter circuits count the number of jets above a predetermined energy threshold. This energy limit is set by the control computer. To accomplish this the jet counter circuits latch the state

of the jet bus at the appropriate point in time as the jet finder ramp threshold is falling. In this way the jet counter circuit latches all of the jet above the predetermined energy threshold. The jet counter circuit then decodes the number of jets using five stages of PROM memory circuits (Fig. 7.16). The output of the PROM memory circuits is a 4 bit binary number representing the number of jets above the enrgy threshold. This 4 bit number is applied to one side of a set of 4 digital comparators. The other side of one of the comparators is preset to 1, the next comparator is preset to 2, the next to 3, and the last comparator is preset to 4. Thus the final output of the jet counter circuit is 4 lines indicating whether the jet counter found ≥ 1, ≥ 2, ≥ 3, or ≥ 4 jets. These lines are used as inputs to the AND-OR network. As many different jet counters as necessary with different programmed energy thresholds may be connected to each jet bus. Then using the AND/OR network many different specific triggers may be operating at the same time with each specific trigger requiring a different number of jets above (or below) different preprogrammed energies.

7.3.9 2D Spatial Correlators

These simple 2D correlation circuits are used to test for spatial correlations among quantities entering into the trigger. An example might be a correlation (or anti-correlation) between a jet and a muon. The correlation circuit tests to see if any section of θ,ϕ space contains both a muon and a hadronic (total energy jet). If some section of θ,ϕ contains both of these then the output of the correlation circuit indicates this. The output of the correlation circuit is used as an input to the AND/OR network. A specific trigger that is formed in the AND/OR network can require the presence or absence of any of these spatial correlations.

7.3.10 DIRECT IN Test Triggers

Inputs to the AND/OR network are provided for DIRECT IN test triggers. Using a pulse generator connected to a DIRECT IN test trigger input and programming a specific trigger with this as the only term one can generate level one triggers for testing. In response to this test trigger a certain preset group of data crates (determined by the specific trigger vs. crates digitized lookup table) will be digitized and readout for analysis by a test program.

7.3.11 Intermediate Latch

All of the output signals that have been generated in the circuits described above pass through the intermediate latch before entering the AND/OR network or the output data block. The intermediate latch is necessary for two reasons. First, it stabilizes all data entering the AND/OR network so that all of the digital logic levels are in a well defined state. Secondly, it allows the gated integrate and hold circuits to begin to reset before the end of the decision making cycle so that they may be fully reset before the next beam crossing.

7.3.12 AND/OR Network

The AND/OR network is where specific triggers are generated. As designed the network can simultaneously generate up to 32 specific triggers. A specific trigger is made using any combination of the terms in the AND/OR network. These terms are listed in Table 7.3. Any combination of specific triggers can be enabled at the same time by setting the corresponding bits in the Trigger Enable Register. The Trigger Enable Register is set by the control computer.

If a specific trigger (e.g., a low bias E_T only trigger) runs at too high of a rate a prescaler can be included in the circuit for that specific trigger. The prescaler ratio is set using the control computer. The AND/OR network has two outputs: a global output indicating if any of the specific triggers has fired and a line from each specific trigger so that the second level trigger can quickly determine which specific level one trigger has fired. As an example we look at the specific trigger to study the reaction

$$W^{\pm} \text{---> } e^{\pm} + \nu.$$

For this reaction the AND/OR network could be programmed for: EM jets above energy threshold > 1; E_T(EM) > threshold; no zero level trigger vetoes; and, if the rate from this specific trigger AND/OR network program were too high, EM jet with no H jet spatial correlation

7.3.13 Beam Crossing Scalers

The trigger system includes scalers for determining the number of beam crossings that were examined by the level one trigger and the number of beam crossing that were missed because either the trigger system was waiting for the information to make the 1.5 level decision or it was waiting for the data acquisition system to finish a cycle. The information from these scalers is included in the first level trigger data block and they can also be read by the first level trigger control computer. Information about the number of beam crossings examined by the level one trigger can be used in calculating the integral luminosity to which the detector has been exposed. Information about the number of beam crossings missed by the level one trigger can be used to analyze the amount and source of dead time.

7.3.14 Specific Trigger Scalers

Scalers are included for counting the number of times each of the specific triggers has fired. This information is useful in adjusting the rates of the individual specific triggers and for finding runaway triggers. The information from the trigger scalers is included in the level one trigger data block and it can also be read by the level one trigger control computer.

7.3.15 Level One Trigger Output Data Block

The output data block from the level one trigger is a well defined block of data that is passed from the level one trigger to the level two trigger in the event buffer. This data block will arrive in the dual port memory of a second level trigger processor a few hundred microseconds after the level one trigger fires. This gives the second level trigger quick access to a block of data that has a fixed structure so that the second level trigger can quickly utilize the basic features of the event without unpacking all of the data from the main data acquisition system. The data included in the level one trigger data block is listed in Table 7.4. The total size of the level one trigger data block is about 2.5 kbytes.

7.3.16 Control Computer Interface to the Level One Trigger

The level one trigger system is connected to a control computer which performs a number of function. The functions include: testing of the level one trigger system by use of the test pulser at the input of every trigger tower channel, setting of all the control parameters listed in Table 7.2, and monitoring the operation of the trigger system when it is in use in the DO experiment. The testing features built into the triggering system allow not

only basic testing of the system to verify that all of the circuits are operating properly, but also testing of triggering algorithms. The control computer is the device that loads all of the control parameters into the trigger system. In this way the control computer can set up and enable different specific triggers, and control the trigger rates. The control computer has access to the data block that is generated by the level one trigger system and this allows the computer to monitor the operation of the trigger system. The control computer will be able to display information about rates of different specific trigger, generate histograms of the various specific triggers, and provide information about the quality of the accelerator beams from information that is in the data block about the zero level trigger vetoes.

The level one trigger data block flows into the second level trigger dual port memory not through the control computer but rather through one of the data cables that is used by the main data acquisition system. This allows the level one trigger data block to be completely transferred to the level two trigger dual port memory within a few hundred microseconds after the trigger. Because the level one trigger data block is quickly transferred in this way the level tow trigger system can immediately begin examining the basic features of the event while the main data acquisition system is digitizing and reading out the information in the detector.

7.3.17 Specific Trigger vs. Crates Digitized Lookup Table

In response to a specific trigger only certain data crates should be digitized. The selection of the crates to be digitized is controlled by a lookup memory table. This memory array has dimensions of number of specific triggers × number of data crates or typically 32×48. This memory array is

loaded by the control computer. Using this lookup memory array a specific first level trigger will cause a preset group of data crates to be digitized. Each digitization crate provides a busy signal. In this way triggers not involving these crates can be re-enabled without waiting for the completion of the digitization process.

7.3.18 Fast Timing Generator

As discussed above, one of the functions of the "level 0" trigger is to provide a fast timing signal. Timing pulses coming before and after the beam crossing will be derived from this signal. The level one trigger will use these timing pulses to control the sequencing of the trigger logic. The timing pulses will be available for other uses such as the control of the before and after signals to the baseline-subtractor circuits. The timing generator will also provide level signals to indicate the state of the first level trigger, e.g., trigger state. In Table 7.5 we list the timing sequence for the level one trigger.

TABLE 7.1 Primary First Level Trigger Input Signals

1. 1600 Electromagnetic Trigger Towers
2. 400 Hadronic Trigger Towers
3. Event Vertex z Location
4. Muon Data
5. Direct in Test
6. Zero Level Trigger Vetoes
7. Experiment Beam Crossing Clock
8. Other Triggers

TABLE 7.2 Secondary (Control) First Level Trigger

Input Signals

1. E_T EM Thresholds
2. E_T Hadron Thresholds
3. E_T Total Thresholds
4. MP_T Total Thresholds
5. EM Jet Finder Low Energy Cut
6. Total Energy Jet Finder Low Energy Cut
7. Muon p_T Cut
8. Jet Counter Energy Limits
9. AND/OR Network Program
10. Specific Trigger Prescale Ratios
11. Specific Trigger Enable Register
12. Specific Trigger versus Crates Digitized Look-Up Table

TABLE 7.3 Input Terms to AND/OR Network

1. Vertex location
2. E_T(EM) > threshold
3. E_T(H) > threshold
4. E_T(Total) > threshold
5. MP_T > threshold
6. EM jet multiplicity above a programmed energy
7. Total Energy jet multiplicity above a programmed energy
8. Muon count above cutoff > lower limit
9. Jet-Jet spatial correlation
10. DIRECT IN test triggers
11. Zero level trigger vetoes
12. Trigger Enable Register
13. Other Triggers

TABLE 7.4 Contents of the Level 1 Trigger Data Block

1. All input terms to the AND/OR network
2. MP_T 8 bits
3. E_T(EM) 8 bits
4. E_T(H) 8 bits
5 E_T(Total) 8 bits
6. Vertex Location 3 bits
7. Location of each jet 12 bits each
8. ADC result from each trigger tower 8 bits each
9. Status of the specific triggers
10. Contents of the beam crossing scalers
11. Contents of the specific trigger scalers

TABLE 7.5 First Level Trigger Timing Sequence

Time (msec)	Trigger System State
0.0	Beam Crossing
1.1	90% of Charge Collected
1.4	Outputs of θ Slice Cards Are Stable to 5% Jet Finder Sweep Starts Mp_T and E_T Circuits Settle
2.4	Fast ADCs for Mp_T and E_T Begin 100 nsec Cycle
2.5	Jet Finder Sweep Ends Jet Bus is Stable Jet Engines Start 400 nsec Cycle Outputs of Fast ADCs Stable Mp_T and E_T PROMs and Comparators Begin Cycle Gated Integrate and Hold Circuits Begin to Reset
2.9	All Inputs to Intermediate Latch are Stable Clock Intermediate Latch Outputs of AND/OR Network Stable Declare Trigger State YES/NO If YES: Inhibit the Before Gate Pulse to the Baseline Subtractor-Multiplexer for the Next Beam Crossing Inhibit All Gate Pulses While in Trigger State
3.5	Next Beam Crossing

FIGURE CAPTIONS - CHAPTER 7

7.1 Trigger cross-section for two-jet events versus total E_T.

7.2 Trigger cross-section for two-jet events versus missing p_T.

7.3 Trigger cross-section versus jet E_T threshold for two-jet events.

7.4 $\mu^{\pm}$ yields integrated over angle as a function of p_T.

7.5 Muon rates exiting the steel from various sources as a function of angle.

7.6 Comparison of rates for all particles, particles exiting the calorimeter, and particles exiting the steel as a function of angle.

7.7 x_B vs. x_c hit map.

7.8 x_B vs. x_c hit map for $p_T > 5$ GeV/c.

7.9 Summary of B • C Coincidence rates at 90°, 20°, and 12°.

7.10 Trigger efficiency.

7.11 Beam-beam muons in CF. Upper quadrant non-bend plane. x_B vs. x_c hit map.

7.12 Schematic diagram of the level 1 trigger.

7.13 Liquid argon calorimeter trigger pulses.

7.14 Schematic of the jet-finding algorithm circuit.

7.15 Illustration of the jet-finding algorithm.

7.16 Schematic of the jet counter circuits.

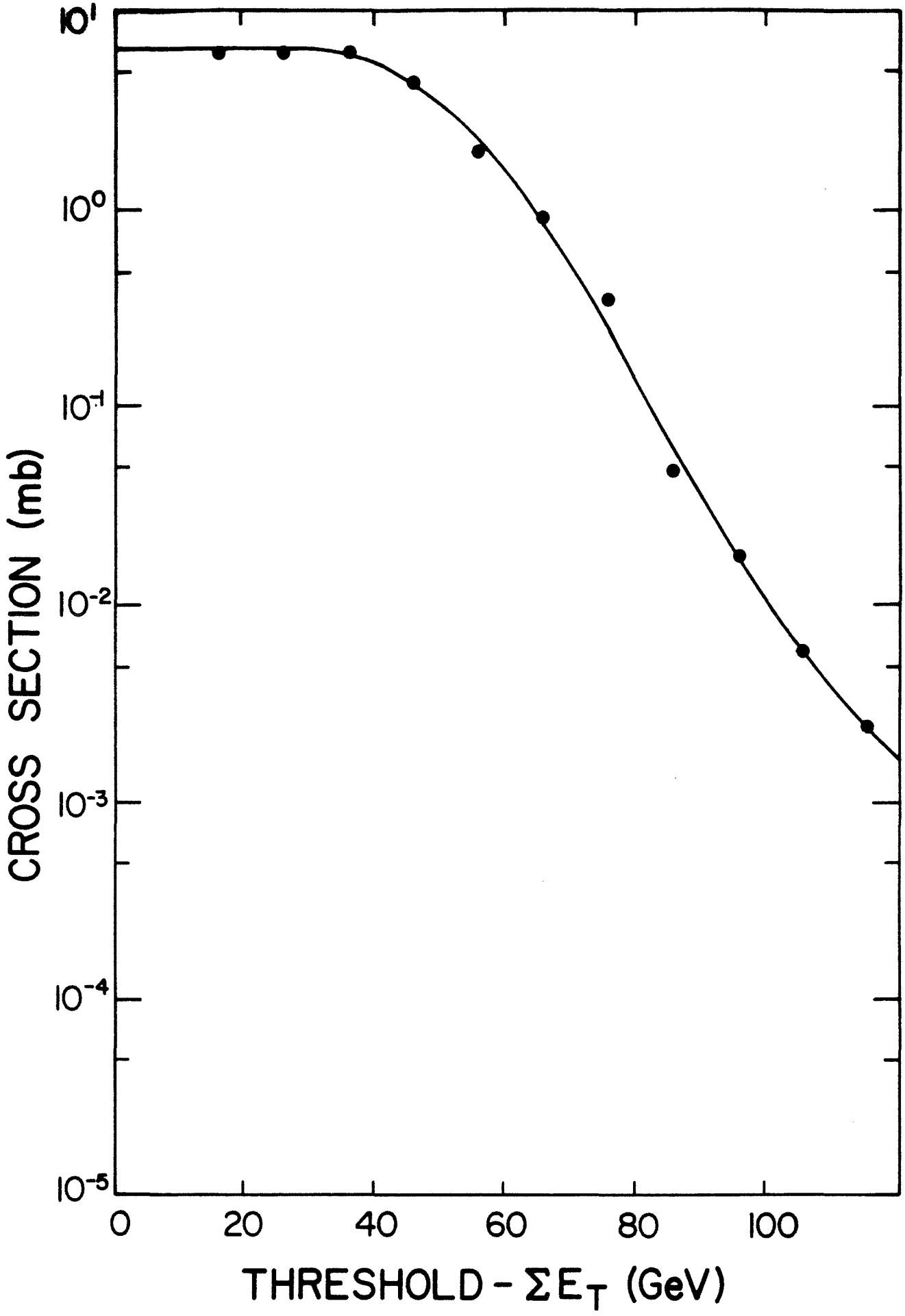
CROSS SECTION (mb)
10¹
10⁰
10⁻¹
10⁻²
10⁻³
10⁻⁴
10⁻⁵
0
20
40
60
80
100
THRESHOLD - ΣE_T (GeV)

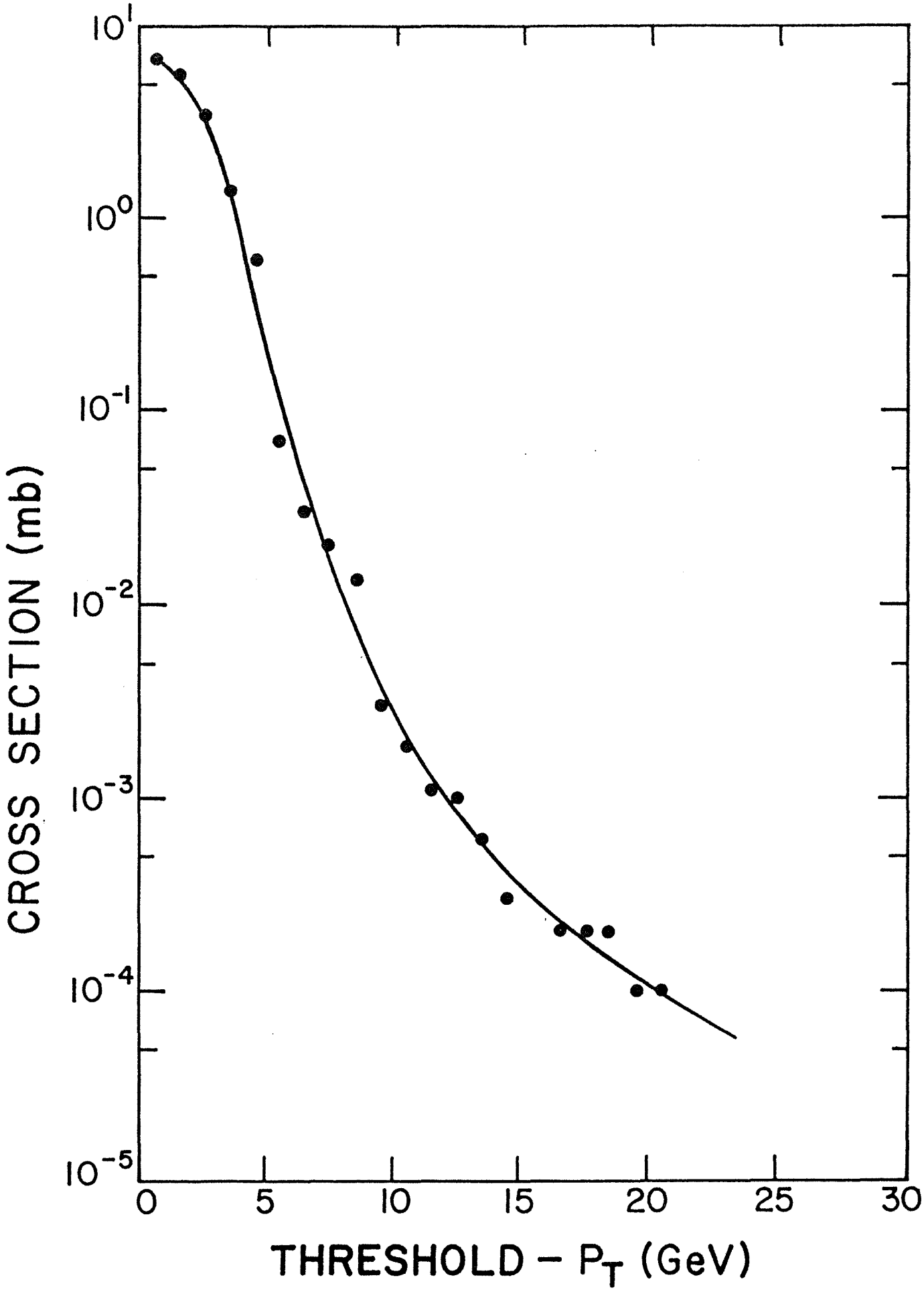
CROSS SECTION (mb)
10^{1}
10^{0}
10^{-1}
10^{-2}
10^{-3}
10^{-4}
10^{-5}
0
5
10
15
20
25
30
THRESHOLD – P_T (GeV)

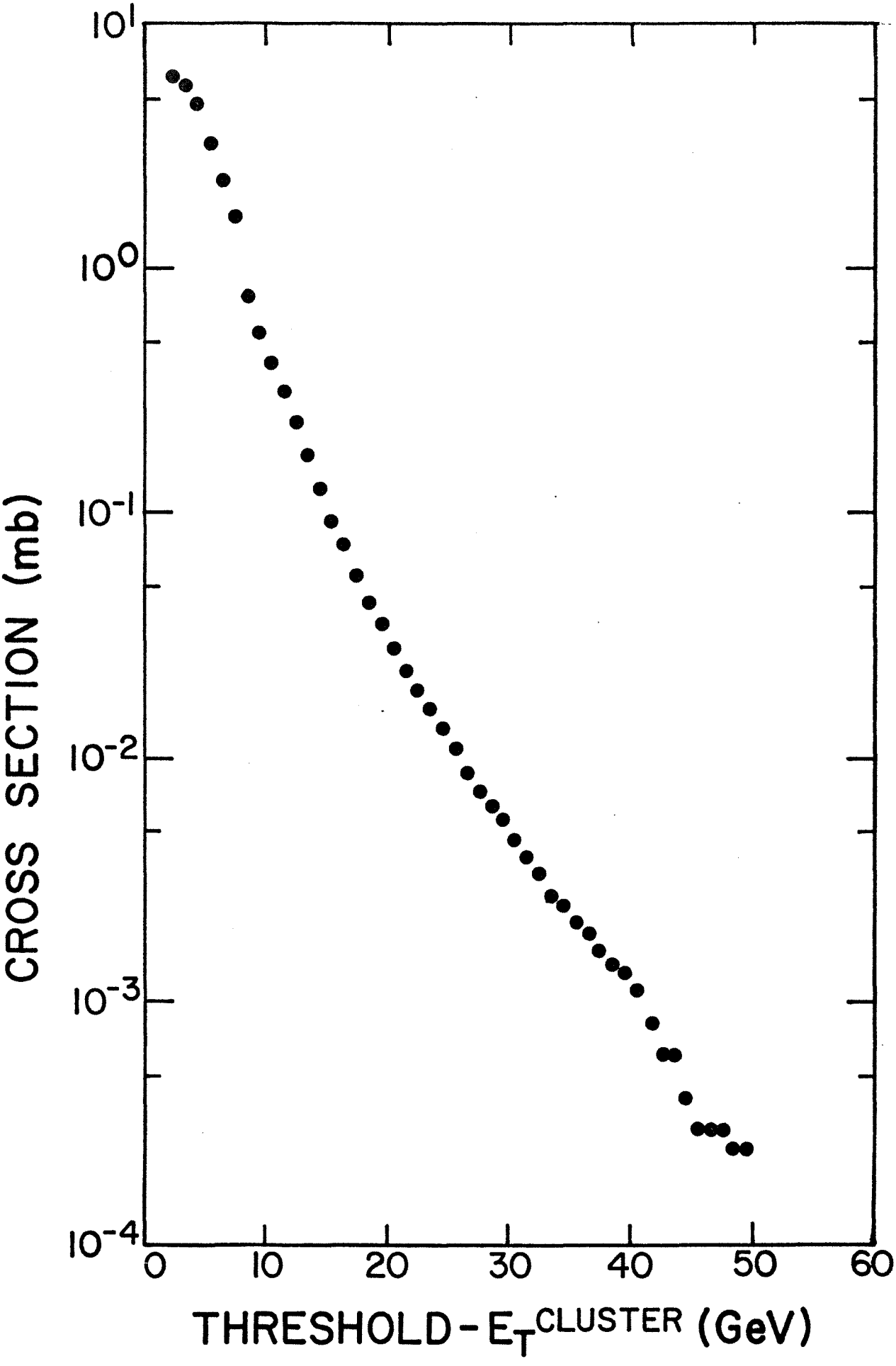
CROSS SECTION (mb)
10^{1}
10^{0}
10^{-1}
10^{-2}
10^{-3}
10^{-4}
0
10
20
30
40
50
60
THRESHOLD - $E_T^{CLUSTER}$ (GeV)

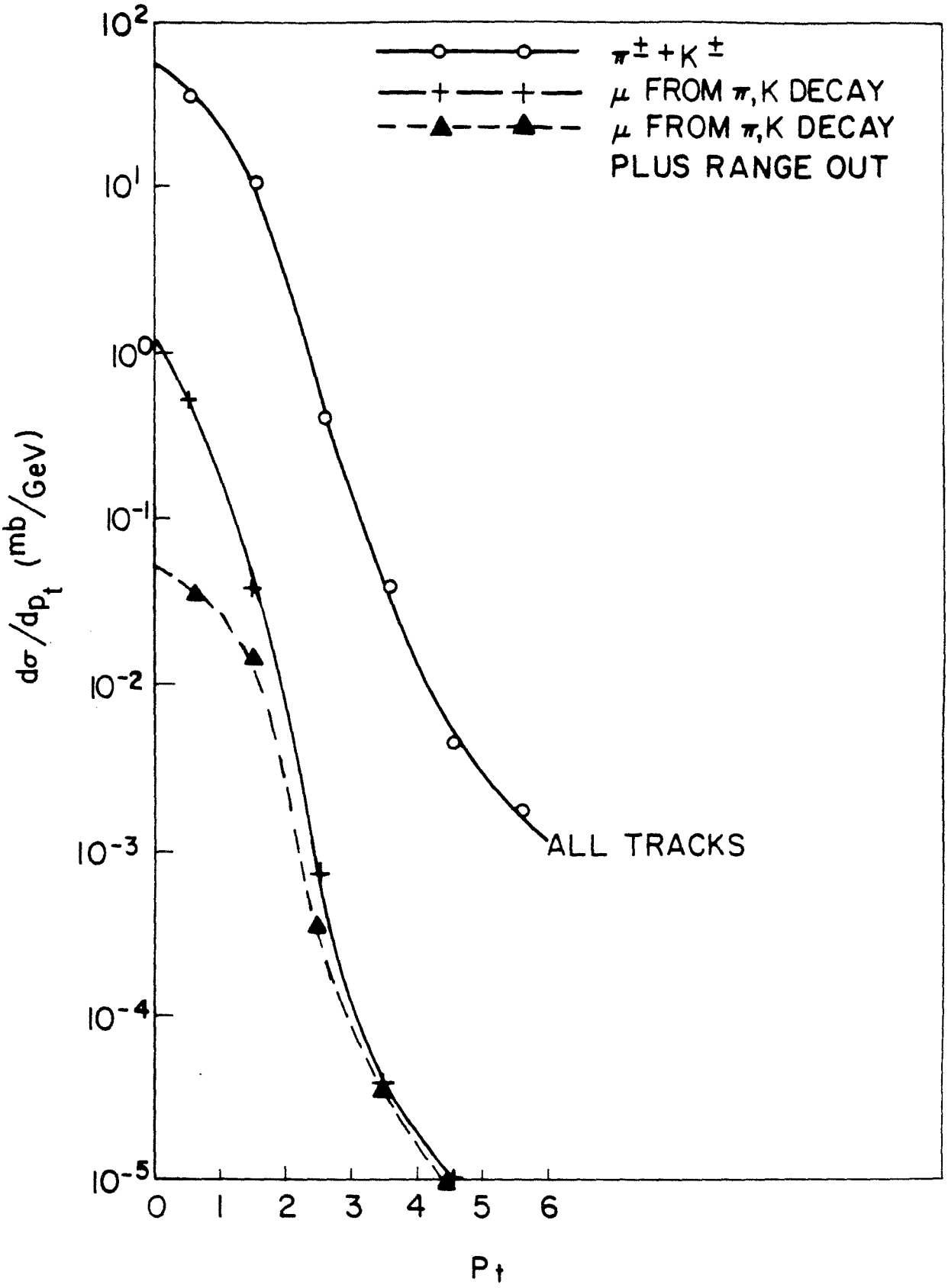
10^2
10^1
10^0
10^{-1}
10^{-2}
10^{-3}
10^{-4}
10^{-5}
$d\sigma/dp_t$ (mb/GeV)
0 1 2 3 4 5 6
P_t
$\pi^{\pm} + K^{\pm}$
μ FROM π,K DECAY
μ FROM π,K DECAY PLUS RANGE OUT
ALL TRACKS

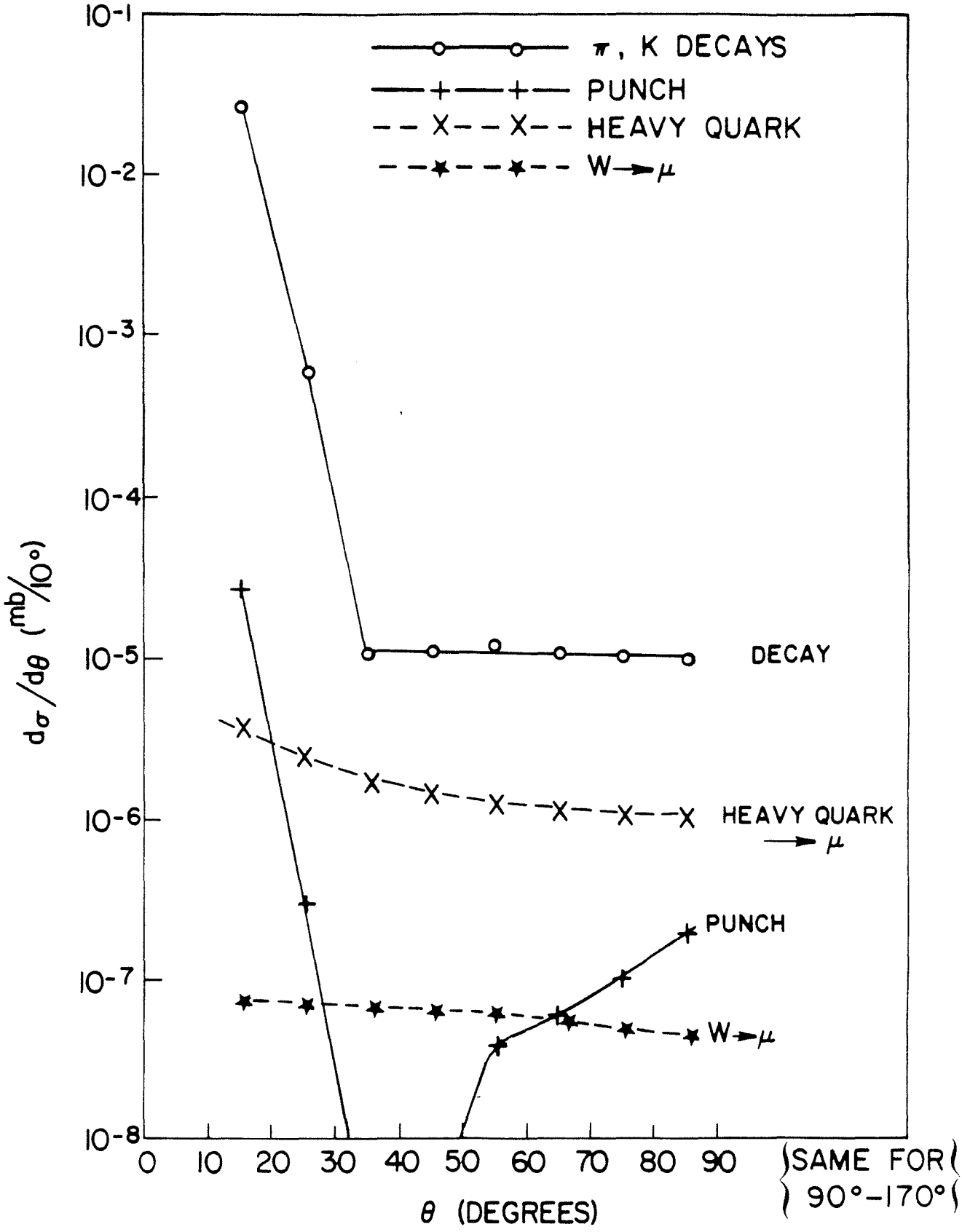
π, K DECAYS
PUNCH
HEAVY QUARK
W→μ
DECAY
HEAVY QUARK → μ
PUNCH
W→μ
dσ/dθ (mb/10°)
θ (DEGREES)
SAME FOR 90°-170°
10-1
10-2
10-3
10-4
10-5
10-6
10-7
10-8
0
10
20
30
40
50
60
70
80
90

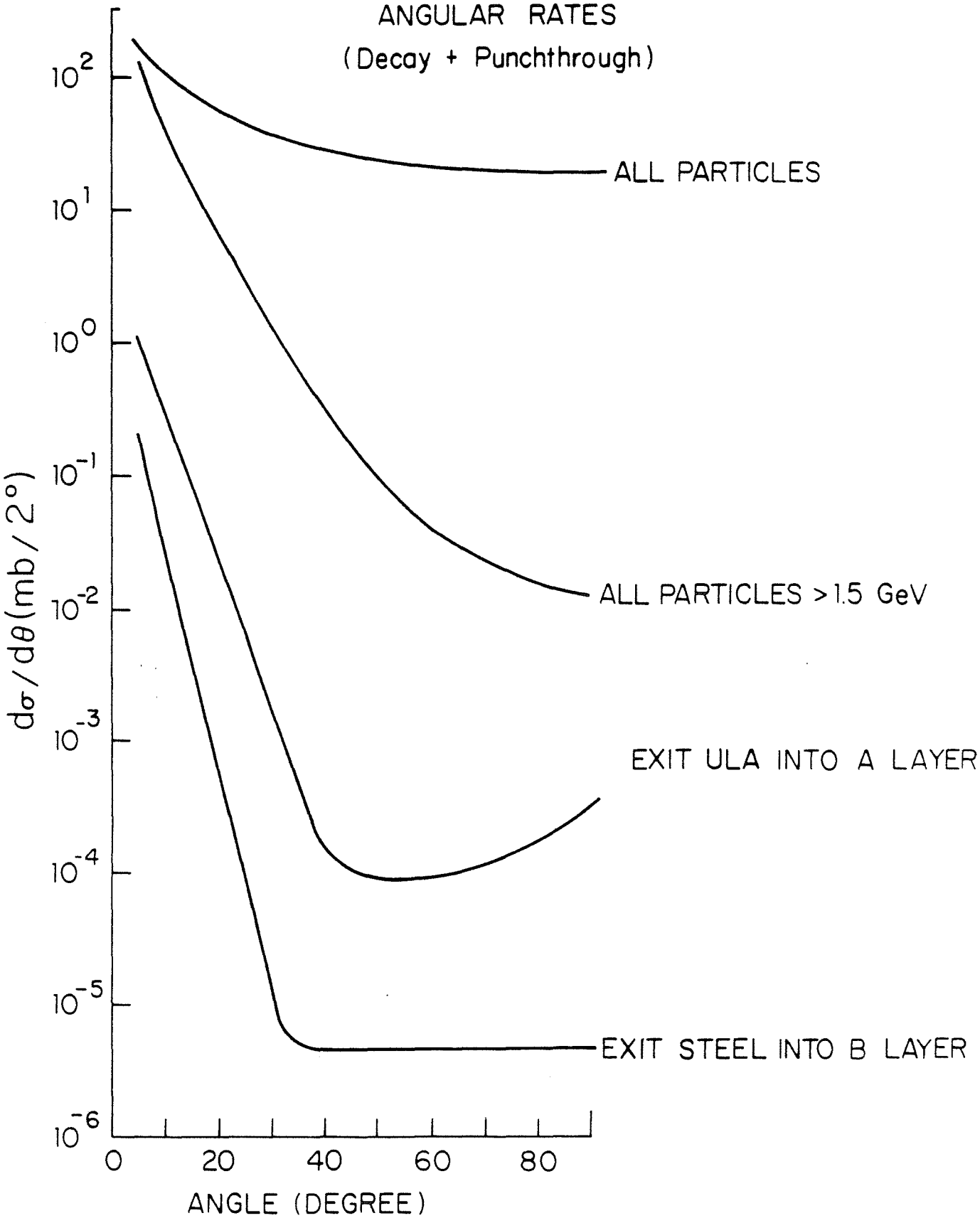
ANGULAR RATES
(Decay + Punchthrough)
ALL PARTICLES
ALL PARTICLES >1.5 GeV
EXIT ULA INTO A LAYER
EXIT STEEL INTO B LAYER
dσ/dθ(mb/2°)
10^2
10^1
10^0
10^-1
10^-2
10^-3
10^-4
10^-5
10^-6
0
20
40
60
80
ANGLE (DEGREE)

EF X_B vs X_C HIT MAP

$250 > |X_C| > 500$ cm

$14° \gtrsim \Theta \gtrsim 27°$

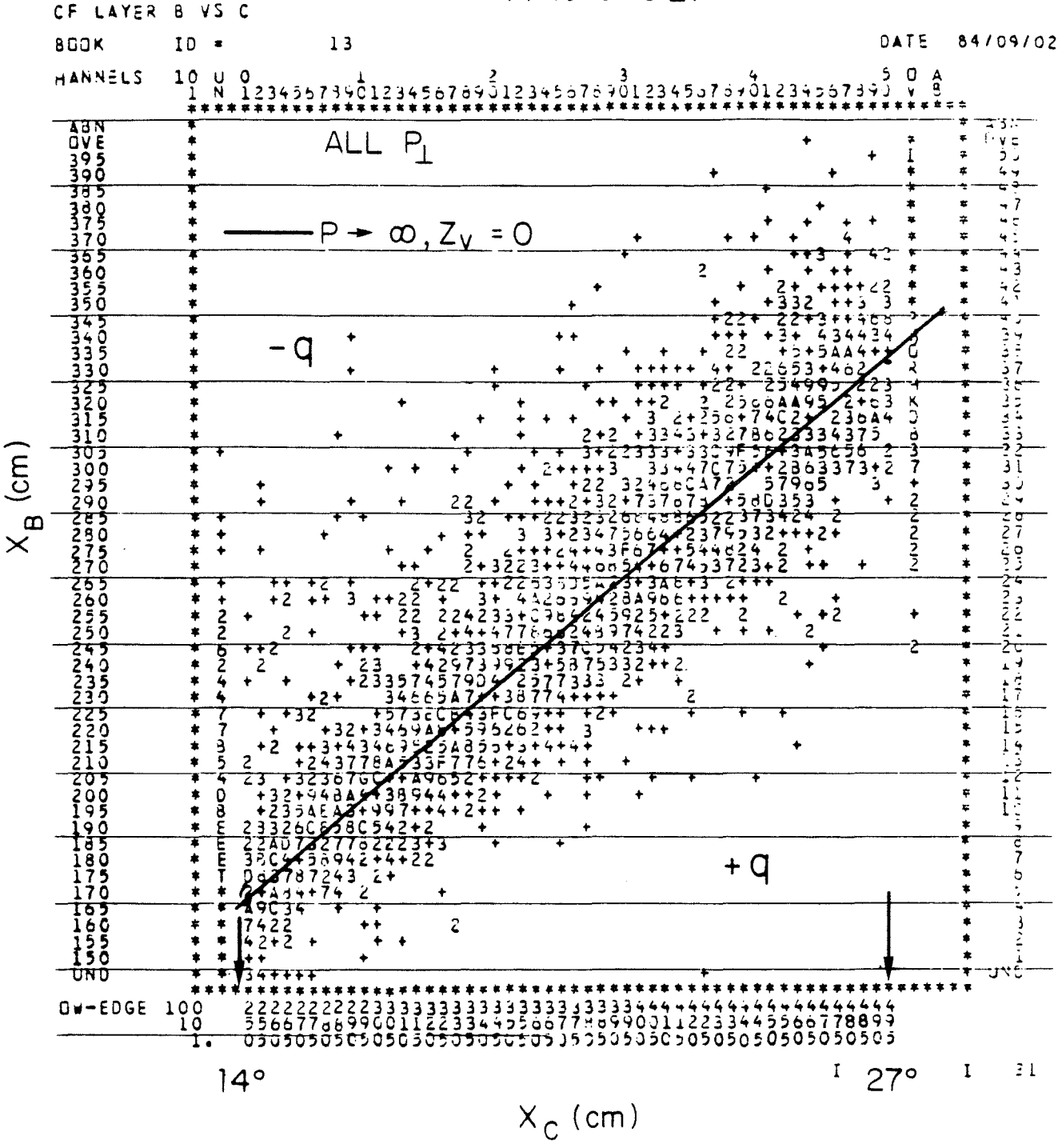

EF X_B vs X_C HIT MAP

$250 > |X_C| > 500$ cm

$14° \gtrsim \Theta \gtrsim 27°$

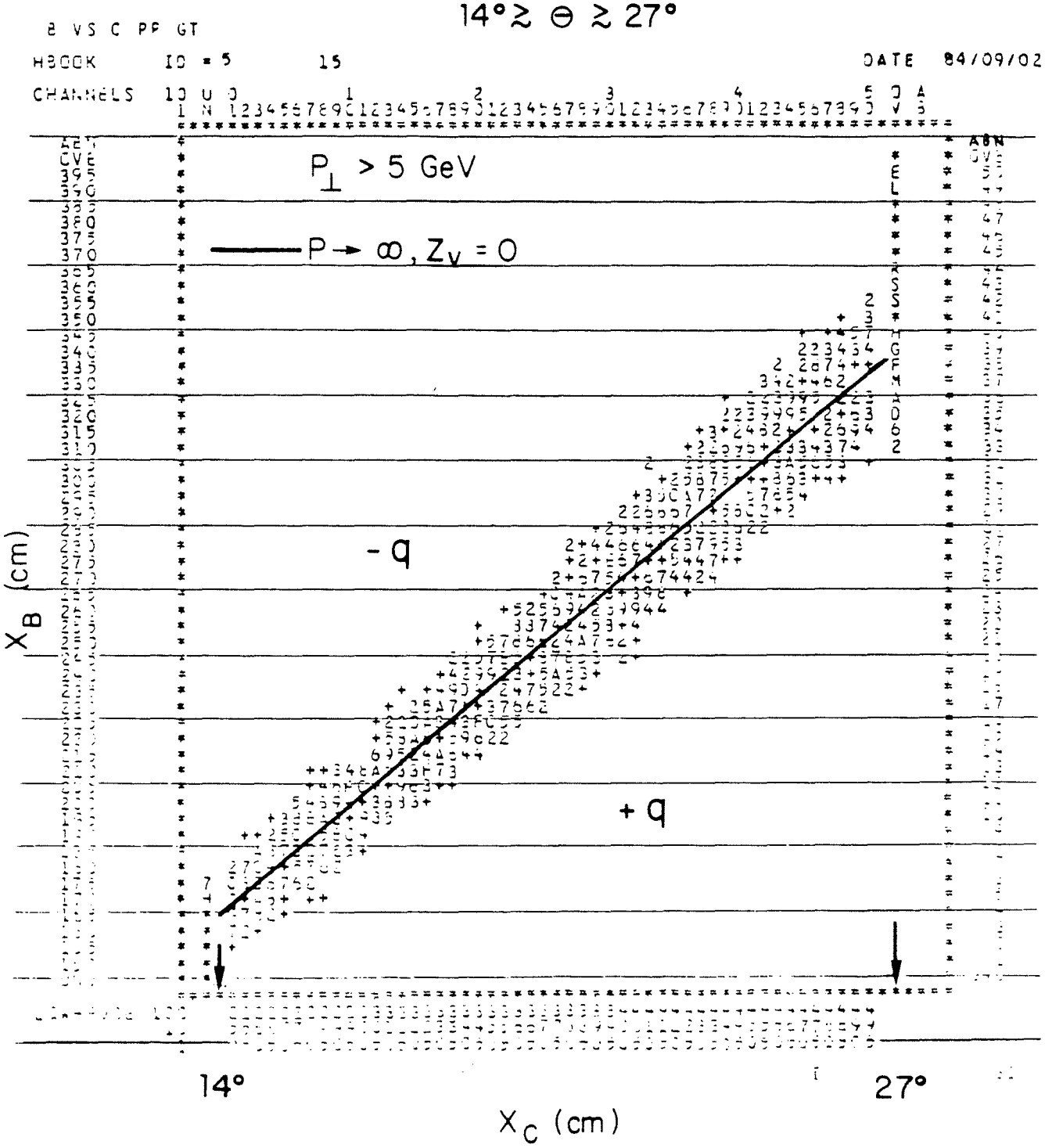

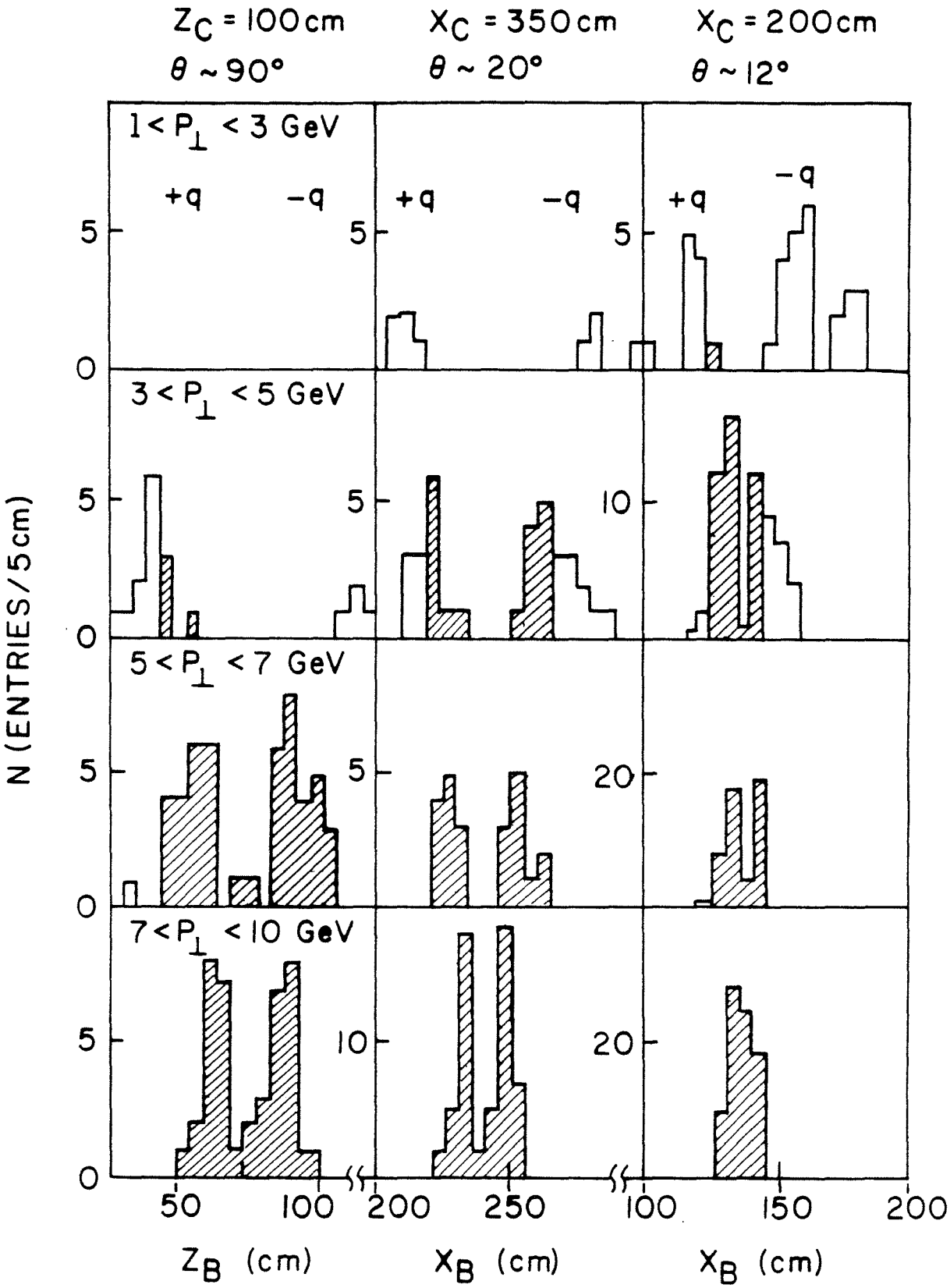
Z_C = 100 cm
θ ~ 90°
X_C = 350 cm
θ ~ 20°
X_C = 200 cm
θ ~ 12°
1 < $P_\perp$ < 3 GeV
3 < $P_\perp$ < 5 GeV
5 < $P_\perp$ < 7 GeV
7 < $P_\perp$ < 10 GeV
+q
−q
N (ENTRIES/5cm)
Z_B (cm)
X_B (cm)
X_B (cm)

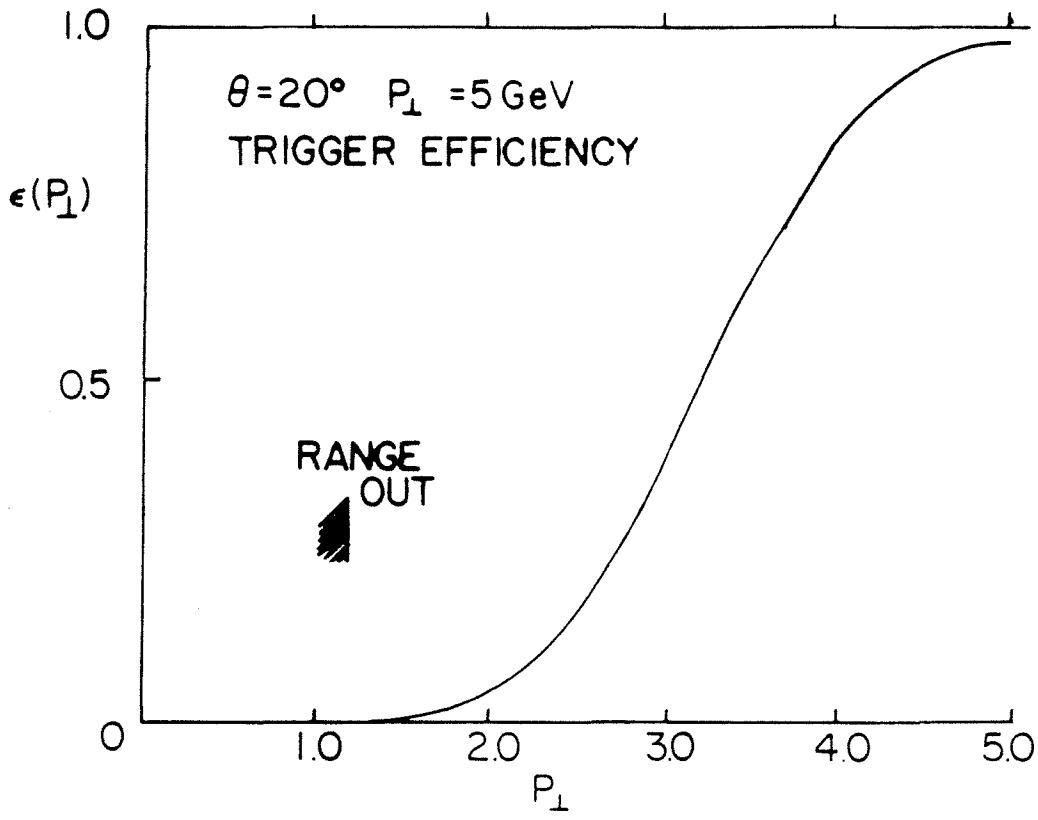
1.0
θ=20° P⊥ =5 GeV
TRIGGER EFFICIENCY
ε(P⊥)
0.5
RANGE
OUT
0
1.0
2.0
3.0
4.0
5.0
P⊥

CF Y_B vs Y_C

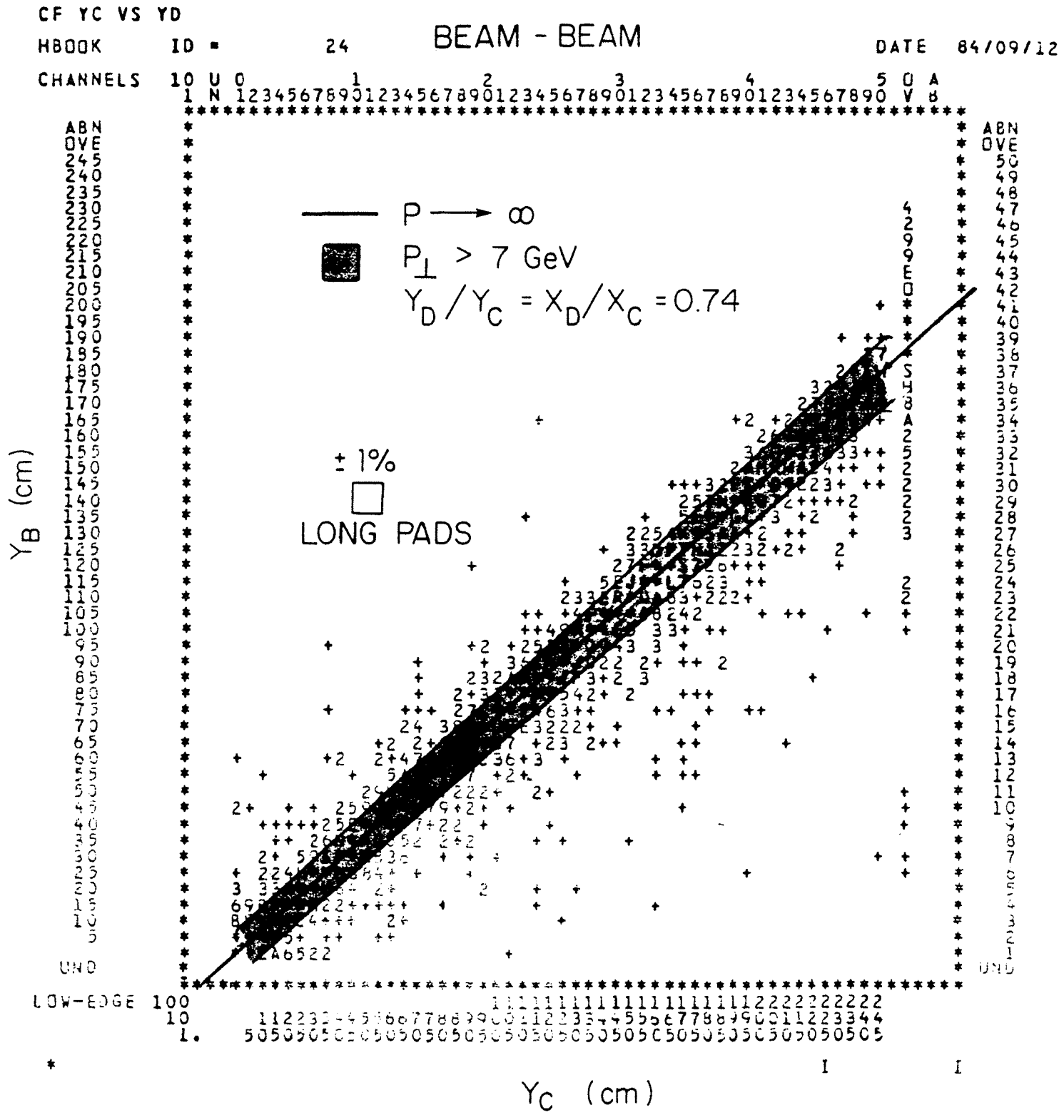
CF YC VS YD
HBOOK ID = 24
BEAM - BEAM
DATE 84/09/12
CHANNELS
P ⟶ ∞
$P_\perp$ > 7 GeV
$Y_D / Y_C = X_D / X_C = 0.74$
± 1%
LONG PADS
Y_B (cm)
Y_C (cm)
LOW-EDGE 100
10
1.

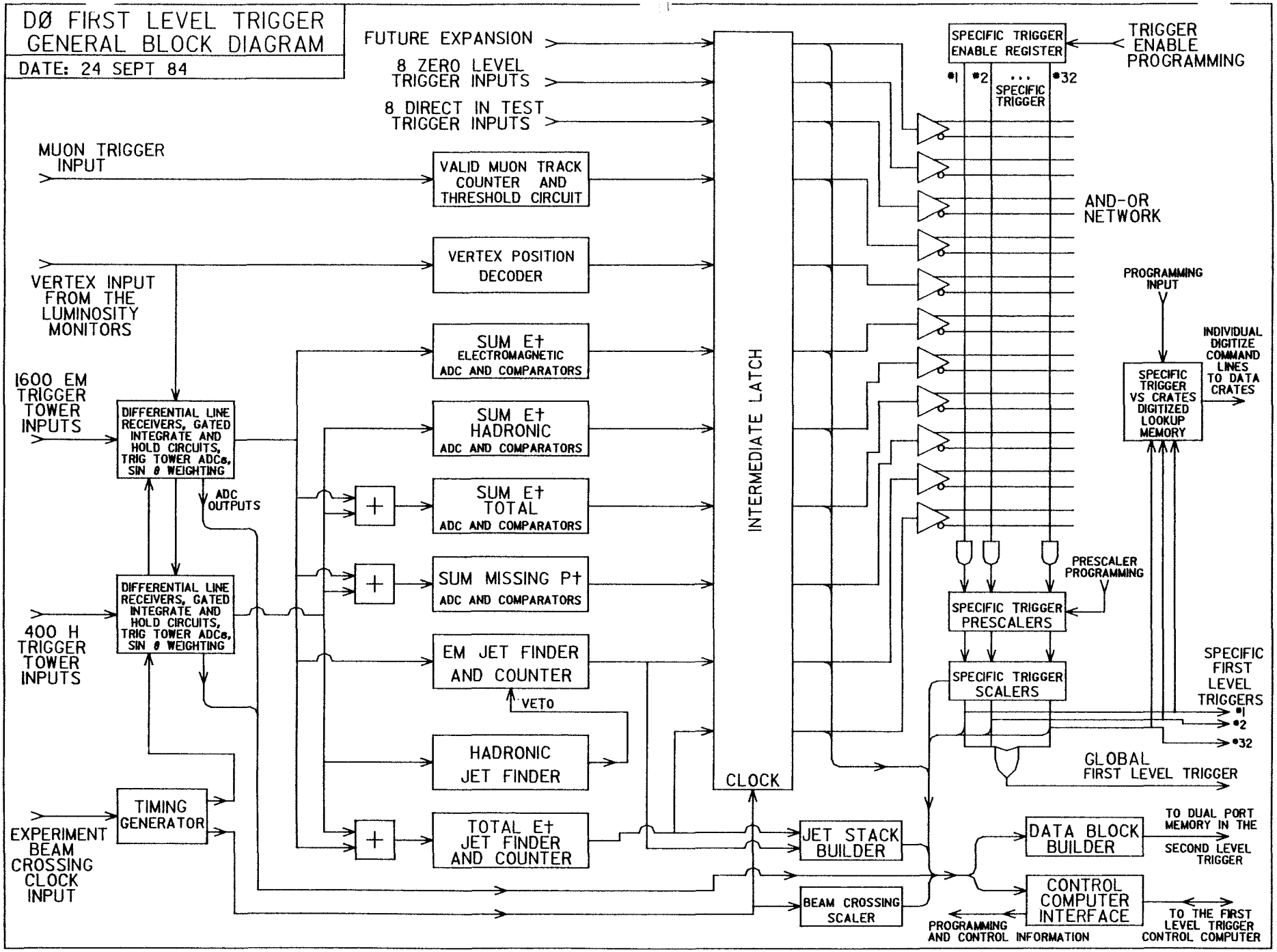
DØ FIRST LEVEL TRIGGER
GENERAL BLOCK DIAGRAM
DATE: 24 SEPT 84
FUTURE EXPANSION
8 ZERO LEVEL TRIGGER INPUTS
8 DIRECT IN TEST TRIGGER INPUTS
MUON TRIGGER INPUT
VALID MUON TRACK COUNTER AND THRESHOLD CIRCUIT
VERTEX POSITION DECODER
VERTEX INPUT FROM THE LUMINOSITY MONITORS
SUM E† ELECTROMAGNETIC ADC AND COMPARATORS
SUM E† HADRONIC ADC AND COMPARATORS
SUM E† TOTAL ADC AND COMPARATORS
SUM MISSING P† ADC AND COMPARATORS
EM JET FINDER AND COUNTER
HADRONIC JET FINDER
TOTAL E† JET FINDER AND COUNTER
1600 EM TRIGGER TOWER INPUTS
DIFFERENTIAL LINE RECEIVERS, GATED INTEGRATE AND HOLD CIRCUITS, TRIG TOWER ADCs, SIN θ WEIGHTING
ADC OUTPUTS
400 H TRIGGER TOWER INPUTS
DIFFERENTIAL LINE RECEIVERS, GATED INTEGRATE AND HOLD CIRCUITS, TRIG TOWER ADCs, SIN θ WEIGHTING
VETO
EXPERIMENT BEAM CROSSING CLOCK INPUT
TIMING GENERATOR
INTERMEDIATE LATCH
CLOCK
SPECIFIC TRIGGER ENABLE REGISTER
TRIGGER ENABLE PROGRAMMING
#1
#2
...
#32
SPECIFIC TRIGGER
AND-OR NETWORK
PROGRAMMING INPUT
INDIVIDUAL DIGITIZE COMMAND LINES TO DATA CRATES
SPECIFIC TRIGGER VS CRATES DIGITIZED LOOKUP MEMORY
PRESCALER PROGRAMMING
SPECIFIC TRIGGER PRESCALERS
SPECIFIC TRIGGER SCALERS
SPECIFIC FIRST LEVEL TRIGGERS
#1
#2
#32
GLOBAL FIRST LEVEL TRIGGER
JET STACK BUILDER
BEAM CROSSING SCALER
DATA BLOCK BUILDER
TO DUAL PORT MEMORY IN THE SECOND LEVEL TRIGGER
CONTROL COMPUTER INTERFACE
PROGRAMMING AND CONTROL INFORMATION
TO THE FIRST LEVEL TRIGGER CONTROL COMPUTER

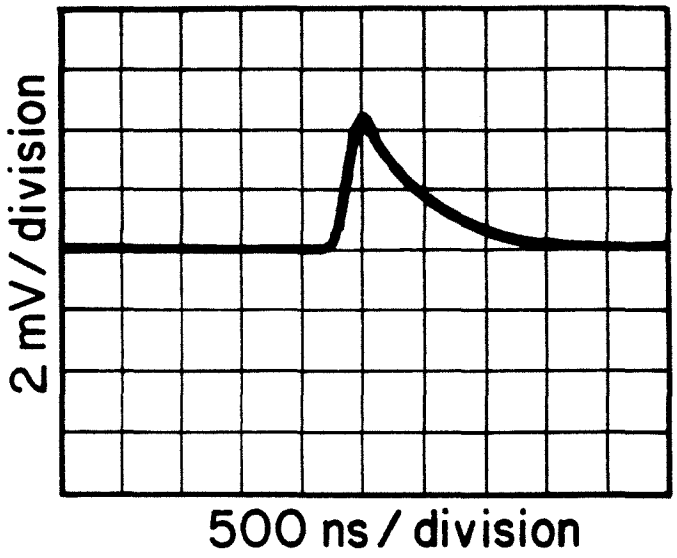

Liquid Argon Chamber Preamplifier Trigger Output for 80 MeV Total Energy Input.

DO FIRST LEVEL TRIGGER JET FINDER

DATE: 24 SEPT 84

NOTES:

Four adjacent Trigger Tower Signals are added to form a Cluster Signal.

Cluster Signals are examined to find jets. A Cluster Signal is examined by comparing it to a decreasing ramp threshold. If at some point the Cluster Signal exceeds the ramp threshold then the jet register is set if it has not been vetoed.

If a Cluster Signal has more energy then an adjacent neighbor then it vetoes that neighbor from qualifying as a jet.

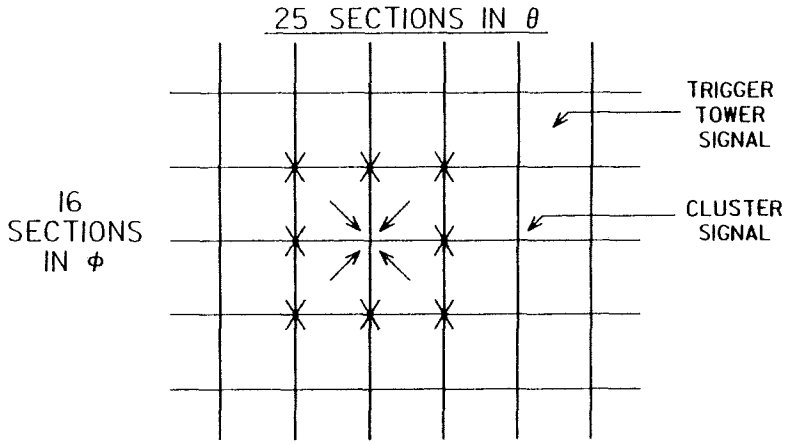

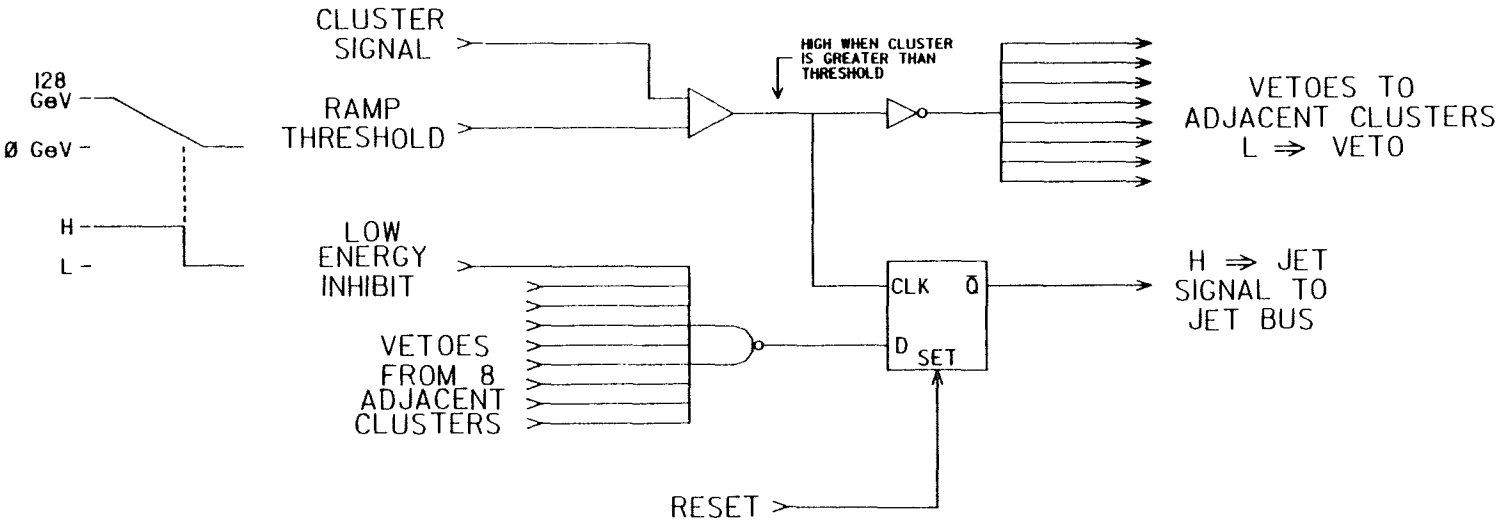

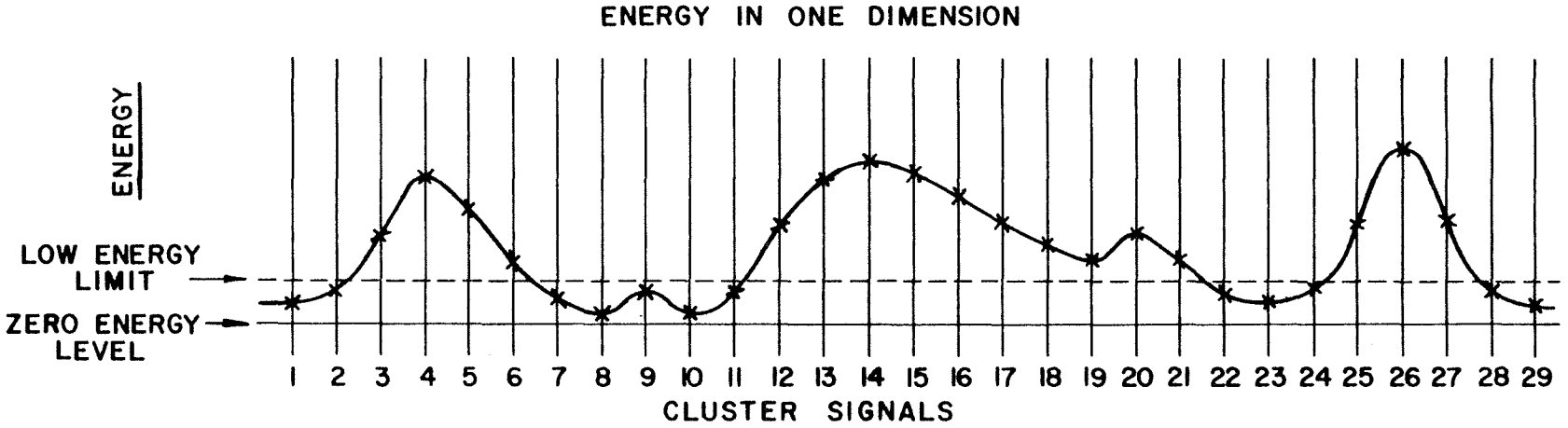

ILLUSTRATION OF THE JET FINDING ALGORITHM

DO FIRST LEVEL TRIGGER JET COUNTER

DATE: 24 SEPT 84

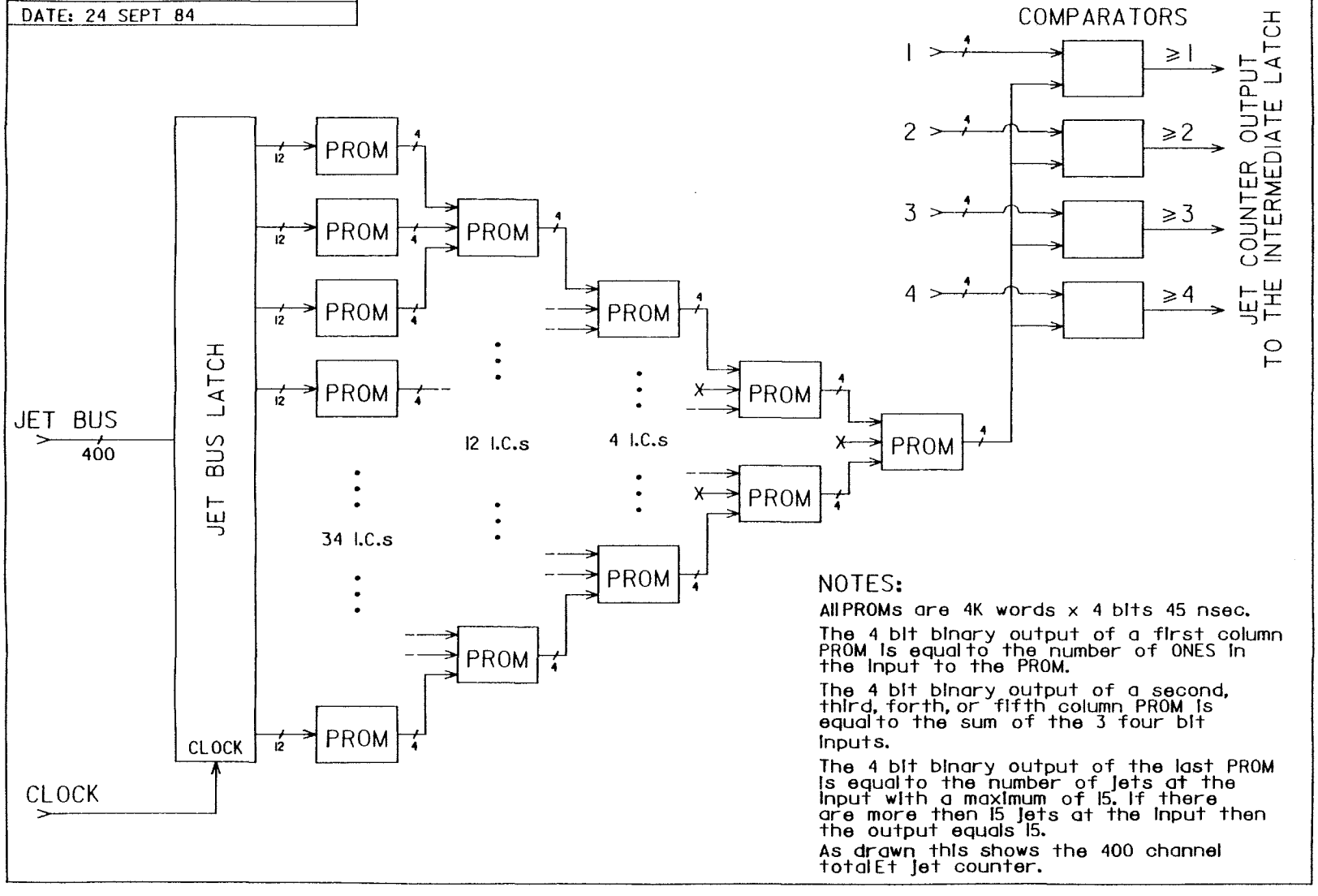

NOTES:

All PROMs are 4K words x 4 bits 45 nsec.

The 4 bit binary output of a first column PROM is equal to the number of ONES in the input to the PROM.

The 4 bit binary output of a second, third, forth, or fifth column PROM is equal to the sum of the 3 four bit inputs.

The 4 bit binary output of the last PROM is equal to the number of jets at the input with a maximum of 15. If there are more then 15 jets at the input then the output equals 15.

As drawn this shows the 400 channel totalEt jet counter.

8. DATA ACQUISITION AND COMPUTING

8.1 Introduction

The DO data acquisition and processing chain will begin with 50 to 100 Kbytes of data representing the digitization of detector signals for an event recognized by the hardware trigger system as being of potential interest. Up to several hundred such events per second will be input into the system. Each event will then be organized and reviewed by one of a number of microprocessors which will determine which events will actually be kept. While typical recording rates of one or two events per second are anticipated it is recognized that provision must be made to record some types of events at certain times at substantially higher rates. These events must then be further analyzed and selected offline to produce a final from which physics results will be obtained. In addition to supporting directly this flow of data, the DO data acquisition and online computing systems must perform the following auxiliary functions:

1. Support the installation and debugging of detector elements.
2. Monitor the performance of various subsystems and the detector as a whole.
3. Calibrate the detector.
4. Maintain data bases describing the continuous state of the detector.

Likewise, the offline system, in addition to analyzing the data from the detector, must perform extensive Monte Carlo calculations to give test detector configurations and acceptances.

Over the course of the DO project, software activities will require hundreds of man-years of effort. In an attempt to maximize the efficiency of this effort, DO will use a single computer architecture over as wide a range of applications within the project as possible. The DEC VAX architecture has

been selected and the range of applications include data acquisition, data reduction, event filtering, detector control, detector monitoring, detector calibrating, support systems monitoring, offline interactive computing, and all program development. This approach has been made practical by the introduction by DEC of the MicroVAX, a relatively inexpensive and powerful VAX compatible microprocessor. At the lowest and highest levels of the DO data chain, other computer architectures are likely to be required. The embedded processing in the individual digitizing systems is expected to be done by a variety of special function processors which will have to be dealt with uniquely as will the hardware trigger system. At the highest level, where massive production analysis of events will be required, the optimal choice of processor cannot now be anticipated. Therefore, it is important that current choices do not exclude reasonable future options in this area. However, in the region between these highest and lowest levels a very serious effort will be made to standardize on the VAX architecture.

By using a single architecture, the number of computer systems with which the programmers and physicists must be familiar is limited to one. For example, the utilites such as editors, linkers, file, and code management systems with which one must deal are unique and fully integrated. Further, experiment specific utilities such as event-data access routines need only be written once for use at all levels of processing. One important pattern of code development anticipated by DO is the migration of algorithms originally developed and used in offline analysis, first to the online analysis, and finally down into the data reduction and filtering processors. Such migration is trivial if the processors at the various levels are architecturally identical.

Among the advantages of the architecture selected by DO are the existence within the group of considerable VAX expertise, the presence of considerable VAX compute power already installed, and the presence in the high-energy physics community of a significant library of VAX software which can be adapted for use by DO. In addition, the VAX architecture is supported by a commercial network product, DECnet, a powerful and very user-friendly system for local area networks, which can also be implemented across both leased phone lines and X.25 protocol networks to connect remote processors and networks. Thus, DO expects to have a homogenous network connecting together the site of the experiment with the various institutions which make up the collaboration. This network will allow experimenters, from their home institutions, to communicate with each other, to participate in cooperative software development, to monitor and calibrate detectors, and eventually, to review the status of runs in progress.

A unified approach is being used across the entire software effort in which a core of people such as the online group or the offline group will provide the basic structure, utilities, and global algorithms of a software system, while the applications associated with the individual detector systems will be written by the groups responsible for the design and construction of those systems. These detector groups will designate from within their group individuals whose primary task will be the writing of this software and who will work within the framework and to the specifications set by the online and offline core groups. Among the specific responsibilities of the detector groups are the writing of the Monte Carlo routines which simulate their detector, the filtering algorithms associated with their detector, the debugging, monitoring, and calibrating routines for their detector, and the

detector analysis routines. It is also intended to optimize cooperation and communication between software and hardware efforts.

8.2 DATA ACQUISITION AND LEVEL 2 TRIGGER

All events which survive the hardware trigger are digitized. In order to reduce the number of events saved on tape or disk to one or two per second, a further selection with a rejection factor of order 100/1 is necessary. This additional event selection is accomplished with a filter program running in about 50 microcomputers connected in parallel. Each micro is essentially an isolated system which receives an event directly and analyzes it completely. Implementation of this step is straight forward, since it is based on commercial hardware and software. As mentioned earlier, we have chosen as this microcomputer the DEC MicroVAX II. Specifically, the level 2 trigger will consist of an array of MicroVAXes running the VAXELN run-time operating system and linked via Ethernet to a central host VAX which collects those events that survive filtering.

The structure of the data acquisition system is shown in Fig. 8.1. The fast electronics digitization and readout crates are grouped into seven sections; each section reads out on its own data cable, which is daisy chained to each microcomputer in the array. A separate MicroVAX, the "Acquisition Supervisor," controls the event flow--allocating the data cable within the readout section and assigning which analysis MicroVAX will receive the event. To perform control functions, the Supervisor is interfaced to all elements of the acquisition system: the level 1 trigger, the readout crates, and the level 2 analysis units.

The level 2 trigger is accomplished by routing the complete data for one event from the digitization crates to one microcomputer which runs the entire filter program. In this mode the micros operate in an independent but parallel fashion. We expect that the MicroVAX's performance will be comparable to that of a VAX-11/780, that it will have sufficient direct memory for the com-

plete analysis program and event data, and that it will be available on a time scale suitable to our experiment. To provide a means of loading the data into the analysis unit, we are using a locally-designed dual-port memory board. This memory has a 32-bit wide external port which cycles at 100 nsec., for a bandwidth of 40 Mbytes/sec. We plan to have eight dual-port input channels per level 2 box loaded in parallel with event data and accessed by the MicroVAX via Q-BUS block mode transfers.

The MicroVAX level 2 units are interfaced to the digitization crates via data cables (simple ribbon cables) which carry a few control lines supporting a simple protocol (no handshaking), 32 data lines, and parity. Each of the units is linked to a host VAX via Ethernet for shipment of events which pass the software filter as well as for initial program downloading. A second Ethernet line is used for interaction with the micros from terminals on the host system. To enable real-time control of the acquisition process, each unit is linked (to the Supervisor) via "extended registers." To meet the level 2 trigger requirements, we expect to incorporate in the system approximately 50 MicroVAX processors. With such a system, filter algorithms are possible which require on average 100-200K instructions.

As indicated above, the Supervisor is a separate MicroVax (running a separate VAXELN task) which exercises the data acquisition control function, such as deciding:

1. which level 2 units are free and which one should receive the next event;
2. which level 1 triggers should be enabled;
3. given a level 1 trigger, which electronics readout crates should initiate digitization;
4. as digitizations complete, which crate should use the data cable associated with its readout section.

As described below, in several areas these control functions are aided by special external hardware. In addition to the seven data cables associated with the readout crates, one cable is used by the level 1 trigger to ship the fast trigger data (about 4 Kbytes) directly to the selected level 2 analysis unit. Preliminary analysis of this data can give rise to a fast abort signal communicated to the Supervisor, which in turn could terminate unfinished readouts and reset the digitization buffers.

The Supervisor is linked to the level 1 trigger via an external "fast trigger memory." This simple interface acts as a "switch-matrix," with one dimension being lines associated with each of the different hardware triggers and the other dimension providing the corresponding patterns of electronics crates to be enabled for digitization. Another interface similar to the "fast trigger memory" assists the Supervisor in controlling the readout data from the digitization crates. With this external unit (preloaded by the Supervisor) the use of each of the data cables is automatically sequenced. For calibration and test purposes the Supervisor can select a particular readout and route the data to a specific analysis unit. As a system diagnostic aid, the Supervisor could direct a number of level 2 systems to read simultaneously a single event and analyze it identically. Because of its central role in the acquisition, the Supervisor is connected to the host VAX via a separate Ethernet line.

A number of additional interfaces are used by the acquisition system. The various detector readout devices transmit data via data cables described earlier. The simple protocol of these cables allows straightforward interfacing of the special calorimeter electronics, CAMAC, and FASTBUS. To enable overall control of the digitization crates and to permit downloading to local crate intelligence, interfaces similar to the "extended register" used in the filtering units couple each of the electronics crates to the Supervisor.

Calibration and detector monitoring and development are important uses of the acquisition system, vital for the commissioning of the detector and in fact the major tasks during most of any year. The parallel analysis scheme is well suited for this operation, since each of the microcomputers can be used as isolated systems for some specialized analysis. Appropriate trigger types are routed to that unit by the Supervisor. In this way, many users operating simultaneously on the host VAX, can acquire and analyze data for debugging, monitoring, or calibrating different portions of the detector. Indeed, by suitably loading the fast trigger memory and its interfaces to the detector electronics, the Supervisor can allow such operations to continue while collecting normal data from the rest of the detector. In this scheme the Supervisor can also orchestrate special operation of the electronics appropriate to the calibration.

A key element in our design is the use of commerically available system software. With our choice of the microcomputer system, the new DEC software package VAXELN provides the complete framework for the development and operation of the level 2 analysis software, encompassing the host VAX and all the satellite MicroVAXes. This "software product for the development of dedicated real-time systems for VAX processors"[1] runs as a task under VMS on the host VAX. The task image is then downloaded to the appropriate MicroVAX(es) over Ethernet. The analysis software can be written entirely in high-level languages: "EPASCAL" for the control functions and standard VAX/VMS FORTRAN for the level 2 filter code. Downloading from the host to the MicroVAXes is supported, as is remote symbolic debugging. The VAXELN program in each of the MicroVAXes has little system overhead, yet is multitasking (each interrupt service routine can be a separate task), and has transparent Ethernet support. Thus a user at a terminal on the host can access any MicroVAX, and the VAXELN program in a MicroVAX can read and write the host's disks and tapes. All

these aspects of VAXELN make it very desirable, especially since it is a currently available and supported product.

At present we have an operational test system consisting of three MicroVAX-I units linked via Ethernet with a host VAX-11/750, and have verified the ease of program development, downloading, remote debugging, and real-time operation of the microcomputers. One particular concern was the bandwidth of Ethernet for event transfer from the level 2 units to the host, which, though adequate for our design of one or two events per second passing level 2, may not have the capacity for a significantly higher event rate or expanded event size. As one alternative, we have considered using another MicroVAX as a tape (or optical disk) server, so that the Ethernet event pipeline would be between DEQNA interfaces on MicroVAXes; we are verifying that this link would come much closer to using the full intrinsic bandwidth of Ethernet. Other aspects of the design are being tested and developed with our system, and we anticipate shortly assembling a full-scale prototype acquisition system based on the MicroVAX-II processor.

8.3 ONLINE COMPUTING

The online system will be the point of access to the experiment for the experimenters. It must support the installation and debugging of the detector elements. It must allow the calibration of the detector systems and monitoring of their performance and that of their support systems such as cryogenics and high voltage. It must maintain the data base of code, constants, and parameters which describe the operating states of the detector. It is responsible for recording the event data, constants, and conditions. Among the conditions monitored and recorded are those of the interaction region and the collider itself. In addition, the online system will be required to perform a physics level monitoring of the system as a whole by performing a modified version of the offline analysis on some small sample of the events as they are being taken.

In general, the online computing must be interactive computing of the highest possible quality. It must also feature flexibility and a high level of reliability.

The DO detector with a total channel count of about 100,000, will consist of at least three separate major detector subsystems, each of which will be further subdivided many times. It is thus clear that at times of peak demand, such as just before data-taking runs, one must be prepared to support at least 20 simultaneous serious interactive users accessing the detector through this online system. An interactive user of this type can easily consume 20 percent of a VAX-11/780 equivalents. The basic hardware configuration which will be used for DO, as indicated in Fig. 8.2, will consist of a large VAX cpu (probably a VAX-VENUS whose announcement is expected in the course of the next year) augmented by a small VAX (perhaps a VAX-11/750) which will serve as a backup for the large cpu. There will be large disk capacity (at least 5 Gbytes) and substantial mass storage capability (either ~ four 6250 BPI tape

drives or a video disk system). The system will be tied together using the DEC VAX cluster protocol so that if the backup computer is required to operate in the place of the large cpu the switch-over will be trivial and all data bases will be available. Decnet/Ethernet connected MicroVAX work stations based on the same processor used in the data acquisition system will augment the large VAX. This technique offers a transparent and cost effective manner of expanding the compute capacity of the online system to meet increasing demand.

In addition, the system will contain appropriate quantities of terminals, printers, and graphics (hardcopy as well as video). The system will be networked so as to be accessible to experimenters at other locations on site and by experimenters at their home institutions.

VAX/VMS will be the operating system used for the online computer. Code which is certain to remain strictly online code will be written in any appropriate VAX language and its extensions. Code which is identified as being of potential general use, such as in the offline program, will be written in FORTRAN 77 with a small list of acceptable extensions.

The online system will consist of a number of relatively independent tasks which are capable of accessing the detector and its data through a single detector server task. This server task will handle all communication with the detector and will feed data via shared global commons to individual consumer tasks. These consumer tasks will be able to start up, attach to the data distribution system, receive selected data from the detector until some objective is accomplished, disconnect from the system and log out. This approach has the advantage of using the VAX multitasking system to protect users from each other and the server task from users while at the same time permitting ready access to the data. When the detector is being run in a mode other than event data gathering it will also be possible for the individual

consumer tasks to request changes in the running mode of portions of the detector.

Event recording, physics monitoring, and some global detector monitoring functions will be run as "standard" consumer tasks while detector-specific tasks will be started up and run to satisfy specific debugging, monitoring, or calibrating needs. Additional low-bandwidth communication between tasks will be conducted by mailboxes. Special tasks and utilities will be used to control the sharing of resources such as graphics devices, cpu cycles, etc. It is expected that while the tasks are totally independent they will utilize common utilities and perhaps have a common structure.

It is intended that under normal event data taking conditions a number of parallel recording streams will be maintained. The events will be categorized on the basis of findings of the hardware trigger and the filter microprocessor and recorded in separate disk files. When an individual disk file reaches an appropriate size it will be written to tape or optical disk. This initial selection process will allow offline analysis to work from concentrated data sets. It will especially facilitate the accelerated analysis of event types of particular interest.

8.4 OFFLINE SOFTWARE

Most of the offline software for DO will be developed on VAX computers. To facilitate the transfer of code to other computers the language is restricted to ANSI standard FORTRAN 77 with minimal use of VAX FORTRAN extensions. The central software library will reside on a VAX at BNL. It is expected that most of the groups in the DO collaboration will have VAX computers available to them with easy access to the BNL VAX, either directly or via Fermilab. A 9600 baud line will be leased to provide a link between BNL and Fermilab. Similar links are expected between various universities and the national laboratories (BNL, Fermilab, and LBL). Rapid communication is essential in order to keep centralized control over the software effort and avoid unnecessary proliferation and duplication of code.

Software developed for CDF is being used as a starting point for the DO library. In particular, the YBOSS data and memory management package provides the basic underlying structure. The programs are intended to be highly modular so that each detector component and specific task can be incorporated or removed without affecting the overall program performance. Each detector component is controlled via driving subroutines. It is the responsibility of the group developing a particular component to also provide the corresponding software for data reduction.

A Monte Carlo program (DOSIM) is being developed with the same overall structure as the data reduction program. Its goal is to generate Monte Carlo data files with the same format and characteristics as the expected data. A preliminary version of this program will be available by the end of 1984. The DOSIM program will be used not only to evaluate the detector performance but also to help develop and test the data reduction programs. At present smaller, special purpose, Monte Carlo programs are being used to help design

detector components and answer specific questions. DOSIM is intended to be a fully integrated global Monte Carlo.

REFERENCES

1. Digital Equipment Co.: "VAXELN PROGRAMMING" page 1.1 (AA-Z451A-TE)

FIGURES CAPTIONS - CHAPTER 8

8.1 Schematic diagram of the level 2 microprocessor trigger system.

8.2 Online computing configuration.

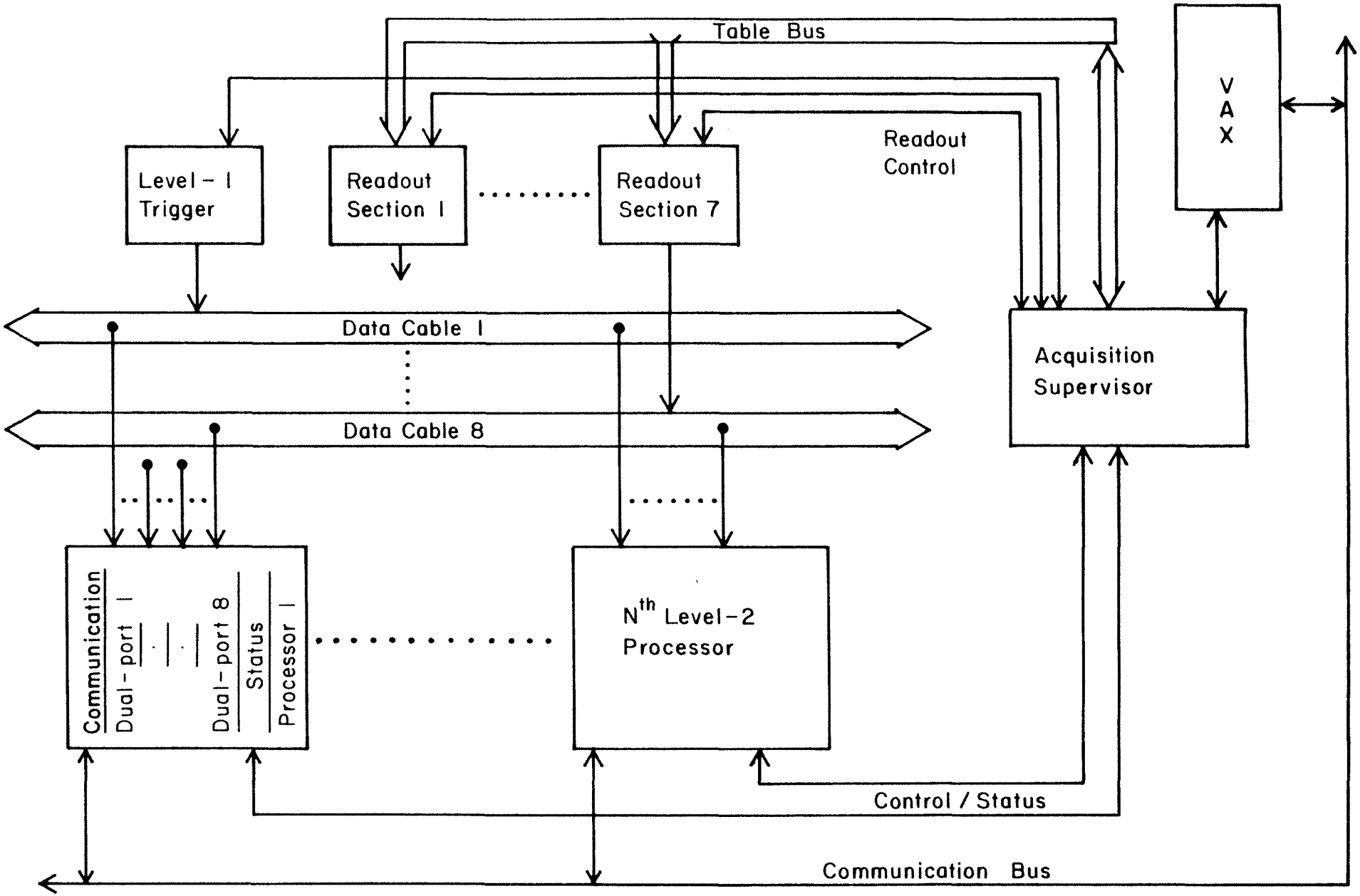
Table Bus
VAX
Level - 1 Trigger
Readout Section 1
Readout Section 7
Readout Control
Data Cable 1
Data Cable 8
Acquisition Supervisor
Communication Dual-port 1
Dual-port 8
Status
Processor 1
Nth Level-2 Processor
Control / Status
Communication Bus

FIGURE 8.1

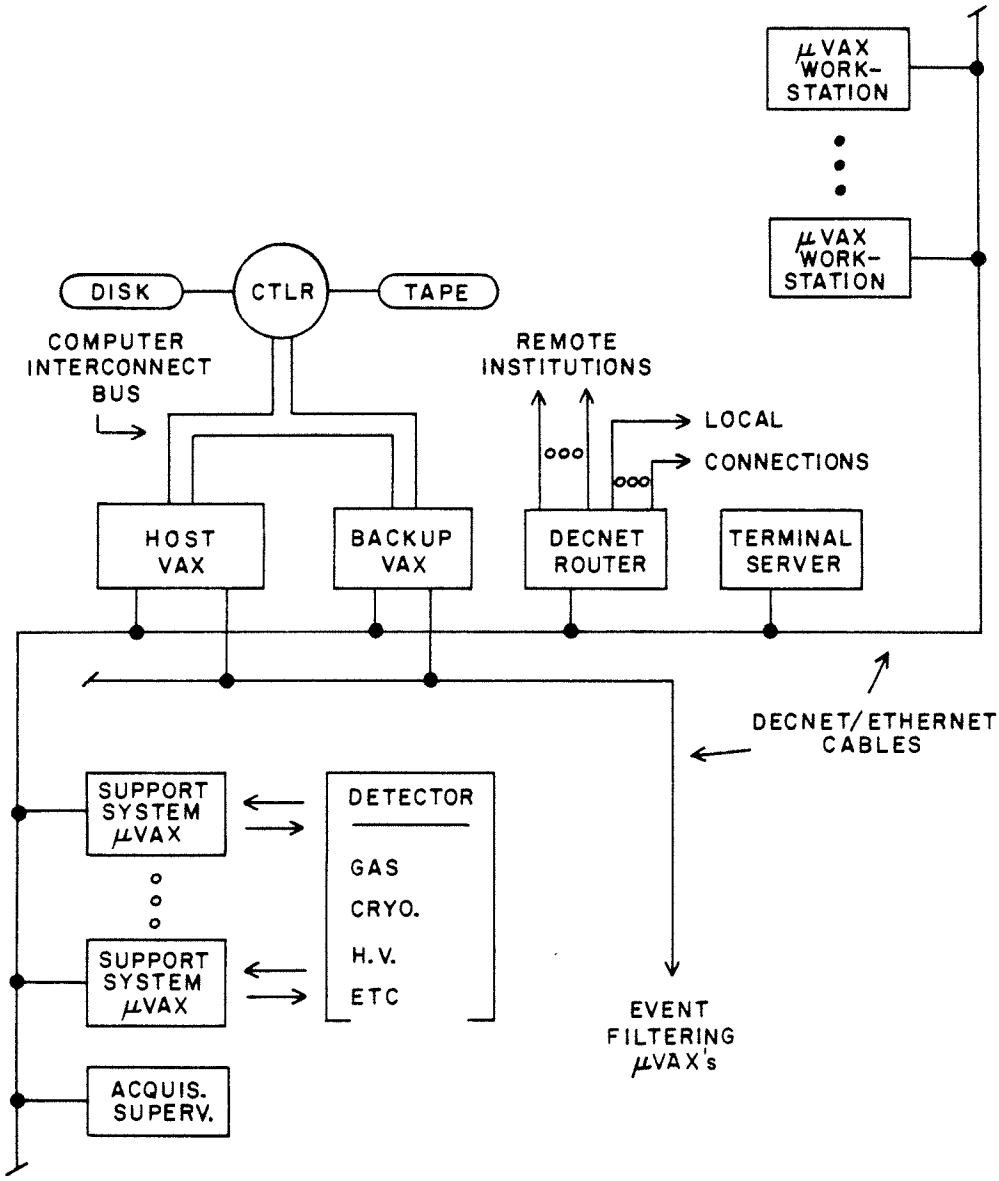

ONLINE COMPUTING CONFIGURATION

9. DETECTOR ASSEMBLY AND SERVICES

In the TeV II (fixed target) operation, the DO collision hall is used for extraction magnets. To change to colliding mode these magnets must be removed and replaced by the superconducting low-beta quadrupole strings. Then the DO detector will be moved into the collision hall from an assembly area and positioned on the beam line. The detector will move as a single unit on a steel platform which contains the detector movement and leveling equipment, cryogenic and electrical services, electronics, cabling, and support for the muon PDT chambers below the detector.

The collision area is to be separated by a stacked-concrete shield wall from the assembly region. In this area the detector is to be constructed on the steel platform from modules weighing less than 50 tons. The platform will be built and parked and supplied with hookups for power and cryogenics in the assembly hall. The magnets will be powered, and the cryostats will be filled with liquid argon at only two discrete positions--parked in the assembly hall and in the on-beam position. During movement of the detector, the cryostats will be drained but kept cold. It is expected that power to the detector electronics will be kept on at all times, including during the movement onto the beam.

In this section we describe the experimental area and services that have been designed to facilitate these operations, as well as the logistics for construction of the experiment.

9.1 DO EXPERIMENTAL AREA

The DO experimental area, shown in Figs. 9.1-9.5 is comprised of the collision hall and the assembly and control area, separated by a stacked-concrete shield wall. There is a three-level area for detector work and a five-story adjoining control and work space.

The lowest level (elevation 701 ft), 22 ft below beam height, consists of a pit 4×5 ft wide by 132 ft long. This pit spans both the collision and assembly area and contains the platform which transports the detector in and out.

At the middle level, (elevation 707 ft. 6 in.) is a "sidewalk" which completely surrounds the pit. The sidewalk height matches the top of the detector platform and permits parts of the detector to be rolled on and off the platform. The sidewalk is wide enough to permit complete disassembly of the detector pieces in the assembly area (see Fig. 9.2) and to permit access to the central tracking system. In the assembly area the sidewalk also provides work space around the detector.

In the assembly area there is a third level, an upper staging area, (elevation 737 ft) serviced by the 50-ton building crane. This area of 75 ft×75 ft, permits delivery of detector components through a truck ramp. The door, 19 ft wide × 20 ft high, will allow delivery of the huge cryostats. In this area detector components will arrive and be subassembled and checked out. During the transition between fixed-target and collider-beam modes, the shield wall separating the assembly and collision halls will be unstacked by the building crane and the blocks stored in this upper level.

The cryogenic liquid storage nitrogen at grade level, and argon at sidewalk level will be along the south side of the assembly area. On the north side of the assembly area is an attached five-level work area. The

bottom level will be used for the experimental control room, and level 2 trigger system. The second level will house the online computer. The third level contains office space, meeting rooms, and clean work space. The top two levels have been reserved for building mechanical utilities such as pumps, chillers, fans, etc.

Running along the north sidewalk will be a three-story moving counting house (MCH) which houses the fast electronics. The MCH is connected by a simple festoon to the detector permitting the distance from MCH to detector to increase to allow the shield wall to be stacked in between them (see Fig. 9.6). Emanating from the MCH are the computer lines and power cables, which festoon between the MCH and the control area. Use of the MCH provides a factor of three reduction in the detector cable length, drastic savings in cable festoon systems, and in manpower to install them.

The shield door between the collision hall and the assembly area is similar to that for UA1 and UA2 at CERN. The door consists of two layers of blocks which are stacked to provide 6 ft of additional space on whichever side the detector sits. Thus when the detector is in the collision hall the blocks start 6 ft away from the door opening. This also provides crane coverage into the collision hall by removing the "cap" that seals the door at the top (see Fig. 9.5).

9.2 DETECTOR PLATFORM

The entire detector will be supported by a steel platform. The platform shown in Fig. 9.7 spans the width of the pit (45 ft) and is 38 ft long. It will be constructed of two longitudinal and two transverse "built-up" box-beams as shown in Fig. 9.7. It will weigh about 40 tons.

Underneath the transverse members of the platform will be four hydraulic rams to move the detector. Only two rams will be used at a time as the detector will always be pushed. Each ram will have a capacity of 300 tons and have a self-locating foot which pushes against cross ties in the rails. The loaded platform will move on Hillman rollers of 500-ton capacity. In the parking position, the load is transferred from the rollers to 32 mechanical screw jacks, allowing the platform elevation and level to be adjusted by hydraulic cylinders.

On top of the platform, the muon toroids will move on 300-ton rollers on hardened tracks. Each toroid piece will be driven by a pair of 50-ton screw jacks which will pull or push against tongues on the tracks. These tracks will be duplicated on the sidewalk to permit motion of the pieces on or off the platform. The sidewalk tracks can be placed at any location and can be independently leveled to the platform tracks.

Along the center of the platform will be an iron beam 44 ft long, 5 ft wide, and 3 ft 6 in. high. This central beam completes the magnetic circuit for the central and end toroids, and also provides the mechanical support for the (fixed) central calorimeter, and (moveable) end calorimeters.

The top and bottom surfaces of the platform will be covered as completely as possible with PDT planes to provide coverage for downward going muons. These PDT's will be covered by gratings to provide personnel access without disturbing alignment.

The interior volume of the platform will be utilized for detector services (see Fig. 9.8). The calorimeter BLS electronics and trigger cluster summing electronics will be located here as well as the digitization electronics for the central tracking system. All of the detector electronics power supplies will be placed in the table and monitored remotely. Cryogenic and vacuum hookups, magnet power and cooling connections will be made through the table. Chilled water for cooling electronics as well as fans for air cooling and platform ventilation will also be installed. Finally, space is reserved for monitoring systems (gas flow, etc.) and for chamber gas buffer volumes.

9.3 MOVABLE COUNTING HOUSE AND CABLING

In order to minimize cable runs between the detector mounted electronics (i.e., ADC, TDC, etc.) we have designed a moveable counting house (MCHO, containing the digitization electronics, connected to the detector by a simple cable umbilical which allows MCH to follow the detector from assembly to collision hall (see Fig. 9.6).

The MCH consists of three floors, each 25 ft long × 15 ft wide. Each floor corresponds in elevation to a floor of the controls and computer area on the north side of the assembly area. The MCH has two parking spots on this north sidewalk at the east end when the detector is in the assembly area, and at the west end when the detector is in the collision hall. When parked in either of these spots,the MCH can communicate with the controls area through doors on each level.

All levels of the MCH have 16 racks of electronics in two rows, as shown in Fig. 9.9. This allows space for service behind the racks as well as ample space for personnel and scopes between the row for installation and checkout of electronics. Communications between levels and with the control area will be by intercom. Each level of the MCH is equipped with a raised computer floor to facilitate cabling, power, and cooling (mostly by chilled water).

The estimated number of signal cables to be brought from the detector to the moving counting house is 25,000 twisted pair. The breakdown from specific detector groups is as follows: Approximately 10,000 twisted pair (tw pr) from central tracking; approx. 3500 tw pr multiplexed from all calorimeters (based on 25k central individual signals, 10k × 2 endcap, 5k × 2 endplug), and 8k tw pr from calorimeter triggers (4000 towers × 2 (em and hadronic)); approximately 1200 tw pr from muon signals and 1200 tw pr from muon trigger. With additional monitoring and spare cables the DO detector should plan on 25,000 tw pr of signal cables to the movable counting house.

The type of cable we plan to use is the Spectra-Strip twist'n'flat ribbon cable, 34 conductor/17 twisted pair, either standard or jacketed (with ground planes surrounding signal lines). With this type of cable we would have approximately 1500 ribbon cables with a cross-section of about 21 in. × 21 in. The cable run from the detector to the movable counting house would be 150 ft with a total weight of about 6.3 tons (84 lbs/ft).

The signals from individual detectors are brought to electronics modules mounted on or in the detector support table. The individual detector's ribbon cables are grouped in bundles and are taken up along I-beams, which are placed at the corners of the detector table, which in turn support 48-inch wide tray structure at the top of the detector (see Figure 1). The individual bundles are led to one corner (the fixed counting room side) and to an 8 ft high support structure. Here the individual bundles are grouped together and go as a unit up the support structure to where the cables are lifted over the shielding door. Shielding material is placed around the umbilical over the main shielding blocks. The umbilical bundle then goes horizontally about 20 ft in a loop to a festoon car where the bundle is supported and secured. The festoon car is mounted on the side of the movable counting house, at the top. The bundle is then fed down and fanned out to appropriate locations in the movable house.

The distribution of the individual detector's signal cables in the movable house start on the top level. The top level is for the central tracking and TRD signal processing, followed in turn by calorimeter signal processing on the middle level and trigger and detector monitoring on the bottom level.

The movable counting house processes the analog, track positioning, triggering, and monitoring signals. The processed information is now in

digitized form and is then sent along a much reduced bundle of cables to the fixed counting room. This bundle, now about 3 in. in diameter and 100 ft long, is supported by a small festoon system mounted on the fixed counting house wall.

Emanating from the MCH are the cable buses to the level 2 trigger. The total area of this bundle is 15 sq in. (a two order of magnitude reduction) which must be festooned between the MCH and the fixed control/computer areas. In addition, power cables-supplying the 250 kW for the MCH, and 100 kW for the detector mounted electronics, and chilled water for cooling, must be supplied to both detector and MCH. This will be accomplished by two fixed connections and a temporary hookup for travel in between.

9.4 COMPUTER AND CONTROL ROOMS

Housed in the lowest two levels of the five-story work area on the north side of the assembly area, are the experimental control and computer area.

The lowest level, is at the same elevation as the sidewalk in the assembly area. This level contains the level 2 microprocessor system, the control room area, and a clean electronics work area. The control room contains all detector monitoring systems, accelerator monitors, cryogenics control systems, and the magnetic tape units for data.

The second floor houses the online computer and contains space for many terminals and users. It is expected that most software development will be done on the second floor, while hardware checkout and debugging will be done from the control room.

9.5 ASSEMBLY LOGISTICS

Because of the size and weight of the major detector pieces, the sequence of assembly in the hall will be tightly constrained. The first job after beneficial occupancy of the hall will be the fabrication of the detector platform and its associated hydraulics. Then two end toroids (EF) will be fabricated on the table and then rolled off the table and parked on the sidewalks close to the shield door. At this point the central iron clamshells (CF) can be constructed on or off the platform. Then one can be parked on the rear sidewalk and the other on a temporary stand in the pit near the shield wall. This will complete the heavy construction and welding to be done in the hall and work on the cryogenic calorimetry construction can begin. The central calorimeter cryostat will be installed on the central beam of the platform, and the work of installing the uranium plate-readout stack modules will start. Simultaneously the work of installing PDT planes around the parked iron sections can proceed. The endcap calorimeters can then either be assembled on the platform or at any of several places on the back of side sidewalks. The two-plug calorimeters, weighing less than 50 tons, can be assembled outside the hall and be installed intact by the building crane.

It has been determined that all testing of magnets and any work with cryogenic liquids will only be performed on the detector platform, and only when the platform is in its parked position at the end of the pit. This simplifies safety considerations and also reduces the number of cryogenic and power spigots required in the hall.

9.6 ACCESS IN THE COLLISION HALL

During TeV I operation, it is expected that access to the detector can be made during machine down periods. These periods will probably be several hours every few days and two days every two weeks. It is imperative that maintenance and repair of detector components be accomplished within these periods.

During the short periods it will be possible to service all of the externally accessible components. The major fraction of these will be located within the detector platform. This includes the fast digitization electronics for calorimetry and tracking and power supplies for all detector mounted electronics. In addition the electronics mounted on all of the external PDT planes will be accessible.

If access is needed to the central tracking system or to the calorimeter preamps buried inside the detector, this will be done during a two-day down period. The detector has been designed to permit each of the iron pieces to open up to 4 ft from the closed position. Opening the iron will allow access to calorimeter electronics. For access to the tracking system the endcap calorimeters will also be moved back. We have designed the detector to allow 3 ft of movement before the endcap will be limited by the plug calorimeter. The plug calorimeter stays fixed while the end iron that supports it rolls out beneath it.

A two day down period will allow sufficient time to drain and refill an endcap, but it is hoped to design the system such that this will not be necessary.

FIGURE CAPTIONS - CHAPTER 9

9.1 DO experimental area location.

9.2 DO experimental area plan at sidewalk elevation.

9.3 DO experimental area plan at beam elevation.

9.4 DO experimental area plan at upper assembly area elevation.

9.5 DO experimental area elevation.

9.6 Moving counting house and cable connection to detector.

9.7 Detector platform construction.

9.8 Layout of electronics racks, and services in detector platform.

9.9 Moving counting house details.

D-O EXPERIMENTAL AREA

6-3-1

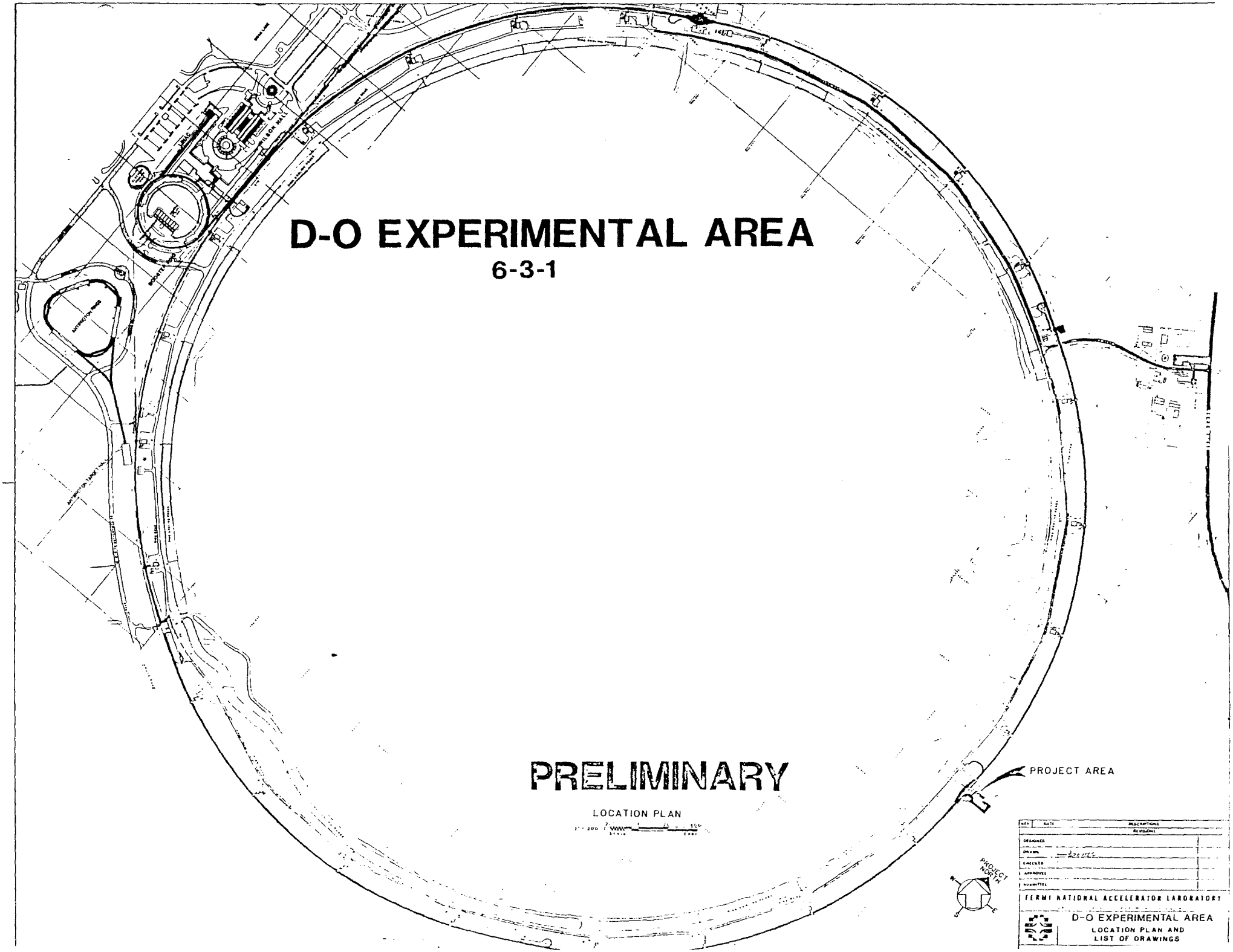

PRELIMINARY

LOCATION PLAN

PROJECT NORTH

FERMI NATIONAL ACCELERATOR LABORATORY

D-O EXPERIMENTAL AREA

LOCATION PLAN AND LIST OF DRAWINGS

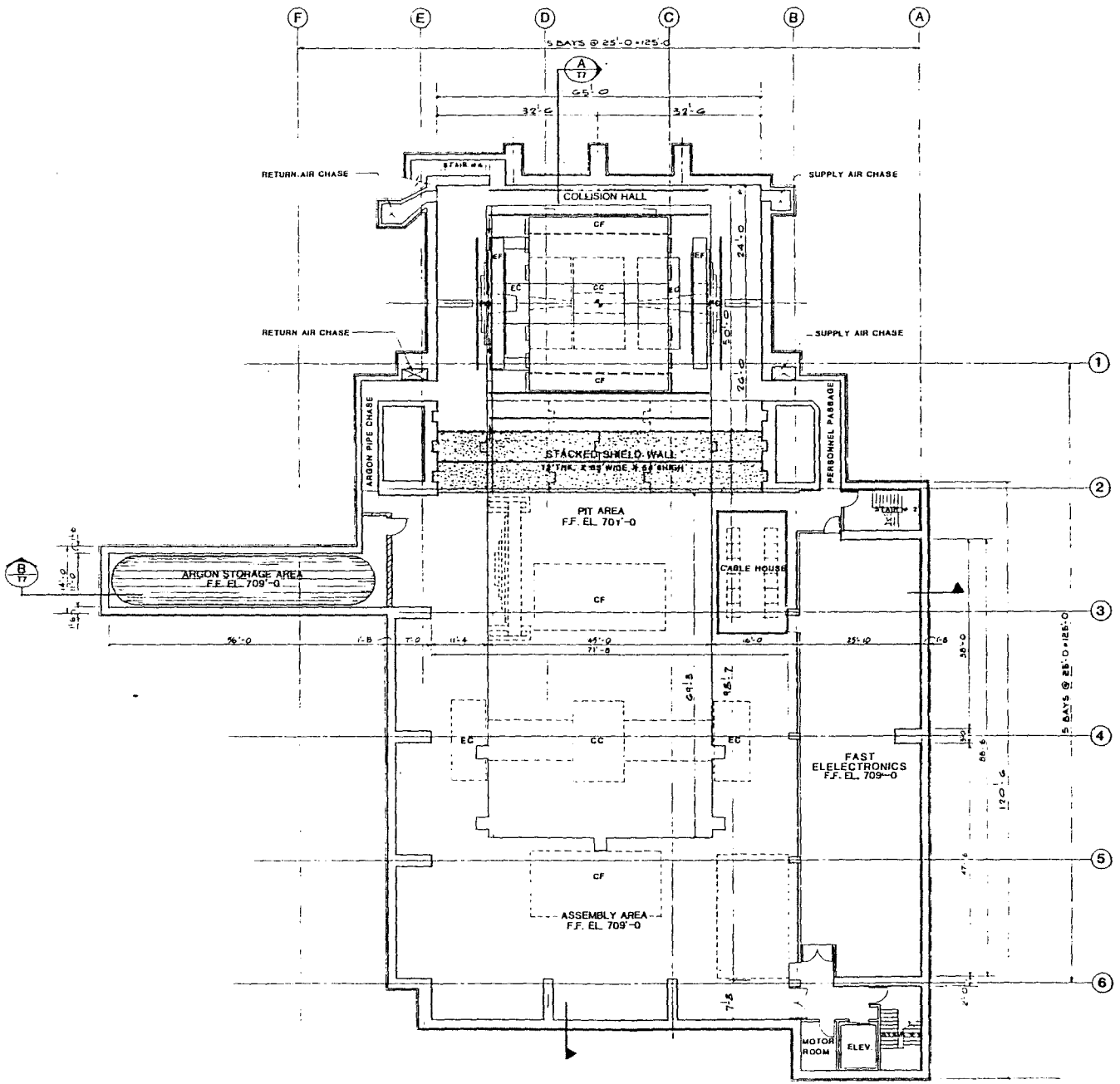

PLAN AT EL. 709'-0

REV	DATE	DESCRIPTIONS
		REVISIONS
DESIGNED		W. WESTANDER
DRAWN		
CHECKED		
APPROVED		
SUBMITTED		

PROJECT NORTH

FERMI NATIONAL ACCELERATOR LABORATORY
UNITED STATES DEPARTMENT OF ENERGY

D-O EXPERIMENTAL AREA

PLAN AT EL. 709'-0

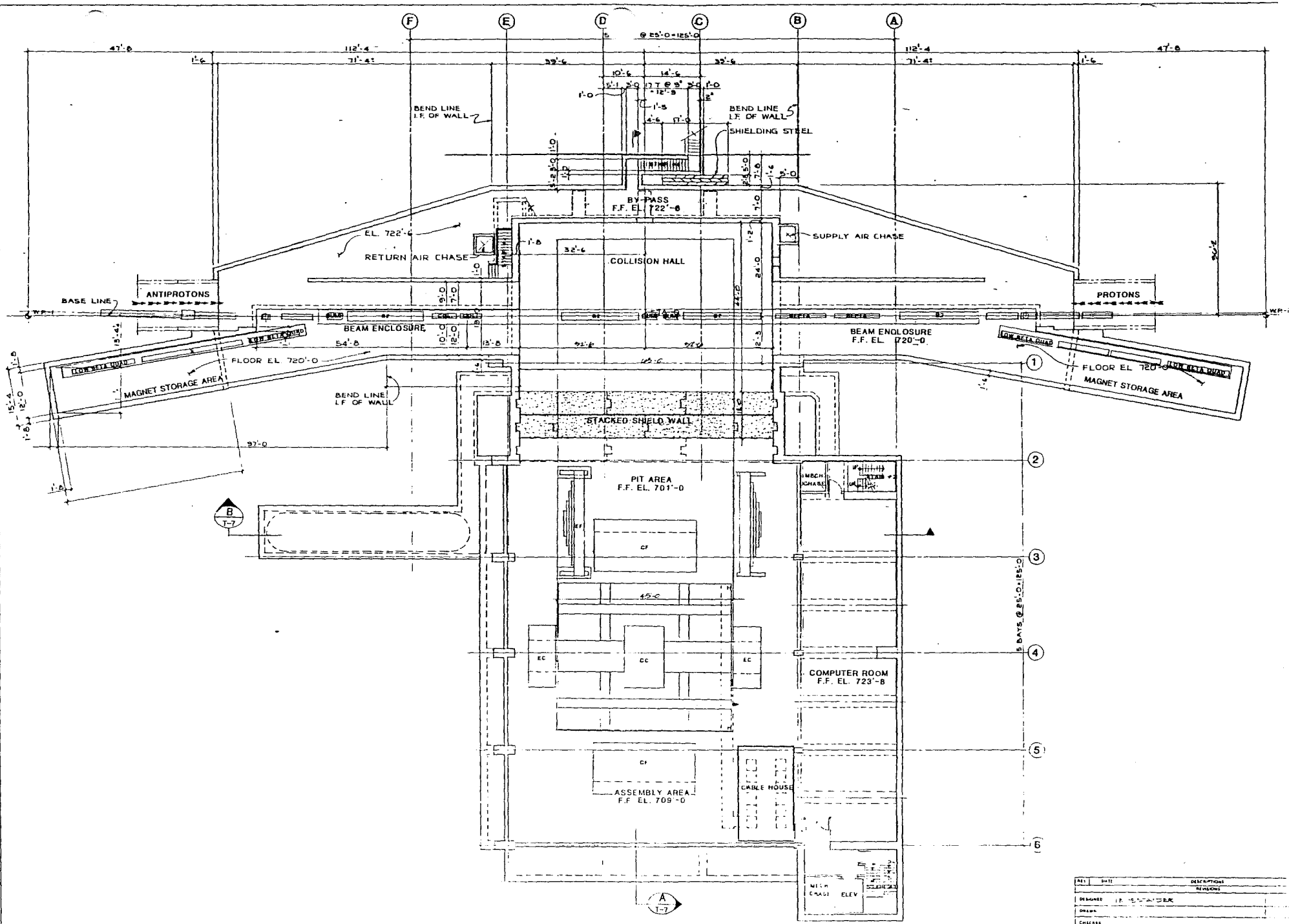

PLAN AT EL. 722'-6

PROJECT NORTH

FERMI NATIONAL ACCELERATOR LABORATORY

D-O EXPERIMENTAL AREA

PLAN AT EL. 722'-6

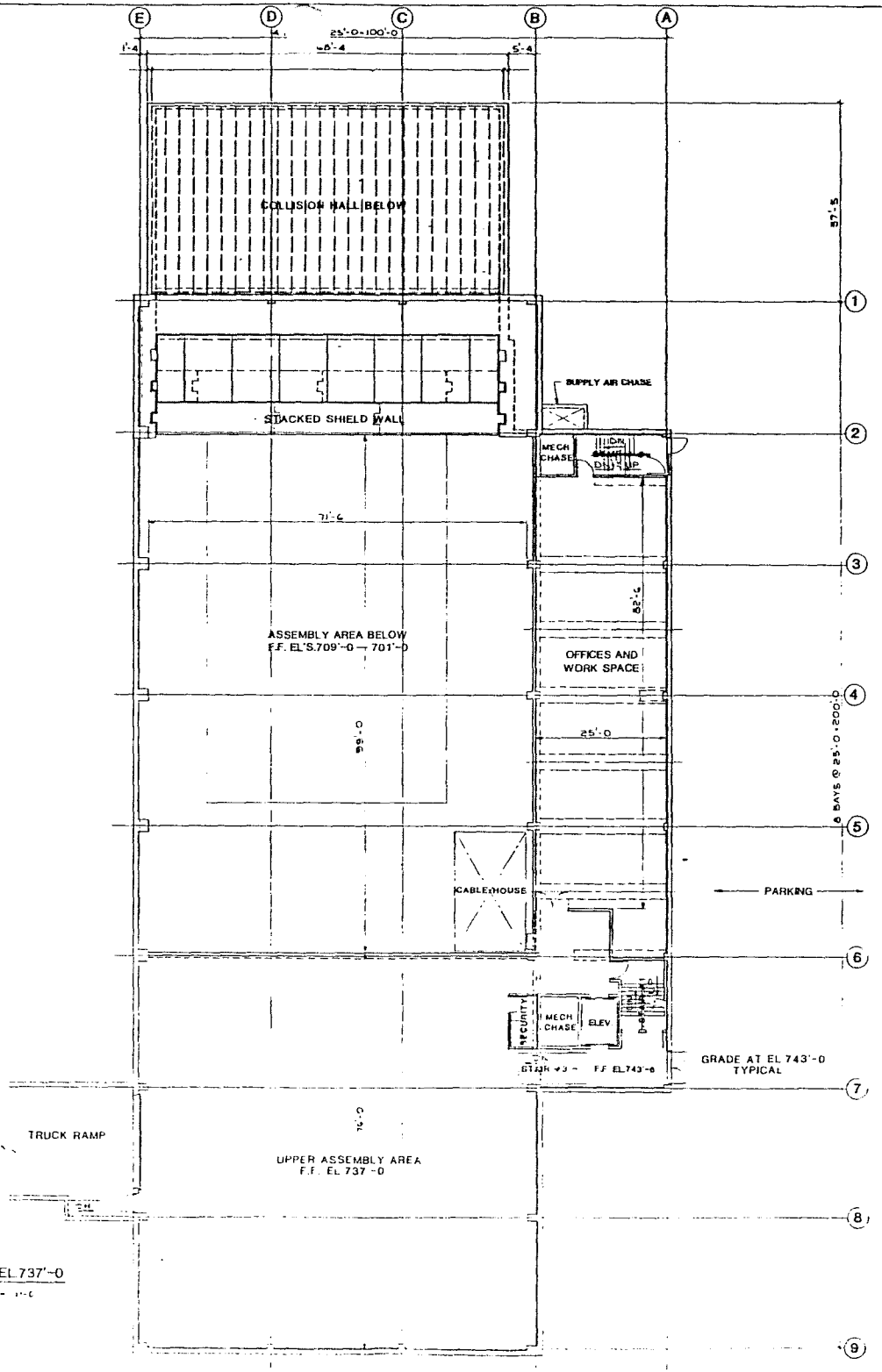

PLAN AT EL 737'-0

SCALE: 1/8" = 1'-0

REV	DATE	DESCRIPTIONS
		REVISIONS
DESIGNED		A. ALEXANDER
DRAWN		M. BOBEK
CHECKED		
APPROVED		
SUBMITTED		

FERMI NATIONAL ACCELERATOR LABORATORY

D-0 EXPERIMENTAL AREA

PLAN AT EL 737'-0

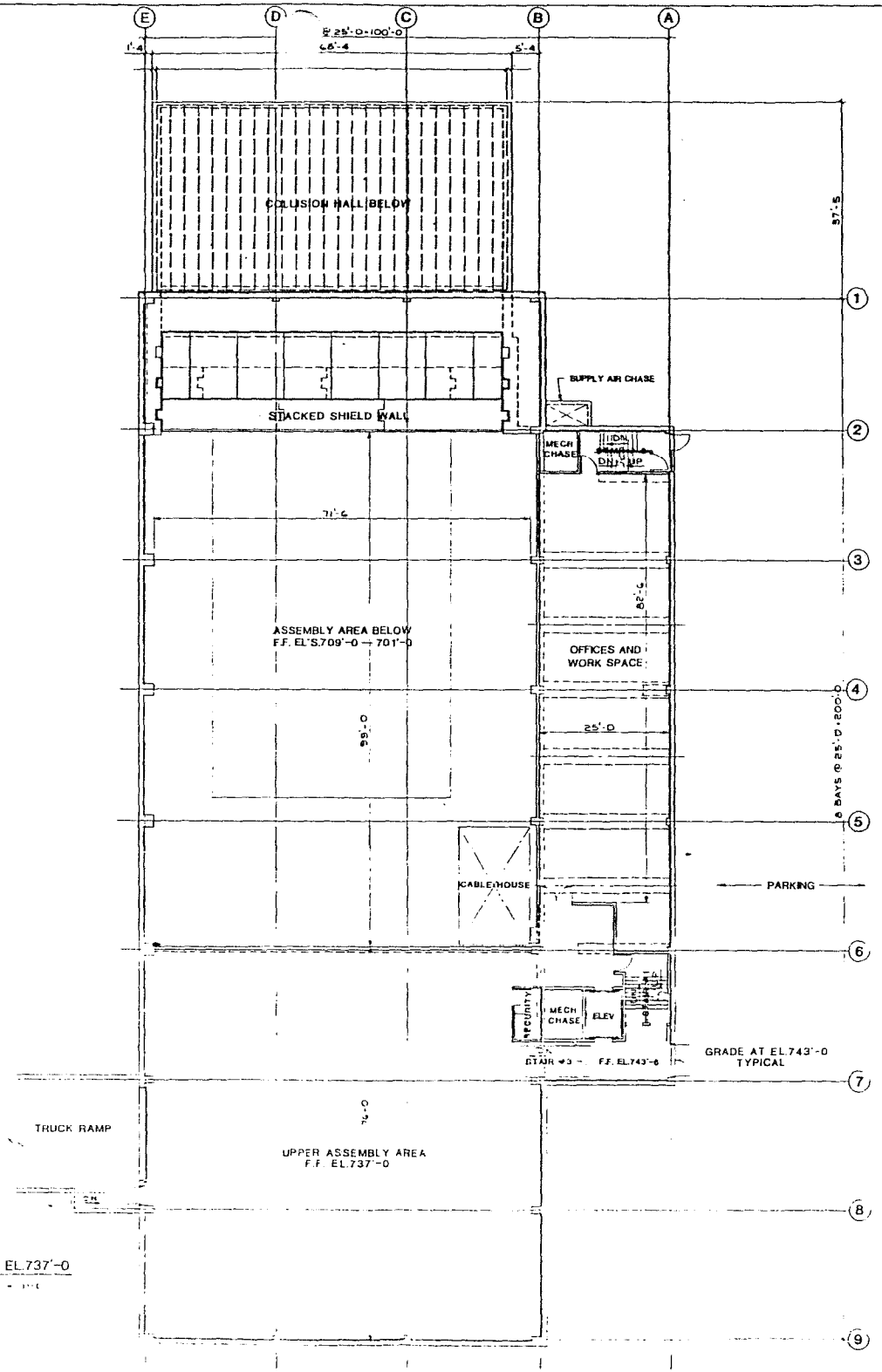

PLAN AT EL 737'-0

SCALE: 1/8" = 1'-0"

Fig 9.5

REV	DATE	DESCRIPTION
		REVISIONS
DESIGNED		A. HERTANDER
DRAWN		M. BOBEK
CHECKED		
APPROVED		
SUBMITTED		

FERMI NATIONAL ACCELERATOR LABORATORY

D-0 EXPERIMENTAL AREA

PLAN AT EL 737'-0

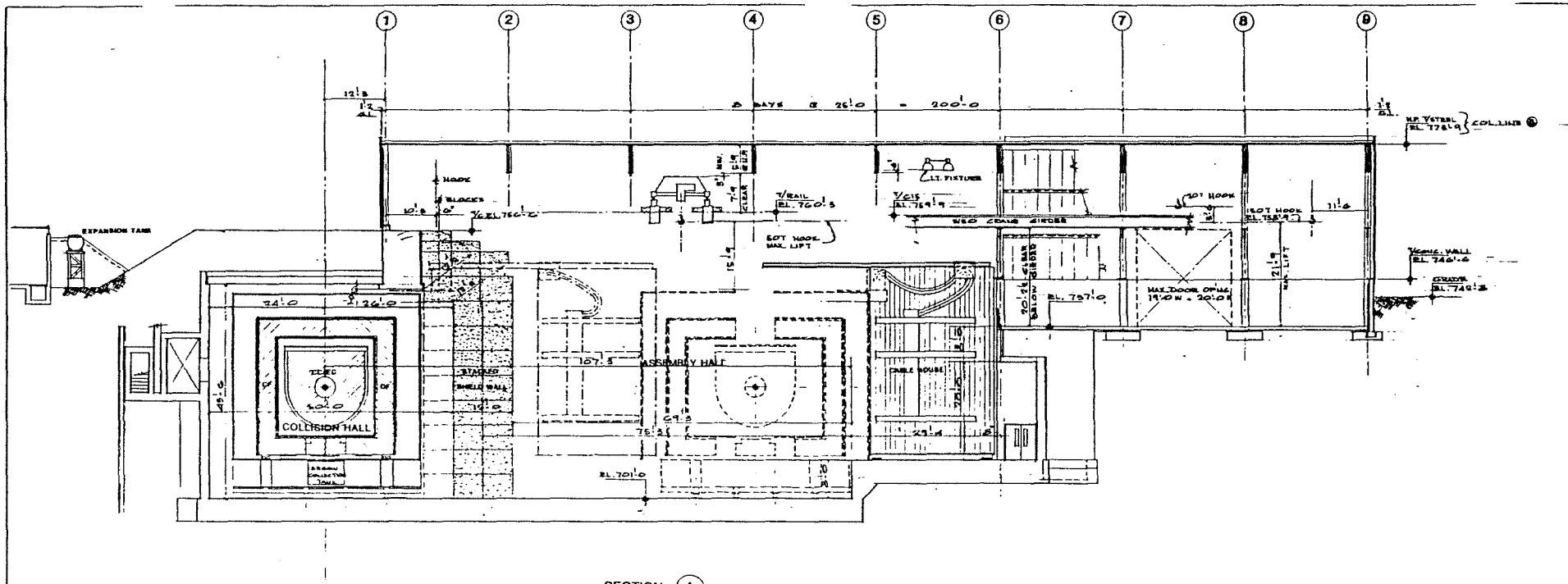

SECTION (A)

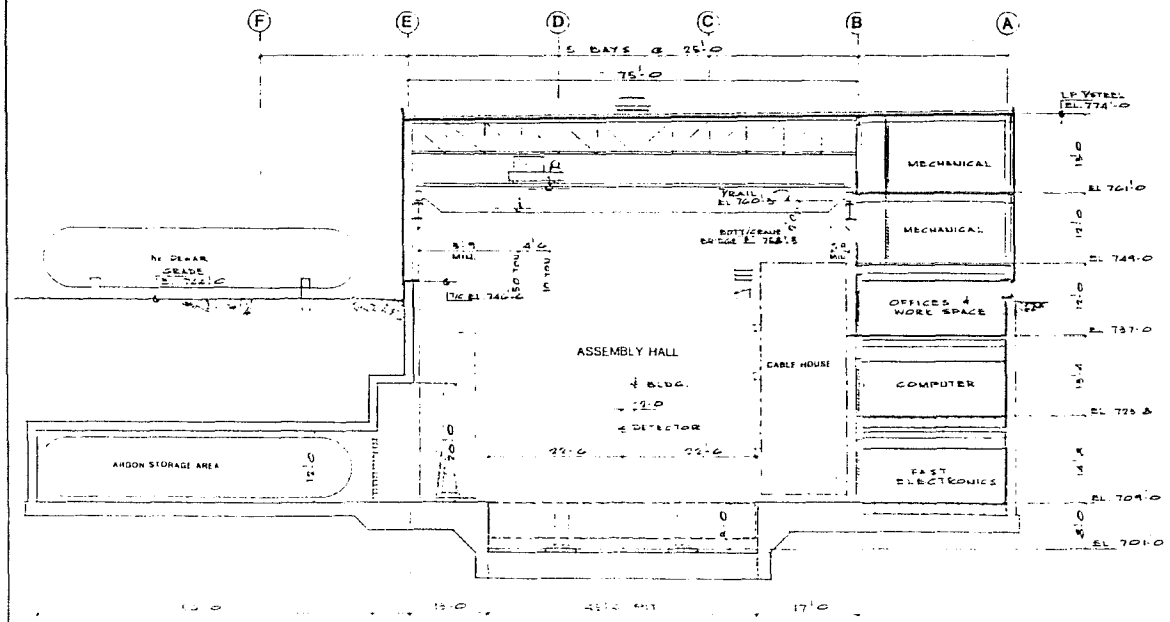

SECTION B

REV	DATE	DESCRIPTIONS REVISIONS
DESIGNED	W. SESTANOVICH	
DRAWN		
CHECKED		
APPROVED		
SUBMITTED		

FERMI NATIONAL ACCELERATOR LABORATORY

D-0 EXPERIMENTAL AREA

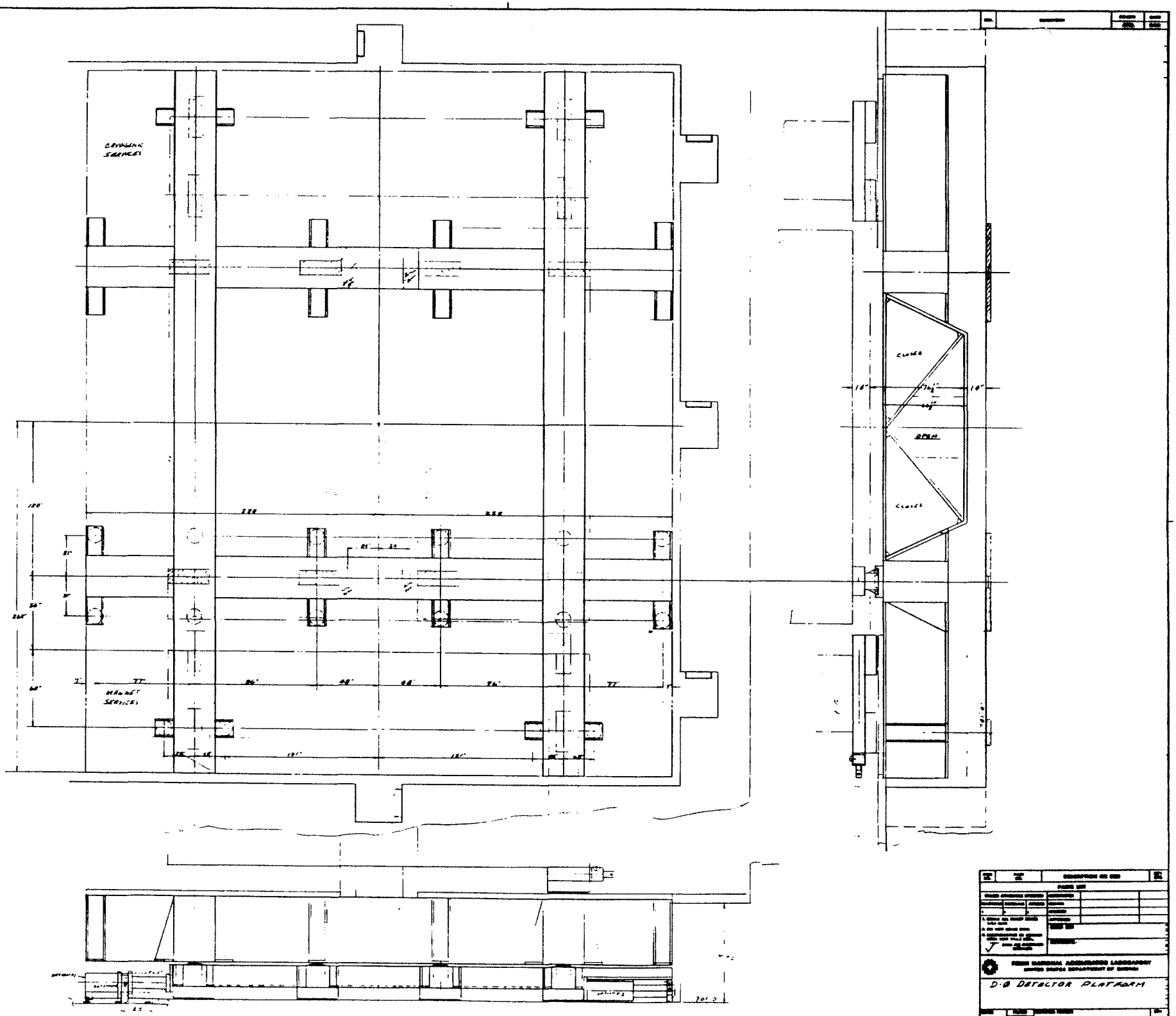

D·Ø DETECTOR PLATFORM

9230-700-MB-301747

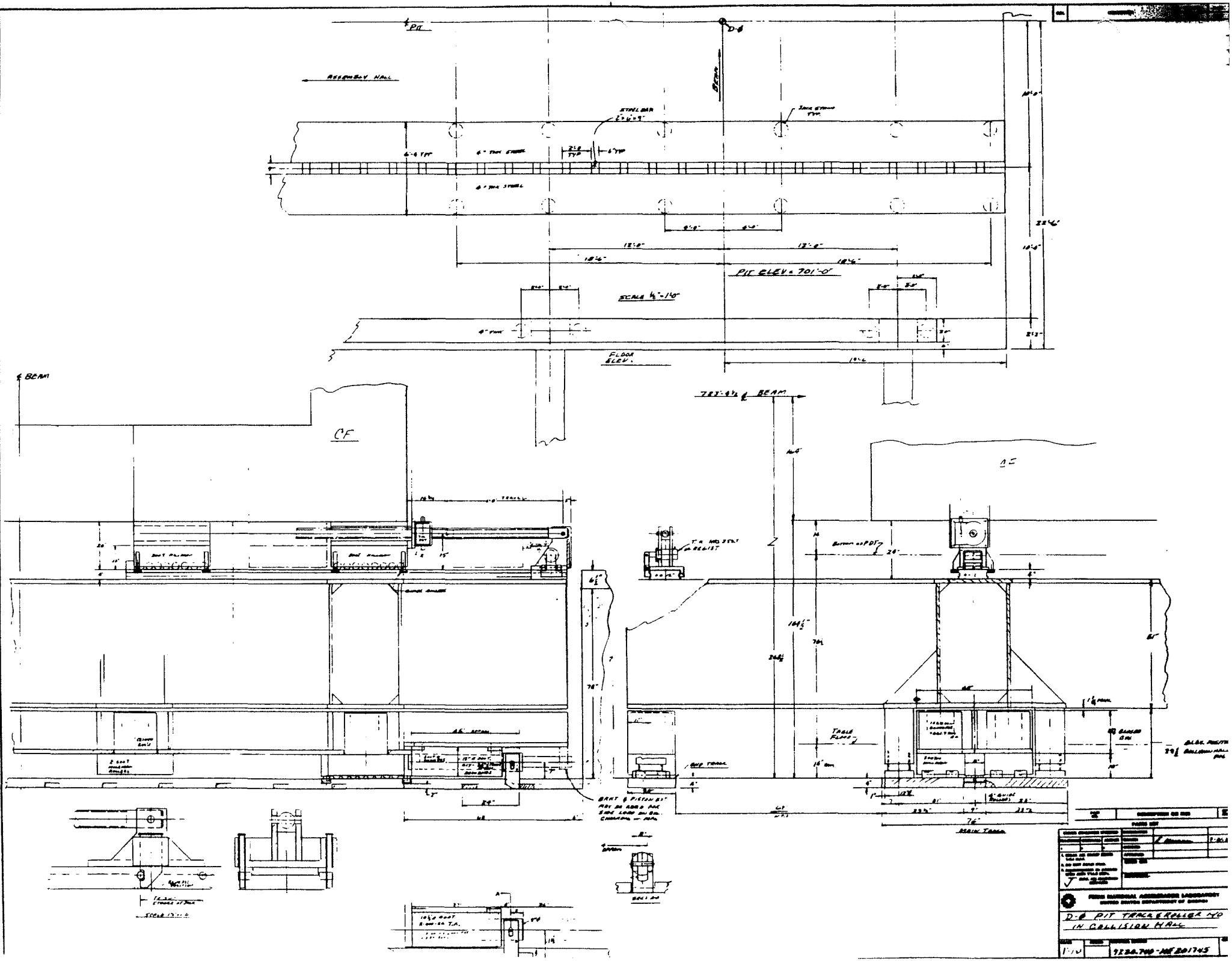

D-Ø PIT TRACK & ROLLER NO
IN COLLISION HALL

FERMI NATIONAL ACCELERATOR LABORATORY

1:10

9220.740-ME201745

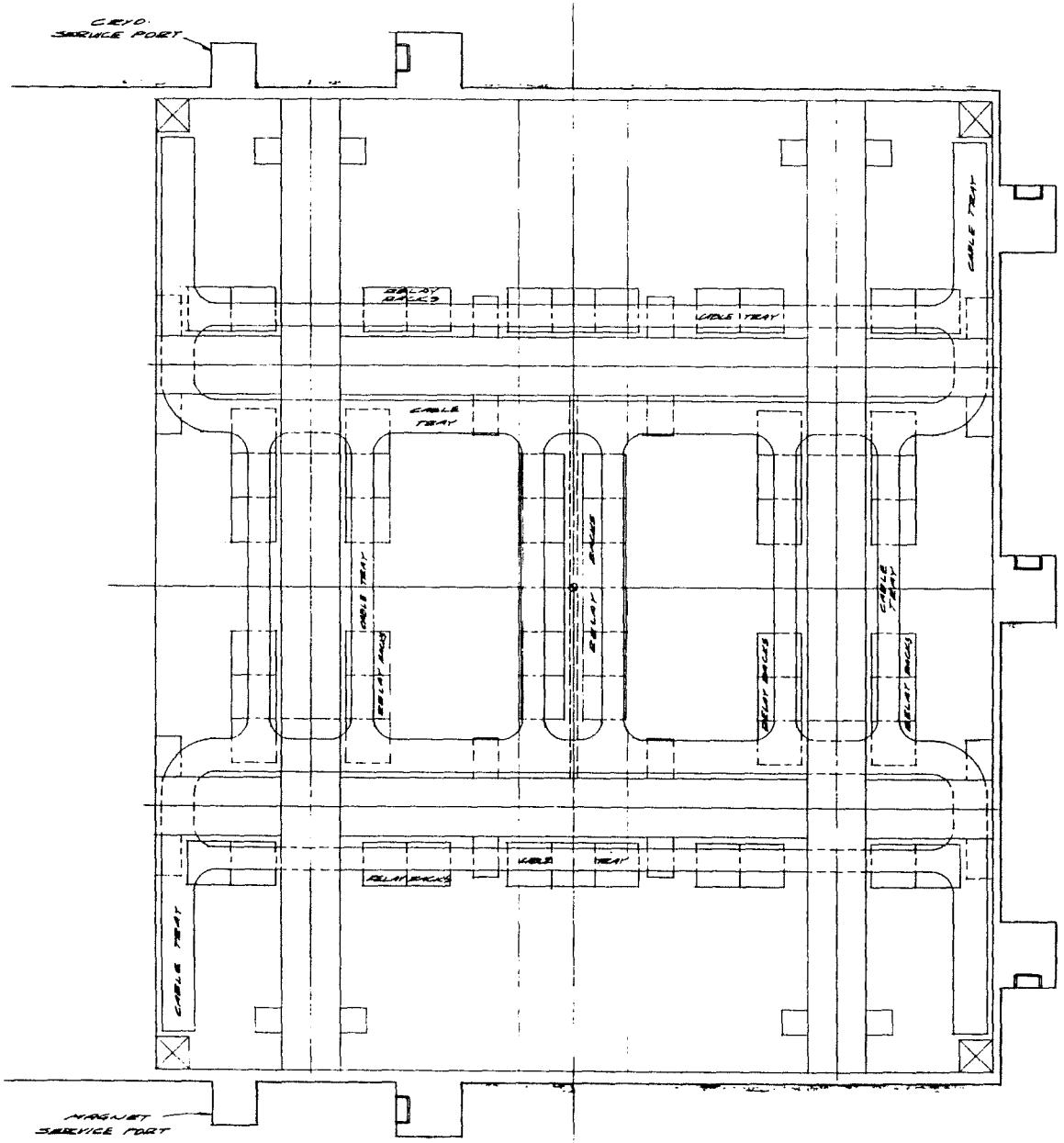

		PARTS LIST	
		DRAWN	RJOHNSON 9/5/01
		CHECKED	
		APPROVED	
		DATE	
		SCALE:	

FERMI NATIONAL ACCELERATOR LABORATORY
UNITED STATES DEPARTMENT OF ENERGY

DD TABLE PLAN
RELAY RACKS &
CABLE TRAY PROPOSAL